Effects of Photocatalytic Nanoparticle Interfaces on Biological Membranes and Biomacromolecules

Manoranjan Arakha

Department of Life Sciences
National Institute of Technology Rourkela

Effects of Photocatalytic Nanoparticle Interfaces on Biological Membranes and Biomacromolecules

Dissertation submitted in partial fulfillment

of the requirements of the degree of

Doctor of Philosophy

in

Life Sciences

By

Manoranjan Arakha

(Roll Number: 512LS1006)

based on research carried out

under the supervision of

Dr. Suman Jha

February, 2017

Department of Life Sciences

National Institute of Technology Rourkela

Department of Life Sciences
National Institute of Technology Rourkela

February 18, 2017

Certificate of Examination

Roll Number: 512LS1006

Name: Manoranjan Arakha

Title of Dissertation: Effects of photocatalytic nanoparticle interfaces on biological membranes and biomacromolecules

We the below signed, after checking the dissertation mentioned above and the official record book (s) of the student, hereby state our approval of the dissertation submitted in partial fulfillment of the requirement of the degree of *Doctor of Philosophy* in *Life Sciences* at *National Institute of Technology, Rourkela*. We are satisfied with the volume, quality, correctness, and originality of the work.

Suman Jha
Principal Supervisor

S. K. Bhutia
Member, DSC

N. Sarkar
Member, DSC

B. Nayak
Member, DSC

A. K. Panda
External Examiner,
N.I.I. New Delhi

B. Mallick
Chairperson, DSC

S. K. Bhutia
Head of the Department

Department of Life Sciences
National Institute of Technology Rourkela

Dr. Suman Jha
Assistant professor

February 18, 2017

Supervisor's Certificate

This is to certify that the work presented in this dissertation entitled *"Effects of photocatalytic nanoparticle interfaces on biological membranes and biomacromolecules"* by *"Mr. Manoranjan Arakha"*, Roll Number 512LS1006, is a record of original research carried out by him under my supervision and guidance in partial fulfillment of the requirements of the degree of *Doctor of philosophy* in *Life Sciences*. Neither this dissertation nor any part of it has been submitted for any degree or diploma to any institute or university in India or abroad.

Suman Jha
Assistant professor

DEDICATED TO MY PARENTS

Manoranjan Arakha

Declaration of Originality

I, *Manoranjan Arakha*, Roll Number: 512LS1006 hereby declare that this dissertation entitled *"Effects of photocatalytic nanoparticle interfaces on biological membranes and biomacromolecules"* presents my original work carried out as a doctoral student of NIT Rourkela and, to the best of my knowledge, it contains no material previously published or written by another person, nor any material presented for the award of any degree or diploma of NIT Rourkela or any other institution. Any contribution made to this research by others, with whom I have worked at NIT Rourkela or elsewhere, is explicitly acknowledged in the dissertation. Works of other authors cited in this dissertation have been duly acknowledged under the section "Bibliography". I have also submitted my original research records to the scrutiny committee for evaluation of my dissertation.

I am fully aware that in case of my non-compliance detected in the future, the Senate of NIT Rourkela may withdraw the degree awarded to me on the basis of the present dissertation.

February 18, 2017
NIT Rourkela

Manoranjan Arakha

Acknowledgment

This research was supported by the Department of Science and Technology, the Ministry of Human Resource Development, and the National Institute of Technology Rourkela, India. In last four years, I have gained one of the most valuable experiences of my life. At this juncture, I would like to express my appreciation to one and all those have contributed to successfully complete the work.

First of all, I would like to express my heartfelt gratitude towards Dr. Suman Jha for his expert guidance, supervision, advices, and for giving me the opportunity to learn advanced techniques and its applications in the field of Nanoscale biophysics. I would also like to thank Dr. Jha for the enlightening discussions and suggestions on designing experiments, scientific writing, and various other matters that has and will help in advancing my career.

My special thanks are to Prof. S. K. Sarangi, Ex-Director, and Prof. A. Biswas, Director, National Institute of Technology, Rourkela for making all the facilities available to successfully complete the work.

I am also very thankful to all the members of my doctoral scrutiny committee Dr. B. Mallick (chairman), Dr. S.K. Bhutia (member), Dr. N. Sarkar (member), and Dr. B. Nayak (member) for their thoughtful suggestions, inspiration and continuous encouragement throughout the research work.

Additionally, I thank Dr. Bibekananda Mallick for providing me the mammalian cell culture facility and Dr. Mohammed Saleem for his expert guidance and support during my research work.

I also take this opportunity to thank Dr. Bairagi C. Mallick, Ravenshaw University, Odisha, and Dr Mamata Mohapatra, Department of Hydro & Electrometallurgy, Institute of Minerals and Materials Technology, Bhubaneswar, Odisha, India for helping me with electron microscopy image analysis and atomic absorptions spectroscopy analysis, respectively. I am also thankful to Dr. Anupam Nath Jha, Department of Molecular Biology and Biotechnology, Tezpur University, Assam, India for his kind help during various computational studies for the work.

I would like to acknowledge all the faculty members and the supporting staff members, Department of Life Sciences, N.I.T. Rourkela for their timely co-operation and support at various phases of experimental work.

I would like to extend special thanks to my dear friends, Sandip kumar Rath, Kirtikant Sahoo, Avadhoot Bhosale, Kanti Kusum Yadav, Parth Sarthi nayak, Shreyashi Asthana, Asutosh Prince, Anuj Tiwari, Stuti Pradhan, Sweta Pal, Abhipsa Swain, and others for their valuable suggestions and encouragements during my Ph.D. carrier.

I will be failing in my duty, if I do not acknowledge the constant co-operation and support of my family members, who have always been a source of inspiration for me.

Above all, I would like to thank the Almighty for his enormous blessings and guiding me in the right direction in life.

.

February 18, 2017
NIT Rourkela

Manoranjan Arakha
Roll Number: 512LS1006

Abstract

Inside the biological milieu, nanoparticles come in myriad shape and size those upon interaction with different biomolecules form nano-biomolecular complexes. The interface formed as a result of nanoparticle and biomolecular interactions determines fate of both the nanoparticle and biomolecules inside the biological milieu. Accordingly, investigating the interaction pattern at different interfaces will help in optimizing the use of nanoparticle for relatively wider biomedical applications. Hence, the thesis intends to study the effects of different photocatalytic nanoparticle interfaces on biological membranes, like prokaryotic and eukaryotic membranes, and biomacromolecules, like nucleic acid and protein. To this end, photocatalytic nanoparticles, such as zinc oxide (ZnONP), iron oxide (IONP) and silver (AgNP) nanoparticles, were synthesized using chemical synthesis or green synthesis methods. Initially, the effects of interfacial potential and interfacial functional groups were studied against Gram-positive and Gram-negative bacteria. The studies demonstrated that the interfacial potential and surface functionality significantly affect interaction pattern at the interface, which defines anti-bacterial/cytocompatible property of nanoparticles. In addition, second part of the thesis explored the effect of nanoparticle surface defects on cytotoxic and antimicrobial propensities of nanoparticle. The study revealed that energy band gap reduction significantly enhances the oxidative stress in cells, leading viable cells into non-viable cells. The second part, unlike the first part of the thesis where the focus was cell membrane functionality, focused on the interface effects on nucleic acid. Third objective of the thesis observed photocatalytic nanoparticle interaction with antimicrobial peptide (AMP), like nisin, and its effect on the peptide conformational and functional dynamics. The interaction leading into nisin assembly onto AgNP interface enhanced the efficacy of peptide by many folds, without significant change in peptide conformation. Whereas in fourth objective, interaction with globular protein, like lysozyme, showed that the assembly onto ZnONP interface led into conformational rearrangement that hinders the amyloidogenic propensity of lysozyme in studied conditions. Nevertheless, with increase in ZnONP fraction in the conjugate mixtures, the protein attains relatively more regular conformation than partially unfolded conformation at pH 9. Insignificant conformational changes in lysozyme assembled onto ZnONP interface was observed at pH 7.4. Thus, the findings, altogether, suggested that the physico-chemical properties of photocatalytic nanoparticle interface significantly affect the fate of biomembrane and biomacromolecules inside the biological milieu.

Key Words: nanoparticle; Biomacromolecule; surface potential; nano-bio complex; interface.

Contents

List of Figures

Chapter 1

Introduction

1.1. Nanoparticle

Fifty seven years ago, on the evening of 29th December 1959, best known paper of nanotechnology entitled "There's Plenty of Room at the Bottom" was delivered by physicist professor Richard Feynman to the American Physical Society at the California Institute of Technology in Pasadena[1]. In the paper, Dr. Richard Feynman described about the possibilities, if we could learn to control single atoms and molecules[1]. The work led the community into the era of nanotechnology. Hence, the essence of nanotechnology is based on the ability to work at the molecular and atomic level to formulate fundamentally new molecular structure with advance physico-chemical properties[1-2]. The combination of science and technology for the nature of material at nanoscale provides a strong foundation for nanotechnology[3]. The growth of nanotechnology is a convergence and divergence process. For example, the convergence in understanding of nanotechnology reached its maximum strength by 2000 AD, and one may expect divergence in applications of nanotechnology in coming decades[3].

Among various nanotechnology fields, nanobiotechnology has been considered as a most emerging field, all because of its various applications in molecular diagnostics, material sciences, and bioengineering. The definition of nanoparticles has been suggested by National Nanotechnology Initiative (N.N.I.), U.S.A. According to N.N.I., particles with size range from 1 to 100 nm in at least one dimension are called nanoparticles[4]. Moreover, the widely applied term 'nano' is adapted from a Greek word, meaning 'dwarf'. 'Nano' is also used as a prefix for 10^{-9} magnitude[5]. Nanoparticles have drawn great scientific interest as they bridge the physico-chemical gap developed between bulk (macroscopic) material and atomic or molecular structure[5]. The unique characteristic properties of nanoparticle are quite different from macroscopic material. The differences are mainly developed from high surface to volume ratio as well as improved percentage of grain boundaries of nanoparticles[6]. These unique features of nanoparticles have drawn the attention of various research groups to employ nanoparticles in various fields of science and technology. Hence, to do so, the synthesis of different nanoparticles with advanced physico-chemical properties has become a major interest in current era.

1.2. Synthesis of nanoparticles

Different protocols have been optimized to synthesize different types of nanoparticles that meet the requirements of different nanoparticle-mediated applications. The synthesis protocols are broadly divided into two categories such as top-down (physical process) and bottom-up (chemical and biological processes) approaches[7-8]. Generally, in top-down approach, the nanoparticles are formulated from their bulk material or constituents. Examples of some top-down approaches are high energy ball milling, where the nanoparticles are produced from the milling of their respective bulk material. Another approach is wire explosion method, conducting metal nanoparticles are produced from an explosion due to a sudden high current pulses. In inert-gas condensation method, evaporated atoms from bulk material are condensed in a matrix, and the respective nanoparticle growth is achieved. Laser ablation approach is another physical method for nanoparticle synthesis, where higher energy laser is used to induce evaporation. In the top-down approaches, shape, size and composition of nanoparticles can be monitored by controlling different physico-chemical parameters. The methods produce lager quantity of nanoparticles, however with polydisperse nature[7].

In the later approach, *i.e.* in bottom-up (chemical or biological processes) approaches, the elements generated from respective ion reduction, assemble into nanoparticles. Since the process is initiated from atoms, the processes are also known as bottom-up approaches[7-8]. Few examples, in chemical approaches, the reducing agent like sodium borohydride ($NaBH_4$) helps in reduction of metal ions into atoms, and the reduced atoms assemble to form nanosize crystals, hence nanoparticles. Photochemical synthesis is another method for nanoparticle synthesis, which is assisted by light. Nanoparticles are synthesized with the help of ultrasound in sonochemical routes. Microemulsion is an approach for synthesis of nanoparticles using water in oil or oil in water emulsions. Additionally, in solvothermal synthesis, the synthesis of nanoparticles happens in a closed system from solvents at lower temperature, for example the coacervation or emulsion methods for protein nanoparticle synthesis.

It is reported that decreasing hydrophobic interaction during protein unfolding triggers the protein nanoparticle formation[9], which is an example of bottom-up approach. The protein nanoparticles are formed due to the conformational changes of protein, which depends upon its composition, cross linking, concentration, different chemical conditions

like pH, ionic strength, type of solvents etc[10]. During unfolding process, protein expresses different interactive groups like disulfides, thiols, hydroxides etc. Interestingly, thermal and chemical cross linking of the groups lead to formation of protein nanoparticles with entrapped drug molecule (Figure 1.1).

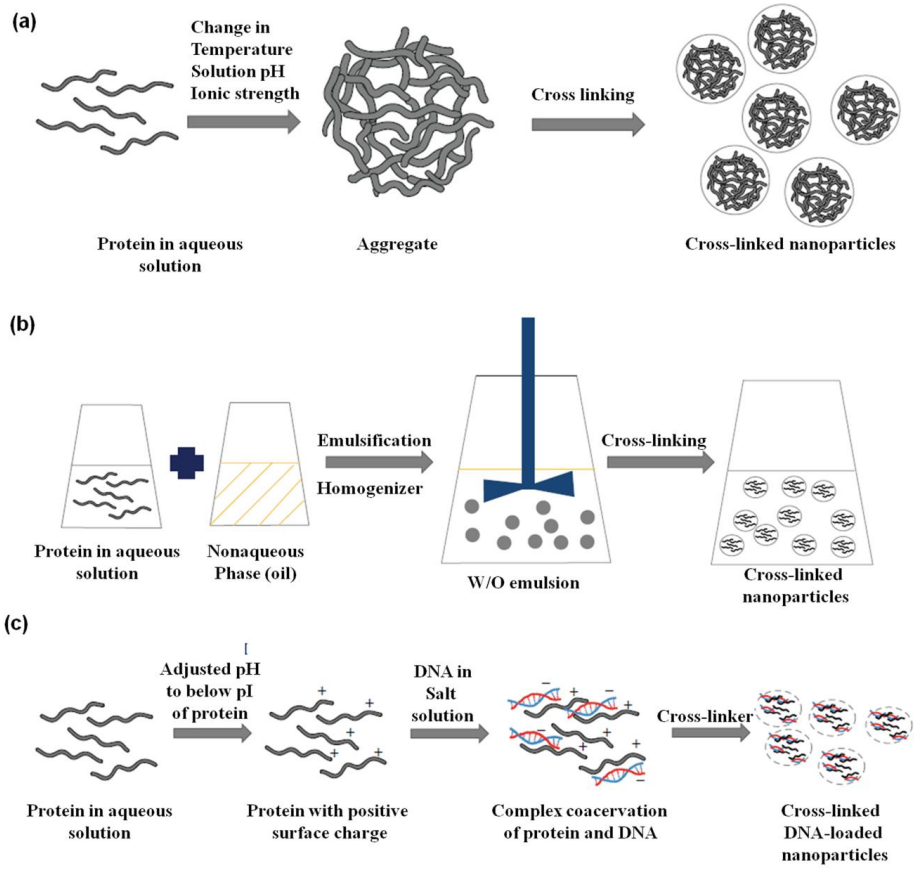

Figure 1.1. Protein nanoparticles prepared by (a) coacervation or phase separation, (b) emulsion/solvent extraction method and, (c) complex coacervation method, reproduced from Lohcharoenkal, W. *et al*[10].

Coacervation/desolvation process is one of the two well-known methods for protein nanoparticle synthesis. The process is based on differential solubility of proteins in different solvents, which is a function of solvent pH, polarity, ionic strength and electrolytes presence. As shown in figure 1.1, the process helps in reduction of protein solubility, which leads to phase separation. The de-solvating agent helps in protein conformational change leading into protein coacervation or precipitation. Size of the protein nanoparticle, formed in the process, can be controlled by controlling the processing parameters like pH, ionic strength etc. The formed nanoparticles are cross linked by different agents like glutaraldehyde and glyoxal[11]. In addition to coacervation method, emulsion/solvent extraction is another method for preparation of protein

nanoparticles. In this method, a high speed homogenizer/ultrasonic shear are being used to emulsify the aqueous solution of protein in oil. As shown in figure 1.1, the protein nanoparticles are formed at the interface of water/oil, upon emulsification. Additionally, phosphatidylcholine and/or span-80 are generally used as stabilizers for formed protein nanoparticle using the method[10, 12]. The organic solvents are used to remove the oil phase of the solution leading to formation of protein nanoparticles. The method is generally used to prepare different protein nanoparticles like albumin, whey protein etc.

Although, various physical and chemical methods have been optimized for synthesis of nanoparticles, the use of strong and weak chemical reducing agents along with protective agents like sodium borohydride, sodium citrate, and alcohols for synthesis of nanoparticles are not advisable. Most of these chemicals are expensive, toxic, flammable, and possess various environmental issues. Additionally, the processes show low production rate[8]. In many cases, elevated temperatures are required for synthesis of nanoparticles[8, 13]. Hence, in order to avoid the limitations of physical and chemical methods, biological methods (also known as green synthesis method) have been adopted for synthesis of metal and metal oxide nanoparticles, a step to avoid toxic chemicals and to make the synthesis process eco-friendly[14-15]. In addition, the biological methods are less toxic, safe, and energy efficient than the other two methods. Biological agents, commonly used for synthesis of nanoparticles, are plant extracts, extracts from microorganisms and fungi etc[14]. It is also reported that the biological agents help in reduction of metal ions at a faster rate than in other two methods, and require ambient temperature and pressure[8]. Additionally, shape and size of nanoparticles can be modulated by change in metal to extract ratios, pH, temperature of the reduction reaction, agitation etc. In this approach, metallo-enzyme present in biological agents reduces metal ions into respective elements or molecule, and the resultant elements are capped at nanosize by same biomolecules or other present in the reducing medium. Hence, nanoparticles synthesized by the method have functionalized surface because of absorption of different cellular moieties as a capping agent or stabilizer[8].

1.3. Different kinds of nanoparticles

According to different applications of nanotechnology, different methods have been optimized to fabricate different kind of nanoparticles. Different nanoparticles are metal/metal oxide nanoparticles for antimicrobial-/magnetic-/photocatalytic-/heavy metal

adsorption applications, liposome nanoparticle for microRNA/drug delivery application, protein nanoparticle for biocompatible drug delivery application etc. Following is the description of different kinds of nanoparticles.

1.3.1. Zinc oxide nanoparticle (ZnONP)

Due to presence of wide band gap (3.37 eV) as well as large excitation binding energy (60 meV at room temperature), ZnONP possesses unique features like UV light absorption, semiconducting, catalytic, and antimicrobial properties etc[16-17]. In addition, ZnONP possesses unique features that are completely different from bulk ZnO material like proportion of atoms on the surface of ZnONP, electronic band gap etc[17]. Hence, ZnONP are widely used in different fields such as water and air disinfection, anticancer agents, antimicrobial agents, remediation of hazardous waste etc[16]. Along with these applications, these nanoparticles are also used for solar cells, photocatalytic applications, antivirus agent in coating, biosensors, biological imaging, etc[16, 18-19].

1.3.2. Iron oxide nanoparticle (IONP)

Due to supermagnetic nature of iron oxide nanoparticles (IONPs), they are widely used as passive and active targeted imaging agents[20]. The superparamagnetic iron oxide nanoparticles (SPIONs) contain iron oxide as the core, and an outer layer of dextran or other biocompatible compounds to make the core stable in physiological medium[21-23]. The commonly used SPIONs are magnetite (Fe_3O_4) and maghemite (γFe_2O_3). Interestingly, these SPIONs exhibit superparamagnetism in size dependent manner, so that in presence of external magnetic field they become magnetized and become neutral upon removal of the field. Additionally, SPIONs are degraded into iron and/or iron oxide molecules, which are metabolized further and stored in cells in bound form with ferritin, and finally incorporated into hemoglobin[24]. Since different magnetic nanoparticles, like SPIONs, are biocompatible in nature, chemically stable, and possess magnetic behavior, they are widely used in different biomedical applications[25]. These nanoparticles are also used for delivery of various drugs to their targeted tissues by employing external magnetic field[25]. Additionally, they are used in analytical chemistry, antigen diagnosis, tissue repair, pathogen detection, protein separation etc[24-26].

1.3.3. Silver nanoparticle (AgNP)

Even before the evolution of nanotechnology, silver metal had been used in various applications. Moreover, the understanding of nanotechnology has enhanced the applications of silver by many fold, but as AgNP[8]. Recently, because of antimicrobial property the efforts are being made to incorporate AgNP into different medical devices, surgical instruments, surgical masks etc[27]. In addition, many studies have reported the wound healing capacities of ionic silver; silver sulfadiazine is being replaced by AgNP to treat wounds[27-29]. Due to enhanced physico-chemical properties of AgNP, they are widely used in biomedical imaging, nanomedicine, biosensing, catalysis, drug delivery, nanodevice fabrications etc[27, 30]. Additionally, due to strong antimicrobial activity, the nanoparticle is widely used in production of sterile materials[8]. AgNP is synthesized from the reduction of silver salt with the help of different reducing agents like sodium citrate, sodium borohydride etc[27]. However, different stabilizing agents, such as polyvinyl alcohol, bovine serum albumin (BSA), cellulose, citrate etc., are used during the synthesis of AgNPs. Commonly used methods for the nanoparticle synthesis are chemical reduction in solution, sonochemical method, microwave assisted method, microemulsion method etc[31]. Along with these synthesis approaches, production of AgNPs using green synthesis methods have also drawn the attention of various research groups.

1.3.4. Liposome

Liposome is considered as one of the first nanoparticles formulation which were described in 1965 as a cellular membrane model[20, 32]. These are spherical vesicles containing a single or multiple bilayer of lipids, and self-assemble upon suspension into aqueous solution[33]. The unique features of liposome, which increases its use in biological applications are diverse ranges of available compositions, able to carry and protect encapsulated/adsorbed molecules, biocompatible, and biodegradable nature[20, 33-34]. Hence, the liposomes are used as transfection agents for different genetic materials like microRNA into a cell. The process is commonly known as lipofection[35]. The process forms aggregates of cationic lipids with anionic genetic material. Similarly, the liposomes are also used as therapeutic drug carriers[32].

1.3.5. Albumin functionalized NPs

In biomedical sciences, nanoparticles are widely used as drug delivery agents, since nanoparticles have the potential to protect the target drug from degradation, enhance the drug absorption efficacy, improve intracellular penetration and distribution, and modify

drug tissue distribution profile[36]. In addition, nanoparticles are widely accepted agents for drug delivery since they withstand different physiological stress, improve biological stability, high possibility of oral delivery etc[36]. Among different nanoparticles, protein-based nanoparticles have drawn the attention of researchers for their better stability during storage as well as non-cytotoxic nature[36]. Albumin is being used as a drug delivery vehicle for cancer treatment, since it act as a natural carrier for different hydrophobic molecules like water insoluble plasma substances, vitamins, and hormone etc[37]. Albumin bound nanoparticles are important class of nanoparticles which carry the hydrophobic molecules in bloodstream using endogeneous albumin pathways [38]. Albumin binds hydrophobic molecules non-covalently and avoids solvent based toxicity[39]. Hence, albumin based nanoparticles are used as drug delivery vehicles.

1.3.6. Polymeric NPs

Polymeric nanoparticles are another group of nanoparticles those are formed from the polymers having biocompatible and biodegradable properties, and are extensively used as therapeutic drug carriers, for example dendrimer encapsulated nanoparticles (DEN), protein nanoparticles (pNP) etc[40]. These are formulated from block–copolymers having different hydrophobicity. In an aqueous environment these co-polymers spontaneously self-assembled into core-shell micelle[41]. The hydrophilic and hydrophobic drugs, proteins, and nucleic acids can be encapsulated on the polymeric nanoparticles for different biological applications[42]. Polymeric nanoparticles are very much important because they help in safety and efficacy of drug they usually carry. Protein nanoparticle, one of the polymeric nanoparticles, are being treated as potential delivery agent for the anticancer drugs, since pNPs are relatively safe, easy to prepare and to control size distribution[43]. For example, albumin-based nanocarrier system has made an impact for cancer treatment[10]. Balancing of attractive and repulsive forces in protein is the key factor for formulation of protein nanoparticle. On the other hand, DEN is primarily used as a catalyst, because of very high surface to volume ratio, highly monodisperse nature[40]. DEN is made of dendrimer, commonly used dendrimer like poly(aminoamine), which is attached terminally to a metal ion. In presence of reducing agents like sodium borohydride, reduction of metal ions into metal element leads into dendrimer encapsulated nanoparticle formation. Size of the nanoparticle can be easily controlled by choosing the degree of aminoamines polymerization[40].

1.3.7. Quantum dot

Quantum dots are generally semiconductor particles having size less than 10 nm. These were first discovered in 1980. Quantum dots are well known for unique electronic and optical properties[44]. Among different physico-chemical properties, the particles have very broad absorption spectra and possess very narrow emission spectra. Quantum dots possess long lifetime, emit bright colors, and efficiency of the quantum dots is high. Hence the quantum dots are widely used in different optical applications. Additionally, these are widely used in biological fields for cell labeling, biomolecule tracking etc[45-47]. In addition, QDs have numerous advantages than other fluorophores like organic dyes, fluorescent proteins etc[48]. It is important to note that, conventional dyes commonly suffer from narrow excitation spectra and require specific light wavelength for excitation, which varies from one dye to another, whereas QDs having broad absorption spectra require wide range of light wavelengths for excitation. This property of QDs can be exploited to excite different colored QDs by a single wavelength simultaneously[48].

1.4. Physico-chemical properties of nanoparticles

1.4.1. Shape, size, and curvature

Shape, size and curvature of nanomaterials greatly influence the internalization of nanomaterials inside a cell. It has been reported that kinetic of nanomaterials cellular uptake vary with the shape and size of nanomaterials[49]. When discussing about the internalization of nanomaterials based on their shape, it has been reported that spherical particle of same size are internalized quickly than the rod shape, since longer membrane wrapping time is required for rod shape nanomaterial than spherical shape. In other ways, size and curvature also play crucial roles for cellular uptake of nanomaterials, as size and curvature of nanoparticle strongly affect the binding and activation of membrane receptors, and subsequently affect the respective protein expression, hence affect the cellular uptake[50]. From various *in vitro* and *in vivo* studies, it was found that nanomaterials inside a biological milieu display variant outcomes due to aggregation of nanomaterials into various sizes. However, the shape and size of nanomaterials greatly influence the toxicity/compatibility of nanomaterials towards mammalian and/or bacterial cells.

The interaction of proteins on nanoparticles surface is also affected by different physico-chemical parameters of nanoparticles. The conjugation of proteins with colloidal nanoparticles has been widely studied from the development of immune probes in 1970s. Some experiments regarding adsorption of proteins or peptides on different size of gold

(Au) or silicon oxide (SiO_2) nanoparticles have been performed. It has been studied that some proteins like lysozyme, catalase, trypsin and horseradish peroxidase bind strongly to SiO_2NP generally in the size range from 9 to 40 nm[51]. From these studies, it has been reported that there was partial loss of protein structure and a significant loss of enzymatic activity[51]. Based on these ideas Vertegel *et al* have studied different size silica nanoparticles effects on the activity of adsorbed lysozyme[51]. The work observed that the lysozyme-silica nanoparticles interaction is strongly influenced by the nanoparticle size (Figure 1.2)[51].

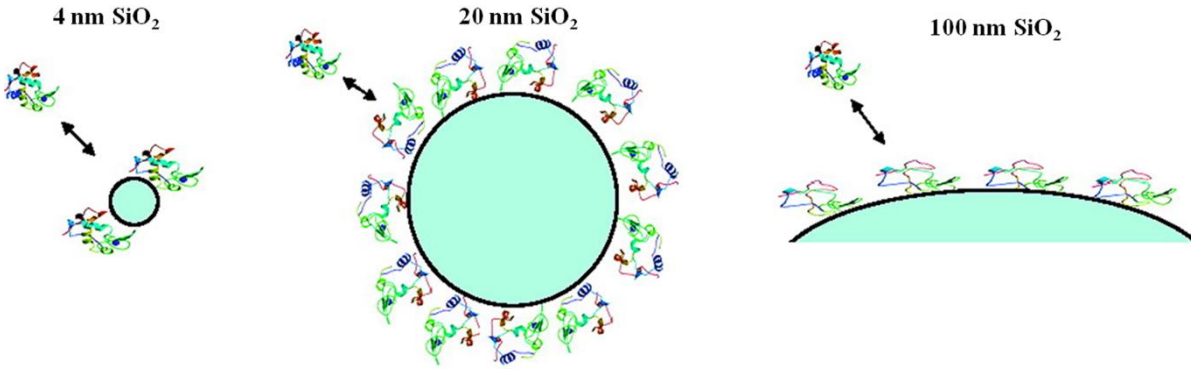

Figure 1.2. Schematic diagram of lysozyme interaction with silica nanoparticles of varying sizes. Reproduced from Vertegel, A.A. *et al*[51].

Figure 1.2 shows schematic representation for interaction of lysozyme with different size of silica nanoparticles. Generally, smaller nanoparticles possess high surface curvature and larger nanoparticles possess smaller surface curvature. Hence, when a protein interacts with a smaller nanoparticle, the interaction is weak (both columbic and hydrophobic), since the edge of the protein molecules are at a greater distance from nanoparticle surface, and *vice versa* for larger nanoparticles. Therefore, for small nanoparticles the structure of protein remains intact, and for larger it change depending upon the interaction pattern. Similar results were found for interaction of silica nanoparticle with RNaseA as studied by Shang *et al*[52]. Hence, these studies concluded that the size and curvature of nanoparticles significantly influences the structural dynamics of proteins upon interaction.

1.4.2. Surface concentration

Apart from size and curvature, the surface concentration also plays a major role in defining conformational dynamics of proteins upon interaction with surface/interface. Higher surface concentration of nanoparticles facilitates more proteins to be adsorbed onto the nanoparticles surface, so that a crowded environment is created which favors the

protein-protein interaction. But at lower surface concentration, the interaction between nanoparticles and proteins become more prominent[53]. Figure 1.3 shows the unfolding kinetics of lysozyme upon binding with different concentrations of silica nanoparticles. Wu *et al* calculated the unfolded fraction of adsorbed lysozyme at different concentrations of silica nanoparticles keeping the concentration of protein constant[54]. As shown in the figure, lysozyme at low nanoparticle surface concentration was unfolded to a greater amount than higher surface concentrations in equilibrium state. The result confirmed the existence of a higher energy barrier in a crowded environment that helps in unfolding of protein[54].

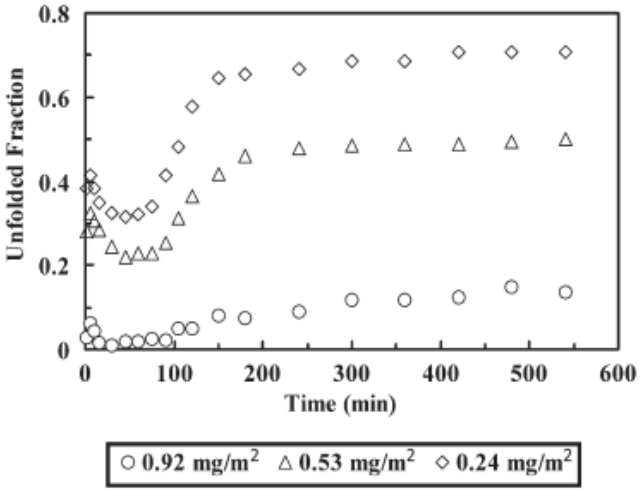

Figure 1.3. Unfolding kinetics of lysozyme adsorbed onto silica nanoparticle surface at different surface concentration at neutral pH and low salt concentration. The normalized tryptophan fluorescence intensity of lysozyme at 380 nm indicates the unfolded protein fraction with varying surface concentrations. Reproduced from Narsimhan, W. X. *et al*[54].

At a lower nanoparticle surface concentration, the molecular interactions exist between proteins and hydrophobic surface of silica nanoparticle. The interaction potential induces the unfolding of protein molecules due to available free space and absence of energy barrier. But at higher nanoparticle surface concentration, i.e. in crowed environment, the distance between the neighboring protein molecules will be small. The interaction exists between protein molecules on the nanoparticle surface, hence the unfolding behavior is limited. The energy barrier raised from the interaction from protein molecule decreases the extent of unfolding at higher nanoparticle surface concentration [54].

1.4.3. Surface functionality

Inside the biological milieu, the interaction of nanomaterials with different biomolecules depends on the properties of nanomaterials like shape, size, surface charge etc. Here, first we will discuss how the neutral surface charge influences the interaction of nanoparticles with cell membrane. In addition to shape and size of nanomaterials, the accessible surface functional groups present over the nanomaterial surface dictate many important properties of nanomaterials, like solubility, nanomaterial cell surface interaction etc, including the internalization of the nanoparticle. Moreover, upon nanomaterial administration into a biological medium, nanomaterial absorb serum proteins which help the nanomaterial for internalization by receptor mediated endocytosis[55].

However, for many biological applications, surface functionality of nanoparticles possessing potential not to interact with the cell membrane is also desirable. For example, non-specific absorption of protein onto nanoparticle surface can happen during the *in vivo* applications, which lead to the aggregation and clearance from the reticular-endothelial system. Hence, the absorption hinders the potential of nanoparticle for drugs/genes delivery to target site. The nanoparticle can also binds to cellular membrane non-specifically, which reduces its efficiency for targeting. Hence, various research groups have taken attempts to avoid the issue by coating nanoparticles with neutral ligands, like poly(ethylene glycol), PEG. For example, Xie, J. *et al* have coated Fe_3O_4 nanoparticles with PEG which resulted in negligible aggregation of nanoparticles in culture medium, and reduction in uptake of nanoparticles by macrophage cells non-specifically[56].

1.4.4. Surface potential

In comparison to charged surfaces, nanomaterial with neutral surface is relatively good delivering agents, since charged surfaces have many non-specific binding partners in a biological milieu. Hence, most of the charged accessible functional groups are generally responsible for nanomaterial interaction with cells (Figure 1.4)

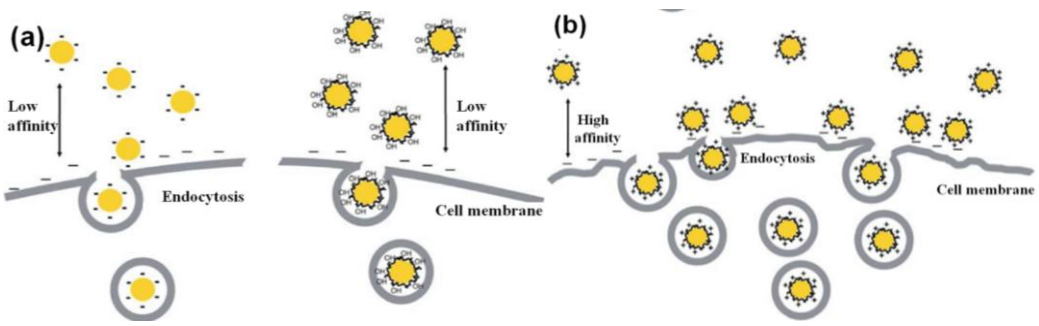

Figure 1.4. Illustration of gold nanoparticle, with different surface charges, interaction with SK-BR-3 breast cancer cell. (a) Low affinity interaction of cell membrane with citrate-coated and PVA coated gold nanoparticles, (b) high affinity interaction of poly(allyamine hydrochloride)-coated gold nanoparticles. Reproduced from Verma, A. *et al*[49].

Based on the surface charge of nanomaterials, cationic charged nanoparticles have shown stronger interaction with anionic cell membrane via electrostatic interaction, and translocate easily into the cell membrane (Figure 1.4). Due to stronger interaction of cationic nanoparticles with anionic membrane, these nanoparticles are exploited as synthetic agents for drug and gene delivery[49]. However, various studies have approved the internalization of negatively charged nanoparticles through the cell membrane, despite of the unfavorable interactions between the interfaces. In this context, Harush-Frenkel *et al*. have performed studies on endocytosis of charged nanoparticles through the cell membrane. They observed that the positively charged particle translocated easily via clathrin-mediated pathway, whereas the particles with negative charge showed less efficiency for endocytosis[57]. Surprisingly, the nanoparticles with negative charge bind non-specifically with some positive particles on the plasma membrane (relatively less than negatively charged domain), and get internalized through endocytosis[49, 57].

1.5. Physico-chemical properties of biological membranes and biomacromolecules

1.5.1. Cell membrane

Generally, the cell membranes of both prokaryotic and eukaryotic system are complex as well as dynamic in nature, which is made up of different phospholipid molecules. In addition, it contains different components such as lipopolysaccharides, extracellular polymeric substances, and protein, embedded and/or superficially attached to the membrane[58]. Besides providing the buffer against mechanical stress to cell, cell membrane helps in separating the intracellular components from extracellular environment. Additionally, the cell membrane maintains an anisotropic fluid phase which helps in supporting proteins as well as in regulating molecular transport into and out of the cell[58]. Depending upon interfacial composition of membrane, the prokaryotic cells have been divided majorly in two categories, Gram-positive and Gram-negative bacteria. Both kind of bacterial interface behave differently to different surfaces like nanoparticle interface, adherent surfaces etc.

1.5.2. Bacterial cell wall

The primary role of the bacterial cell wall is to provide shape, strength, and rigidity to the cell. Additionally, it protects the cell from the mechanical damage and osmotic rupture[59]. Based on their structure and functions, the bacterial cell walls are categorized as Gram-positive and Gram-negative bacteria (Figure 1.5). The cell membrane of Gram-positive bacterium contains a thicker layer (20-50 nm) of peptidoglycan attached to the teichoic acids. These teichoic acids are generally embedded in the peptidoglycan layer, whereas the lipoteichoic acids are found to be extended into the cytoplasmic membrane of the bacteria[59-60]. However, the cell membrane of Gram-negative bacterium contains a relatively thinner layer of peptidoglycan, and an additional outer membrane covers the cell membrane. The outer membrane of these bacteria is linked to a thinner peptidoglycan layer by lipoproteins. The peptidoglycan layer is placed within the periplasmic space formed between the outer and cytoplasmic membranes. In addition, porins and lipopolysaccharide molecules are also found in outer membrane. Hence, Gram-negative cell membrane is more complex both, structurally and chemically, compared to Gram-positive. Due to presence of lipopolysaccharide molecules in outer membrane, the surface potential of Gram-negative bacterium is more negative than Gram-positive bacterium. However, surface functionality, because of peptidoglycan, is more diverse in Gram-positive bacterium than gram-negative bacterium[59].

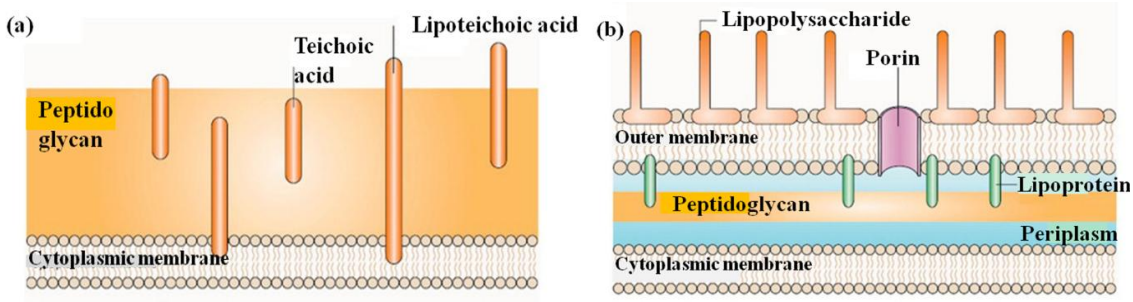

Figure 1.5. Structure of bacterial cell, (a) Gram-positive and (b) Gram-negative bacterium. Reproduced from Hajipour, M. J. *et al*[59].

1.5.3. Eukaryotic cell membrane

The basic frame work model to understand the structure and function of eukaryotic cell membrane was the Fluid—Mosaic Membrane Model, first introduced in 1972[61]. It is composed of phospholipid bilayers with embedded proteins (Figure 1.6). Generally 70% of total lipids present in mammalian cells are phospholipids[62]. Phospholipids contain one

polar part and another non-polar part, hence amphiphilic in nature[63]. Although, plasma membrane is predominantly composed of phospholipids, the lipids have different functional roles, beyond forming the lipid bilayers.

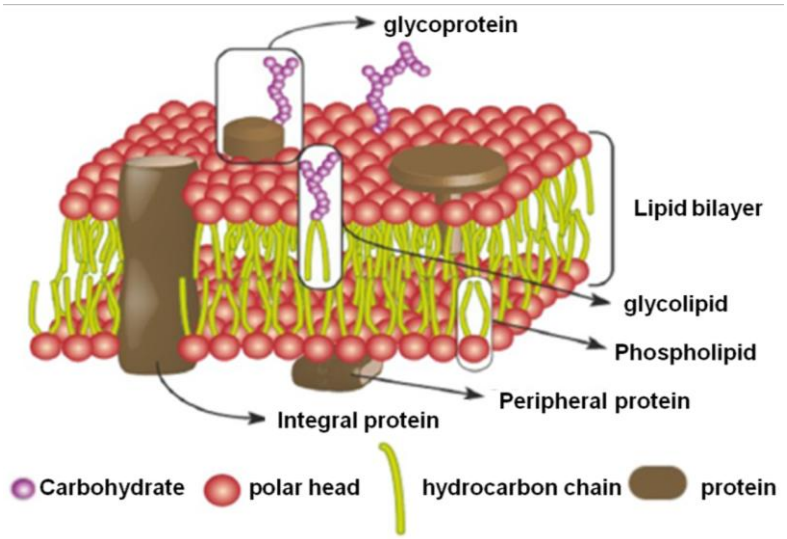

Figure 1.6. Structure of eukaryotic membrane, reproduced from Lombard, J. *et al*[63].

Plasma membrane, which is selectively permeable membrane, acts as a boundary for the cell, and maintains a viable intracellular environment. When discussing about the permeability of membrane, it comes into focus that membrane allows small and nonpolar molecules like O_2 and CO_2 to diffuse through it. Whereas, polar molecules like ions and nanoparticles of relatively larger size are restricted to diffuse across the lipid bilayer. Generally, proteins of nano-scale size and important ions diffuse across the lipid bilayer through different passive membrane-transport protein channels. Other nanoscale molecules and supra molecular assemblies are transported through a process of endocytosis, where the particles are enclosed in membrane vesicles, and the cellular uptake happens[49]. It is reported that, in case of some nanoparticles, the nanoparticles are confined in membrane bound vesicles (endolysosomes), which restrict their path to reach the cytosol. However, the process is not limited to all nanoparticles. Additionally, it is reported that many nanoparticles possess the inherent property to penetrate the cell membrane. In those cases, the nanoparticles form pores in cell membrane which lead to cellular toxicity, since they destroy the balance of intracellular and extracellular ions, proteins, and other vital macromolecular concentrations that are essential for the normal function of a cell[49]. Additionally, different approaches have been adopted for transporting nanoparticles into a cell cytoplasm, like (i) endosome disruption and entry of NP into the cytosol through spong-effect mechanism[64], or using chloroquine[65] (ii) direct

microinjection of nanomaterials into cells[66-67], (iii) use of electroporation[68], and (iv) conjugation of nanoparticle with natural cell-penetrating/fusogenic chaperons [49, 69]. However, the interaction of nanoparticles with cell membrane depends on the chemical functionalities of surface, shape and size[49].

1.5.4. Nucleic acids biomacromolecules

Nucleic acids which are principal constituents of all living organisms are considered to be possessing significant importance as protein, which are involved in cell division, growth[70]. Nucleic acids are also considered as biological information storage block which are relatively physico-chemically stable, and possess the potential of self organization[71]. The DNA (deoxyribonucleic acid), a long chain polymer made from nucleotide, is commonly known as hereditary material. Generally, nucleotide consists of sugar, heterocycle, and phosphate. The ribose or deoxyribose, and sugar are found in cyclic, and furanoside form. These are connected by β-glycosyl linkage and produce four normal nucleosides such as adenosine, guanosine, cystidine, and thymidine etc. Using the process of hybridization, a single stranded DNA binds its complementary strand and forms 1 to 3 dimensional structutre[71]. From the last decade, the scientists are trying to interact various nanoparticles with DNA by both covalent and non-covalent interactions for different therapeutic approaches[72]. However, the DNA macromolecule is considered as suitable material for fabrication of nanostructures, and utilization of DNA has gained interest for highly specific molecular recognition which is based on the DNA hybridization[73]. In addition, for specific bindings of DNA with different nanoparticles, DNA molecules can be modified with different functional groups[73]. Interestingly, in biomedical sciences, DNA/RNA molecules are the important molecules which play key role as carriers for genetic information as well as they also provide specific interactions with different target molecules like complementary DNA molecules, cell receptors, and proteins[73]. Hence, nucleic–nanoparticle interaction plays vital role in biomedical sciences.

1.5.5. Protein biomacromolecules

Protein, one of the essential biomolecules to sustain life, consists of long chains of amino acids. Upon synthesis, nascent protein attains tertiary structure, which defines the functional attributes of the protein. The tertiary structure of protein is governed by a network of interaction, predominantly non-covalent interactions like hydrogen bonds, electrostatic interactions, salt bridge, van der Waals interactions, hydrophilic/hydrophobic effects, dipole-dipole interactions etc. The network of interactions, governing tertiary

structure, is so fragile that perturbation of even one non-covalent interaction may lead into conformational rearrangement or complete loss of the function. Furthermore, conformational changes of proteins are associated with different properties of proteins like self-assembly, tendency to aggregate, transportation, and cytotoxicity[74]. Since the biomolecule is most dynamic and functional entity of a cell, any additives to cell, like nanoparticles, drugs, will likely to interact and affect the structure and function of the biomolecule. In past decades, folding have received enormous attention of different researchers to understand different biological phenomenon like from genetic information to molecular diagnostics[74].

1.5.5.1. Protein folding

Protein folding is one of the most fundamental and spontaneous phenomenon occurring in a cell, where the entire polypeptide chain efficiently folds into a physiologically active conformation (called native conformation), and execute different functions needed for cell survivality[75]. Various studies are being carried out to understand the mechanism of protein folding along with the kinetic and thermodynamic analysis of the intermediates[76]. The "folding funnel" or "energy landscape theory" of protein folding elucidates a statistical description of free energies of all the molecular configurations (Figure 1.7).

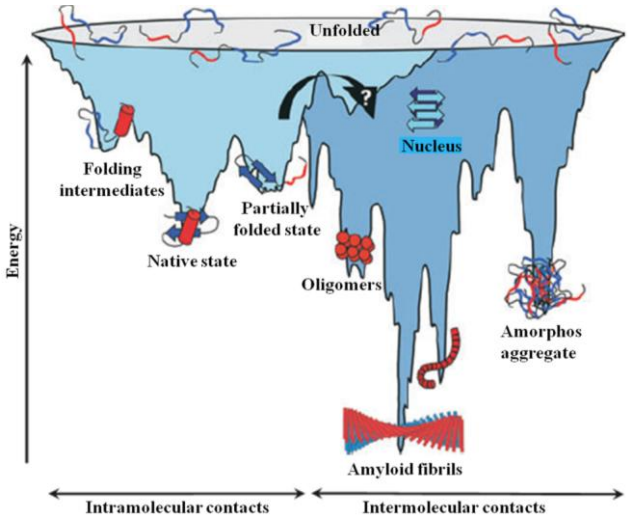

Figure 1.7. Schematic figure showing energy landscape of protein folding and aggregation. Although, the surface shows multiple conformations, however with the help of intramolecular contact formations, conformations 'funnelling' towards native state or with the help of intermolecular contact the conformations 'funnelling' towards amyloid fibrils. Reproduced from Jahn, T. R. *et al*[76].

The unfolded protein starts from the top of the funnel, and as it descends the funnel, the free energy is lowered due to the formation of intramolecular interactions. The reduced number of possible conformations at each stage simplifies the folding process and finally reaches the unique natively folded conformations of the lowest energy level. However, in case of larger proteins and a few small proteins, the folding funnel does not remain "smooth" but becomes "rugged". This happens due to the presence of transiently stable intermediate conformation(s) in the folding pathway of such proteins[77]. Sometimes during the folding process, protein gets kinetically trapped in the local energy minima as an intermediate state and needs to cross a certain energy barrier in order to reach the native state at bottom of the folding funnel. These transiently populated states, known as intermediate states are partially folded protein conformations, and are required to traverse during the folding into native state. The folding pathway traversed by such proteins is termed as 'Non-cooperative' or 'Multistate folding'. In some cases, these intermediates may lie off the productive folding pathway, and are known as "off pathway intermediates". Once these intermediates accumulate above a threshold concentration during the folding process, owing to their exposed hydrophobic core, the intermediate(s) interact with each other to form aggregates. Thereby, the process shifts the equilibrium towards protein aggregation, where intermolecular interactions rule over the intramolecular interactions. The aggregates are generally categorized as either amorphous or highly ordered amyloid fibril (Figure 1.7)[76].

1.5.5.2. Protein misfolding and diseases

As mentioned above, perturbation of the interaction network is easy for most of the proteins, and can be misarranged/broken by slight change in local chemico-physical environment of the protein, resulting in partially unfolded to completely unfolded conformations. In both the conformations, protein loses its physiological function(s), resulting in degradation by proteostasis network of the cell. However, when these confirmation goes uncheck of proteostasis network in cells, exposed hydrophobic core drive the conformation into self-assembly of monomers into pathogenic amyloid fibrils[78]. During the self-assembly into amyloid fibrils, the process is accompanied by different intermediates with cytotoxic propensity[79-80]. The cytotoxic nature of intermediate(s) result in several degenerative diseases like Alzheimer's disease, Huntington's disease, Parkinson's disease, amyloid polyneuropathy, diabetes type-2, spongiform encephalopathy etc[78]. The degenerative diseases associated with amyloid fibrils are

generally of three types: (1) neurodegenerative diseases like Alzheimer's diseases: amyloid fibril mainly degenerate the brain cells, (2) non-neuropathic localized amyloidosis: the fibril-mediated cell death occurs to a kind of cells other than neuronal cells, (3) non-neuropathic systemic amyloidosis: amyloid fibrils cause cell death to multiple kind of cells other than neuronal cells[78].

Since the root of amyloid disease is formation of misfolded protein conformation with amyloidogenic propensity, development of effective drugs against the conformation has been a key issue for last decade. In spite of many attempts, the scientific community have failed to develop therapeutic agents to combat/hinder the amyloid fibrillation. These insoluble deposits (fibrillar assemblies) are irreversible aggregates of misfolded proteins. Thus, the reversal of protein aggregation would have been an attractive strategy for development of therapeutic agents against the diseases[81]. Accordingly, first vaccine "Doblin-based Elan Pharmaceuticals' AN-1792" was developed against Alzheimer's diseases. The vaccine helped in dissolution of visible aggregate, and resulted in recovery of dementia in tested mice models. However, its trial on human proved disaster with meningoencephalitis and microbleed as the side effects in treated patients[82-84]. Development of second generation vaccines with different approaches against amyloid diseases are still in clinical trials[85]. In last decade, scientists have also looked several other types of molecules with tendency to induce anti-amyloidogenic conformations/conditions, like synthetic peptides, heat shock proteins, and chemical compounds (resveratrol)[86-88]. Apart from the studies, recently nanoparticles have been suggested as one of a possible inhibitor of amyloid fibrillation[81, 89-91].

1.6. Nanoparticle interfacial interaction with biological membranes and biomacromolecules

In current era, nanoparticle is considered as promising tool with different applications in biomedical science, like biosensing, drug delivery, imaging etc. However, it is a matter of intensive research to understand the synthetic materials interaction with different biomolecules, cells, and tissues before considering the applications in biological sciences[92]. In biological medium nanoparticles come in myriad shape and size, and interact with different biomolecules forming nano-bio complexes. The physico-chemical properties of both the nanoparticle and biomolecule are affected by interaction patterns at nano-bio interface[93]. Additionally, the interface helps in thermodynamic exchanges

between nanomaterial and different biological components, like membranes, proteins, phospholipids, DNA etc[93]. As shown in figure 1.8, the different components developed as a result of nanoparticle biomolecule interactions are (i) surface of nanoparticle, (ii) solid-liquid interface, (iii) contact zone of solid liquid interfaces with biological substrates[93]. However, the most important factors determining the surface properties of nanopaticle are chemical composition of material, shape and size, angle of curvature, porosity, surface crystallinity, roughness, functionalization, heterogeneity, hydrophilicity/hydrophobicity etc[93]. However, when the nanoparticle is dispersed in a medium, the developed quantifiable properties, like effective surface charge (zeta potential), aggregation propensity of particle, stability, biodegradability, state of dispersion, rate of dissolution, hydration and functionality of interface depend on the characteristics of the suspending medium[93]. Additionally, ionic strength, pH, temperature, and presence of organic molecules also affect the particle properties[94]. The acquired properties of nanoparticles contribute actively for the interaction of nanoparticles with the biological medium. However, forces like long-range forces, which arises from van der Waals (attractive in nature) and electrostatic double layer interactions, and short range forces, which arise from charge, solvent interaction, steric hindrance, depletion etc., are found at the nanoparticle media interface responsible for interaction with biomolecules[93].

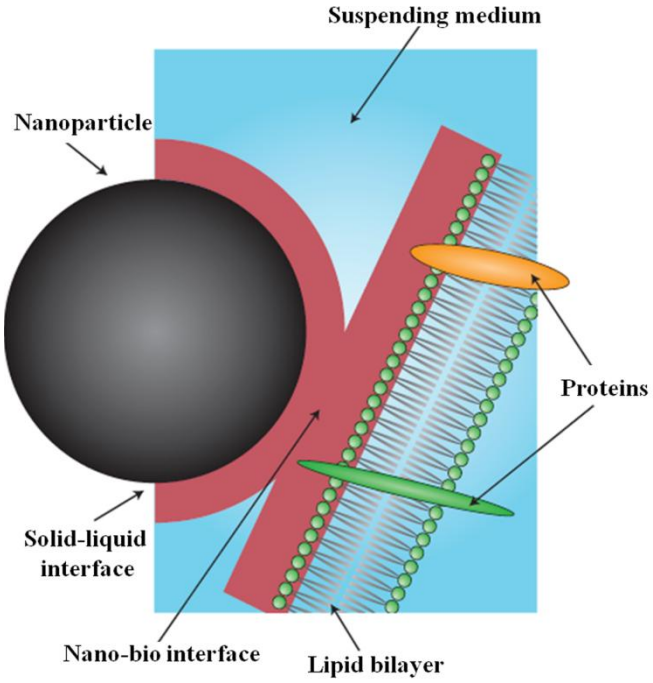

Figure 1.8. Depiction of nano-bio interface, reproduced from Nel, A. E. *et al*[93].

1.6.1. Nanoparticle-biological membrane interaction

Increasing bacterial resistance towards traditional/conventional antibiotics is a major global health concern in current era[95-96]. Some bacterial strains have the potential to produce slime, which facilitates the adhesion and formation of biofilms on any artificial surfaces or implantable devices. The formation of biofilms enhances the possibility of bacterial survival by preventing antibiotic action[95-96]. Additionally, the interaction of nanoparticle to bacteria is a research focus of nanoecotoxicity; bacteria play major role for maintaining normal ecosystem[97]. Moreover, bacteria are generally used as representative model for single cell organisms. However, the nanoparticle interaction with bacteria helps, in broad view, us to understand the adhesion of nanoparticle on a cell membrane, and its uptake. Although, the toxicity of nanoparticles towards microbes is a well established research area[98-99]. However, to explore whether the toxicity caused upon interaction with membrane or internalization or both is essential to understand the mechanism of nanotoxicity. Different non-specific interactions like electrostatic, dipole-dipole, H-bond, hydrophobic, and van der Waals interactions are responsible for adhesion of bacteria on any material surfaces, triggering bacterial biofilm formation[95]. Hence, before screening any nanoparticle mediated approach as possible antibiotics, the material must have anti-microbial property to reduce the microbial adhesion. The NPs with photocatalytic properties have the potential to reduce biofilm formation[95]. Inside microbial medium, the interactions between accessible functional groups of nanoparticle and biomolecules like lipopolysaccharide (LPS), phospholipid, protein, and lipoteichoic acid (LTA) present over the bacterial envelop contribute in interaction pattern at the interface. The functional groups of biomolecules enhance adhesion of bacteria to different surfaces, and help their proliferation[97]. Hence, the accessible functional groups present at bacterial envelop and nanoparticle surfaces, along with the physico-chemical property of nanoparticle, determine the fate of bacteria as well as the nanoparticle (whether nanoparticle will be compatible or toxic to bacteria) in biological milieu.

1.6.2. Cellular internalization of nanoparticles

Nanoscale materials are being formulated for different biological applications. For successful biomedical applications, sometimes nanoparticles are often functionalized with different ligands, coated with different biopolymers to target a specific cell[100]. Upon conjugation/encapsulation with drug molecules, cell internalizes the nanoparticle through

different pathways (Figure 1.9), and releases the drug molecule successfully. However, the efficacy of nanoparticle-based approaches depends on physico-chemical parameters of the nanoparticle like shape and size, surface potential, surface functionalities etc. In addition, different physico-chemical properties of the membrane such as (i) stretching and elasticity of membrane, (ii) thermal fluctuation of cell membrane, and (iii) hydrophobic exclusion of polar surfaces by membrane, resist the nanoparticle against the permeabilization[93, 101]. Interestingly, the nanoparticles upon interaction produces sufficient energy at the interface to overcome these forces[93].

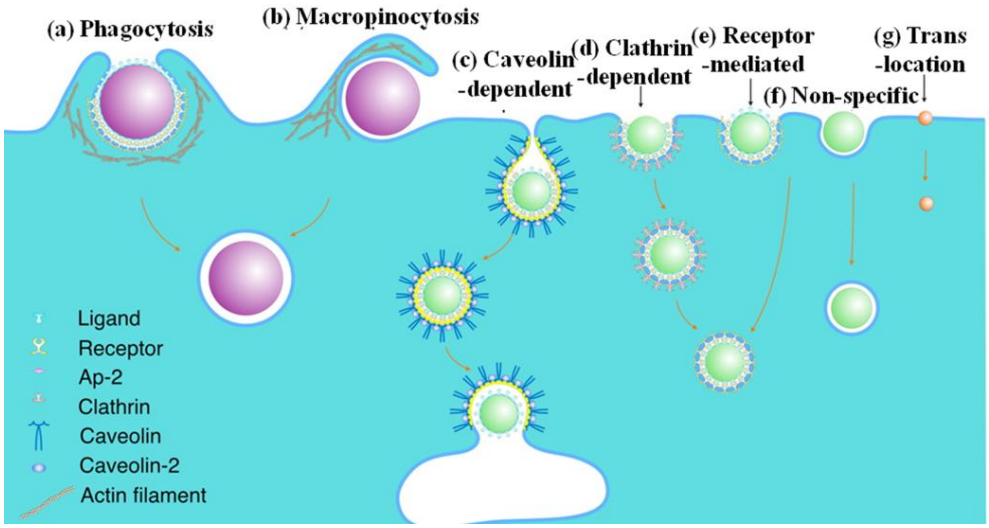

Figure 1.9. Nanoparticles internalization pathways, reproduced from Zhang, S. *et al*[100].

1.6.3. Nanoparticle-nucleic acid interaction

Exploring the interaction between the nanoparticle and biomolecule is an active research area, in current era. Nanoparticles, having high surface free energy, show high affinity to interact with biomolecules, especially biopolymers resulting in various applications like development of novel biosensor for clinical diagnosis, imaging, drug delivery, and pathogenic bacteria detection[102]. Recently, various metal and metal oxide nanoparticles like Au and Ag are identified to interact strongly with nucleic acid like DNA[102]. Hongjie An *et al* have elaborated about the possible covalent interaction between the nanoparticles and DNA with the help of different functional groups like –SH, -OH, $-NH_2$, and –COOH[103]. However, non-specific binding of nanoparticles to DNA can also be possible through non-covalent interactions[103]. The non-specific binding, leading into DNA-nanoparticle conjugation, make the nanoparticles as a better DNA carriers in case of targeted delivery, which can replace the commonly used liposomes having various drawbacks[103]. Additionally, in delivery of plasmid DNA, antisense oligonucleotides, small

interfering RNA (siRNA), nanoparticles have also replaced the commonly used viral vectors possessing unpredictable immune response[103].

1.6.4. Nanoparticle-protein interaction

Generally, with decrease in size of material, the free energy content of material/molecule increases[104]. When nanoparticle is dispersed in biological fluid, it interacts with biomolecules to lower the surface free energy content. Thus, nanoparticle interaction with biomolecules helps in proper dispersion of nanoparticles. In chemist's word, when nanoparticle is placed in biological fluids, nanoparticle interface form attractive interactions with different moieties present in the fluid, resulting into release of free energy content of the nanoparticle. Thus, attractive interaction with moieties present in biological fluid helps in dispersion of nanoparticle in monomeric form, i.e. the interaction acts against agglomeration of nanoparticles. The concept applies for the case of protein biomacromolecules, which interacting with nanoparticles in biological fluids and forms 'nanoparticle-protein corona'. According to the proposal given by Monopoli *et al*, biological 'corona' obtained upon interaction of nanoparticles with biomacromolecules is one of the major elements of biological identity for the nanoparticle in biological milieu[104]. Additionally, nanoparticle properties like size, shape, solubility, surface charge and surface functionalities play vital roles in defining the strength and kind of interactions with biological moieties, thus the biological response and distribution[105-109]. Among all the biological moieties adsorb on nanoparticle interface, influence of protein-nanoparticle complexes to living system is now an emerging area of research[110-112]. When dispersed inside the biological medium, the nanoparticle obeys the universal rule of the material science, *i.e*. the material always covers itself by biomolecules present in biological milieu upon interaction[113]. Hence, the nanoparticles inside the biological medium are also covered with proteins forming nanoparticle-protein corona. Studies have shown that plasma proteome consists of approximately 3700 proteins, and minimum of 50 proteins have been observed to bind with different nanoparticle interfaces[114-117]. Opsonins, components of nanoparticle corona, act as a "molecular signature" which is recognized by immune cells and determines fate of the particle, like kind of cell reaction, route of internalization, rate of clearance, volume of distribution, and organ disposition[110-111, 118]. For example in one study, single walled carbon nanotubes and silica nanoparticles coated with albumin were observed to induce anti-inflammatory responses in macrophages. However, in another experiment, a modified nanoparticle interface, using non-ionic

surfactant (Pluronic F 127) to reduce adsorption of albumin, resulted in relatively lower anti-inflammatory response [112, 119]. All these properties of nanoparticles like rate and root of clearance from body, organ deposition, and volume of distribution are dependable on nanoparticle-protein corona[110, 118]. Studies have shown that all the biological responses to nanoparticles are because of surface area rather than mass[120-122]. When particles become smaller, the surface area of particles shrinks much more slowly than their volume, resulting in larger surface-to-volume ratio. Due to larger surface-to-volume ratio, relatively higher protein population fraction binds to the nanoparticle surfaces[114]. Furthermore, the biological response and bio-distribution of the particles are influenced by the nanoparticle-protein complexes. The nanoparticle-protein complexes are possibly responsible for the side effects[123-124], since on interaction with nanoparticle, certain proteins have shown sign of conformational rearrangement leading to loss of normal physiological functions[125]. The protein abnormality on interaction with nanoparticle interface induces unpredicted biological reactions including cytotoxicity[126]. Thus, the biological property of nanoparticle basically differs according to the physico-chemical nature of the nanoparticle interface that defines biological interaction partners of the nanoparticle (Corona), which ultimately defines fate of the nanoparticle in biological system.

1.6.4.1. Protein conformational rearrangement upon interaction with NP interfaces

Proteins are polymers of 20 naturally occurring amino acids. The linear sequence of these amino acids fold spontaneously forming tertiary structures (3D) in physiological media and these tertiary structures are relatively stable and functional in nature. When protein binds to the planar surface, overall structure of protein changed because of the additional interactions at interface. On the other hand, fine nanoparticle with relatively high curvature helps proteins to retain their tertiary structure on interaction. Nonetheless, studies on nanoparticle-protein interaction suggested that perturbation of the structure vary in extent depending upon the physico-chemical properties of nanoparticles[53]. When lysozyme and β-lactoglobulin are adsorbed on the silica nanoparticles, conformational changes of proteins occur at both secondary and tertiary levels[54, 127]. Different studies on nanoparticle-protein interactions have shown that the adsorption leads to decrease in α-helical fraction, with or without increase in β-sheet fraction[51, 127]. Bovine serum albumin (BSA) has been taken as a model protein for nanoparticle protein interaction, since BSA undergoes conformational changes at different pH values[53]. The interaction of BSA with

gold nanoparticles has shown that the interaction resulted in α-helical fraction decrease, and a significant increase in sheets and turns[127]. Although, from various studies it has been concluded that protein retains its conformational stability when bind to nanoparticles, but in certain cases the stability decreases due to which conjugated protein become relatively sensitive to chemical denaturants such as urea[52].

1.7. Applications of nanoparticle-biomolecular interactions in biological sciences

Due to huge potential in nanotechnology and having advanced physico-chemical properties such as high surface to volume ratio, nanoparticles have drawn the attention of various scientific communities for over a century. Hence, the particles are widely used in biomedical science and engineering. Few of the remarkable applications in biomedical engineering are nanoparticle as targeted drug delivery vehicles, diagnostic imaging, biosensors, anticancer agents, antimicrobial agents etc[8, 27]. However, among different nanoparticles, metal and metal oxide nanoparticles having photocatalytic activity have shown enormous applications in different fields of biomedical science. Easy synthesis and modification of these nanoparticles with various functional groups allow them to conjugate easily with different ligands, antibodies, and drugs of interest, hence opens different application windows in biomedical sciences and engiennering[27]. For example different metal and metal oxide nanoparticles like zinc oxide (ZnO), silver (Ag), silver oxide (AgO), titanium dioxide (TiO_2), gold (Au), silicon (SiO_2), calcium oxide (CaO), and magnesium oxide (MgO) having high photocatalytic activity possess high antimicrobial and cytotoxic activity, hence the biological applications[128]. The effectiveness of these nanoparticles depends on surface functionalities, defects, and size of the particle.

1.7.1. Nanoparticles as novel antibiotics

The emergence of different antibiotic resistant bacterial strains becomes a serious threat to public health. Hence, various research groups are trying to replace the conventional antimicrobial agents to check the bacterial infection. It is reported that, most of the bacterial infections (approximately 70 %) are resistant to different commonly used antibiotics[128-129]. Hence, research groups are trying to develop novel antibiotics which can replace the traditional antibiotics. Due to small size and high surface to volume ratio, nanoparticles are assumed to be possible antimicrobials against various resistant strains. Metal and metal oxide nanoparticles like zinc oxide (ZnO), iron oxide, silver (Ag), silver

oxide (Ag_2O), titanium dioxide (TiO_2), copper oxide (CuO) exhibit strong antimicrobial activities[128]. However, the mechanism of antimicrobial activities of these nanoparticles varies from particle to particle. From different studies, various research groups have proposed possible mechanisms like membrane damage, release of metal ions, ROS production etc. for antimicrobial activity[128-129].

1.7.2. Nanoparticle-mediated approach for cancer diagnosis and therapy

The exploration of nanotechnology has opened several possibilities in biomedical sciences like drug delivery. Accordingly, various nanotechnology formulations are being developed to obtain safer therapeutics for different clinical applications, for example nanoparticle-based approach in cancer treatment[10]. Now a days, although cancer is a major reason for death of millions people, still not an effective treatment is available for eradication of the disease. The commonly used methods adopted for cancer treatment are surgery, chemotherapy, radiation-therapy, immunotheraphy *etc*[10]. However, all these processes have advantages and disadvantages, and for better efficiency a combination of these processes are needed. It is important here to discuss that most human cancer are solid tumors and current strategy for treatment of cancer include chemotherapy to shrink the developed tumor before its removal by surgery. Despite of many efforts to treat cancer, the toxic side effects remain major issues in current era. Hence, various drug delivery carriers are being used to improve the efficacy of cancer therapy. Among these carriers, small size nanoparticles with biodegradable and biocompatible properties have received enormous attention of scientists working in cancer therapy research. The basic characteristics of anticancer strategies to be effective for cancer treatment are first it should actively reach the target site upon administration, without loss of content. Secondly, at the target site it should have the potential to kill the tumor cells without killing the normal cells. Thirdly, it should be released safely in controlled manner[10].

The rationale behind considering the nanoparticles to treat cancer is that reduction of the materials to nanoscale lead to development of advanced physico-chemical properties[130]. A number of research groups have reported that very low concentration of different metal and metal oxide nanoparticles have the potential to kill cancer cells[131-133]. Additionally, the anticancer efficiency of the metal and metal oxide nanoparticles can be increased by functionalizing them with specific antibodies and other ligands against cancer cells[130]. Different nanoparticles having anticancer activities are silver, zinc oxide,

iron oxide, titanium dioxide, cerium oxide, copper oxide, silica nanoparticles etc[134-135]. In addition to drug carrier, nanoparticle-mediated approaches have been adopted for cancer biomarker imaging and early detection[130]. It is reported that ZnONP capped with polymethyl methacrylate can be used for detection of low abundant biomarkers[130, 136]. Additionally, ZnO nanorods are being used as cancer biomarkers for detection of telomerase activity even at low concentration[137]. Along with ZnONP, iron oxide nanoparticles can be used as contrast agents for detection of cancer. Additionally, iron oxide nanoparticles having oleic acid coating modified with pluronic and tetronic block copolymers with iron oxide core are used for *in-vivo* tumour imaging[130].

1.7.3. Nanoparticle acting as a protein folding chaperone

Various studies have reported that in some cases, perturbation of protein structure happens to some extent upon adsorption on the nanoparticles. Surprisingly, some studies have proved that some nanoparticles might act as a chaperone to help in protein folding[53]. In the native structure of a protein, the hydrophobic cores are buried inside, and hydrophilic residues are present over the surface that interacts with the aqueous environment and keeps hydrophobic core hidden from aqueous media. However, unfolding of protein causes exposure of hydrophobic surfaces leading to protein aggregation. In such cases, different chaperons like GroEL/GroES binds selectively to the unfolded protein through different non-covalent interactions, and stabilizes the protein from aggregation, hence helps in proper folding[53, 138-139]. It is also reported that during the refolding process, the aggregation of intermediate protein folds are prevented by surfactants and cyclodextrins[140-141]. Rozema, D. *et al* have reported that the refolding of protein is enhanced in presence of low molecular weight surfactants along with cyclodextrins, acting as a stripping agent[142]. However, it becomes difficult to remove surfactant completely after treatment. Although, water soluble polymers like poly-(ethylene-oxide) and polyamino acids are also used for preventing protein aggregation [143-144], however the efficacy of these chemicals are found low.

Hence, currently researchers are focusing on nanoparticles to avoid the limitations of using these traditional chemical chaperones. Researchers have found that two types of nanoparticles can help in refolding of proteins[53]. Among them, one is nanogel, acting as a molecular chaperon, which is fabricated by pullulan self-aggregation with cholesterol group (CHP)[53]. When the β-cyclodextrin was added to the complex, the release of trapped

carbonic anhydrase B (CAB) was observed and its refolding was observed upon CHP-nanogel dissociation[53]. Figure 1.10 shows the detail mechanism of refolding of CAB on the assistance of artificial molecular chaperons. Here, during the refolding process CHP trapped the unfolded proteins of intermediates to prevent aggregation. The process is very similar to the process as adopted by GroEL/GroES, and β-cyclodextrin act as an ATP molecule that helps in release of folded protein from complex[53]. In addition, another study Nomura Y. *et al* have also reported the chaperon like activity of nano-gel mediated protein refolding[145].

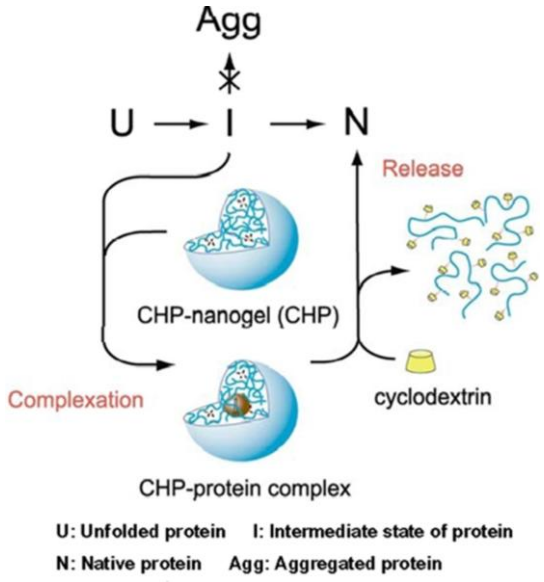

Figure 1.10. Schematic representation of artificial molecular chaperones, reproduced from Fei, L. *et al*[53].

1.7.3.1. Nanoparticle interface that enhances amyloid fibrillation kinetics

As shown in figure 1.11, it is suggested that nanoparticles have the potential to increase the possibility of amyloidosis and other protein misfolding diseases[146]. Accordingly, the research done by various groups about catalytic property of nanoparticles in protein fibrillation proved that some nanoparticles have the potential to accelerate the process of protein fibrillation. Proteins are generally considered as potentially important molecules from biological point of view. The binding of proteins either in native or denatured state depends on the surface charge of protein, hydrophobicity, intrinsic stability and the characteristic of interacting particles. Hence, nanoparticles interact with proteins resulting in different pathological consequences. Additionally, surface charge and high surface area to volume ratio of nanoparticles greatly influence the interaction with protein molecules. However, size of nanoparticle also affects the interaction of nanoparticles with protein. It

is well known that protein fibrillation kinetics which is a nucleation-dependent mechanism is triggered by various external factors[147]. External factors, like presence of nanoparticle, polymeric charged surfaces, salts etc., act as a moderator for protein fibrillation. The process of amyloid fibrilliation is assisted by some nanoparticles[148-149]. Like the findings of Wu, W. H. *et al*, where he found that TiO_2NP have the potential to assemble Aβ into amyloid fibrils *in vitro*, by accelerating nucleation process[150]. Additionally, Linse, S. *et al* in their study suggested that the association of protein at nanoparticle surface led into protein conformational rearrangement[151], in addition to many fold increased local concentration. The conformational rearrangement and increased local concentration act as seed for amyloid fibrillation, hence enhance the rate of amyloid fibrillation[146, 151]. The work also indicated that mature fibrils, formed upon protein-nanoparticle interaction, had no affinity for the studied nanoparticle[151].

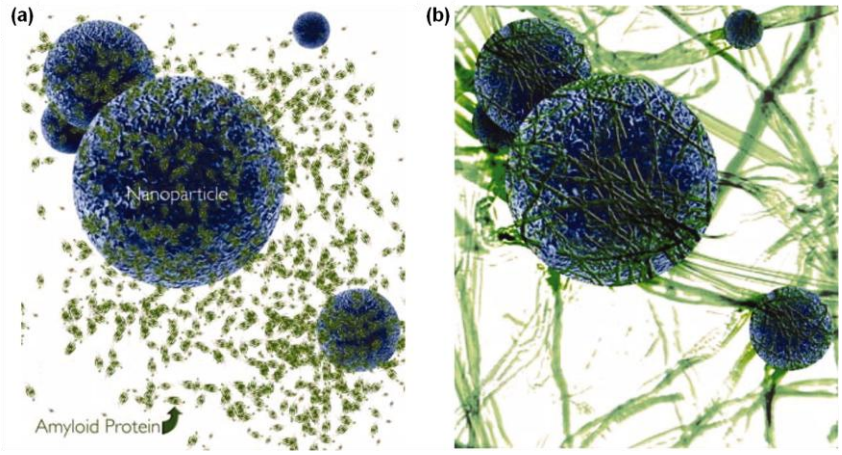

Figure 1.11. Amyloid protein fibrillation in presence of nanoparticles. (A) Shows nanoparticles (blue) and amyloid proteins (green) in its monomeric state. (B) The amyloid proteins are associated on nanoparticle surfaces generating small oligomers which are considered as precursors of fibrils. Reproduced from Colvin, V. l. *et al*[146].

1.7.3.2. Nanoparticle interface that reduces amyloid fibrillation kinetics

Generally proteins in the folded state possess hydrophobic residues inside and polar groups on the surface. The hydrophobic effects or π-π stacking interactions or both between non-polar residues present in hydrophobic core help to maintain its tertiary structure[152]. For unfolded protein, chaperones like hsp 26/70/94, GroEL/GroES assist the unfolded conformation to attain a physiologically active tertiary conformation[152]. Protein folding process follow two steps, as described by Rozema and Gellman, (1) the capture step- the unfolded conformation bind with a host molecule, which assist the conformation

against misfolding, and (2) release step- in this step host molecules take the help of competitive guests to get removed from the refolded protein[152-153]. Generally GroEL/GroES are considered to be hosts, which have hydrophobic inner compartment where unfolded protein goes and bind (capture step). Other molecules which are used for the purpose are linear dextrins, hydrophobic carbohydrate nanogels, liposomes, and stimuli responsive polymers, all are hydrophobic in nature[153-154]. Examples of hydrophilic/amphiphillic additives used for refolding of protein are polyamines, amino acids and polyethylene glycol etc[152]. Hydrophobic compounds bind to hydrophobic domains of protein, whereas hydrophilic compounds bind with exposed charged residues of unfolded protein[155].

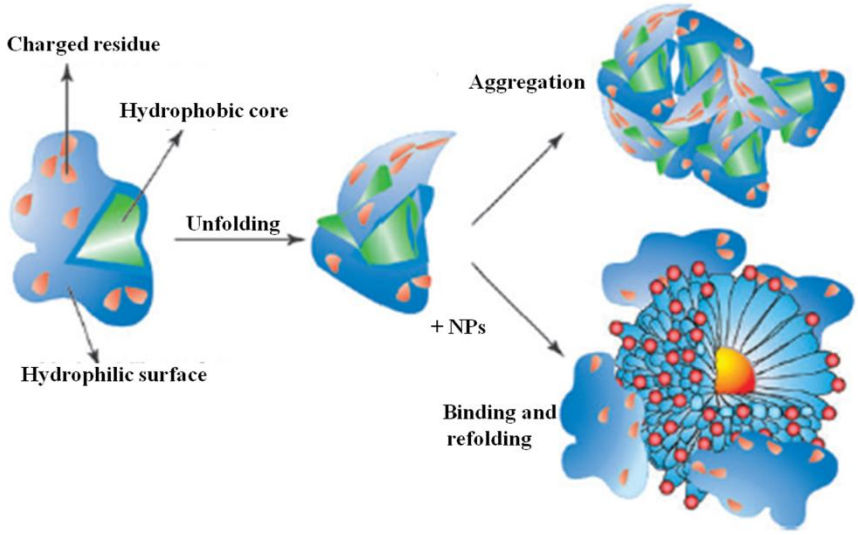

Figure 1.12. The unfolding of protein and exposure of hydrophobic core followed by either aggregation of protein or refolding of protein depending upon the presence of amphiphilic nanoparticles, reproduced from De, M. *et al*[152].

The refolding capacity of nanoparticles was studied by De, M. *et al* as shown in figure 1.12. In the study, they have chosen protein having positive residues on the surface. These positive charges prevent protein aggregation. They unfolded the protein by thermal denaturation so that the hydrophobic inner core becomes exposed. In this state the protein aggregates by intermolecular association of hydrophobic domains on refolding. During this unfolded stage they introduced malonic acid functionalized gold nanoparticles (AuDA), which on interaction with denatured protein formed a nanoparticles-protein complex. This is due to electrostatic interaction of nanoparticles with positive residues of protein. Zeta potential measurement studies demonstrated that high negative charge of these nanoparticles protein complex prevent protein aggregation, thus promoting correct

folding[152]. Shemetov, A. A. *et al* (2012) studied the inhibition of Aβ-fibril formation using biocompatible nanogels. The nanogel was prepared from polysaccharide of pullulan backbone and hydrophobic cholesterol moieties. The gel used as an artificial chaperone to inhibit the Aβ-fibrils[156].

1.7.4. Detection of protein aggregation using nanoparticles

Protein aggregation is the primary cause for many degenerative and incurable diseases like Alzheimer's disease, cystic fibrosis, and prion diseases etc. In addition, it is important to study protein aggregation for development and storing of protein based biopharmaceuticals[157]. Hence, different analytical tools such as: UV-Visible spectroscopy, dynamic light scattering (DLS), ultracentrifugation, and size-exclusion chromatography (SEC) are some well known methods to study protein aggregation[157]. However, many of these processes are not sensitive to low concentrations of proteins as well as the methods are time consuming. Additionally, microtiter assays like thioflavin T (ThT) is commonly used to study protein aggregation. However, the assay have also limitations for low concentration, aggregate size etc[157]. Hence, research groups are trying to develop simple, novel, and cost effective methods for detection of protein aggregation. In this context, Pihlasalo *et al* formulated a novel protein aggregation assay based on nanoparticles. In this assay they have utilized time-resolved luminescence energy transfer (TR-LRET) to detect protein aggregation at picomolar concentration range[157] (Figure 1.13).

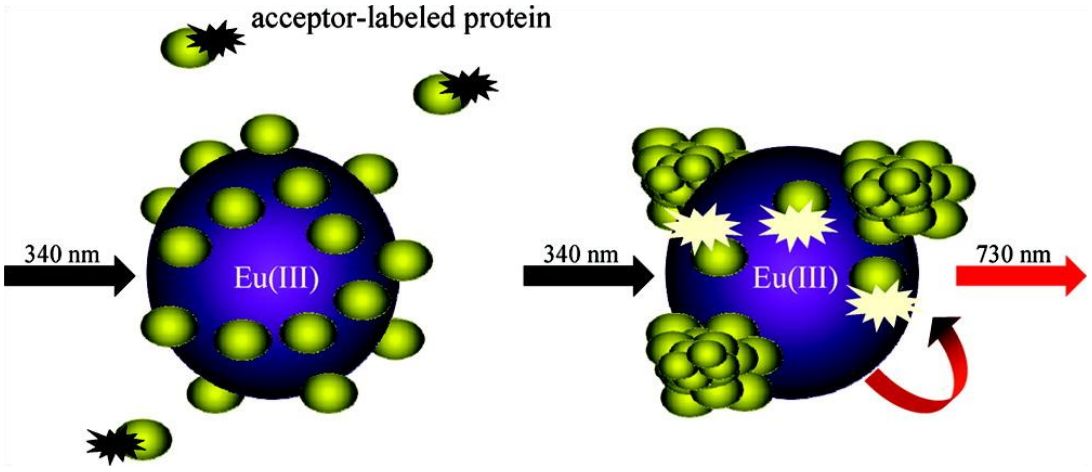

Figure 1.13. LRET assay based protein aggregation analysis with the help of europium(III) doped polystyrene nanoparticles. Low LRET signal is detected in case of non-aggregated protein, since these kinds of proteins are adsorbed on the nanoparticle that prevents the adsorption of labelled protein (left). However, the aggregated proteins are not efficiently adsorbed on the particles that

lead to adsorption of labelled protein, hence high LRET signal (right). Reproduced from Pihlasalo, S. *et al*[157].

When the LRET-acceptor labeled proteins are absorbed on the europium(III)-doped polystyrene particles, the signal of TR-LRET is monitored. The energy from the europium(III)-doped polystyrene particles is transferred to the γ-globulin labeled with Alexa Fluor 680, and the emission is detected at 730 nm in time-resolved luminescence mode using a microtiter plate, luminometer. There is a change in signal when the aggregated protein attempts to displace the labeled protein. Since the concentration of the protein remains constant, the change in signal measures the rate of aggregation. However, the non-aggregated proteins are covered on the surface of the particles, so that the absorption of labeled protein is prevented. Hence, the process of protein aggregation detection becomes fast and inexpensive.

1.7.5. Advantages of nanoparticles based therapeutics over conventional therapies for amyloidoses

A brief mechanistic discussion about protein misfolding and amyloid formation concluded that formulation of possible therapeutic strategies intend to rescue the native protein conformation or stabilize the intermediate or misfolded protein conformations. Based on these concepts, although many chemical compounds and their derivatives were found to be having potential to inhibit the protein aggregation, however no successful therapeutic approach has been formulated for human being to treat protein misfolding diseases. Furthermore, many are in trails like Doblin-based Elan Pharmaceuticals, AN-1792 against Alzheimer's disease. Moreover, all amyloid-β-centric approaches have failed in phase-III clinical trials[158]. Many of them like tramiprosate, tarenflurbil and semagacestat have been discontinued[158]. Hence, scientists are looking forward for alternative strategies to cure protein misfolding diseases. Since the problems, entirely or partly, pose a significant social burden due to the increasing numbers of affected people and severity of the disease, the necessity for improved health care, diagnostics and treatment is immediate need of the society. However, nanotechnology based treatments involving the design and application of nanoscale medicines and drug delivery systems have been employed to optimize the therapeutics. It includes metal nanoparticles, solid lipid nanoparticles, polymeric nanoparticles, microemulsion, nanoemulsion, nanostructured lipid carriers and liquid crystals. One specific example of nanotechnology in advanced experimental treatment of Parkinson's disease (PD) is the brain-targeted delivery of dopamine[159]. The *in vitro*

cytotoxicity of dopamine-loaded chitosan nanoparticle was found to be less than the free dopamine[160]. Nanodelivery of dopaminergic agonists like bromocriptine[161], levodopa[162], and ropinirole[163] is being pursued because of their potential to improve brain uptake, and reduce its associated side effects. Hence, the nanosystems prove to be more effective as drug delivery agents specifically targeted to the CNS, because of good bioavailability and therapeutic efficacies. Ikeda and co-workers have shown that biocompatible nanogels of 20-30 nm diameter can prevent aggregation of proteins and inhibit amyloid fiber formation[164]. Hence, nanoparticles can be adopted as a novel therapeutic approach to treat protein misfolding diseases.

1.8. Objectives

Objectives of the thesis are to study the effects of different photocatalytic nanoparticle interfaces on biological membranes and biomacromoleculs like:

(a) (i) Effect of interfacial potential on antimicrobial propensity of ZnONPs
    (ii) Effect of surface functionality on antimicrobial propensity of IONPs
(b) Effect of ZnONP surface defects on cytotoxic and antimicrobial propensities
(c) Effect of interfacial assembly of antimicrobial peptide on conformational and functional dynamics of the peptide
(d) Effect of interfacial interaction with globular protein on conformational dynamics of the protein (lysozyme)

First objective of the thesis will shed light on underlying mechanism of antimicrobial activity of photocatalytic nanoparticles, emphasizing on the role of interfacial potential and functional groups at the nano-bio interfaces. Whereas, the second objective explored the effects of nanoparticle surface defects and crystallinity on cytotoxic and antimicrobial activities of the particle. Third and fourth objectives of the thesis evaluated the role of protein interfacial assembly or interaction onto nanoparticle in defining the conformational and functional dynamics of the protein. Interfacial assembly of protein onto nanoparticle is a resultant of the physico-chemical properties of the particle/protein, hence the behavior of interface against protein varies accordingly. The findings may be adopted in designing nanoparticle mediated approaches to enhance the functionality of peptides as well as to evaluate the role of conformational rearrangement upon interaction in amyloidosis diseases.

Chapter 2

Materials and Methods

2.1. Materials

2.1.1. Chemicals

Zinc acetate dihydrate, urea, glutaraldehyde, sodium hydroxide were purchased from Merck, India, whereas ferrous chloride tetrahydrate, ferric chloride hexahydrate, silver nitrate, lysozyme, nisin, silver nanoparticle were purchased from Sigma Aldrich, USA. Nutrient broth, nutrient agar, tannic acid, DMEM medium were purchased from Himedia, India. 2', 7'-Dichlorodihydrofluorescein diacetate (DCHF-DA) used for oxidative stress measurement was purchased from Cayman chemicals USA.

2.1.2. Bacterial Strains

Different bacterial strains used for antimicrobial studies, like *Bacillus subtilis* (MTCC 736), *Bacillus thuringiensis* (MTCC 8998), *Staphylococcus aureus* (MTCC 737), *Escherichia coli* (MTCC 443), *Shigella flexneri* (MTCC 1457), *Proteus vulgaris* (MTCC 426), were purchased from Institute of Microbial Technology (IMTECH), Chandigarh, India.

2.1.3. Cell culture

Human Embryonic Kidney (HEK 293) and fibrosarcoma (HT1080) cell lines were purchased from National Centre for Cell Sciences (NCCS), Pune. Cell lines were cultured in DMEM media supplemented with 10% fetal bovine serum (FBS) and penstrep (1% (v/v)).

2.2. Synthesis of nanoparticles

2.2.1. Synthesis and surface modification of zinc oxide nanoparticle

The zinc oxide nanoparticles (ZnONPs) of different morphology were prepared by chemical precipitation method using zinc acetate dihydrate and urea. Briefly, zinc acetate dihydrate (0.1 M) and urea (0.1 M) solutions were prepared and mixed in a beaker at the volumetric ratio of 1:4. The mixture was stirred at room temperature and heated at 115 ^{o}C in a muffle furnace for 1.5 hrs. The white precipitate formed as a result of reaction

between zinc acetate and urea was collected by centrifuging at 6,000 rpm for 10 min and washed three times to remove absorbed chemicals and ions using deionised water. The pellet was dried at 100 ^{o}C and different fraction of the obtained powder were calcinated in silica crucible at different temperatures like 300, 500, 700 ^{o}C for two hrs.

The ZnONP synthesized was found to have positive surface potential (p-ZnONP). To obtain negative surface potential ZnONP, surface modification of ZnONP (calcinated at 300 ^{o}C) prepared earlier was done using sodium citrate. Briefly, 20 grams of ZnONP was suspended in 1% sodium citrate, 10 mM HEPES buffer, pH 7.4, and vigorously vortexed for 5 mins followed by sonication for 10 mins. The above solution was centrifuged at 6000 rpm for 30 mins, and the pellet was collected and washed twice in deionised water. Thereafter, the pellet was dried in hot air oven to get the negative surface potential ZnONP (n-ZnONP)[165].

The XRD patterns of both p-ZnONP and n-ZnONP were recorded on an Ultima IV model Rigaku X-ray diffractometer (Tokyo, Japan) using CU-Kα radiation at a scan rate of 20 ^{o}/mins with a step size of 0.05 degree over 2θ range of 25^{o} to 70^{o}. The X′-pert high score software having search and match facility was employed to study the different phases present in the samples. The morphological features like shape and size of synthesized NPs were studied using FE-SEM (Nova Nano SEM 450, FEI company), whereas the surface plasmon resonance properties of both types of NPs were analyzed using UV-Vis spectrophotometer (Cary 100, Agilent Technology, Singapore) in absorbance mode. The FTIR spectra of both types of NPs were recorded on an alpha platinum attenuated total reflection fourier transform infrared (ATR)-FTIR spectrophotometer (Bruker, Germany). The spectra were obtained in ATR mode with 128 scans and 8 cm^{-1} resolution in a range of 2500–500 cm^{-1} on diamond crystal, and the surface potential was studied using a zeta analyzer (Malvern Zetasizer Nano ZS90, Netherland).

2.2.2. Synthesis and surface modification of iron oxide nanoparticle

The iron oxide nanoparticle (IONP) was synthesized from ferrous chloride tetrahydrate ($FeCl_2.4H_2O$) and ferric chloride hexahydrate ($FeCl_3.6H_2O$) by co-precipitation method, following the protocol described by Bellova *et al*[89] with some modifications. Required amounts of 0.1 M $FeCl_2.4H_2O$ and 0.2 M $FeCl_3.6H_2O$ were added to 100 mL of deionised water, and stirred using a magnetic stirrer until a homogeneous solution was formed. The

solution was sealed and heated at 60 ^{o}C for 15-20 mins in a water bath followed by the addition of 14 mL of 25% sodium hydroxide (NaOH). The black precipitate formed upon completion of the reaction was centrifuged at 7000 rpm for 15 mins, and washed three times with deionised water, followed by drying at 60 ^{o}C to get the powder form of IONP. For surface modification of IONP, the protocol adopted by Samani S. M. *et al.*[166] was followed. In Brief, 20 mg of chitosan was dissolved in 100 mL of deionized water containing 1 M of acetic acid, and vortexed for 5 mins. 70 mg of synthesized IONP was dissolved in the above prepared chitosan solution, and kept overnight (~18 hrs) on a magnetic stirrer at room temperature (25 ^{o}C). During the process, chitosan molecules absorbed upon the IONP surface resulting into color change from black to brown. After the change in color, suspension was centrifuged at 7000 rpm for 30 mins, and pellet was collected. The pellet was further washed two times with deionised water to remove unabsorbed chitosan molecules and traces of acetic acid, and dried to powder at 70 ^{o}C to obtain surface modified IONP. The two IONPs obtained were named as n-IONP and p-IONP for iron oxide nanoparticle as synthesized and chitosan modified iron oxide nanoparticle respectively.

The XRD patterns of both iron oxide and chitosan coated iron oxide NPs were recorded on a X-ray diffractometer (Ultima IV model Rigaku, Tokyo, Japan) using CU-Kα radiation at a voltage of 30 KV and a current of 40 mA with a scan rate of 20 ^{o}/min and step size of 0.05 ^{o} over 2θ range of 25^{o} to 70^{o}. The different phases present in the synthesized sample were evaluated using X′-pert high score software having search and match facility. The field emission scanning electron microscopy (FE-SEM, Nova Nano SEM 450, FEI Company, Netherland) was employed to analyze the morphological features of synthesized IONPs at an accelerating voltage of 10 KV upon gold coating for 3 mins. The UV-Visble spectrophotometer (Cary 100, Agilent Technology, Singapore), was employed to study the surface plasmon resonance properties of both n-IONP and p-IONP at desired dilutions using deionised water. Fourier transform infrared (FTIR) spectra of both types of the IONPs along with chitosan were recorded on a alpha platinum attenuated total reflectance (ATR)-FTIR spectrophotometer (Bruker, Germany) in ATR mode with 128 scans and 8 cm^{-1} resolution in a range of 2000–500 cm^{-1} on diamond crystal, whereas the surface potential of both IONPs was measured using zeta analyzer (Malvern Zetasizer Nano ZS90, Netherland). Moreover, the concentrations of Fe^{3+} present in our synthesized IONP samples were determined using atomic absorption spectrophotometer (Perkin Elmer

AA200, Singapore). Specific cathode lamps were employed and the instrument tuned to corresponding wavelengths. Air-acetylene flame was used for atomization of IONP suspension. Initially, the flame absorptions were calibrated by using respective standard solutions in the range of 1-2 mg/L. Following the calibration, concentration of the synthesized IONP samples were found 18.1 ppm of Fe. On applying the empirical formula of magnetite (Fe_3O_4) present in the nanoparticles, since our synthesized iron oxide is magnetite as reported by XRD results, the equivalent concentration of iron oxide in suspension were estimated to be 101 µM. The different concentrations in reactions were obtained by dilution with respective buffers or broth.

2.2.3. Synthesis of silver nanoparticls using bacteria from coal mine- A green synthesis approach

2.2.3.1. Isolation of bacterial samples

For isolation of bacterial strains, 100 mg coal powder was measured and dissolved in 1mL of autoclaved distilled water, followed by 10000 dilutions using autoclaved distilled water. 20 µL of the solution was spread on agar plate, and kept for overnight incubation at 37 ^oC. The slant cultures of bacterial strains were prepared for further use by taking single colonies from the plates. Many strains were isolated and randomly chosen three among them for our further experimental works.

2.2.3.2. Determination of $AgNO_3$ minimum inhibitory concentrations against extracted bacteria

Minimum inhibitory concentration (MIC) was determined to check resistance of extracted bacteria against silver metal ions in comparison to normal chemical conditions. The mother cultures of the bacteria were prepared by inoculating a loop full of bacteria into 5 mL nutrient broth, and incubated overnight at 150 rpm and 37 ^oC. Different reaction mixtures were prepared in 96 well plate taking different concentrations (0, 0.019, 0.15, and 1.25 mM) of $AgNO_3$ and 20 µL of bacterial culture, and the volume was adjusted to final volume of 300 µL using nutrient broth. The growth of bacteria was observed by taking O.D. at 600 nm using micro-plate reader (Synergy H1 hybrid reader, Biotek, USA) at 37 ^oC at regular time interval. Colony forming unit (CFU) measurements were performed to estimate the number of viable bacteria cells present in different reaction mixtures. The samples were taken from early stationary phase of the growth curve from respective bacteria culture in presence of 0, 0.019, 0.15, and 1.25 mM $AgNO_3$. The

samples were spread on nutrient agar plate after 10000 times dilutions. The plates were kept overnight in incubator at 37 ^{o}C for their proper growth in colony, and the colonies were counted and expressed as percentage of viable cells. The percentage of viable cells was measured by comparing the number of colonies obtained in bacterial growth found in absence of $AgNO_3$. Additionally, three bacteria were characterized using the standard protocol of Gram staining to know whether the bacteria are Gram-positive or Gram-negative. From the above study, first two tested bacteria found resistant to $AgNO_3$ and the third one sensitive to $AgNO_3$. So, two resistant bacteria were taken for synthesis of AgNPs.

2.2.3.3. Synthesis of silver nanoparticles

For synthesis of AgNPs, 5 mL of mother cultures of two bacteria ware prepared in nutrient broth, and kept overnight at 37 ^{o}C and 150 rpm. 1 mL of the culture was added to 100 mL of nutrient broth and left for growth at 37 ^{o}C and 150 rpm agitation. Appropriate amount of $AgNO_3$ was added at the mid log phase of growth so as to obtain the MIC value (0.15 mM) of $AgNO_3$ in growth medium. The reaction mixtures were incubated further for 24 hrs at 37 ^{o}C with agitation at 150 rpm for nanoparticles synthesis. The bacterial culture containing the nanoparticles was sonicated followed by centrifugation at 6000 rpm for 15 mins, and the supernatant was collected for characterization of AgNPs. The nanoparticle samples obtained from the two bacteria were named as AgNP1 and AgNP2 respectively.

2.2.3.4. Characterization of silver nanoparticles

The synthesis of silver nanoparticles (bioreduction of silver ions to silver nanoparticles) was confirmed using UV-Visible spectroscopy (Cary 100, Agilent Technology, Singapore) within the range of 350-600 nm. Dynamic light scattering is a technique to determine the size distribution of particles in aqueous solution. Here, we have used Zeta analyzer (Malvern Zetasizer Nano ZS90, Netherland) to measure the distribution of nanoparticles in the aqueous solution synthesized using the bacteria. To check the stability of nanoparticles, the zeta potential of the above two nanoparticle samples were also measured using zeta sizer. The morphology of bacteria after treatment of $AgNO_3$ at MIC was studied using Field Emission Scanning Electron Microscopy (FE-SEM, Nova Nano SEM 450, FEI, Netherland). The samples were prepared following the protocol adopted by Arakha *et al.*[167]. In brief, the $AgNO_3$ treated bacterial samples were collected from the stationary phase of growth kinetics and centrifuged at 5000 rpm for 5 mins. Pellets were collected and washed twice using PBS buffer and resuspened in PBS buffer again. One

drop of the resuspened bacteria sample was put on glass slide and kept for dying at 37 ^{o}C in incubator. The dried bacterial samples were flooded with glutaraldehyde (2.5%) and kept for overnight (~18 hrs) incubation at room temperature. After incubation, 1% of tannic acid was flooded over the slides, and the slides were kept for 5mins at room temperature. The slides were again washed with distilled water and dehydrated with ethanol series (30, 50, 70, 90, and 100%), and kept for drying. The samples were scanned for bacterial as well as nanoparticle morphology using FE-SEM after gold coating of the samples for 3 mins. The elemental composition of synthesized nanoparticle sample was determined using energy dispersive X-ray spectroscopy attached with the FE-SEM. The samples were characterized by ATR-FTIR spectroscopy (α2 model, Bruker, Germany) to observe the bond level vibrations of different bonds present in the synthesized samples. For this, samples were sonicated and analyzed putting on the diamond platform of ATR-FTIR with 128 scans at 8 cm^{-1} resolution in a range of 2000-500 cm^{-1}.

2.3. Effect of interfacial potential on antimicrobial propensity of ZnONPs

2.3.1. ZnONP-bacteria interfacial potential measurement

The mother cultures of all bacteria were prepared by inoculating a single bacterial colony into nutrient broth followed by incubation at 37 ^{o}C with constant shaking at 150 rpm. For surface potential measurement at zeta analyzer, bacterial cells were harvested by centrifugation at 5000 rpm for 10 mins at 4 ^{o}C from the overnight culture, followed by two times washing using 1X PBS buffer, and resuspended in PBS buffer prior to the measurement.

For surface charge neutralization study, 100 µL of bacteria culture in Muller Hinton Broth (MHB), grown overnight at 37 ^{o}C and 150 rpm, were inoculated into 5 mL of fresh MHB. The culture was allowed to grow at 37 ^{o}C until the bacterial concentration reached ~3×10^{8} colony forming units/mL ($O.D._{600}$ ~ 0.1). The culture was diluted using fresh MHB to 3×10^{5} CFU/mL. ZnONPs were suspended in 10 mM HEPES buffer (pH 7.4 containing 150 mM NaCl) with stock concentration of 5 mg/mL, and sonicated for proper dispersion. Dilutions of ZnONPs were prepared to final concentrations of 160, 250, 500, 1000, and 2500 µg/mL, using HEPES buffer. For neutralization reactions, 100 µL of the diluted ZnONPs concentrations were added to 900 µL of bacterial culture, and

incubated for approximately 2-3 hrs (higher incubation time for *B. subtilis*) at 37 ^{o}C with shaking, prior to zeta potential measurements. Positive control was 900 µL bacterial cultures diluted with 100 µL of the medium. For zeta potential measurements and ROS study, *B. subtilis* and *E. coli* cell cultures were taken only, as representatives for Gram-positive and Gram-negative bacteria.

2.3.2. Bacterial cell viability in presence of ZnONPs

The strain specific antibacterial activity of p-ZnONP was studied against the bacterium. All growth kinetic studies were performed by measuring O.D. at 600 nm using a UV-Visible spectrophotometer (Perkin Elmer, Lambda 35, Singapore) with temperature controller peltier system (PTP 1+1 peltier system, Perkin Elmer, Singapore) at 37 ^{o}C in static condition. In an aseptic condition, 100 µL of respective bacteria culture was diluted to 3 mL using nutrient broth, followed by growth till mid log phase. Thereafter, an appropriate amount of p-ZnONP suspension (prepared in sterilized nutrient broth) was added to get the final p-ZnONP concentrations of 16, 25, 50, 100 and 250 µg/mL (additional 500 µg/mL data point was taken for *Bacillus thuringiensis*) in culture, by keeping total volume constant. Culture without p-ZnONP was taken as positive control. In each case, p-ZnONP was added to the reaction mixture at mid log phase of growth kinetics, since at this phase the organisms are most potent/viable. Hence, the requirement of p-ZnONP to inhibit the growth is relatively high, that lead to precise determination of the MIC of p-ZnONP[168]. In addition to above study, similar growth kinetics of bacteria was performed for n-ZnONP.

The number of viable cells, after p-ZnONP treatment at mid log phase of their kinetics, were determined by CFU study. For the study, upon completion of the growth kinetics (from stationary phase) 10 µL of the bacterial samples were taken and spread on the nutrient agar plates after 10000 fold dilution. The plates were incubated overnight at 37 ^{o}C. Colony forming units were quantified and compared with control to check the viability of bacterial cells upon treatment with varying concentrations of p-ZnONP.

2.3.3. ROS detection

The production of ROS in the bacterial cultures treated with different concentrations of the ZnONPs was evaluated using 2', 7'-dichlorodihydrofluorescein diacetate, DCFH-DA. *E. coli* and *B. subtilis* cultures were incubated at 37 ^{o}C with 200 µM of DCFH-DA, and

fluorescence emission was observed at 523 nm with excitation at 503 nm using micro-plate reader (Synergy H1 hybride reader, Biotek, USA). The stock concentration of DCFH-DA was calculated using 59,500 $M^{-1}cm^{-1}$ molar extinction coefficient at 500 nm. At the mid log phase of bacterial growth, the ZnONP suspensions were added to the final concentration of 16 and 250 µg/mL. To determine the ROS variation, the emission intensity of the treated cultures was compared with both, positive (without ZnONP treatment) and negative (culture media without DCFH-DA only) controls.

2.3.4. Bacterial morphology on ZnONP treatment

Initially, the morphology of bacteria upon p-ZnONP treatment was visualized using phase contrast microscopy (Olympus CKX41, JAPAN) with U-CMAD3 digital live camera and Q-capture pro7 software, taking samples directly upon the slide from stationary phase of growth kinetics. To gain more insights into the morphological features, the samples using SEM and FE-SEM were scanned. For the imaging, samples were prepared using the protocol given by De, J. *et al*, with some modifications[169]. In brief, from the stationary phase of growth kinetics, 1 mL of bacterial cultures were taken, and centrifuged at 5000 rpm for 5 mins at 4 ^{o}C. The pellet was collected, washed twice, and resuspended in 1X phosphate buffer saline (PBS). One drop of the resuspended culture was put on glass slides, and bacterial cells were fixed by incubating overnight in 2.5% glutaraldehyde (prepared in 1X PBS). The fixed slides were suspended in 1% tannic acid for few mins, and washed with distilled water followed by dehydration using increasing concentration of ethanol (30, 50, 70, 90, and 100%). The fixed, washed, and dehydrated bacterial cells were coated with platinum and gold for SEM (Jeol-JSM-6480 LV SEM, Japan) and FE-SEM (Nova NanoSEM 450/FEI), scanning, respectively.

2.4. Effect of surface functionality on antimicrobial propensity of IONPs

2.4.1. Growth kinetic analysis

Initially, effects of interaction pattern at IONP-bacteria interface was studied by following growth kinetics of *B. subtilis* and *E. coli* in absence and presence of different n-IONP and p-IONP concentrations. The mother cultures of test organisms were prepared in nutrient broth taking loop full of bacteria from the specified slant culture, and cultured overnight at 37 ^{o}C and 150 rpm agitation. Different concentrations of both, n-IONP and p-IONP, taken were 2.5, 5, 10, 25, and 50 µM. The IONP stock solution was prepared by dispersing

IONP in sterilized nutrient broth and sonicated for 10 mins followed by UV radiation sterilization before use. The reaction mixtures without NPs were taken as controls. Briefly, 20 µL of bacterial mother cultures were added to the different reaction mixtures prepared in 96-well plate, and the reaction volumes were adjusted by adding nutrient broth to a final volume of 300 µL with nanoparticle. The growth kinetic studies were performed by measuring optical density (O.D.) at 600 nm using plate reader (Synergy H1 hybrid reader, Biotek, USA) at regular time interval. At approximately mid log phase of bacterial growth, respective concentrations of NPs were added to the respective reaction mixtures. Upon addition of the NP, data collection for growth curve was immediately started with dead time of 10 mins.

2.4.2. CFU measurement

The number of viable cells was quantified by measuring colony forming units (CFUs) for both types of bacteria upon treatment with different n- and p-IONP concentrations. For CFU measurement, 10 µL of sample from the stationary phase of growth kinetics were taken from different reaction mixtures having different n-IONP and p-IONP concentrations (2.5, 10, and 50 µM), and spread on the nutrient agar plates after 10000 times dilution in autoclaved distilled water. The plates were incubated overnight at 37 ^{o}C. The number of viable cells after treatment with different IONPs were quantified and compared with positive control (culture without NP) to evaluate the antimicrobial propensity of IONPs.

2.4.3. ROS detection

The production of ROS, predominantly responsible for the toxicity of NPs, was evaluated using 2', 7'-dichlorodihydrofluorescein diacetate (DCFH-DA). Generally, DCFH-DA, a peroxynitrite indicator, having the potential to detect both nitric oxide and hydrogen peroxide (considered as ROS) inside as well as outside of the cells[170]. The bacterial cells were treated with DCFH-DA (200 µM), and fluorescence emission at 523 nm was measured using synergy H1 hybrid reader (Biotek, USA) with an excitation at 503 nm. Different n-IONP and p-IONP concentrations (0, 2.5, and 50 µM) were added to respective wells at log phase of the growth kinetics. ROS variation was determined comparing the fluorescent intensities of different wells with that of positive control (without NPs treatment). For error bar these experiments were done in triplicate.

2.4.4. LIVE/DEAD BacLight fluorescence microscopy assay

The fluorescence microscopy assay is one of the important methods to visualize the effect of interaction pattern on antimicrobial propensity of the NPs in the bulk culture. The fluorescence microscopy (Olympus IX71, Germany) with 20X objective lens was employed for imaging bacteria cells (control) and NPs (50 µM) treated bacterial cells to distinguish viable cells from dead cells with the help of LIVE/DEAD BacLight Bacterial Viability Kit (L7007, Molecular probes, invitrogen). In brief, 30 mL of each culture, *B. subtilis* and *E. coli*, were prepared in separate flasks by inoculating 29 mL of nutrient broth with 1 mL of overnight cultures. At mid log phase of bacterial growth, the NP solutions were added to the final concentration of 50 µM NPs, and allowed to grow till late log phase. From these cultures, 25 mL of each bacterial solution were centrifuged at 7000 rpm for 15 mins. The supernatant were discarded, and the pellets were suspended in 2 mL of HEPES buffer (10 mM, pH 7.4, containing 150 mM NaCl). 1 mL of the bacterial cell suspensions were added to 20 mL of HEPES buffer in two separate tubes. Both samples were incubated at room temperature for one hour (with mixing every 15 mins). The suspensions were centrifuged at 7000 rpm for 15 mins, pellets were collected and suspended in 20 mL of HEPES buffer, and centrifuged at 7000 rpm for 15 mins. Finally, the pellets were resuspended in 10 mL of HEPES buffer in separate tubes, and optical density was measured at 670 nm. 3 µL of dye mixture (equal volume of component A and component B of the kit) was added to each 1 mL of the prepared bacterial samples, and incubated in dark for 15 mins after proper mixing of bacterial suspensions. Fluorescence images were taken by trapping 5 µL of stained bacterial samples between a slide and cover slip.

2.5. Effect of ZnONP surface defects on cytotoxic and antimicrobial propensities

2.5.1. Cell culture and ZnONP stock solution preparation

Fibrosarcoma (HT1080) cell lines were purchased from National Centre for Cell Sciences (NCCS), Pune. Cell lines were cultured in DMEM media supplemented with 10% fetal bovine serum (FBS) and penstrep (1%, v/v). Stock solutions of ZnONPs were prepared in autoclaved PBS buffer. Trypsinization was done to harvest the cells and the number of cells was counted using hemocytometer.

2.5.2. Cytotoxicity of ZnONPs

The cytotoxicity of ZnONPs synthesized at different calcinations temperatures was evaluated following the protocol adopted by Arakha M. *et al*[23] against fibrosarcoma cell line (HT1080) using Alamar blue dye reduction assay. Briefly, 5000 cells of HT1080 cells/well were seeded in 96-well plate with proper medium (DMEM, Himedia, India), with 10 % fetal bovine serum (FBS). Following 24 hrs of incubation in a CO_2 incubator, the culture media were replaced with fresh DMEM media containing different ZnONPs at different concentrations (0, 2.5, 5, 10, 25, and 50 μg/mL). The cells were further incubated for another 24 hrs in CO_2 incubator. Alamar blue dye (10% v/v), Invitrogen, USA) was added to different wells and fluorescence intensity was detected at 590 nm (emission wavelengths), with an excitation at 544 nm. Percentage of viable cells for ZnONPs treated and untreated (control) samples were calculated from the ratio of fluorescence intensity of treated and untreated cells.

2.5.3. ZnONPs induced ROS generation

Intracellular ROS levels generated due to treatment of different ZnONPs were evaluated using 2,7-dichlorodihydrofluorescein diacetate oxidation (DCFH-DA, Invitrogen) using multimode fluorescence microplate reader (Synergy H1 hybrid, Biotek, USA), following the protocol adopted by Kang, M. A. *et al.*[171]. In brief, HT1080 cell was seeded in a black/clear bottom 96-well plate at a density of 5000 cells/well, followed by incubation in a CO_2 incubator for 24 hrs. Following the incubation, cells were washed using PBS buffer and treated with 25 μM DCFH-DA dye for 1 hr. Cells were then re-washed with PBS, and treated with different ZnONPs (50 μg/mL). The generated ROS level was detected measuring the fluorescence intensity at 523 nm with an excitation at 502 nm. Level of ROS variation was determined by comparing the obtained fluorescence intensity of treated samples with control. Triplicate experiments were performed to determine the standard error of mean.

2.5.4. Comet assay

The possibility of DNA damage upon ZnONP treatment was analyzed using comet assay. For the same, approximately $2*10^5$ cells were seeded in a six well tissue culture plate and treated with different types of ZnONPs (fabricated at 300, 500, and 700 ^oC calcination), and prepared for comet assay following the protocol adopted by Olive, P. L. *et al*.[172].

2.5.5. Cell cycle analysis

Cell cycle analysis was carried out upon ZnONP treatments by staining the obtained DNA with ethidium bromide followed by flow cytometric measurement. For the same, approximately $2*10^5$ cells were seeded in a six well tissue culture plate. Following 24 hrs incubation, the cells were treated with ZnONP of different concentrations (5, 25, and 50 μg/mL), and incubated for further 24 hrs followed by removing the medium and stored until further analysis. The obtained ZnONP treated cells and control cells were washed using 1X PBS and trypsinized followed by harvesting in stored medium, and centrifuged at 1000 rpm for 15 mins. The obtained pellet was re-washed using PBS and fixed in ice-cold ethanol (70%) and stored in -20 ^oC. For flow cytometric analysis, the stored cells were washed using PBS and stained with ethidium bromide, and analyzed using flow cytometry (BD Bioscience, USA).

2.5.6. ZnONPs induced autophagy

The induction of autophagy was monitored using acridine orange assay. For this, the cells ($2*10^5$) were seeded in a six well plate, and treated with different 50 μg/mL ZnONPs, followed by incubation in a CO_2 incubator for additional 24 hrs. Following the incubation, 1 μg/mL acridine orange (Invitrogen, A3568) was added to the cells and incubated for 15 mins. The cells were then washed using PBS to remove the excess acridine orange and fresh media was added. The induction of autophagy upon the treatment of ZnONP was monitored using fluorescence microscope (Olympus IX71).

2.5.7. ZnONPs induced apoptosis

Apoptosis, which is also known as programmed cell death, plays key role both in development of multi cellular organisms maintaining tissue homeostasis and in many diseases like neurodegeneration, cancer etc. However, initiation of apoptosis progression is due to the caspases mediated activation of a proteolytic cascade[173]. It has been reported that chromatin condensation and fragmentation are two hallmarks of apoptosis[173]. Hence, theses two phenomena were studied in the cell upon ZnONP treatment. For this, upon 24 hrs ZnONP treatment, the HT1080 cells ($2*10^5$) were stained with 4,6-diamido-2-phenylindole dihydrochloride (DAPI) to observe the condensed chromatin. The fluorescence images were taken using an Epi-fluorescence microscope (Olympus IX71, Germany). The condensed nuclei obtained as a result of ZnONP treatment were counted among the total nuclei present in the field, and plotted graphically to demonstrate the percentage of apoptotic nuclei compared to normal nuclei. The induction of apoptosis by

ZnONPs was further confirmed by DNA fragmentation assay following the protocol adopted by Suman, S. *et al*[174]. Briefly, the obtained DNA precipitate was solubilized at 60 ^{o}C in 20 µL of 2 % sodium dodecyl sulfate (SDS) in TE buffer (10 mM Tris-HCl and 1 mM EDTA, pH 8.0), followed by adding 10 µL of loading dye (0.25 % bromophenol blue, 0.025 % xylene cyanol, and 30 % glycerol in water) to 40 µL of processed samples. Finally, the samples were loaded on 2 % agarose gel followed by electrophoresis for 45 mins at 70 V in presence of 0.5 µg/mL ethidium bromide. Upon completion of the electrophoresis, DNA was visualized in a UV trans-illuminator.

2.5.8. Morphological changes

The morphological variation of HT1080 cell upon ZnONPs treatment was observed by FE-SEM analysis, and the samples were prepared using the protocol followed by Wang J. *et al*.[175] with some modifications. HT1080 cells were grown on the slides used for FE-SEM analysis to a semi confluent state, treated with different ZnONPs (50 µg/mL), and incubated in CO_2 incubator for 24 hrs. Most of the media were removed, and the cells were washed with PBS buffer and fixed using 2% paraformaldehyde for 5 hrs at 4 ^{o}C. Cells were re-washed four times with PBS buffer followed by deionised water. Post fixation of samples was done in 1 % OsO_4 solution for 1 hr at 4 ^{o}C, followed by 1 hr tannic acid treatment. Finally, the cells were dehydrated using an ethanol series of 10, 20, 40, 50, 70, 90, and 100 %, and dried at room temperature.

2.6. Effect of interfacial assembly of antimicrobial peptide on conformational and functional dynamics of the peptide

2.6.1. Preparation of AgNP-nisin conjugates

Initially, nisin stock solution of 450 µg/mL was prepared in phosphate buffer (pH 7.4) and stored at -20 ^{o}C for further use. For preparation of AgNP-nisin conjugates, AgNP solution (20 µg/mL) was taken in three micro-centrifuge tubes, and varying volumes of nisin stock were added to respective centrifuge tubes to obtain a AgNP-nisin ratio of 1:0.25 (18 µg/mL AgNP : 4.5 µg/mL nisin), 1:0.5 (18 µg/mL AgNP : 9 µg/mL nisin), and 1:1 (18 µg/mL AgNP : 18 µg/mL nisin) w/w, respectively. The volume of all tubes was adjusted to 1 mL using phosphate buffer, pH 7.4. All samples were incubated overnight on rocker. Following the incubation, AgNP-nisin conjugates were separated by centrifuging the respective reaction mixtures at 14,000 rpm for 30 mins followed by washing twice with

phosphate buffer. The unbound nisin and silver nanoparticles were remained in supernatant, whereas the pellets representing the AgNP-nisin conjugates were separated. The pellets were resuspended in 50 µL phosphate buffer, and kept at 4 ^{o}C for further use. The resuspended precipitates were quantified for nisin using bicinchoninic acid (BCA) assay[176]. The found nisin concentrations were 5, 8 and 17 µM in 1:0.25, 1:0.5 and 1:1 AgNP:nisin ratio conjugates, respectively. From the resuspended volumes of respective ratios, a certain volume of the conjugates were taken for reaction with nisin concentration equivalent to 85, 170 and 340 nM (340 nM=1.2 µg/mL), respectively. 1.2 µg/mL (2.8 nM, approx.) of AgNP in the resuspended conjugates were observed using atomic absorption spectroscope (Perkin Elmer AA200, Singapore). Thus, the control for every antimicrobial measurements done were untreated, 1.2 µg/mL of nisin, and 1.2 µg/mL AgNP treated cells, respectively.

2.6.2. Biophysical characterization of AgNP-nisin conjugates

Initially, the impact of nisin on SPR spectra of AgNP was monitored just after 2 hrs of incubation with nisin using a UV-Visible spectrophotometer (Cary 100, Agilent Technology, Singapore). The conjugation of AgNP with nisin was further confirmed by zeta potential analysis. For the measurement, the AgNP-nisin conjugates were prepared in deionised water to avoid the interference of ions present in phosphate buffer. However, the conformational dynamics of nisin upon AgNP conjugation was analysed using ATR-FTIR (Bruker, Germany) spectroscope with 128 scans and 2 cm^{-1} resolution in the range of 2000–500 cm^{-1} on diamond crystal. To further strengthen IR data, CD-spectroscope (Jasco J-720 spectropolarimeter) was used to analyze the change in secondary structure upon conjugation in the range of 190-260 nm. Additionally, the impact of nisin on the morphology of AgNP was further explored using TEM (Tecnai F30, FEI, The Netherland) and FE-SEM (Nova Nano SEM 450, FEI, The Netherland).

To further strengthen the stability of complex with time, the molecular dynamics simulation of the AgNP core, nisin, and complex were performed by GROMACS 5.0.4,[177] using the GROMOS96 54A7 force field parameter set. An experimentally derived NMR structure of nisin deposited against the PDB entry 1WCO[178] was used for the simulations. The bonded and non-bonded parameters for the modified amino acid residues, didehydroalanine (Dha) and (2E)-2-Aminobut-2-enoic acid (Dbu) present in the peptide were obtained from the Automated topology Database (ATB)[179]. Parameters for D-alanine (Dal) and D-alpha-aminobutyric acid (Dbb) are available in the 54A7 force field set. The

coordinates and parameters for AgNP core were used as given in Kyrychenko *et al*[180]. The simulation was first set up for the modified nisin alone to observe structural changes, if any. First, the peptide was minimised and equilibrated for 10 ns, and then an independent production run for 50 ns was run. RMSD analysis was performed to observe structural change during the production run of 50 ns. Similarly, the AgNP core has been subjected to energy minimisation, equilibrated for 5 ns, and finally exposed to a 50 ns production run. This has been performed in order to ensure that the core does not collapse during the binding simulations. The compactness of the simulated AgNP has been validated by calculating the radius of gyration at the end of the simulation. AgNP and nisin conjugated at an average distance of 7 Å. The complex has been placed in a box with an edge distance of 1 nm. Solvation of the system has been implemented using the simple point charge (SPC) water model. After neutralizing, the system has been minimised using the steepest descent gradient followed by a 10 ns equilibration run at constant volume and 298 K temperature, employing the Berendsen method[181]. A 50 ns production run has been done to find the interaction between the nanoparticle core and nisin. With a time step of 2 fs, in all the simulations, the bond lengths have been kept constant using the LINCS algorithm[182]. Long range electrostatic interactions have been carried out using particle mesh Ewald (PME) summation[183]. Periodic boundary conditions have been applied. All the graphical visualizations have been done using VMD[184].

2.6.3. Antimicrobial activity of AgNP-nisin conjugates

The effect of AgNP-nisin conjugates on viability of bacterial cells was investigated using growth kinetic studies against *Bacillus subtilis*, *Staphylococcus aureus*, *Proteus vulgaris*, and *Escherichia coli*. The different reaction mixtures were prepared in 96-well plate taking 20 µL mother cultures of different bacteria, and the volume was adjusted using autoclaved nutrient broth to a final volume of 300 µL with respective concentrations of the AgNP-nisin conjugates. The growth kinetics of different bacteria was monitored recording the optical density (O.D.) at 600 nm with the help of a multi mode plate reader (Synergy H1 hybride reader, Biotek, USA) at a regular time interval of 5 minutes. 20 µL of AgNP-nisin conjugate suspension was added to respective well at mid log phase of growth kinetics, and data collection was started immediately with a dead time of 10 mins. In addition to growth kinetic studies, the number of viable cells in control, nisin, AgNP, and AgNP-nisin conjugates treated bacteria were measured following the protocol adopted by Arakha M. *et al*[167].

2.6.4. Interfacial and intracellular ROS detection

The generation of ROS due to the interaction of AgNP-nisin conjugates with bacterial membranes was evaluated using the DCFH-DA dye[23]. Different reaction mixtures were prepared in 96-well plate taking 20 µL of mother culture of bacteria, and nutrient broth was added to adjust the final volume of 300 µL with AgNP-nisin conjugates. After adding the dye with final concentration of 200 µM in reaction mixture, the fluorescence intensity at 523 nm was measured using the plate reader at an excitation wavelength of 502 nm. 20 µL of different AgNP-nisin conjugates were added to respective wells in the log phase of growth kinetics and fluorescence measurement was continued with a dead time of 5 mins.

2.6.5. Membrane destabilization and internalization of AgNP-nisin conjugates

The LIVE/DEAD BacLight fluorescence microscopy assay was performed to distinguish the live cells from the dead cells, upon treatment with AgNP-nisin conjugates using fluorescence microscope (Olympus IX71, Germany) with 20X objective lens, following the protocol adopted by Arakha M. *et al*[23, 167]. Additionally, the morphological changes of bacteria upon the conjugate treatment was studied using Scanning Electron Microscope (Jeol JSM6480, Japan), following the protocol adopted by Arakha M. *et al*.[167].

For labelling of the AgNP-nisin conjugates with fluorescein, the conjugates were prepared and suspended in deionised water. Upon washing the conjugate, the pellet was resuspended in 50 µL of fluorescein stock (1 mM stock in DMSO), and incubated in dark for 2 hrs at room temperature for labelling of fluorescein to the conjugate. The labelled AgNP-nisin conjugates were centrifuged at 14,000 rpm for 30 mins, and washed twice with deionised water to remove the residual free dye. Finally, the obtained pellet was resuspended in deionised water for further use. For confocal microscopic study, the studied bacteria were cultured in nutrient broth until mid-log phase of growth curve. At the mid log phase, the labelled AgNP-nisin conjugates were added to the bacterial culture and incubated overnight at 37 ^{o}C. The bacterial samples were analysed using the confocal microscope (Leica, TCS-SP8).

2.7. Effect of interfacial assembly of globular protein on conformational dynamics of the protein

2.7.1. Preparation of ZnONP solution

For all experimental purpose, colloidal ZnONP solution was prepared by dissolving 1 mg/mL of synthesized and characterized ZnONP powder (300 ^{o}C) in respective buffer followed by sonication at full amplitude for 5 minutes. The sonicated solution was filtered using 220 nm membrane filtered paper and analyzed using Atomic absorption spectroscope (AAS) for concentration determination. The concentration of colloidal ZnONP was found to be 3 mM using. The solution was stored in 4 ^{o}C for further use. Since ZnONP have the potential to aggregate in colloidal solution, hence to avoid aggregation, the colloidal solution of ZnONP was sonicated each time before use.

2.7.2. Preparation of lysozyme:ZnONP conjugates

The lysozyme-ZnONP conjugates (1:5, 1:10, 1:20,1:50, and 1:100 M/M) were prepared in two buffers (phosphate buffer pH 7.4 and glycine NaOH buffer pH 9) by dissolving different concentrations of ZnONP to 10 μM lysozyme solution followed by incubation of reaction mixture on rocker for overnight at room temperature.

2.7.3. Circular Dichroism (CD) Spectropolarimetry

The structural change of lysozyme upon interaction of ZnONP was evaluated using Circular Dichroism (CD) Spectropolarimetry (Jasco J-720 spectropolarimeter) with an average of three scans from 200 to 260 nm. The contribution of respective buffer was subtracted from the protein spectra to obtain the final spectra.

2.7.4. Intrinsic tryptophan fluorescence spectroscopy

Steady-state intrinsic tryptophan fluorescence spectra of the native and samples treated with varying concentrations of ZnONPs (overnight incubation) at pH 7.4 and pH 9 were recorded in LS 55 luminescence spectrofluorometer (LS55, Perkin- Elmer, USA). The excitation wavelength of 280 nm was used at a scan speed of 100 nm/min, and the emission spectra were recorded between 300 and 400 nm with excitation and emission slit of 3 nm each. Baseline correction was done with buffer without protein for all samples.

2.7.5. ANS fluorescence studies of lysozyme

The steady-state fluorescence measurements were performed on LS 55 luminescence spectrofluorometer. Both excitation and emission slits were set at 3 nm. For ANS binding experiment, protein samples (incubated overnight with and without ZnONPs) at pH 7.4 and pH 9 were incubated with optimized concentration of ANS (100 μM) for 30 min at 25

^{o}C in dark. The excitation wavelength for ANS fluorescence was set at 350 nm and the emission spectra were recorded from 400 to 600 nm.

2.7.6. Lysozyme tryptophan fluorescence quenching study using acrylamide

Fluorescence quenching of lysozyme was studied using different concentration of acrylamide (0-400 mM) in presence and absence of ZnONPs. Intrinsic tryptophan emission spectra were measured in the range of 300-400 nm after adding acrylamide, followed by incubation for 30 mins at 25 ^{o}C. Intrinsic tryptophan fluorescence intensities were measured in the emission wavelength range of 300-400 nm upon an excitation wavelength of 280 nm.

2.7.7. Thioflavin T assay of lysozyme fibrillation kinetics

Thioflavin T (ThT) stock solution was prepared in deionised water and filtered using 220 nm membrane filter paper and the concentration of the stock was determined using the molar extinction coefficient (ε_M = 36,000 $M^{-1}cm^{-1}$) at 412 nm. Different conjugates of lysozyme:ZnONP (1:5, 1:10, 1:20,1:50, and 1:100 M/M) were prepared at both pH (pH 7.4 and 9) keeping the concentration of lysozyme (10 µM) constant followed by overnight incubation on rocker at room temperature. The lysozyme and lysozyme:ZnONP conjugates were added with 100 µM SDS and 20 µM ThT. The fibrillation kinetics was observed by measuring fluorescence intensity at 490 nm upon excitation at 440 nm using a multi mode plate reader (Synergy H1 hybride reader, Biotek, USA).

2.7.8. Transmission Electron Microscopy study

To analyze the morphological features of the lysozyme amyloids, samples were taken from the stationary phase of fibrillation kinetics of lysozyme in absence and presence of ZnONP and prepared following the procedure adopted by Jha S. *et al*[185-186]. Briefly, 10 µl of the samples (control and 1:100, lysozyme:ZnONP conjugate) were put on carbon coated cupper grids (Ted Pella) and incubated at room temperature for 20 mins followed by negative staining with 2% osmium tetraoxide (OsO_4) for 2 mins. Electron microscopy images were recorded using FEI Tecnai transmission electron microscope (Tecnai F30, FEI, Netherland).

2.7.9. Circular Dichroism (CD) Spectropolarimetry

The structural change of lysozyme upon interaction of ZnONP in presence of 100 µM SDS was evaluated using Circular Dichroism (CD) Spectropolarimetry (Jasco J-720 spectropolarimeter) with an average three scans from 200 to 260 nm. The contribution of respective buffer was subtracted from the protein spectra to obtain the final spectra.

Chapter 3

Results and discussions

3.1. Synthesis and characterization of nanoparticles

3.1.1. Zinc Oxide nanoparticle

Synthesis of nanoparticles is a promising area of research in nanobiotechnology that aims to control the size, shape, and composition of nanoparticles, since each of these factors plays critical role in determining different applications[187]. Among different nanoparticles, zinc oxide nanoparticles (ZnONPs) have received enormous attention due to their wide band gap energy, high transmittance, and good electrical conductivity etc[18]. Hence ZnONPs are widely used in different fields like biosensors, gas sensors, solar cells, biological imaging, drug releasing, waste water treatment etc[18-19]. Although, various methods like sol gel, microemulsion techniques, pyrolysis, laser ablation, thermal evaporation, hydrothermal synthesis, microwave methods etc. have already been well established for synthesis of ZnONP. However due to their relatively higher surface free energy content, nanoparticles aggregate easily[18]. Hence, this study optimized a synthesis method to get control of surface potential, size and shape of nanoparticle with varying calcination temperatures, such as 300, 500 and 700 ^{o}C calcinations.

Initially, the formation of ZnO nanocrystals were confirmed from the analysis of X-ray diffraction (XRD) spectra of ZnONPs. The XRD spectra (Figure 3.1a) revealed that the ZnONP samples, prepared at different calcination temperatures were crystalline in nature with peaks at different diffraction 2θ angle values of 31, 34, 36, 47, 56, 62, 66, 67, and 68^{o} corresponding to different indices (100), (002), (101), (102), (110), (103), (200), (112) and (201), respectively. The indices are well indexed to the hexagonal structure of bulk ZnO lattice parameters[16, 188-189]. Additionally, the analysis of XRD spectra of ZnONPs using X'-pert high score software with search and match facility demonstrated that the synthesized ZnONPs have hexagonal Zn-O packing (JCPDS reference code–80-0074). The average particle size of different ZnONPs obtained at different calcination temperatures were determined using Scherrer's equation

Particle size = $K*\lambda/\beta \cos(\theta)$, Eq (1)

Where λ is the wavelength of X-ray ($1.540*10^{-10}$ m), K= 0.9 (shape factor), β is the full width at half of maximum (FWHM) in radians, and θ is the Braggs angle. From the Scherrer's equation, the average particle size of ZnONPs was 30, 35, and 45 nm for 300, 500, and 700 ^{o}C calcination temperatures, respectively. In addition, it was observed in the XRD spectra that upon increasing the calcination temperature, sharpness of the peaks increases while the FWHM decreases (Figure 3.1b). The FWHM value for crystals obtained at 700 ^{o}C was 0.220, which is significantly very low compared to crystals obtained at 300 ^{o}C (0.435). The lower FWHM values and increase in intensity of peaks implied that the synthesized ZnO powder become more crystalline with increase in the calcination temperature (Figure 3.1b).

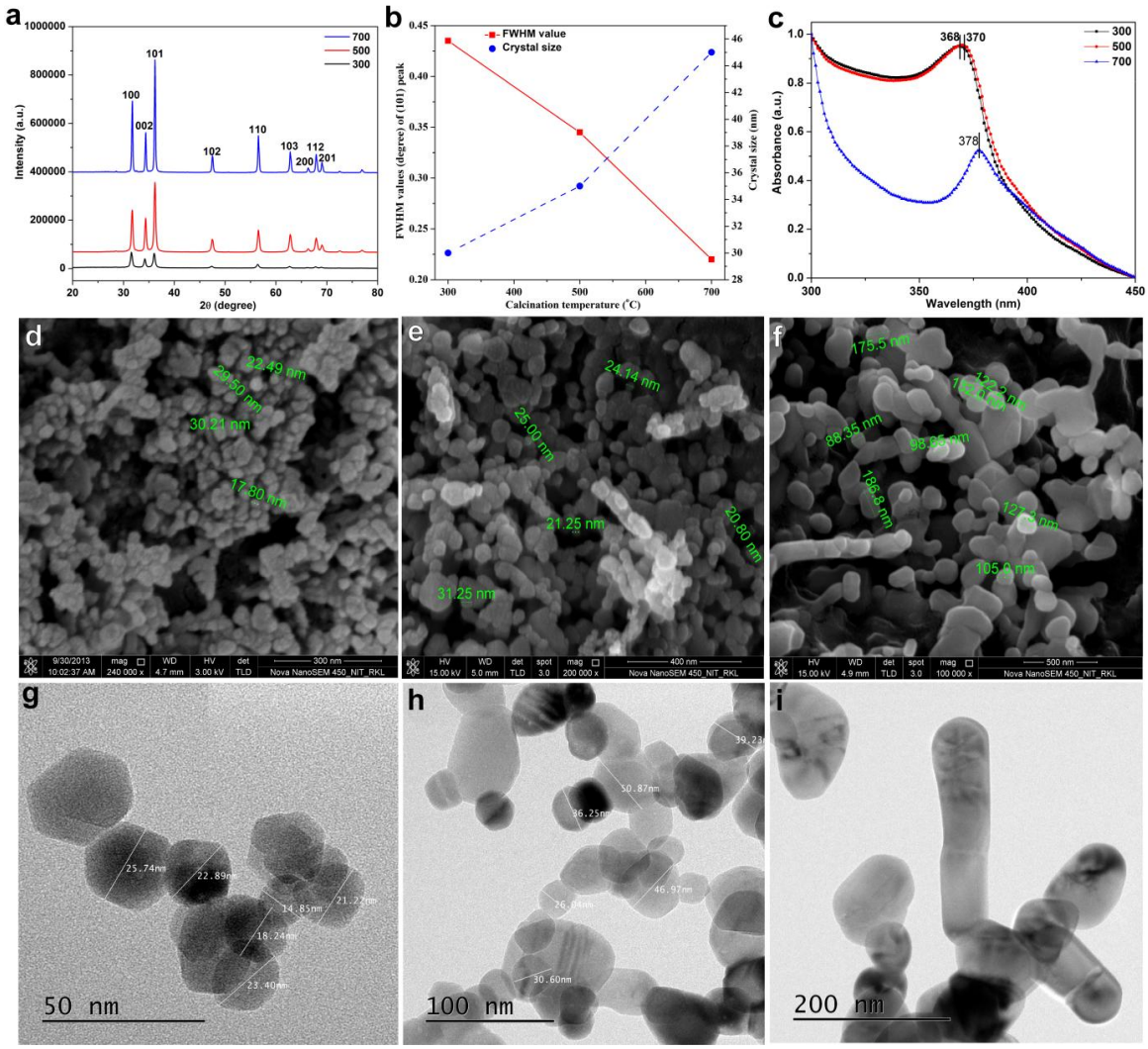

Figure 3.1. (a) XRD spectra of ZnONPs, (b) peak FWHM values (degree) and crystal size with respect to caclination temperatures of ZnONPs, (c) UV-Visible absorption spectra of ZnONPs, representative FE-SEM images for (d) 300 ^{o}C, (e) 500 ^{o}C, (f) 700 ^{o}C, and TEM images for (g) 300 ^{o}C, (h) 500 ^{o}C, (i) 700 ^{o}C calcinated ZnONPs, respectively.

Figure 3.1c represented the UV-Visible absorption spectra with absorption peaks at 368, 370, and 378 nm for ZnONPs calcinated at 300, 500, and 700 ^{o}C, respectively. The peaks are attributed to the SPR properties of respective ZnONPs. The shifting of absorption peak towards higher wavelength with increasing calcination temperature was due to increasing surface defects occurred at higher calcinations temperature, leading into decreased energy band gap. The energy band gap (E_{bg}) of synthesized ZnONPs was determined using the equation, $E_{bg}=1240/\lambda$ (eV)[16], where E_{bg} and λ represent for energy band gap in eV and wavelength in nanometer, respectively. The energy band gap of ZnONPs was found to be 3.36, 3.35 and 3.28 eV respectively, which clearly demonstrated the decrease in energy band gap with increase in calcination temperature. The XRD and UV-Visible spectra analysis, together, concluded that the calcination temperature significantly affect the crystallinity of ZnONPs, as ZnONPs crystallinity increased with increasing calcination temperature.

The bond level vibrations of different bonds present in ZnONPs were analyzed using ATR-FTIR spectroscope (Figure A1, Appendix). Strong absorption peaks at 1529 and 2337 cm^{-1} for each ZnONPs were due to bending vibrations of N-H and the asymmetric stretching vibration of C=O bonds, respectively. Additionally, peaks at 1680 cm^{-1} was due to C=O bond vibration. However, peaks below 800 cm^{-1} were due to metal-oxygen (Zn-O) bond vibration[190], which were found at 546 and 632 cm^{-1} confirming the presence of Zn–Oxygen bonds in the prepared sample. Moreover, peak at 3193 cm^{-1} was due to C-H vibrations, and at 3617, 3735 and 3850 cm^{-1} were attributed to the presence of elongation vibration of O-H bonds present in the ZnONPs[191].

The morphological features of the ZnONPs synthesized at different calcination temperatures were explored using Field Emission Scanning Electron Microscopy (FE-SEM), and Transmission Electron Microscopy (TEM). As shown in figures 3.1(d-f), nanoparticles possess various shapes in samples calcinated at 300 ^{o}C with most of them spherical in shape having diameters in the range of 10-30 nm. However, an increase in calcination temperature from 300 to 500 ^{o}C significantly increased the particle size without change in shape. Interestingly, with further increase in calcination temperature to 700 ^{o}C, besides the increase in size of the particle, the shape of particle became irregular. The morphologies of synthesized ZnONPs were further investigated using TEM. Figure 3.1(g-i) represented the images of ZnONPs synthesized at different calcination temperatures of 300, 500, and 700 ^{o}C, respectively using TEM. Most of the particles in

300 ^{o}C samples were approximately spherical in shape with average size ranging from 10-30 nm, whereas the size of nanoparticles increased to 20-50 nm for 500 ^{o}C sample. Interestingly, the particles in 700 ^{o}C sample were irregular in shape with relatively larger size. The shape of particle calcinated at 700 ^{o}C indicated that at highest calcination temperature the particles self-assembled to form rod-like structures. The morphology as analyzed from FE-SEM and TEM micrographs indicated that the growth of ZnONP was in both lateral and longitudinal direction at the highest calcinations temperature. The finding was also observed when the nanocrystal frabrication pH is changed, in the work of Baruah, S. *et al*[192]. Additionally, the studied SAED patterns of the particles obtained at different calcination temperatures indicated that the particles became more crystalline with rise in the temperature (Figure A2, Appendix).

EDX analysis was carried out to illustrate the elemental composition of the synthesized ZnONPs. As shown in figure A3 (Appendix), prominent peaks for carbon, oxygen, zinc and copper were found in the EDX spectra. However, the peaks for carbon and copper were due to the carbon grid used for analysis, whereas prominent peaks of zinc and oxygen confirmed the composition of crystalline powder as ZnONP. The atomic percentage of zinc and oxygen present in the synthesized samples are listed in table A1 (Appendix). Here, it is noteworthy that the atom percentage of oxygen decreased with increasing temperature. Hence, the finding indicated that the oxygen vacancy created due to high calcination temperature, which is resulting into narrowing of energy band gap[193]. The increase in oxygen vacancies helped in delocalization of the impurity states, and the delocalized impurity states overlap with the edge of the valence band resulting in narrowing of the energy band gap[194-195]. Hence, the ZnONP obtained at 700 ^{o}C calcination temperature showed highest oxygen vacancy demonstrating narrower energy band gap, which further supported the findings from UV-Visible spectroscopic data. In addition, Zhang, X. *et al* have also reported that ZnO nanorods possess higher photocatalytic activity due to presence of abundant oxygen vacancies or defects[16].

The zeta potential values of the synthesized ZnONPs were found to be +24.8, +18.4, and -4.19, respectively. Irrespective of charge, sign the magnitude of zeta potential decreased from 300 ^{o}C to 700 ^{o}C, which possibly played role in lateral and longitudinal assembly of the particle, producing larger size NP with increase in calcination temperature.

3.1.1.1. Surface modification of ZnONP

To elucidate the role of nanoparticle interface and/or interfacial potential affecting the antimicrobial propensity of ZnONP, The surface of ZnONP from positive to negative surface potential so as to obtain two ZnO nanoparticles of opposite surface potential was modulated using sodium citrate. For this, ZnONP synthesized at calcination temperature of 300 ^{o}C was chosen, since the temperature produced small size and spherical shaped ZnONP with insignificant surface defects. The synthesized and surface modulated ZnONPs were named as p-ZnONP and n-ZnONP for positive surface potential and negative surface potential ZnONPs respectively. The XRD data (Figure 3.2a) of p-ZnONP and n-ZnONP revealed that both the samples prepared are crystalline in nature with peaks at different 2θ, i.e. the Bragg's angle values 31, 34, 36, 47, 56, 62, 66, 67 and 68^{o} corresponding to different indices (100), (002), (101), (102), (110), (103), (200), (112) and (201), respectively. The indices are well indexed to the hexagonal wurtzite structure of bulk ZnO lattice parameters. Additionally, the analysis of XRD spectra of p-ZnONP and n-ZnONP using X′ pert high score software with search and match facility demonstrated that both types of the nanoparticles have hexagonal ZnO crystals (JCPDS reference code–80-0074 and 79-0208 for p-ZnONP and n-ZnONP, respectively). Interestingly, it is observed in the XRD spectra that the diffraction peaks of n-ZnONP are slightly shifted towards the lower Bragg angle compared to p-ZnONP (inset of Figure 3.2a). The shifting of peaks revealed the lattice expansion upon sodium citrate coating leading into increased interlayer spacing of n-ZnONP along the c-axis[196]. The average particle size for p-ZnONP and n-ZnONP is determined using Scherrer's equation and found to be 30 and 39 nm for p-ZnONP and n-ZnONP, respectively. The theoretical specific surface area (SA) of synthesized nanoparticles are also determined using the equation SA = 6/(D*ρ), as suggested by Hjiri, M. *et al*, where D and ρ represents the particle size and theoretical density (5.606 g/cm^{3}), respectively[196]. Using the equation, the theoretical specific surface area of p-ZnONP and n-ZnONP are found to be 35.67 and 27.44 m^{2}/g, inferring specific surface area decreases upon surface coating.

The compositions of p-ZnONP and n-ZnONP were, further, analyzed using ATR-FTIR spectroscope, shown in figure 3.2b. Strong absorption peaks at 1531 and 2341 cm^{-1}, for both types of nanoparticles were due to bending vibrations of N-H and the asymmetric stretching vibration of C=O bonds, respectively. The absorption peaks observed at 1680 cm^{-1} was due to vibration of C=O bond present in the residual acetate/carbonate or citrate

formed in the process. The absorption peaks below 800 cm^{-1} provided important information about internal metal-oxygen bond vibration[190]. The spectra of materials showed absorption peak near 542 and 566 cm^{-1} for n-ZnONP and p-ZnONP respectively, corresponding to Zn-O bond stretching vibration present in nanocrystal lattice (Figure 3.2b inset). The shift in peak from 566 to 542 cm^{-1} for Zn-O-Zn bond vibration on surface modulation interpreted that p-ZnONP required higher frequency vibration to vibrate Zn-O-Zn bond compared to the bond present in n-ZnONP; frequency of vibration is inversely proportional to square root of the mass of the vibrating molecule, *Hooke's Law*. Thus, the presence of citrate as coating on the surface of ZnONP was resulting into lower wavenumber vibration for Zn-O-Zn bond present in n-ZnONP compared to p-ZnONP. Additionally, the modification was further confirmed at bond level using ATR-FTIR spectroscopy, where peak intensities corresponding to C=O vibrations, i.e. 2341 and 1680 cm^{-1} were found to be enhanced for n-ZnONP compared to p-ZnONP.

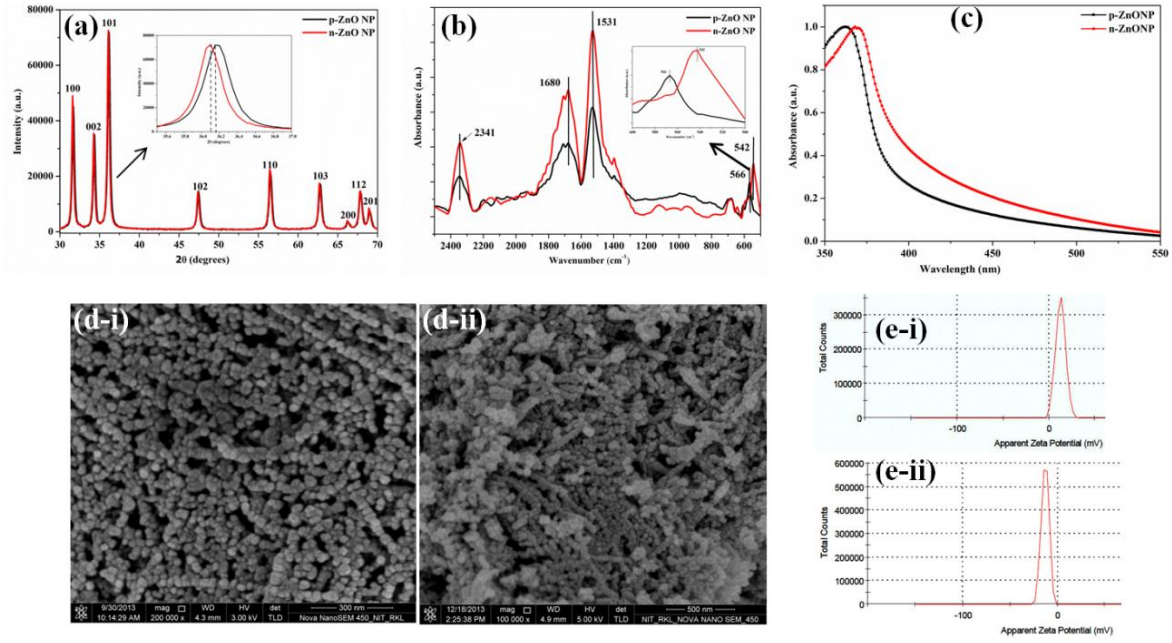

Figure 3.2. Characterization of p and n-ZnONPs. (a) XRD, (b) ATR-FTIR absorption spectra, (c) UV-Vis absorption spectra of p-ZnONP and n-ZnONP, (d) FE-SEM image of p-ZnONP (d-i) and n-ZnONP (d-ii), (e) Zeta potential analysis of p-ZnONP and n-ZnONP showing value of +12.9 mV(e-i) & -12.9 mV (e-ii).

Surface plasmon resonance (SPR) property is a characteristic property of nanoparticles, especially photocatalytic metal nanoparticles with short band gap energy, an energy gap between top vibrational level of valence band and bottom vibrational level of conduction band. Figure 3.2(c) showed the UV-Visible absorption spectra of p-ZnONP

and n-ZnONP with absorption peaks at 362 and 369 nm respectively, which are attributed to SPR property of ZnONPs[16, 197-199]. The absorption peak at 362 nm obtained for p-ZnONP was very close to the absorption peak of 364 nm obtained by Tankhiwale, R. *et al*[197] and 361 nm by Vigneshwaran, N. *et al*[198]. From the figure, it was evident that upon coating by sodium citrate the absorption peak for ZnONP shifted from 362 nm to 369 nm, i.e. red shift, confirming the surface modification of ZnONP. The shifting of absorption peak towards higher wavelength is due to decrease in band gap of nanoparticle, which is due to increase in particle size. The band gap energy (E_{bg}) of synthesized ZnONPs was determined using the equation, $E_{bg} = 1240/\lambda$ (eV) [16], where E_{bg} and λ represent for band gap energy in eV and wavelength in nanometer, respectively. The band gap energy of p-ZnONP and n-ZnONP were 3.4 and 3.3 eV respectively, which were very close to the theoretical values of ZnONP, as supported by different literatures[16, 99, 200].

Field Emission Scanning Electron Microscopy (FE-SEM) images of both positive and negative potential ZnONPs suggested that the particles are spherical in shape with diameter range in 25–35 nm (Figure 3.2d-i) and 35–45 nm (Figure 3.2d-ii), respectively. The significant increase in average size of negative potential ZnONP further confirmed the coating. Zeta potential measurement showed that the synthesized p-ZnONP has surface potential of +12.9 mV, while surface modification with citrate reversed the surface potential to −12.9 mV for n-ZnONP (Figure 3.2e-i&-ii).

3.1.2. Iron oxide nanoparticle and its surface modification

It has been reported that among different types of NPs, magnetic nanoparticles due to their biocompatibility, chemical stability, and magnetic behavior are widely used in biomedical sciences[25]. Magnetic nanoparticles are also being used for delivery of drugs to targeted tissues by application of external magnetic field, which in turn increases stability of the drugs against enzymatic or metabolic degradation[25-26, 201]. Due to outstanding magnetic, physico-chemical, thermal, and mechanical properties, magnetic nanoparticles can also be used in other fields, like analytical chemistry, pathogen detection, antigen diagnosis, tissue repair, hyperthermia etc[26, 202]. Most of transition metal nanoparticles like ions like iron, cobalt, nickel, and their compounds belong to magnetic nanoparticles[203]. Iron oxides coming under magnetic nanoparticles are magnetite (Fe_3O_4), maghemite (γ -Fe_2O_3), hematite (α -Fe_2O_3), and goethite (FeO(OH))[203]. Numerous methods have been formulated for synthesis of iron oxide nanoparticle (IONP), still synthesis of IONPs having small and uniform size distribution with good stability to avoid agglomeration is a matter of

intensive research in current era. Furthermore, evaluation of the role of functional groups on the nanoparticle interface is a key challenge for safe use of IONP. Hence, in this sub-ojective iron oxide nanoparticle (p-IONP) was synthesized by chemical precipitation method, and modulated the surface functional groups using biocompatible chitosan molecule (n-IONP).

The synthesized IONPs were studied using X-ray diffraction spectroscopy. Figure 3.3(a) showed the XRD patterns for both n-IONP and p-IONP. The major diffraction peak at 35° (311) in addition to minor peaks at 30° (220), 43° (400), 53° (422), 57° (511), and 62° (440) confirmed the spinel structure of iron oxide (magnetite-Fe_3O_4 and maghemite- γ -Fe_2O_3)[95], revealing that the synthesized IONP did not not contain any other forms of iron oxide such as hematite (α-Fe_2O_3), goethite (FeO(OH)), or any iron hydroxides in detectable range[95]. Shan Z. *et al.* have suggested that the lattice parameter (α) for magnetite and maghemite are 8.3960 Å and 8.3515 Å, respectively[204]. For the synthesized IONPS, lattice parameter for n-IONP was 8.3840 Å, which was very close to lattice parameter of magnetite, revealing that the synthesized n-IONP contains predominantly magnetite (Fe_3O_4) population. For further confirmation, the 2θ value of the (311) peak was considered. As reported in various literatures, the standard values of this peak (311) for magnetite and maghemite are at 35.423° and 35.631°, respectively[95, 204]. The diffraction angle for the synthesized nanoparticle is 35.47°, which is more close to magnetite index than maghemite index. It indicated presence of predominantly magnetite (Fe_3O_4) lattice with traces of maghemite lattice. From the observations, it is concluded that the synthesized n-IONP has major fraction of magnetite (Fe_3O_4) in the nanocrystal. The surface modification with chitosan molecule does not affect the crystal structure of IONP, since the major peaks at 2θ, 30° (220), 35° (311), 43° (400), 57° (511), and 62° (440), correspond to 8.3840 Å lattice, only. The 2θ value for the peak (311) is 35.46, which is basic characteristic feature of magnetic nanocrystals, as described above[95, 204]. Additionally, the analysis of n-IONP and p-IONP XRD patterns using X' pert high score software with search and match option revealed that the both types of nanoparticle have Fe_3O_4 crystals (JCPDS reference code–75-0033). The particle size of n-IONP and p-IONP was determined using Scherrer equation, and found to be 10.36 +/− 5.1 nm and 11.37 +/− 5.6 nm, respectively. The size obtained was an average of data obtained from peaks present for n-IONP and p-IONP diffractions, respectively. The XRD spectra obtained in the study are compatible with XRD spectra of different literatures[25, 205-207].

Figure 3.3(b) showed FTIR spectra of n-IONP and p-IONP suspended in deionised water. The data were collected in attenuated mode FTIR using diamond crystal. The presence of the metal oxide nano-crystals was confirmed from the peaks at 564 and 555 cm^{-1}, which were due to metal oxygen bond vibrations present in n-IONP and p-IONP nano-crystals, respectively[190]. It was very interesting to observe that there was a peak shift from 564 cm^{-1} to 555 cm^{-1} upon chitosan coating of n-IONP, demonstrating that p-IONP needed lower frequency to vibrate Fe-O bond than n-IONP. Following *Hook's Law*, the lower frequency of vibration indicated that Fe-O bonds present in p-IONP are less stable than the bond present in n-IONP[167], hence more prone to produce electron-hole pair. The absorption peak at 1664 cm^{-1} (for n-IONP and p-IONP), 1702 cm^{-1} (for chitosan), and 1524 cm^{-1} (for all) were due to C = O and N-H vibrations, respectively. In the chitosan spectra, the absorption peak at 1051 cm^{-1} was due to vibration of C-O-C bonds[208], which shifted to 1032 cm^{-1} for chitosan coated IONP (p-IONP). However, shifting of peak from 1051 cm^{-1} to 1032 cm^{-1} with lesser intensity peak at 1032 cm^{-1} was attributed to decreased population of the bond on washing of residual chitosan molecules from bulk. The increased intensities of N-H vibrations for p-IONP confirmed the surface coating of chitosan over negatively charged IONP, indicating strong interactions between the amino group on chitosan molecules and IONP. Thus, the data supported both XRD and UV-Visible data for successful coating of IONPs with chitosan molecule.

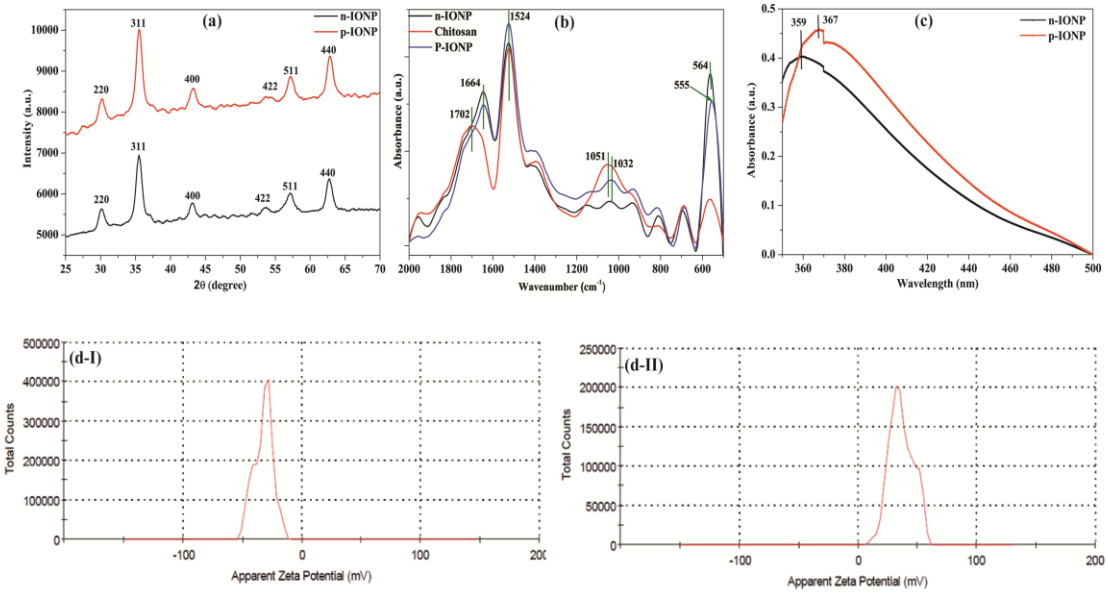

Figure 3.3. (a) XRD spectra (b) ATR-FTIR absorption spectra, and (c) UV-Visible absorption spectra of n-IONP, and p-IONP, (d) Zeta potential analysis of n-IONP (d–I), and p-IONP (d–II).

UV-Visible spectra of both n-IONP and p-IONP were shown in figure 3.3(c). Due to surface plasmon resonance property, n-IONP showed characteristic absorption peak at 359 nm, whereas p-IONP showed peak at 367 nm which is in accordance with the reported results by ur Rahman O. *et al.*[209]. The red shift in surface plasmon resonance by 8 nm for p-IONP confirmed chitosan coating on n-IONP. In addition, the shift indicates decrease in energy band gap of nanoparticle, i.e. photocatalytic propensity enhanced, strengthening the conclusion of relatively weak Fe-O bond in chitosan coated IONP as drawn from FTIR spectra. The band gap energy for both IONPs was determined using the equation $E_{bg} = 1240/\lambda$ eV[16], where E_{bg} stands for band gap energy in eV, and λ is the wavelength in nanometre. Using this equation, the band gap energy for both n-IONP and p-IONP were found to be 3.4 and 3.3 eV, respectively.

The zeta potential measurements for n-IONP (Figure 3.3d-I) and p-IONP (Figure 3.3d-II) suspension in deionised water showed surface potential of −32.2 mV and +36.3 mV, respectively. p-IONP possesses relatively higher zeta potential magnitude than n-IONP, inferring that chitosan coated IONP is relatively more stable. In addition, reversal of surface potential further supported the XRD analysis and surface plasmon resonance property for chitosan coated IONP. Chitosan is already known for very high adhesive tendency for negatively charged surfaces[210].

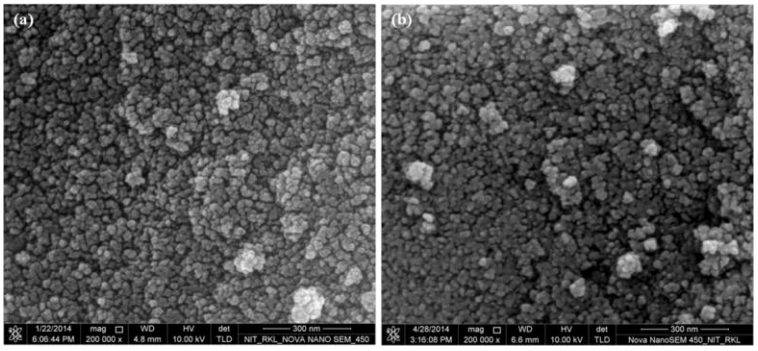

Figure 3.4. FE-SEM image of n-IONP (a) and p-IONP (b).

The images obtained using FE-SEM, figure 3.4, indicated that both types of IONPs are nearly spherical in shape with size ranging from 8–20 nm, which is very close to the estimated particle size by XRD analysis, i.e. ~11 +/− 5 nm. Both, FE-SEM analysis and XRD analysis, suggested that size of the nanoparticles does not change significantly upon chitosan coating. Yu S. *et al.* have reported a similar observation, 8 nm IONP retained its size on coating with poly-(methacrylic acid)[211]. Additionally, slight difference in particle

size for n-IONP and p-IONP may be dedicated to instrumental artefact or sampling artefact or both.

3.1.3. Synthesis of silver nanoparticle using bacteria from coal mine- A green synthesis approach

Among different metal and metal oxide nanoparticles, silver nanoparticles (AgNPs) have drawn the attention of various research groups for various possible biological applications, such as nanomedicine, drug delivery, nanodevice fabrication, biosensing, catalysis, and imaging. Hence, different research groups are trying to synthesize AgNPs by various processes. However, green synthesis approach for AgNP synthesis is considered as non-toxic, eco-friendly and cost effective approach than other physical and chemical approaches. A number of biological resources available in nature including plants, plant products, algae, bacteria, and fungi can be used for synthesis of nanoparticles. Among the microorganisms, bacteria have received the most attention in the area of biosynthesis of nanoparticles. Here, coal mine has been chosen as a place to isolate metal resistance bacteria. Due to local high temperature and low pH, coal mine soil is treated as physico-chemically stressful habitat for soil microorganisms[212], still thermophilic and pH resistant bacteria are found in the coal mine. Additionally, coal mine soil also harbours heavy metal resistant bacteria[213]. Thus, coal mine was found as a suitable place to isolate bacteria, which can withstand high concentration of silver metal ions and adverse physico-chemical conditions like change in pH and temperature during the synthesis of nano/microparticles at industrial scale. Bacterial strains isolated from coal mine, evaluation of their metal tolerance capacity against $AgNO_3$, were used for successful reduction of silver ion into silver nano- and micro-particles.

Minimum inhibitory concentration (MIC) was determined to check resistance of extracted bacteria against silver metal ions in comparison with normal chemical conditions (Figure 3.5). Figure 3.5 showed the viability of three bacteria treated with different concentrations of $AgNO_3$. From the result, it is confirmed that 0.15 mM $AgNO_3$ is the MIC for first two bacteria, whereas bacteria 3 has MIC at less than 0.019 mM. The bacterial growth was only ~ 50 % of the growth happening in absence of the metal ions for first two bacteria, whereas approximately 10 % cells were found viable in presence of 0.15 mM $AgNO_3$ for the third bacteria. Hence, MIC concentration, 0.15 mM $AgNO_3$, has been chosen for synthesis of silver nanoparticles using the two metal ion resistant bacteria.

Bacteria 1 showed relatively higher viability at 0.15 mM $AgNO_3$ than bacteria 2, hence we expected relatively higher amount of reduced silver element in bacteria 1 extract. Interestingly, unlike the bacteria 3 (Gram negative), the other two $AgNO_3$ resistant bacteria were found to be Gram-positive bacteria (Figure 3.6). The sensitivity of third bacterium towards $AgNO_3$ can be explained taking the surface potential of both bacteria and Ag(I) ion into consideration. Having higher surface potential than Gram-positive bacteria, Gram-negative bacterium interacts relatively strongly with positively charged Ag(I) ion, hence the bacterial death occurs to a larger extent in comparison to Gram-positive bacteria.

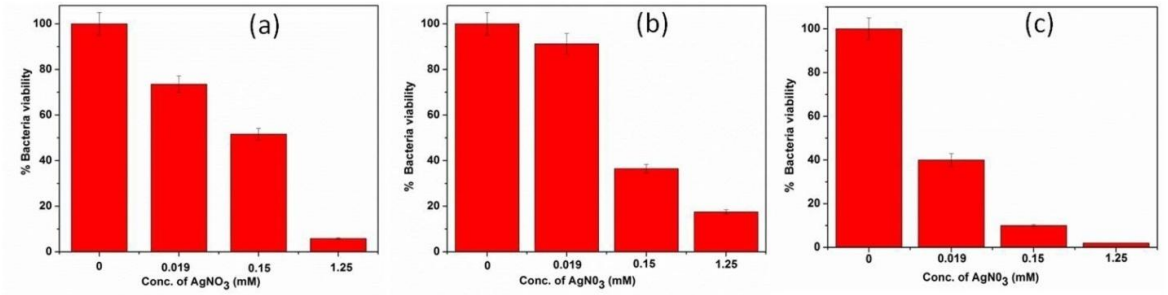

Figure 3.5: MIC of $AgNO_3$ against (a) bacteria 1, (b) bacteria 2 and (c) bacteria 3.

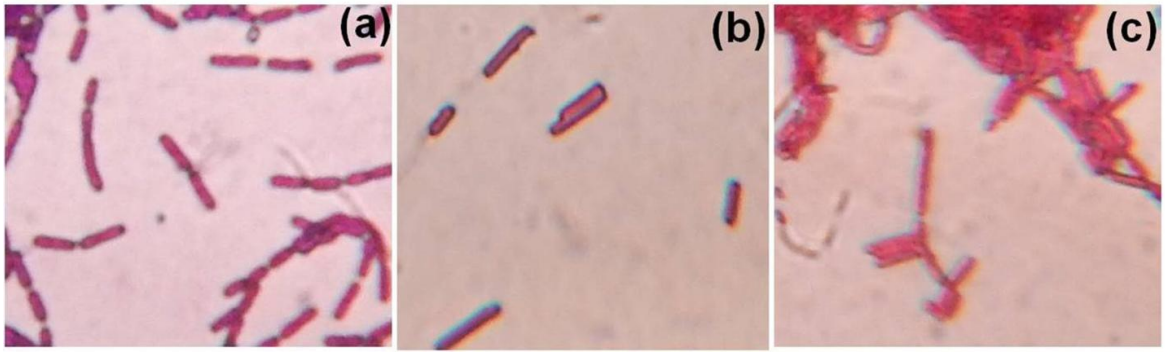

Figure 3.6. Characterization of bacterial strains by Gram staining and found to be (a) bacteria 1-Gram-positive, (b) bacteria 2-Gram-positive and (c) bacteria 3-Gram negative bacteria.

Although, various studies have already been done to synthesize silver nanoparticles using different bacteria, but in most of the studies Ag(I) ions[214-215] are reduced to elemental silver (Ag(0)) nanocrystals using bacterial biomass, i.e. bacterial cytoplasm. However, the objective intends to synthesize the nanoparticles from live bacteria, even if the yield is relatively low, the yield would be enhanced by adopting the approach in bio-fermenter. Hence, from $AgNO_3$ screened bacterial populations, first two Gram-positive bacteria were chosen for green synthesis of silver nanoparticle. Further, 0.15 mM $AgNO_3$ (MIC conc.) was added at mid log phase of the growth curve, i.e. the

phase where bacteria are more potent to adopt the change in physico-chemical conditions. Hence, the bacteria synthesized elemental metal nanoparticles upon internalizing and reducing the metal ions in duration of their further growth. Thus, the nanoparticles are formed during the growth of bacteria without significant change in bacterial viability. The process further, named as "continuous production of silver nanoparticles". Ramanathan, R. *et al*[216] have also synthesized pure copper nanoparticles using the bacteria *Morganella morganii*, which is a silver resistant strain. However in the work, metal ion was added for reduction into elemental copper nanocrystals after the growth of the bacteria, i.e. the bacterial biomass is used to reduce the Cu(II) ion into elemental Cu (0). Unlike Ramanathan's work, the metal ion (MIC concentration) was added at the mid log phase of the bacterial growth, and observed the formation of micro- / nano-particles by live bacteria. Hence, the protocol can be directly adopted for continuous production of silver nanoparticle using the extracted/metal resistant bacteria.

The figure 3.7(a) showed the UV-Visible spectra of silver nanoparticles synthesized using two bacteria. For both the samples, absorption peak at 425 nm confirmed the presence of silver nanoparticle, and the result is in accordance with the published results[217-218]. The strong interaction between light of particular wavelength (photons) and metal nanoparticles results enhanced collective oscillation of valence/conduction electrons of the silver element present at the surface of particle, which in turn results in unusually strong absorption and scattering properties of the metal nanoparticle. The SPR property provides a greater deal of information about the physical state of silver nanoparticle[219]. The broader peaks at 425 nm confirms polydispersity of the nanoparticle that means presence of some microparticles in the fabricated sample. Additionally, the intensity at 425 nm indicated the quantity of the particles; smaller the intensity, lower is the concentration.

The figure 3.7 (b) showed the bond level characterization of AgNP, fabricated using the isolated bacteria. The peaks below 800 $c.m.^{-1}$ in the IR spectra indicated the presence of metal-metal or metal-oxygen bond in samples[167]. Hence, the absorption peaks at 575 and 598 $c.m.^{-1}$ represented the Ag-O/Ag-Ag bond vibrations, confirming the presence of AgNPs in the synthesized samples. The strong absorption peaks at 1657and 1646 $c.m.^{-1}$ for AgNP1 and AgNP2 respectively, are due to the C=O vibrations (amide I). On the other hand, absorbance peaks at 1530 and 1538 $c.m.^{-1}$ for AgNP1 and AgNP2, respectively, are due to the N-H vibrations (amide II). The amide I and amide II bond

vibrations confirmed the presence of proteins in AgNP samples. The proteins are assumed to be responsible either for reduction of $AgNO_3$ to silver nanoparticles or for capping of AgNP or both. In addition to that, the protein(s) from bacteria 1 responsible for either of the factors is predominantly a-helix in secondary structure contents, since 1657 $c.m.^{-1}$ is characteristic IR absorbance peak for a-helix. However, the proteins from bacteria 2 are having predominantly β-sheet in its secondary structure contents.

The EDX spectra (Figure 3.7c) showed the presence of Ag signals at bacterial surface, confirming the synthesis and secretion of silver nanoparticles. Additionally, the strong Si signal in the spectra was due to the glass slide, which was used as a platform for bacterial-nanoparticle sample preparation for FE-SEM analysis. The Au signal is due to the gold coating done prior to imaging. The presence of other signals in the spectra was due to the chemicals used either for preparing the sample for analysis or were integral part of the bacteria. However, the less intense signal of Ag supported our previous findings that synthesized sample contains relatively low amount of silver nanoparticles at the surface of the bacteria.

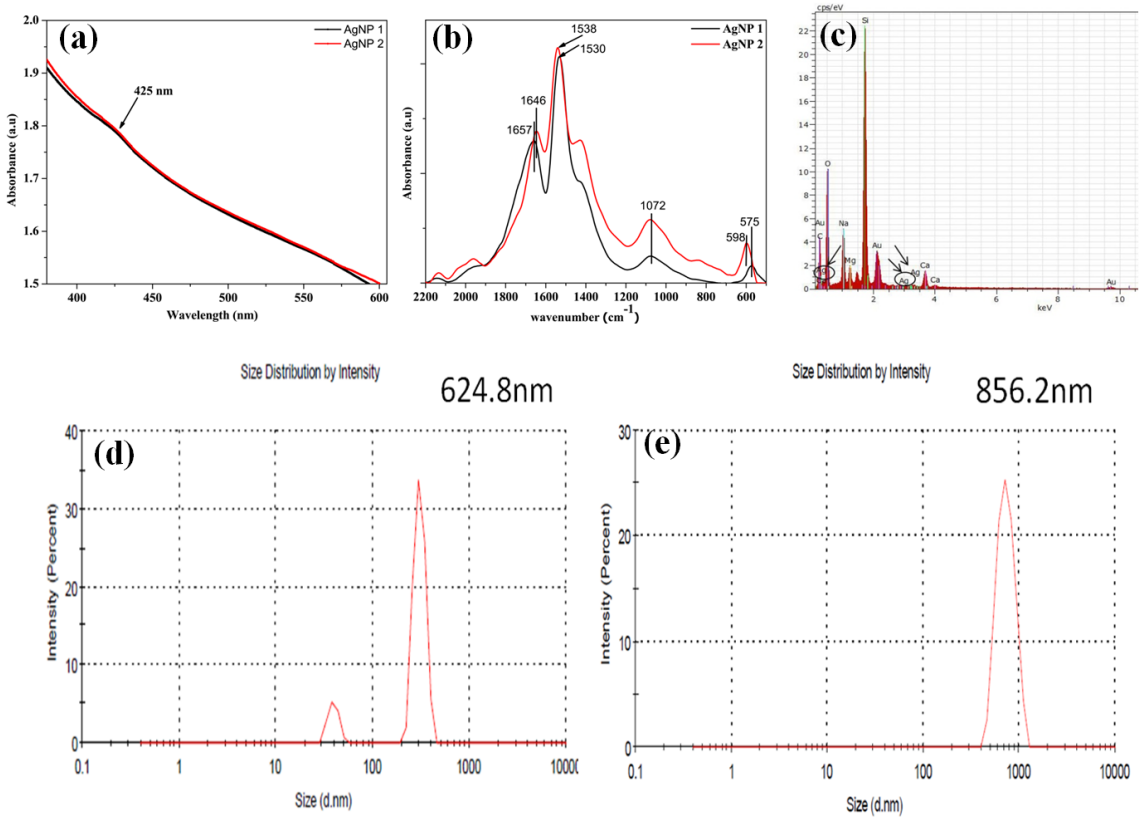

Figure 3.7. (a) UV–Visible absorption spectra of AgNPs synthesized, (b) FTIR spectra showing the bond level vibrations present, (c) EDX spectra showing the presence of elemental silver on bacterial surface, and DLS analysis of silver nanoparticle samples for (d) AgNP1 and (e) AgNP2.

To determine size of particles present in the sample, zeta sizer was used. Figure 3.7(d) and 3.7(e) showed the DLS analysis of silver nanoparticles obtained using two different bacteria. As shown in the figure, average particle size was found to be 624 and 856 nm for AgNP1 and AgNP2, respectively. Hence, the results indicated that some microparticles are also present in addition to the nanoparticles in our synthesized nanoparticle suspension. The observation, further, supported the SPR spectra collected using UV-Visible spectroscope, i.e. broadening of peaks at 425 nm for both the samples indicating the presence of larger size nanoparticles (here, it is mentioned as sub-microparticles).

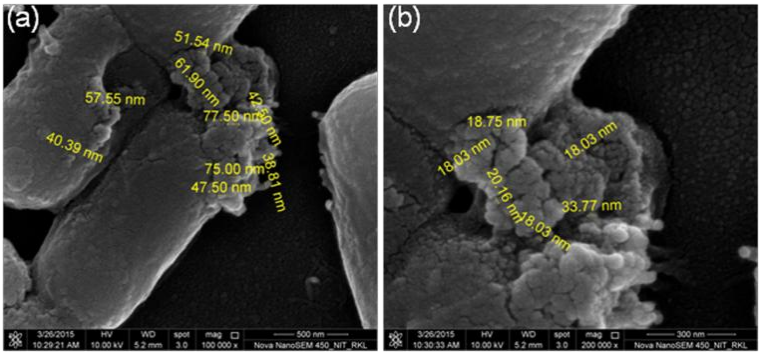

Figure 3.8. FE-SEM micrographs of (a) bacteria 1 with AgNP1, (b) bacteria 2 with AgNP2 grown in presence of 0.15 mM $AgNO_3$.

The figure 3.8 showed the FE-SEM images of two bacteria grown in presence of 0.15 mM $AgNO_3$. Both the bacteria were found to be rod shaped with presence of some particles on the surface of bacteria. Most of the particles are spherical in shape with diameter in nano-meter range, i.e. 20-40 nm. Hence, the images obtained using FE-SEM indicated the synthesis of silver nanoparticle using the extracted bacteria.

The comparison of FE-SEM results with DLS data provides the information about variation of particle size. Generally, FE-SEM gives particular field image of the nanoparticles, however DLS measures the hydrodynamic size of all the particles in aqueous solution, and gives the average of the particles present in solution, i.e. average size of the predominant particle population. Additionally, the variation can be explained taking the physico-chemical parameters of nanoparticles. Nanoparticles being very small in size possess very high free energy content. Thus, when dispersed in biological solution, the nanoparticle interacts with different biomolecules to release its free energy content. In presence of salts or absence of coulombs repulsive interaction, the particles self-assemble to form larger structure, losing the free energy content. The interaction between

biomolecules and nanoparticles spontaneously form nano-bio interfaces. For example, in this objective, the attachment of nanoparticles on the bacteria is an example of nano-bio complex. On the other hand, assembly of nanoparticles with each other creating larger particles, here termed as sub-microparticles, as detected by DLS measurements. Additionally, the zeta potential value of two nanoparticles samples (AgNP1 and AgNP2) was found to be -16.9 and -13.0 mV respectively. These values of zeta potential demonstrate the incipient instability of nanoparticle solutions. Hence, the synthesized nanoparticles have the tendency to aggregate forming sub-microparticles.

The term 'green synthesis' signifies the synthesis of nanoparticles using biological entities such as: microorganisms, plants, and plant products. When micro-organisms mediated synthesis is discussed, it is generally bacteria, fungi, virus etc. However, we can not use all microorganisms for synthesis of metal nanoparticles, and the study is a clear example of it. Initially, the work chose three bacteria for the biofabrication. One out of three bacteria, unlike other two, was sensitive to silver ion. Hence, it could not be used to produce silver nanoparticles. The MIC results followed by nanoparticle characterization results for metal resistant bacteria strongly supported that the bacteria with silver resistance have the potential to reduce the silver ion into silver nanoparticles. It is well reported that the enzymes responsible for reduction of Ag(+) into Ag(0) belong to NADPH dependent enzyme, nitrate reductase[220]. Additionally, many studies have also shown that some of the bacterial proteins are also responsible for biosynthesis of silver nanoparticles[214-215]. However, our study (the findings from ATR-FTIR results) supports the later findings, i.e. bacterial proteins are responsible for biosynthesis of silver nanoparticles at either or both the stages. One stage involves the reduction of metal ion into elemental metal, and another stage involves capping of the elemental metal assembly at nanocrystal size[214-216]. Additionally, the microparticles formation totally depends upon the physico-chemical property of nanoparticles as discussed in DLS analysis section.

Here, fabrication of silver nanoparticle is an intracellular process and the bacterial proteins play major roles in either reduction of silver ions to elemental silver nanoparticle or capping of AgNP or both. Upon completion of the fabrication, the nanoparticle is secreted by exocytosis. Being small in size these nanoparticles possess relatively high free energy content, hence unstable in biological milieu. As a result, the secreted nanoparticles are attached to the bacterial surface (as shown in FE-SEM image) or attached to each other forming larger particles (sub-microparticles as confirmed by DLS measurement).

However, the size could be controlled at nano-meter size by optimizing the pH, temperature, and stages of metal ion feed to the culture[8].

3.2. Effect of interfacial potential on antimicrobial propensity of ZnONPs

To understand the role of interfacial potential on antimicrobial propensity, the antimicrobial propensity of ZnONPs having positive and negative surface potentials against three randomly chosen Gram-positive and Gram-negative bacteria was studied. In order to bring significant changes in microbial viability, the interface needs to develop such a potential that results in either physical rupture of the membrane (membrane depolarization) or enhanced ROS production (at the interface or inside the bacteria or both). Although, the antibacterial activity of ZnONP against different bacterial strains is well established [221-223]. However, the role of interaction profile at the interface in determining antimicrobial propensity of ZnONP had not been reported before.

3.2.1. ZnONP-bacteria interfacial potential

To study the effect of interfacial potential on antimicrobial propensity of ZnONPs, different bacteria with varying surface potential were used for the objective. Figure 3.9 showed the zeta potential values of both Gram-positive and Gram-negative bacteria used in the study. Negative zeta potential values were obtained for all tested organisms. However, Gram negative bacteria exhibited higher negative potential than Gram-positive bacteria, due to the presence of additional layer of negatively charged lipopolysaccharide (LPS) compared to Gram-positive bacteria.

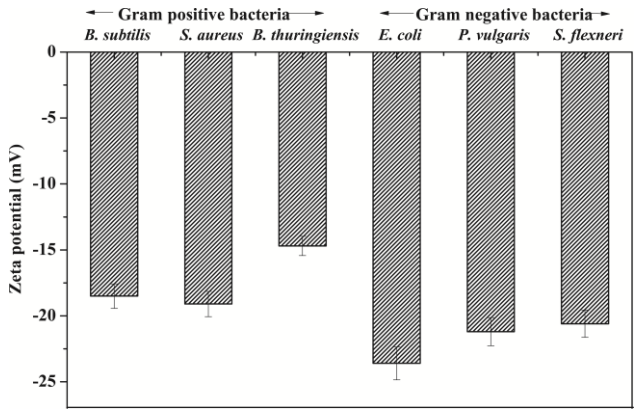

Figure 3.9: Zeta potentials of Gram-positive and Gram-negative bacteria

The growth kinetic studies were carried out in absence and presence of p-ZnONP and n-ZnONP in order to observe the minimum inhibitory concentration (MIC), as shown in figure 3.10. From the figure, it is evident that lower concentrations of p-ZnONP (i.e 16, 25 and 50 μg/mL) show insignificant effect on growth kinetics of the Gram positive bacteria (Figure 3.10a–c). However, 100 μg/mL and higher concentrations of p-ZnONP in culture exerted significant growth inhibition for *Bacillus subtilis* and *Staphylococcus aureus*, while *Bacillus thuringiensis* showed relatively higher resistance against positively charged p-ZnONP. The bacteria only showed significant growth inhibition above 500 μg/mL of p-ZnONP. Although, 250 μg/mL of p-ZnONP delayed the growth of *B. thuringiensis*. However, upon adoption to the stress condition, the bacteria resumed the growth after a short dormant phase. Hence, the complete inhibition of *B.thuringiensis* growth kinetic happened above 500 μg/mL of p-ZnONP. Additionally, the figure 3.10d–f represented the effect of varying concentrations of p-ZnONP on the growth kinetics of Gram-negative bacteria. The growth curves for *Escherichia coli* and *Proteus vulgaris* only showed the inhibition above 50 μg/mL of p- ZnONP. However, in case of *Shigella flexneri*, inhibition of bacterial growth starts from 25 μg/mL of p-ZnONP.

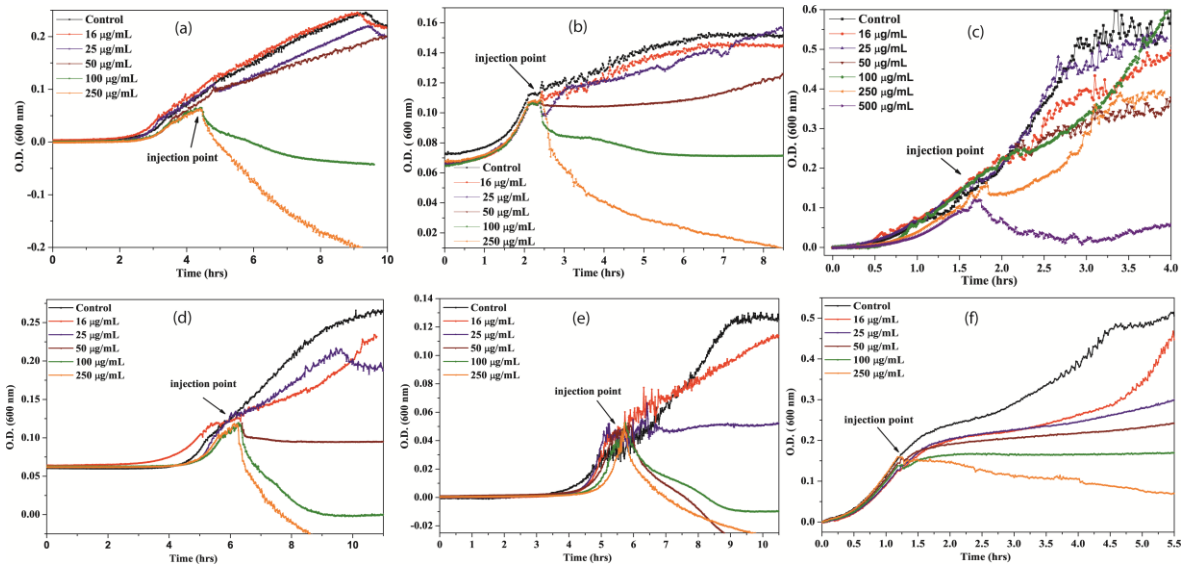

Figure 3.10. Growth kinetics of bacteria (a) *B. subtilis*, (b) *S. aureus*, (c) *B. thuringiensis*, (d) *E. coli*, (e) *S. flexneri*, and (f). *P. vulgaris* in presence of different concentrations of p-ZnONPs. Different concentrations of p-ZnONP taken were 16, 25, 50, 100, 250, and 500 (only for *B. thuringiensis*) μg/mL, and injected at the mid log phase of growth kinetics, as shown by arrow.

Figure 3.11a showed the growth kinetics of *B. subtilis* in presence of n-ZnONP. From the figure, it is evident that the bacteria showed normal growth in presence of n-

ZnONP concentrations below 200 μg/mL, but the inhibition of bacterial growth occurred at 250 μg/mL. The value is more than two folds higher than the concentration of p-ZnONP (100 μg/mL) needed to completely suppress the growth of bacteria. Figure 3.11b–d showed the growth kinetics of Gram-negative bacteria in presence of n-ZnONP. Like Gram positive bacteria, the growth of *E. coli* and *P. vulgaris* are also unaffected in the studied range of n-ZnONP concentrations. However, 250 μg/mL of n-ZnONP completely inhibited *S. flexneri* growth. Nevertheless, the inhibition concentration is much higher than those observed for p-ZnONP against the bacterium.

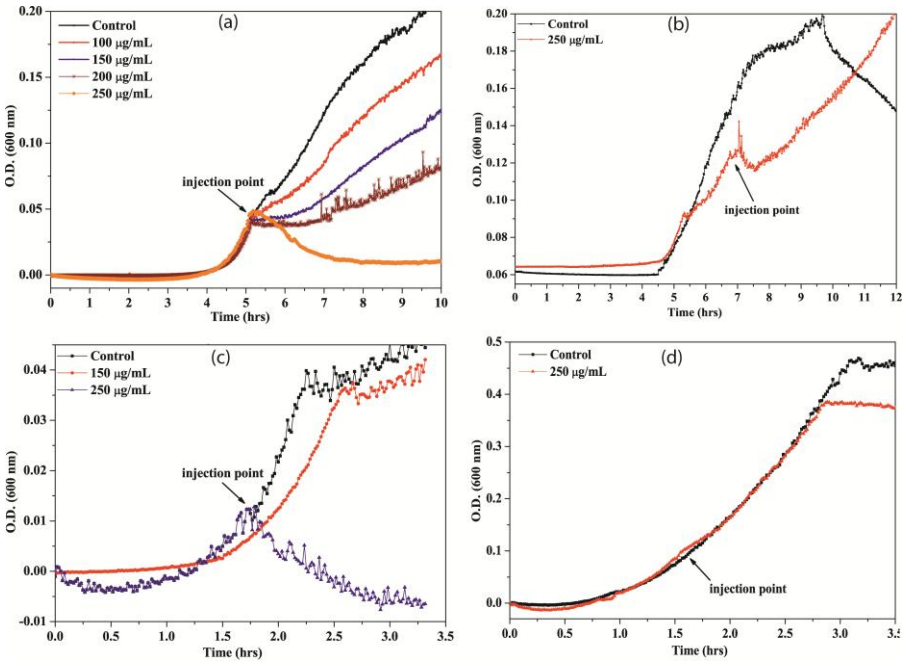

Figure 3.11. Growth kinetics of bacteria in the presence of different concentrations of n-ZnONP. In each case, black line shows the growth kinetics of untreated bacteria. Both Gram positive (a) *B. subtilis* and Gram negative (b) *E. coli*, (c) *S. flexneri*, (d) *P. vulgaris* bacteria were treated up to 250 μg/mL of n-ZnONP, injected at the mid log phase of growth kinetics, as shown by arrow.

Moreover, LIVE/DEAD BacLight Bacterial Viability fluorescence Kit was used to distinguish the non-viable cells from viable cells, which resulted from disintegration of the membrane upon the nanoparticle treatment. According to the principle and as shown in the figure 3.12,viable bacterial cells having intact cell membrane are stained green by membrane permeable DNA binding Syto9 fluorescent dye, whereas nanoparticle treated bacterial cells with deformed cell membrane are stained red by relatively stronger membrane impermeable DNA binding propidium Iodide fluorescent dye[224]. As shown in figure 3.12a-i & 3.12bi, untreated *B. subtilis* and *E. coli* cells exhibited green fluorescence indicating presence of 100% viable bacterial cells, whereas the p-ZnONP treated bacterial

samples showed a mixture of red and green fluorescence confirming a mixture of viable and non-viable cells (Figure 3.12a-ii & 3.12b-ii). In presence of 250 μg/mL of p-ZnONP, the fraction of bacterial cells exhibiting red fluorescence is upto 90%, indicating loss of the membrane integrity and cell viability (Figure 3.12a-iii & 3.12b-iii).

The cell viability of both Gram-positive and Gram-negative bacteria in presence of different concentrations of p-ZnONP was further supported by the colony forming unit (CFU) study, as shown in figure 3.13. The CFU results were in accordance with growth kinetic study of both Gram-positive and Gram-negative bacteria, as well as the BacLight fluorescence microscopic study. The MIC of p-ZnONP for both types of bacteria was evaluated from CFU measurement, shown in table 3.1. The reduction in number of viable cells with increasing concentrations of ZnONP, further, confirmed the antibacterial activity of ZnONP against the selected bacteria.

Table 3.1: Minimum inhibitory concentration (MIC) of p-ZnONP against different Gram-positive and Gram-negative bacteria.

Bacteria name	Gram-positive/MIC	Gram-negative/MIC
Bacillus subtilis	105. 17 ± 15.81	
Staphylococcus aureus	118. 66 ± 21.66	
Bacillus thuringiensis	120.27 ± 20.26	
Escherichia coli		47.25 ± 9.29
Shigella flexneri		25.58 ± 5. 24
Proteus vulgaris		83.97 ± 6.7

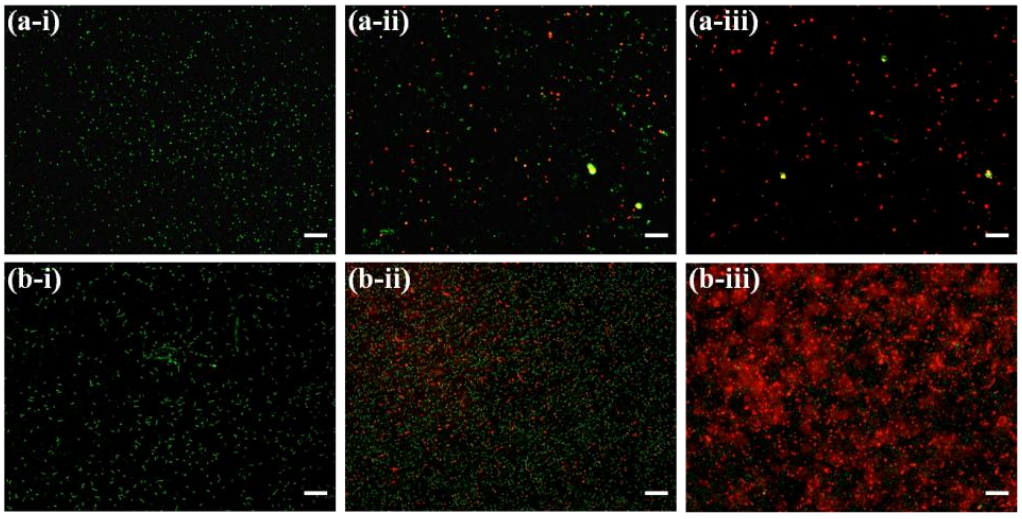

Figure 3.12. Fluorescence microscopic images of the green and red fluorescence *B. subtilis* and *E. coli* in absence and presence of p-ZnONP; *B. subtilis* (a-i), *B. subtilis* in presence of 100 µg/mL p-ZnONP (a-ii), and 250 µg/mL p-ZnONP (a-iii), *E. coli* (b-i), *E. coli* in presence of 50 µg/mL p-ZnONP (b-ii), and 250 µg/mL p-ZnONP (b-iii). The scale bars represent for 20 µm.

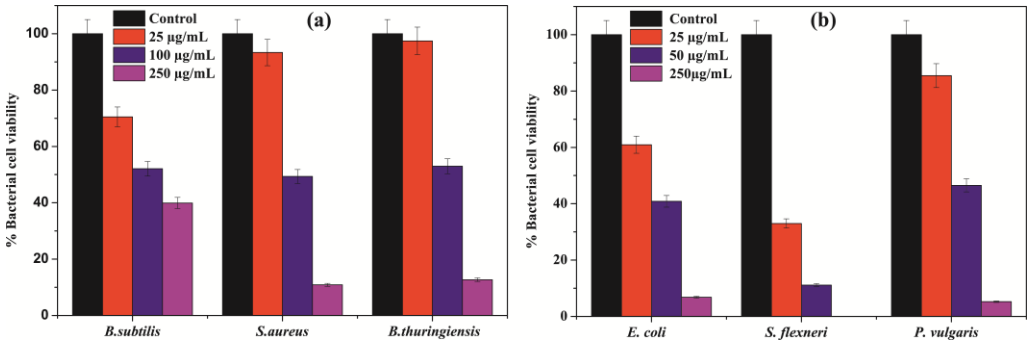

Figure 3.13. Colony forming units (CFU) were quantified for both Gram positive and Gram negative bacteria, and expressed as percentage of viable cells.

3.2.2. Surface potential neutralization of *B. subtilis* and *E. coli* by ZnONPs

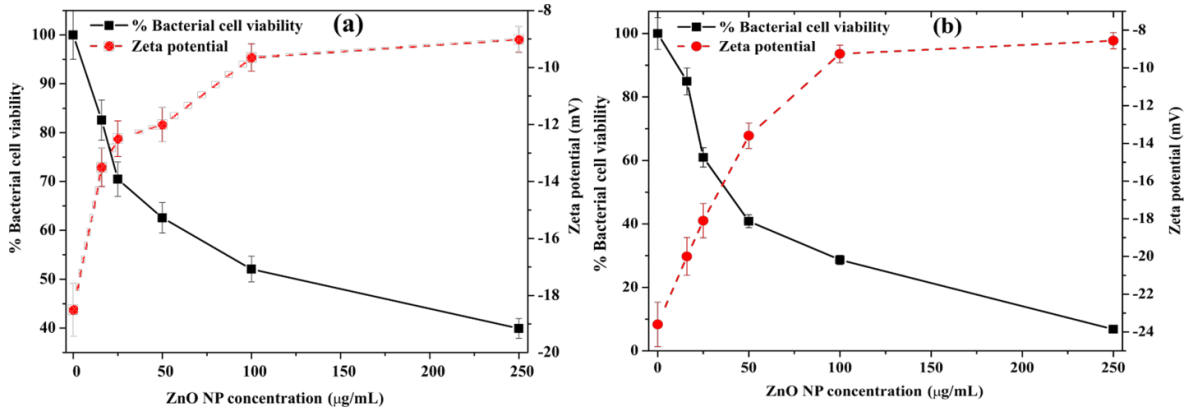

Figure 3.14. Percentage cell viability and cell zeta potential of *B. subtilis* (a) and *E. coli* (b) cells when treated with increasing concentrations of p-ZnONP like 16, 25, 50, 100, and 250 µg/mL. Solid black lines represent the relative percentage of viable bacterial cells, whereas dashed red lines correspond to zeta potential values at different concentrations of p-ZnONP. Triplicate experiments were done for each reaction, and error bar represents the standard error of mean.

Zeta potential measurements were carried out to examine the effects of ZnONPs on the membrane surface potential. As shown in figure 3.14, *B. subtilis* and *E. coli* cells display zeta potential of -18.5 mV and -23.6 mV, respectively. However, the potential moved to neutral upon addition of increasing concentrations of p-ZnONP. On the other hand, addition of increasing concentrations of n-ZnONP showed insignificant change in interfacial potential for both the bacteria. The observation indicated insignificant potential

neutralization upon n-ZnONP addition. Although, the interfacial potentials at highest studied concentrations of p-ZnONP for both the bacteria are same, but change in magnitude of interfacial potentials are capable of destabilizing the respective bacterial membrane via enhanced ROS production and/or surface tension. Both the factors are explored in next section using the fluorescent dye, 2', 7'-Dichlorodihydrofluorescein diacetate (DCFH-DA) and using the SEM/FE-SEM for high resolution images for any possible membrane deformities.

3.2.3. Enhanced ROS production in presence of ZnONP-bacteria interface

The surface potential neutralization of bacteria triggers the production of ROS, which is considered responsible for lipid, protein and DNA damage, resulting into non-viable bacterial population[225-226]. Change in ROS production upon addition of ZnONP has been evaluated using the fluorescence dye, DCFH-DA. DCFH-DA is known as peroxynitrite indicator, which detects both hydrogen peroxide and nitric oxide, and considered as ROS indicator[170]. The dye upon oxidation has excitation and emission maxima at 503 and 523 nm, respectively. Thus, in order to study the ROS production, the culture was inoculated with DCFH-DA dye which gets oxidized with production of ROS, and gave the emission at 523 nm on excitation with 503 nm, as shown in figure 3.15.

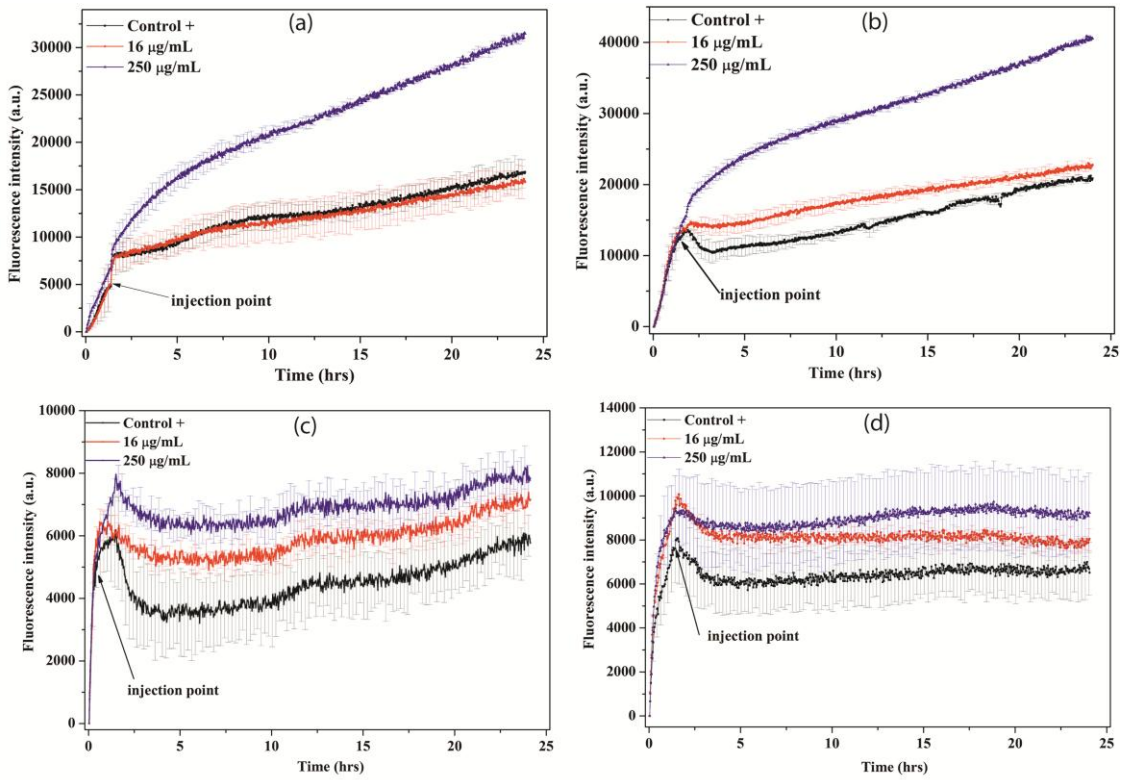

Figure 3.15. ZnONPs induced ROS detection in *B. subtilis* cells (a and c) and *E. coli* cells (b and d) were treated with 16 μg/mL (red curve) and 250 μg/mL (blue curve) of positive potential (panel a and b) and negatively potential (panel c and d) ZnONPs, and ROS were detected by measuring fluorescence emission intensity at 523 nm. In each case, except control, NPs were added in the log phase of bacterial growth. The fluorescence emission intensities are compared with positive control (without injection of NPs, black curve) in each case. Each curve represents the average of three independent measurements with corresponding standard error of mean.

The figure indicates that ROS is produced also in absence of ZnONPs treatment, i.e. in control culture, since the dye is showing increasing quantum yield with bacterial growth (black line, control +). Nevertheless, the produced ROS in non-stress condition is counteracted by ROS scavenging enzymes present in bacteria. However, in presence of 250 μg/mL of nanoparticle, the ROS production is relatively very high, increased by 100–200%, exceeding the capacity of ROS scavengers and resulting in reduced populations of viable bacterial cells (Figure 3.15). On comparing figure 3.15a & 3.15c with figure 3.15b & 3.15d respectively, it is evident that production of ROS is relatively higher in presence of p-ZnONP than n-ZnONP for the species, *B. subtilis* and *E. coli*. Additionally, *E. coli* culture showed higher ROS production on p-ZnONP treatment in comparison to *B. subtilis* culture, which can be rationalized with the difference in magnitude of change in interfacial potential for both the bacterium (Figure 3.14a & 3.14b). Thus, the data, besides supporting observations from the kinetic studies, CFU, BacLight fluorescence measurements, and potential neutralization studies, indicated that the production of ROS on interaction of ZnONP with bacterial membrane mainly result in non-viability of bacterial populations.

3.2.4. Surface morphology of bacteria upon ZnONP treatment

To observe the membrane deformities upon the ZnONPs treatment, the phase-contrast, SEM and FE-SEM were used. The images, obtained using the phase contrast microscopy, showed the clumping or aggregation of cells (Appendix, Figure A5 and A6). For further details, the ZnONPs treated and untreated bacterial cells were scanned using SEM. The images indicated more clumping and membrane rupture in treated cells than the untreated cells (Appendix, Figure A7 and A8). Additionally, images obtained using FE-SEM helped in detail investigation of topological changes in bacterial membrane (Figure 3.16). Upon interaction with p-ZnONP, the bacterial membrane surface potential is neutralized, resulting into increase in surface tension. Above certain p-ZnONP concentration, the interactions result in surface tension change, which possibly leads into the membrane

depolarization. As a result, bacterial membrane showed abnormal textures like membrane rupture, membrane blebs, in images obtained using FE-SEM (Figure 3.16b). The ruptured cells no longer remain discrete, often found in aggregates or clumps (Figure 3.16b).

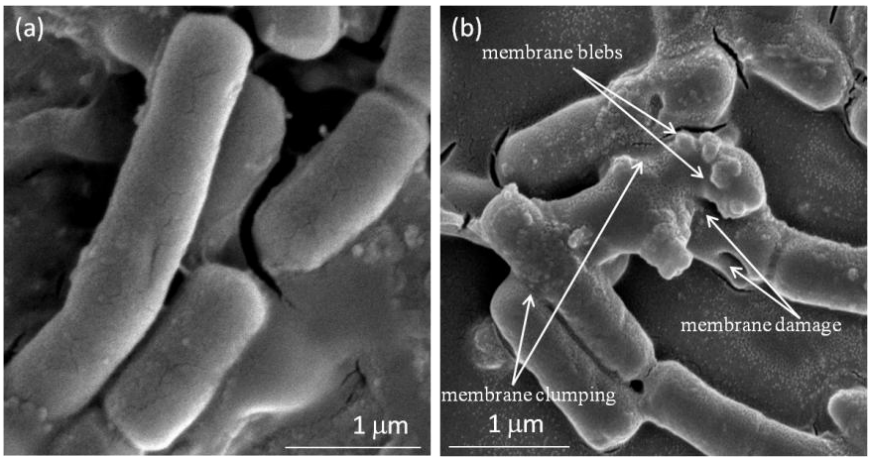

Figure 3.16. Visualization of ZnONP treated *E. coli* cell by FE-SEM, (a) control (without the treatment), (b) showing membrane blebs, membrane damage, and membrane clumping in ZnONP treated cells.

3.2.5. Discussion

Although various biological studies have been done to demonstrate the antimicrobial activity of different nanoparticles against different Gram-positive and Gram-negative bacteria. The mechanism underlying the antimicrobial activity is a matter of intensive research for safe use of nanoparticles as modern antibiotics. As reported by different literatures, various proposed mechanisms of antimicrobial activity of nanoparticles include the generation of ROS (like hydroxyl radicals, superoxide anions, hydrogen peroxide), release of Zn^{2+} ions, cell wall damage, penetration of the cell envelop etc.[223, 227-228]. The objective aimed to explore the mechanism in a new dimension by elucidating the biophysical events happening at the interface of nanoparticle and bacteria, leading into various changes resulting into bacterial non-viability. Here, ZnONP is taken due to its strong antimicrobial activity as reported by different literatures and wide applications in biological sciences[223]. The data altogether from the objective indicated that a sequence of events happen at the interface, like (i) resulting interfacial potential lead to attachment of nanoparticle on bacterial membrane, (ii) simultaneous neutralization of bacterial surface potential resulting into electron-hole pair generation in proximity, which (iii) enhances the production of ROS resulting into cell non-viability.

Due to additional layer of negatively charged lipopolysaccharides, Gram-negative bacteria are more negatively charged than Gram-positive bacteria[229], which were also confirmed from the zeta potential measurements for the bacteria (Figure 3.9). To this end, two types of ZnONPs having opposite potentials (+12.9 mV and -12.9 mV) were synthesized, and bacterial growth kinetic studies have been performed in presence of the NPs. The MIC of p-ZnONP for both Gram-positive and Gram-negative bacteria varied in range of 50–100 μg/mL, which was further supported by CFU measurement studies. Since bacterial surface possess negative potential and citrate modified ZnONP is also having negatively surface potential, there would be a relatively repulsive interaction between the surfaces. The growth kinetic study of *B. subtilis*, which is a Gram-positive bacterium with relatively less negative surface potential among the studied bacteria, showed inhibition at 250 μg/mL of n-ZnONP, only. However, the value is two and half fold higher than that found for p-ZnONP against same bacteria, *i.e*. 100 μg/mL. To investigate more about the interfacial potential between NPs and bacteria surfaces, three Gram-negative bacteria were taken for their relatively higher negative surface potential than Gram positive bacteria. For all the bacteria, higher MIC was observed for n-ZnONP (Figure 3.11b–d) compared to the value found for p-ZnONP (Figure 3.10d–f). The observations clearly indicated that the interaction between the nanoparticle and bacterial membrane surfaces results in the interfacial potential that triggers possible ROS mediated reactions leading into bacterial non-viability.

The term surface neutralization is largely attributed, in biological system, to balance the surface potential that exist between accessible negatively charged, polar and non-polar functional groups on bacterial surface and the interacting entities present on p-ZnONPsurface[229]. Since *E. coli* is a Gram-negative bacterium, possesses a more negative surface potential than *B. subtilis*, which is a Gram-positive bacterium (Figure 3.9). Increasing concentrations of p-ZnONP take the interfacial potential at the p-ZnONP-bacteria interface to neutral, suggesting the neutralization of surfaces by the respective surface functional groups present on the interacting partner. As a result of the neutralization, the energy released is possibly either utilized in production of ROS or membrane surface tension or both, as indicated in the work of Espita P.J.P. *et al.*[230]. The work suggested that generation of ROS on the surface of ZnONP plays role in the antimicrobial activity by ZnONP following the possible reaction steps given below[230].

$ZnONP + h\upsilon \longrightarrow e_{cb}^{-} + h_{vb}^{+}$ Eq (2)

$e^{-}_{cb} + O2 \longrightarrow O2^{\bullet -}$ Eq (3)

$h_{vb}^{+} + H_2O \longrightarrow {}^{\bullet}OH + H^{+}$ Eq (4)

$O_2^{\bullet -} + H^{+} \longrightarrow HO_2^{\bullet}$ Eq (5)

$HO_2^{\bullet} + H^{+} + e^{-} \longrightarrow H_2O_2$ Eq (6)

Since ZnONP is a photocatalytic material having a band gap of 3.3 eV[16]. Hence, energy released higher than the band gap energy, can trigger the movement of electrons from the valence band (vb) to the conduction band (cb) resulting in a positive area in the valence band (electron hole, h^{+}) and free electrons (e^{-}) in the conduction band[231]. When ZnONP is in suspension, the created electron-holes react with H_2O molecules and separate the H_2O molecules into $^{\bullet}OH$ and H^{+}. Simultaneously, dissolved O_2 molecules in the medium are transferred into $O_2^{\bullet -}$ (superoxide anion radicals) and react with H^{+} ions to generate $HO_2^{\bullet +}$ followed by collision with an electron to produce H_2O_2 molecules[230-232]. The reaction occurs at the interface and produces reactive oxygen species, among which hydroxyl radicals and superoxide anion radicals are negatively charged. The negatively charged free radicals can not penetrate the cell membrane, since the bacterial cell membrane is negatively charged[233]. However, modification of the membrane physico-chemistry cannot be ruled out while the generation of ROS is happening in the proximity. Since H_2O_2 is uncharged reactive oxygen species, the molecule can penetrate inside the bacteria and cause the cell non-viability[233]. The amount of ROS generated is directly proportional to the concentration of p-ZnONP in suspension. The increase in concentration of p-ZnONP increases the number of possible interactions leading into ROS production, and hence antibacterial activity increases[230].

The DCFH-DA dye is a cell permeant dye, and indicator of reactive oxygen species. The initial ROS formation, i.e. before injection of NP, is due to metabolic activities (Figure 3.15), that is approximately same for all the bacteria. Above MIC, the fluorescence intensity upon the nanoparticle addition increased many folds (Figure 3.15a, b), supporting the work of Espitia P.J.P. *et al*. It is very interesting to observe that at 250 μg/mL of p-ZnONP, the emission intensity in *E. coli* culture is higher than the intensity observed in *B. subtilis* culture, inferring production of more ROS leading to more cell death. The observation is similar to growth kinetics and CFU results for both the bacteria. In case of n-ZnONP, the increased emission intensity of the dye is insignificant compared

to control cultures. The observations rationalize the interaction between the negative surface potentials result in interface that can not produce or enhance reactive oxygen species generation, hence insignificant cell death.

Effect of the interactions on bacterial cell viability is further explored using the BacLight assay, which distinguishes viable or non-viable cells based on the membrane integrity. The kit uses mixture of two fluorescent dyes, Syto9 and propidium Iodide (PI) dyes, which stains green (Syto9) to viable cells with intact membrane and stains red (PI) to non-viable cells with ruptured membrane. The images obtained using the BacLight kit indicate loss of membrane integrity or alteration in membrane permeability on p-ZnONP treatment[224]. Hence, the resulting interfacial potential on interaction of the nanoparticle with bacterial membrane also result in membrane rupture either because of ROS or increased surface tension of bacterial membrane or both. The latter case is further investigated using FE-SEM through morphological changes in the bacterial membrane. The high resolution images obtained using FE-SEM, indicate occurring of membrane blebs along with the membrane damage/rupture. Upon addition and incubation of p-ZnONP with bacterial cells, neutralization of surface potential was observed; as a result of interaction at the interface leading into increased surface tension. The increased surface tension is capable of affecting the bacterial membrane to a greater extent. As a result of increased ROS and surface tension, bacterial membrane showed some abnormal textures like rupture, blebs etc. The neutralized cell membrane and ruptured cells no longer remain discrete and result in aggregates/clumps[234].

In conclusion, two types of ZnONPs having opposite surface potentials of same magnitude were synthesized. Based on the data, insights into the biophysical events happening at the interface of ZnONP-bacteria were gained. Firstly, the interaction at the ZnONP-bacteria interface was explored to understand mechanism behind the attachment of NPs to bacterial surface. Secondly, the resultant interfacial potential, measured using zeta potential measurement study, and the standard antibacterial activity assay helped us to establish a correlation between the interfacial potential and antimicrobial propensity of the NPs. Together, the bio-nano interfacial potential result in a surface tension generating high lateral stress in the membrane leading to irreversible membrane damage via membrane blebs or rupture, as clearly visible in images obtained using fluorescence microscope, SEM, and FE-SEM. At the end, the molecular events leading to the antimicrobial activity of ZnONP was explored by evaluating ROS production from the interaction at different

concentrations of ZnONPs. Taking altogether, the biophysical and antimicrobial data obtained from the study, it was concluded that the interfacial potential at the ZnONP-bacteria interface is largely responsible for the antimicrobial propensity of ZnONPs.

3.3. Effect of surface functionality on antimicrobial propensity of IONPs

Nanoparticles, when suspended in biological culture medium, encounter with various biological interfaces resulting from the presence of cellular moieties like DNA, proteins, lipids, flavonoids, polysaccharides etc. Fate of the suspended NP depends upon different physico-chemical properties of nanoparticle and interactions present at the nano-bio interface[93]. Understanding the interactions at nano-bio interface, help in adopting approaches for safe use of NPs in biomedical, clinical and pharmaceutical industries. The understanding can help in moderating surface cytotoxic and/or antimicrobial propensities of nanoparticles. Inside biological medium, the interactions between accessible functional groups of NP and biomolecules like lipopolysaccharide (LPS), phospholipid, protein, and lipoteichoic acid (LTA) present over the bacterial envelop or eukaryotic membrane contribute in the interaction pattern at the interface. The same functional groups of biomolecules enhance adhesion of bacteria to different surfaces, and help their proliferation[97]. Hence, the accessible functional groups present at bacterial envelop and NP surfaces, along with the physico-chemical property of NP, determine the fate of bacteria as well as NP (whether NP will be compatible or toxic to bacteria). It has been reported that among different types of NPs, magnetic NPs due to their biocompatibility, chemical stability, and magnetic behavior are widely used in biomedical sciences [25]. Magnetic NPs are being used for delivery of drugs to targeted tissues by the application of external magnetic field, which in turn increases the stability of drugs against enzymatic or metabolic degradation[25]. Due to outstanding magnetic, physico-chemical, thermal, and mechanical properties, magnetic NPs can also be used in other fields, like analytical chemistry, pathogen detection, antigen diagnosis, tissue repair, and hyperthermia[23]. Thus, this objective aims to evaluate the antimicrobial propensity of IONP with a special emphasis on the role of functional groups at the nano-bio interface determining the antimicrobial propensity of IONP.

To explore the effects of functional groups present at nano-bio interface affecting the antimicrobial activity, IONP with magnetite like atomic arrangement and negative

surface potential (n-IONP) was synthesized by co-precipitation method. Positively charged chitosan molecule coating was done to reverse the surface potential of n-IONP, i.e. positive surface potential IONP (p-IONP). The comparative data from fourier transform infrared spectroscope, XRD and zeta sizer indicated the successful coating of IONP surface with chitosan molecule. Additionally, the nanocrystals obtained were found to have spherical size with 10–20 nm diameters. The antimicrobial activity of both types of IONPs was evaluated adopting different antimicrobial and biophysical studies as described below.

3.3.1. Effect of the interfaces upon bacterial cell viability

The growth kinetic studies of *B.subtilis* and *E. coli* in presence of different concentrations of n-IONP and p-IONP are shown in figure 3.17. Figure 3.17a and 3.17c display the growth curve of *B. subtilis* and *E. coli*, respectively, in presence of different concentrations of n-IONP. As shown in the figures, insignificant growth inhibition compared to control were observed for the studied concentrations of n- IONP, whereas the inhibition is relatively very significant for *B. subtilis* (Figure 3.17b) and *E. coli* (Figure 3.17d) in presence of relative p-IONP concentrations.

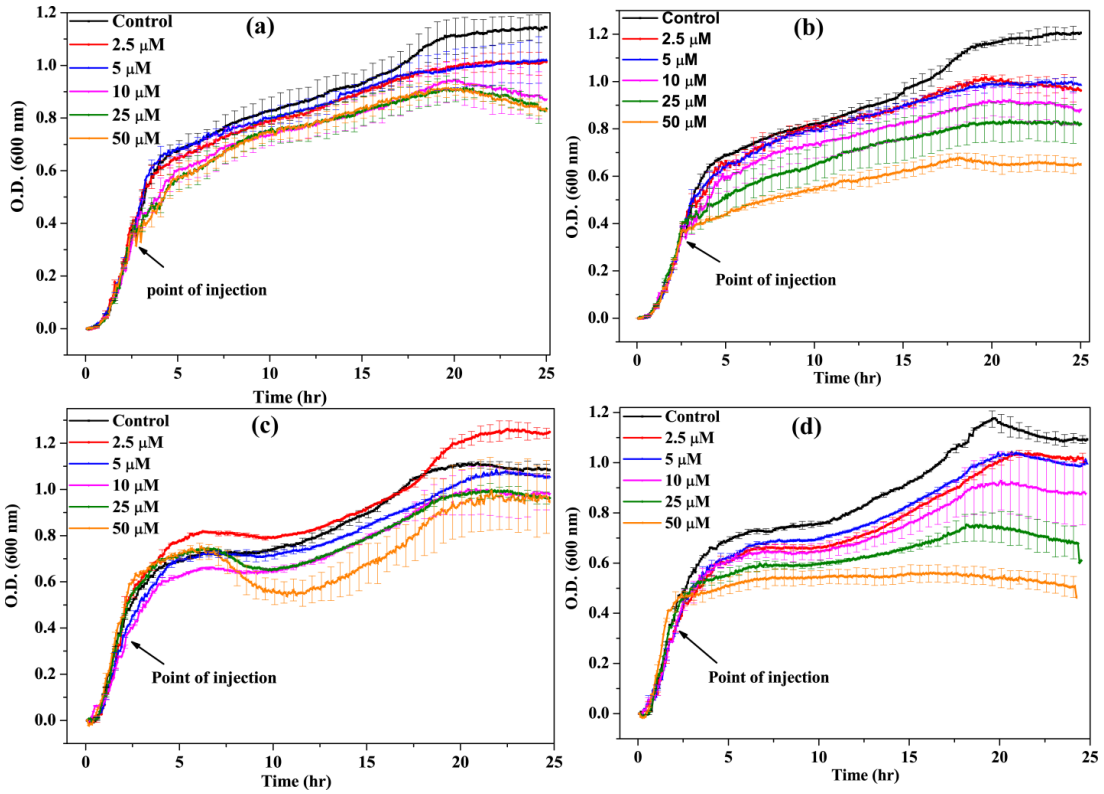

Figure 3.17. Growth kinetics of *B. subtilis* (a and b) and *E. coli* (c and d) in absence and presence of different concentrations of n-IONP, (a) *B. subtilis* and (c) *E. coli*, & p-IONP, (b) *B. subtilis* and (d) *E. coli*. Different concentrations of the NPs taken were 2.5, 5, 10, 25, and 50 μM, and injected at the log phase of growth kinetics (shown by arrow). Triplicate experiments were done for each reaction, and the error bar represents the standard error of mean

However, CFU measurements indicated the antimicrobial activity of n-IONP at higher concentrations (Figure 3.18). The viability of both bacterial cells reduced by approximately 30% in presence of 50 μM n-IONP. However, the coated IONP has significant effect on bacterial viability, viability reduced by 70% in presence of 50 μM p-IONP. The data indicated strong antimicrobial propensity of p-IONP against studied bacterial strains. Additionally, the data support the growth kinetic studies observed in presence of n-IONP and p-IONP.

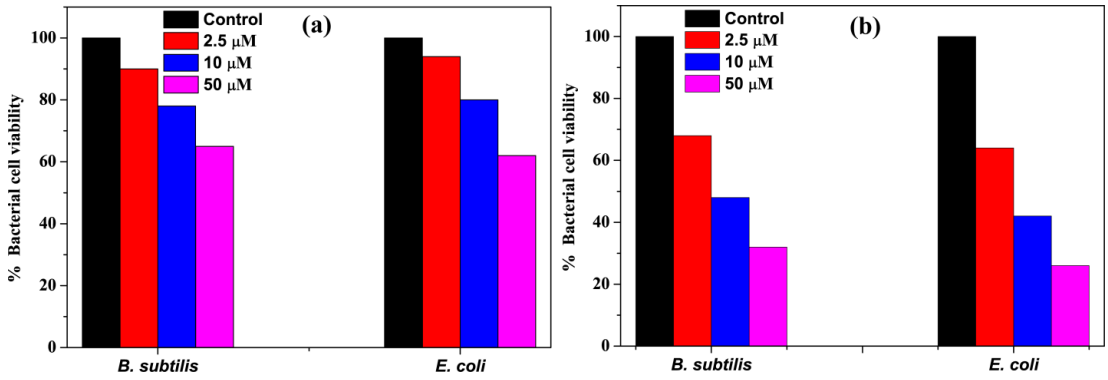

Figure 3.18. Quantification of bacterial cell viability at different concentrations of n-IONP (a) and p-IONP (b). Colony forming units (CFU) were quantified for both *B. subtilis* and *E. coli* cells, and represented as percentage of viable cells in comparison to colony obtained from untreated culture.

Figure 3.19 showed the kinetics of DCFH-DA oxidation upon the bacterial cell treatment with the NPs. The NPs were added in log phase of bacterial growth. ROS is also produced in culture media in the absence of NP treatment, inferring the production of ROS is natural. Bacteria produce ROS in non-stress condition. The produced ROS in non-stress conditions is counteracted by ROS scavenging enzymes present in bacteria like superoxide dismutase in *E. coli*. However, presence of both n-IONP (Figure 3.19a & 3.19c) and p-IONP (Figure 3.19b & 3.19d) resulted in significant increase in the fluorescence intensity, with relatively higher change in p-IONP presence than n-IONP. The change in the fluorescence intensity is directly correlated with the higher amount of ROS production for both, *B. subtilis* (Figure 3.19a & 3.19b) and *E. coli* (Figure 3.19c & 3.19d) cells. The ROS observation and the growth kinetics study, together, indicated that the ROS production is a

reason for antimicrobial activity by both the IONPs. Additionally, it is observed that the amount of ROS produced (as measured from the fluorescence intensity) is higher for p-IONP than n-IONP. The observation rationalized that p-IONP has higher antimicrobial activity than n-IONP.

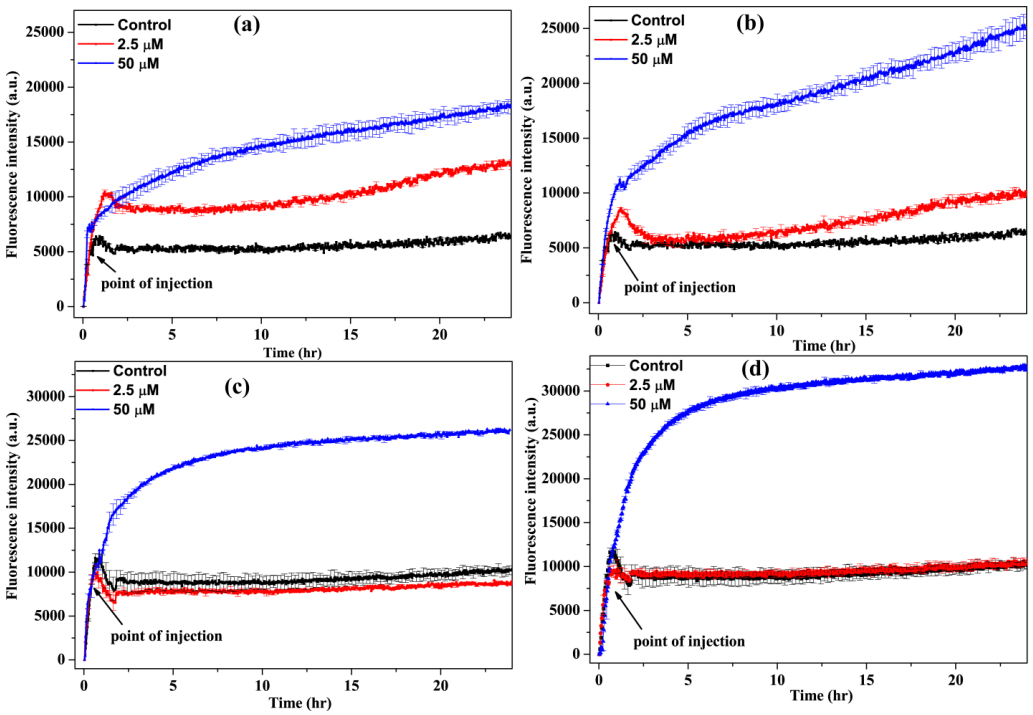

Figure 3.19. n-IONP and p-IONP induced ROS production in bacterial culturess. Panels a and c represent change in fluorescence intensity with DCFH-DA oxidation in presence of n-IONP in *B. subtilis* and *E. coli* cultures, respectively. Whereas, b and d panels represent DCFH-DA oxidation kinetics in presence of p-IONP treated *B. subtilis* and *E. coli*, respectively. Each curve represents the average of three independent measurements with corresponding standard error of mean.

The antibacterial activity of both NPs resulting from the interaction pattern is further explored using LIVE/DEAD BacLight fluorescence Kit. It differentiate viable cells from non-viable cells by staining green and red to viable and non-viable cells, respectively[224]. As shown in figure 3.20, untreated (control) bacterial cells showed green fluorescence inferring presence of 100% viable cells. The n-IONP (50 μM) treated samples showed insignificant fraction (~10%) of non-viable bacterial cells, indicating insignificant antimicrobial activity of n-IONP against *B. subtilis* and *E. coli*, at studied concentration. On other hand, p-IONP (50 μM) treated bacterial culture showed 90% of non-viable bacterial cells, which confirmed the significant change in antimicrobial activity of IONP upon chitosan coating.

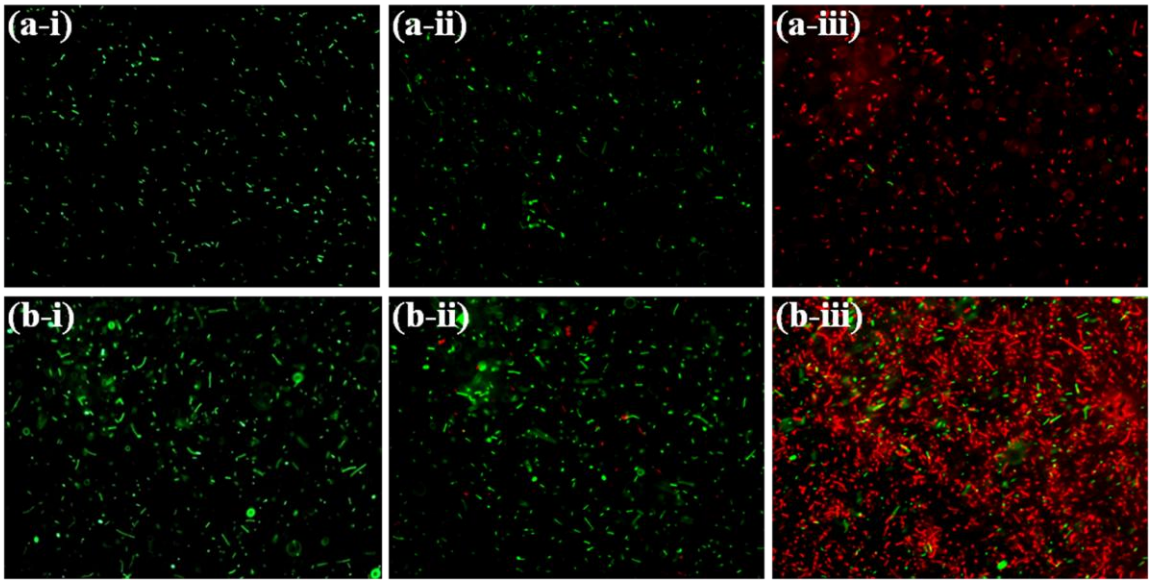

Figure 3.20. Fluorescence microscopic images of *B. subtilis* and *E. coli* in absence and presence of n-IONP and p-IONP. Intact *B. subtilis* (a-i), *B. subtilis* in presence of 50 μM n-IONP (a-ii), and *B. subtilis* in presence of 50 μM p-IONP (a-iii), intact *E. coli* (b-i), *E. coli* in presence of 50 μM n-IONP (b-ii), and *E. coli* in presence of 50 μM p-IONP (b-iii). The scale bars represent for 20-μ m.

3.3.2. Discussion

Studies have been done to demonstrate the antimicrobial activity of IONP[235-237], still the mechanism behind antimicrobial activity is a matter of intensive research, in present. Chatterjee, S. *et al*[236] have demonstrated that IONP has antimicrobial activity against *E. coli*, and the activity increases with increase in concentration of IONP. Borcherding, J. *et al*[238], on the other hand, have shown that IONP have no antimicrobial activity. Here, we have extended the studies taking the help of different antimicrobial and biophysical studies to draw a concluding remark against these contrasting statements, and to explore the mechanism behind the antimicrobial activity of IONPs.

Initially, IONP with negative surface potential (n-IONP) having small size and good stability was synthesized. Surface of the NP was further modified with chitosan to modulate the surface potential and functional groups. Positively charged chitosan molecules are strongly bonded to magnetic n-IONP via electrostatic and/or H-bonding as predominant interactive forces[210]. The chitosan coated IONP has positive surface potential majorly due to the free hydroxyl group (-OH) of chitosan, which interact with the aqueous solution through hydrogen bonds resulting into a stable well dispersed colloidal suspension. Additionally, the coulomb repulsion between the IONPs having positive/negative surface potential also plays a role in well dispersivity of the particle[208].

To explore the effect of interaction pattern at the interface on antimicrobial activity of IONPs, growth kinetic, LIVE/DEAD BacLight Bacterial Viability assay, and CFU measurement studies were done taking both negative and positive surface potential IONPs. The outcome indicated that p-IONP has higher antimicrobial activity than n-IONP. Due to presence of negative potentials on both n-IONP and bacterial surfaces, the interaction between n-IONP and bacteria would not be strong due to dominant electrostatic repulsion at the interface which is the primary cause of non-attachment of the NP on bacterial cell. However at higher concentration, > 50 μM, n-IONP have antimicrobial activity to some extent, as suggested by growth kinetic, LIVE/DEAD BacLight assay, and CFU measurement studies. The finding can be rationalized to the molecular crowding upon increase in the NP concentration, which resulted into net attractive interaction between nano-bacteria interface. Above certain concentrations of NP, despite the negative surface potentials, the particle will be preferentially excluded along with the larger particles or interfaces of same or opposite potentials, like bacterial membrane here. The exclusion, hence, resulted into the net attractive interactions. The net attractive interaction enhances relative ROS production at the interface, as shown in figure 3.19. Hence, higher concentrations of n-IONP in the culture media are capable of enhancing ROS production, a principal reason for the antimicrobial propensity of metal oxide nanoparticles. The findings supported the work of Borcherding, J. *et al*[238] provided the concentration of n-IONP is above the critical concentration.

Considering the role of interfacial potentials on interaction, IONP with positive surface potential will have better surface for bacterial attachment with stronger interactions at interface than n-IONP. The stronger interactions will result in relatively enhanced ROS production. Hence, to strengthen the hypothesis, surface potential of n-IONP was reversed by coating with positively charged chitosan molecule. Chitosan of different molecular weights, above 25% (w/v), shows significant antimicrobial propensity against both Gram-positive and Gram-negative bacteria, as reported by Zheng, L.-Y. *et al*. [239]. In order to nullify the chitosan mediated antibacterial activity, only 0.02% (w/v) chitosan concentration was used for surface modification of n-IONP. Chitosan at 0.02% (w/v) does not show any antimicrobial activity against studied bacteria. Like predicted, p-IONP inhibited the bacterial cell growth relatively at very low concentration than n-IONP, suggesting that p-IONP have higher antimicrobial propensity. Comparison of the fluorescence intensities in figure 3.19 indicates that the interaction at nano-bacteria

interface is relatively stronger for p-IONP than n-IONP. Stronger the interaction, higher is the change in free energy content, resulting into more ROS production. In case of IONP, ROS production follows the Fenton reaction as mentioned below in Eq 7 and Eq 8. From the metabolic activity, hydrogen peroxide (H_2O_2), which is a toxic oxidant causing DNA and protein damage, is produced in cultures of all aerobic organisms [240-241]. *E. coli* produces H_2O_2 at the rate 10-15 μM/s during the growth in oxygen rich glucose medium [241], as also observed in untreated bacterial culture, figure 3.19. However, the produced H_2O_2 is counter-balanced by various scavenging enzymes present in cells like superoxide dismutase for *E. coli*. In this objective, ROS production in culture was measured using a fluorescent dye, DCFH-DA. Upon IONPs dispersion inside the culture media, different oxido-reduction reactions are followed involving both the species present in magnetite, Fe^{3+} and Fe^{2+} resulting into generation of different and more potent reactive oxygen species[241-242]. The reactions are known as Fenton reaction or Haber-Weiss cycle, as following.

$$Fe(III) + H_2O_2 = Fe(II) + OH^- + OH^o \quad \text{Eq (7)}$$

$$Fe(II) + H_2O_2 = Fe(III) + HO_2{}^o + H^+ \quad \text{Eq (8)}$$

OH^o and $HO_2{}^o$ formed in the process are free radicals. Iron in magnetite (Fe_3O_4) NP through a series of reactions is fully oxidized to maghemite (γ-Fe_2O_3) causing oxidative stress to bacterial cells, hence bacterial cell death. In contrast, fully oxidized maghemite is relatively stable in culture medium without any further possibility of electronic or ionic transition. Hence, maghemite formed as end product possesses insignificant *in vitro* cytotoxic propensity[242]. Nevertheless, the amount of free radicals formed in the oxido-reduction process is sufficient to put stress on the viable bacterial cells, causing non-viable cells. The amount of ROS produced at the nano-bacteria interface depolarizes the bacterial membranes, causing membrane damage as suggested by BacLight assay (Figure 3.20) and in our work with ZnONP[167]. However, the membrane depolarization of *B. subtilis* (Figure 3.21) was studied using Scanning Electron Microscopy and the interaction between p-IONP and bacteria was confirmed using energydispersive X-ray spectroscopy (EDX). Unlike control (Figure 3.21a, inset), the EDX spectra of p- IONP treated bacterial surface shows the traces of Fe, confirming the interaction of p-IONP with bacteria catalysing the membrane depolarization (Figure 3.21b, inset). Moreover, the bacterial membrane

depolarization upon p-IONP treatment as suggested by BacLight assay, was further confirmed and illustrated in SEM micrograph (Figure 3.21).

Figure 3.22 showed the proposed schematic model elucidating the detail mechanism described here to understand the p-IONP antimicrobial activity. Although n-IONP has relatively less antibacterial activity, the growth kinetic study, LIVE/DEAD BacLight assay, and ROS detection studies indicated that the surface modification of n-IONP with chitosan makes it more toxic to bacterial cells due to relatively stronger attractive interaction at the interface. Additionally, the cytotoxicity assay using Alamar Blue dye following the procedure adopted by Jha, S. *et al*[185] demonstrated the cytocompatibilty nature of the nanoparticles, IONP and chitosan coated IONP.

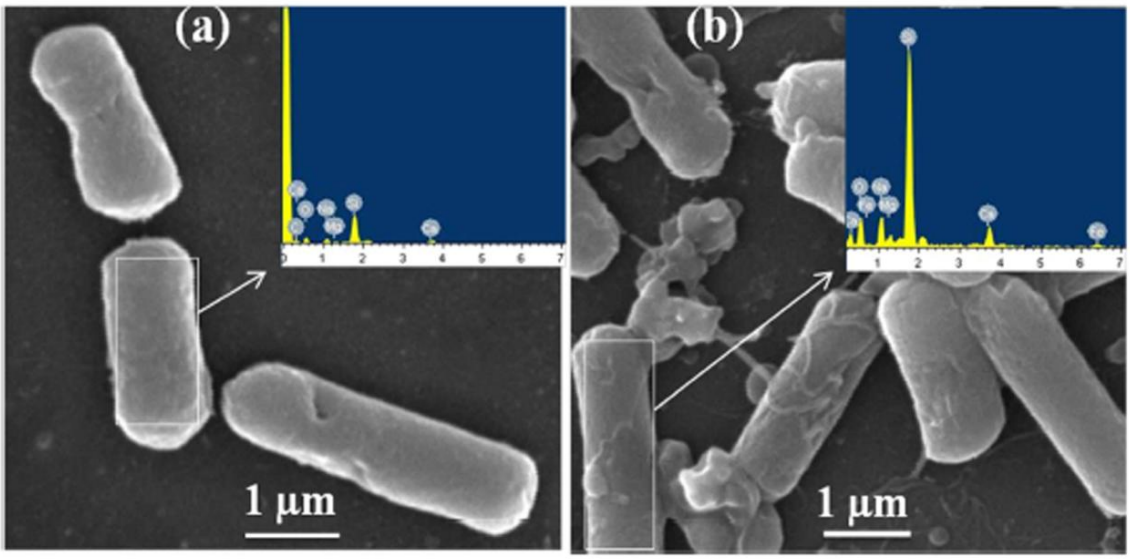

Figure 3.21. SEM micrographs showing membrane deformation/damage of *B. subtilis* upon p-IONP treatment. (a) SEM representative image of control (without p-IONP treatment), and figure inset shows the EDX spectra of *B. subtilis* surface. (b) SEM representative image of *B. subtilis* cells upon p-IONP treatment, and figure inset shows the EDX spectra of *B. subtilis* surface after p-IONP treatment.

The work indicates that the interfacial potential is not only the determining factor for the bactericidal effects of nanoparticle. In addition to interfacial potential, the interacting functional groups at the interface also contribute in the effect through regulating level of ROS production. Hence, adopting the optimized approach, the antibacterial propensity of IONP interface can be modulated using chitosan coating without changing cytocompatibility nature of the nanoparticle. The findings conclude that n-IONP has antimicrobial activity at relatively very high concentrations. The activity,

however, can be moderated by accordingly changing the surface potential and accessible surface functional groups. The changes cause interaction pattern change at the nano-bio interface, hence play crucial role in determining the antimicrobial propensity of IONPs. The enhanced production of ROS because of the interaction potential at the interface is the principal cause for antimicrobial propensity of the NPs. As a conclusion, the interaction pattern at the nano-bio interface plays vital role in determining the antimicrobial activity of metal oxide nanoparticles.

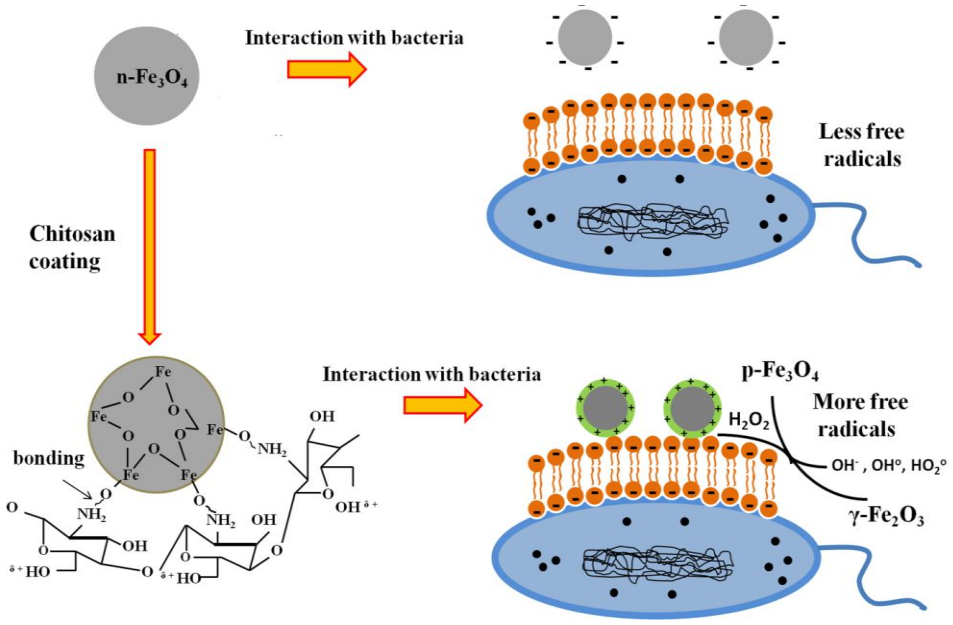

Figure 3.22. Proposed schematic model elucidating the detail mechanism of IONPs against bacterial cells.

3.4. Effect of ZnONP surface defects on cytotoxic and antimicrobial propensities

Due to wide band gap (3.37 eV) and large excitation binding energy (60 meV at room temperature), ZnO nanomaterial has been adopted as a promising material for different biomedical applications[16]. However, cell permeabilization because of small size and high specific surface area is the matter of concern, when the particle is considered for biological applications[16, 243]. Various studies have demonstrated that ZnONPs have the potential to reach different organs during numerous biological applications, and cause hazardous effects to lungs, kidney, liver, stomach, pancrease, testis, spleen, heart, thymus, blood, and brain[243]. Additionally, *in vitro* cytotoxicity has also been observed during culture of many cells, like epidermal cells, human lung, epithelial cells etc[243]. Furthermore, the studies have demonstrated that inhaled ZnONPs translocate to central

nervous system resulting in inflammatory response, hence possibly causes the brain edema[16]. In general, the studies indicated that ZnONP is one among the most toxic NPs[16, 244] to eukaryotic cells. Nevertheless, ZnONP is being regarded as possible treatments for different types of cancer and autoimmune diseases[243, 245].

From the extensive *in vitro* and *in vivo* studies, it has been reported that oxidative stress is one of the mechanisms to elucidate the toxic effects of metal oxide NPs[16]. The oxidative stress is caused from an imbalance between the antioxidant defence system versus different reactive oxygen species (ROS) generated in a cell[16]. In addition, it has been identified that ROS act as a signaling molecules for various pathways which result in both, the cell survival and death[16]. Hence, the ROS production in higher amount, mainly in radical forms, such as superoxide ($^{\bullet}O^{-}_{2}$), hydroxyl radical ($^{\bullet}OH$) , and hydrogen peroxide (H_2O_2) etc., causes cell death by damaging cellular biomolecules[16, 167]. Photocatalytic NPs with low energy band gap, like AgNP, ZnONP, IONP, TiO_2NP, on interaction with the interacting biomolecular surfaces produces the ROS, causing the oxidative stress[23, 167, 246]. Hence, modulating the NPs band gap can change the photocatalytic activity, and the ROS-mediated cytotoxicity.

Being a photocatalytic NP, several efforts have been made to enhance the photocatalytic activity of ZnONPs[16]. The photocatalytic activity of NP is affected by different factors, such as composition of NP, phase structure, particle size, surface functional groups, crystallinity, surface defects etc[16]. In this context, Zhang, X. *et al* have elucidated that the photocatalytic activity of ZnONP primarily depends upon the surface defects of the particle generated due to different calcination temperatures, keeping crystallinity constant[16]. In support to the study, work explored the role of change in ZnONP crystallinity on the photocatalytic activity of ZnONPs in biological milieu. To this end, a correlation between change in crystallinity and energy band gap of ZnONP was explored, since change in the band gap can significantly affect photocatalytic activity. To validate the hypothesis, different ZnONPs were synthesized by varying calcination temperature, 300, 500, and 700 ^{o}C, respectively that resulted in ZnONPs with varying surface defects, hence the band gap. However, the biophysical investigations and molecular studies demonstrated that the oxidative stress, generated due to the variation of crystallinity and energy band gap of ZnONPs, adversely affect the cytotoxic and antimicrobial propensities of the particle. Additionally, the treatment induced autophagy

mediated cell recovery from the stress, while the failure in recovery caused apoptotic cell death.

3.4.1. Cytotoxic propensity of ZnONPs

Cell viability assays are to evaluate the toxicological propensities of additives, since the assay provide key information about the cell death, cell survival, and their metabolic activities[247]. To explore variation in energy band gap and crystallinity on the particle cytotoxic propensity, Alamar Blue (AB) dye reduction assays were observed for varying ZnONP concentrations (2.5, 5, 12.5, 25, and 50 μg/mL) treated HT1080 cells. The data (Figure 3.23a) indicated that degree of reduction of the dye was ZnONP concentration dependent. The AB dye, which is a water soluble dye, is commonly used for quantification of viable cells upon different drug treatments[248]. Additionally, it is stable, cell permeable, and non-toxic to various cells, hence helpful for monitoring the continuous culture of cells[248]. In principle, the AB dye, a resazurin dye, invaginate into cell and the mitochondrial dehydrogenase enzymes convert it into its reduced form, resorufin, which has relatively higher quantum yield. Hence, reduction of the dye by viable cell makes it suitable for cell viability analysis. Interestingly, as shown in figure 3.23a, compared to untreated cell (control), viable cell count is unaffected for 2.5 μg/mL of the particle fabricated at 300 ^{o}C caclination. However, the viability gradually reduced from 95, 77, 51, 46 to 42 % as the ZnONP concentration in culture gradually increased from 2.5, 5, 12.5, 25 to50 μg/mL. On the other hand, the particle fabricated at 700 ^{o}C calcination reduced the viability from 35 % at 2.5 μg/mL to 13 % at 50 μg/mL. Thus, the drastic reduction in viable cell fraction upon the particle treatment was highest for ZnONP fabricated at 700 ^{o}C calcination, compared to other two variants of ZnONPs.

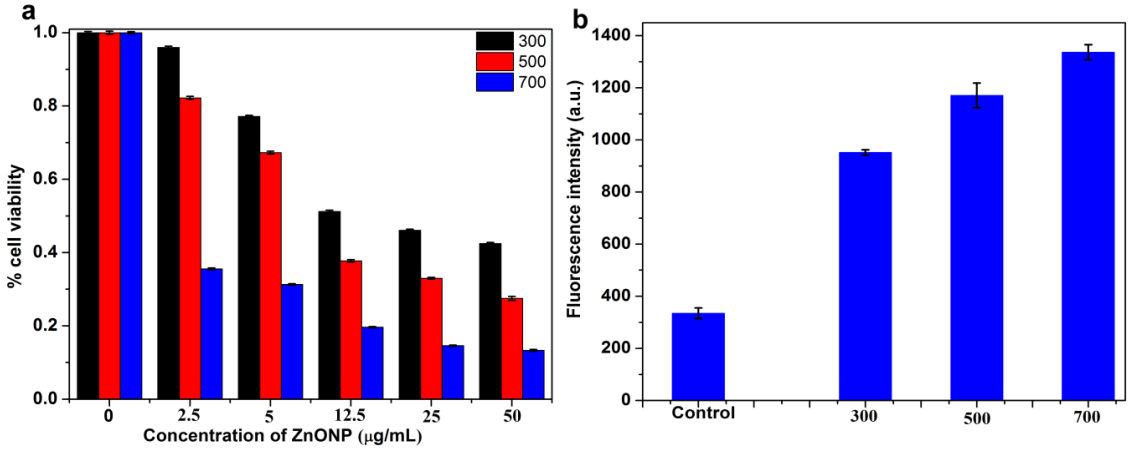

Figure 3.23. (a) Percentage cell viability of HT1080 cell lines upon ZnONPs treatment, using

Alamar Blue dye reduction assay, (b) ZnONPs (50 μg/mL) induced ROS detection in HT1080 cell culture, using 2,7-Dichlorodihydrofluroscein diacetate (DCFH-DA) fluorescent dye.

The oxidative stresses, caused by photocatalytic NP treatment, causing cell death have been extensively studied[23, 167]. The level of intracellular ROS generation upon the particle treatment was detected using the oxidative conversion of the dye DCFH-DA to a fluorescent compound, dichlorofluorescien (DCFH). The oxidative conversion of the dye was also observed for control (cell without NP treatment), which is dedicated to ROS generated from the unstressed cellular metabolism. Most of the eukaryotic and prokaryotic cells have the system to neutralize a threshold amount of ROS[167, 246]. However, enhanced ROS level above a threshold causes oxidative stress to cells. The oxidative stress results in the oxidation of various biomolecules, like carbohydrate, nucleic acid, protein, and lipid. Compared to control, quantum yield of the dye increased by ~ 2.5 folds, from 334 to 951 a.u. for ZnONP fabricated at 300 ^{o}C, whereas for the particle fabricated at 500 and 700 ^{o}C, the yield increased by 3.2 and 3.7 folds, respectively. Hence, the oxidative conversion of the dye increased by 2-4 folds upon the particle treatment (Figure 3.23b). The data indicated that ROS production increases as the calcination temperature for ZnONPs fabrication increases from 300 to 700 ^{o}C, *i.e.* increase in crystallinity or decrease in energy band gap enhanced ROS generation in biological milieu. Hence, the particle treatment caused primarily ROS-mediated HT1080 cell cytotoxicity.

The generation of ROS upon photocatalytic metal NP treatment depends on its photocatalytic property, which is strongly influenced by its energy band gap. Narrowing of the band gap can increase the photocatalytic activity, which in turn increases ROS generation in biological milieu. Hence, the particle with enhanced photocatalytic activity exhibited more cytotoxic effect. Furthermore, it is reported that photocatalytic activity can also be observed in visible light upon narrowing of the band gap[193]. The excitation of semiconductor surface electron results in the e^{-}-h^{+} separation, and the holes with higher oxidative potential helps in formation of the reactive intermediates in proximity of the loci of interaction[193]. When the photocatalyst is inside the biological medium, hydroxyl radical (^{o}OH), one of the primary oxidants in biological milieu, is formed as a result of the reaction between holes and OH^{-} or water[193]. Similarly, ZnONP, being a photocatalytic NP, produces different reactive oxygen species like hydroxyl radical (^{o}OH), superoxide anion (O_2^{-}), H_2O_2 etc. in biological milieu[167]. The enhanced ROS generation is primary cause of

cellular machineries and mitochondrial machineries dysfunctions leading into cell death, which was further supported by the AB reduction assay.

The ZnONP induced DNA damage was further analyzed using comet assay. Comet assay, a combination of DNA gel electrophoresis and fluorescence microscopic analysis, is generally applied to visualize the migration of DNA strands[172]. In principle, when there are breaks in negatively charged DNA, in electrophoresis the DNA migrate relatively faster towards anode due to relaxation of DNA super coils. However, larger size DNA fragment in case of undamaged DNA prevents its migration, hence, is considered as an indispensable tool to study DNA damage[172]. A comet like tail is an indication of a damaged DNA. Comet assay of 50 μg/mL ZnONPs treated cells showed an increase in olive tail moment from 25 pixels to 70 pixels for the fabricated particles with increasing calcination temperature, from 300 ^{o}C to 700 ^{o}C, compared to control cell with olive tail moment of 10 pixels only (Figure 3.24). Additionally, the increasing olive tail moment indicated that the extent of DNA damage increases with the increase in calcination temperature of the fabrication. Thus, the ROS data along with the comet assay indicated that the increasing calcination temperature for ZnONP fabrication enhances the ROS production resulting in extensive DNA damage.

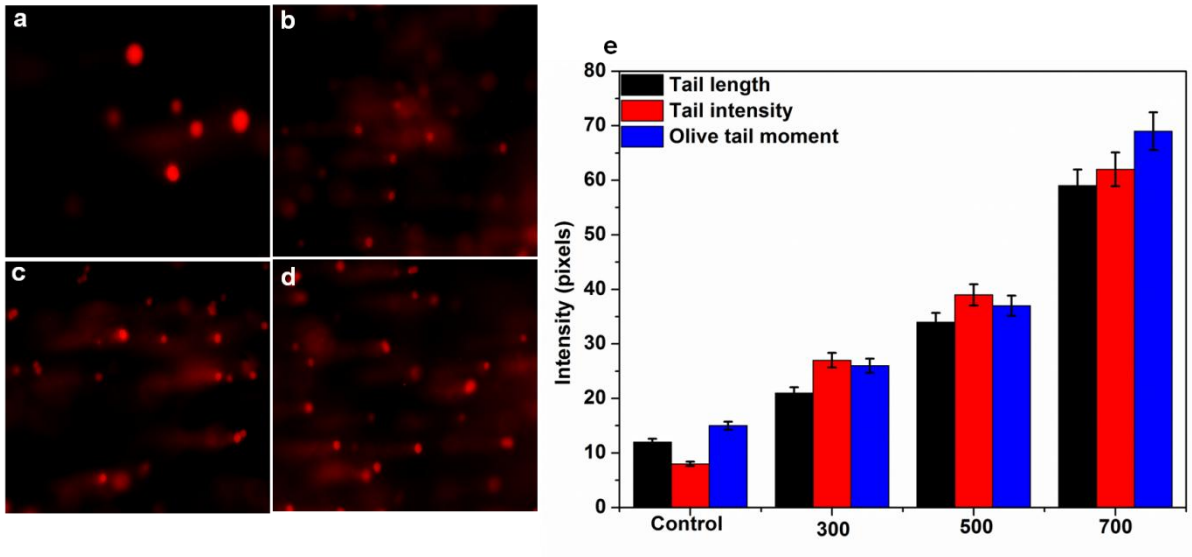

Figure 3.24. Comet assay showing the damaged DNA upon different ZnONPs treatment, (a) control, (b) 300 ^{o}C, (c) 500 ^{o}C, and (d) 700 ^{o}C fabricated ZnONPs. (e) The image J comet assay plugin software was used to determine the key parameters of the obtained comet (shown in histogram), which demonstrate an increased DNA damage from ZnONPs untreated to treated cell.

3.4.2. Effect of ZnONP treatment on the cell cycle

To further support the ROS-mediated DNA damages, cell cycle were observed using flow cytometry, where the early effects would be marked in cell cycle progression. As reported, cells having damaged DNA accumulate in gap1 (G_1), DNA synthesis (S), or in gap_2/mitosis (G_2/M) phase. Whereas, accumulation of cells in subG_1 phase is a clear indication of cells with irreversible DNA damage leading to apoptosis[247]. Hence, we investigated cell cycle of HT1080 cell grown in presence of different ZnONPs to detect different phenomena such as apoptosis, cell cycle arrest and DNA damage. The statistical analysis indicated that major population fraction of treated and untreated cells were in G_1 phase (Figure 3.25), i.e. growth phase, where different enzymes needed for DNA replication are translated[249]. Interestingly, as different variants of ZnONPs concentrations increased in cell culture, cell population fraction in subG_1 phase increased significantly, from 5% in control to 25% in 50 μg/mL treated cells, signifying the induction of apoptosis upon ZnONP treatment. Additionally, an increase in cell population in subG_1 phase simultaneously decreased the cell fraction in G1 phase, from 55 % in control to 37 % in the treated cell culture (Figure 3.25). However, the cell population fractions in other phases were insignificantly affected upon the treatment. Hence, ZnONP primarily affects cells in G1 phase than the cells present in S1 and G2/M phase.

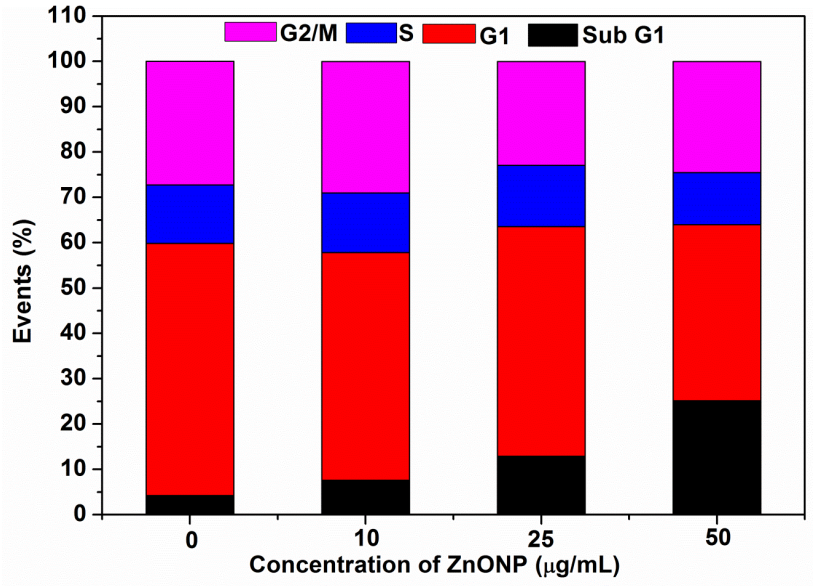

Figure 3.25. ZnONP (700 ^{o}C fabricated) treated HT1080 cell showing gradual increase in subG_1 population with increasing concentrations of the particle. The statistical data are generated by C6 accuri software, and plotted as generated. Histograms for each treatment are included in the Appendix.

3.4.3. Induction of autophagy upon ZnONPs treatment

It is reported that chemical autophagy inducers have the potential to inhibit the growth of tumour cells[250]. The autophagy induction potential of fabricated ZnONPs was evaluated using acridine orange assay. Development of acidic vesicular organelles is a characteristic of autophagy. It has been reported that acridine orange being a lysotropic dye passes freely through the biological membrane, and accumulates in different acidic compartments such as lysosomes, in a pH dependent manner[251]. Acridine orange acts as a hydrophobic green fluorescent molecule at neutral pH, whereas in acidic conditions it becomes protonated and forms aggregates with red fluorescence[252]. As shown in figure 3.26, control cells treated with acridine orange dye showed green fluorescence with relatively small percentage (~ 15 %) of red fluorescence. However, ZnONP treated cells displayed significant increase in percentage (from 15 % to 84 %) of red fluorescence, representing presence of acidic vesicular organelles (AVOs). The merged images indicating orange cells represent viable cells with autophagosomes, while red cells represent non-viable cells with acidic environment. Hence, as observed from figure 3.26, the population of autophagosomes in different ZnONPs treated HT1080 cell indicated that the particle with lower energy band gap induces more cell with acidic environment/autophagosome than the particle with higher energy band gap. Hence, the particle fabricated with calcination temperature of 700 ^{o}C is more potent to trigger autophagy mediated cell death, in the studied cancer cell.

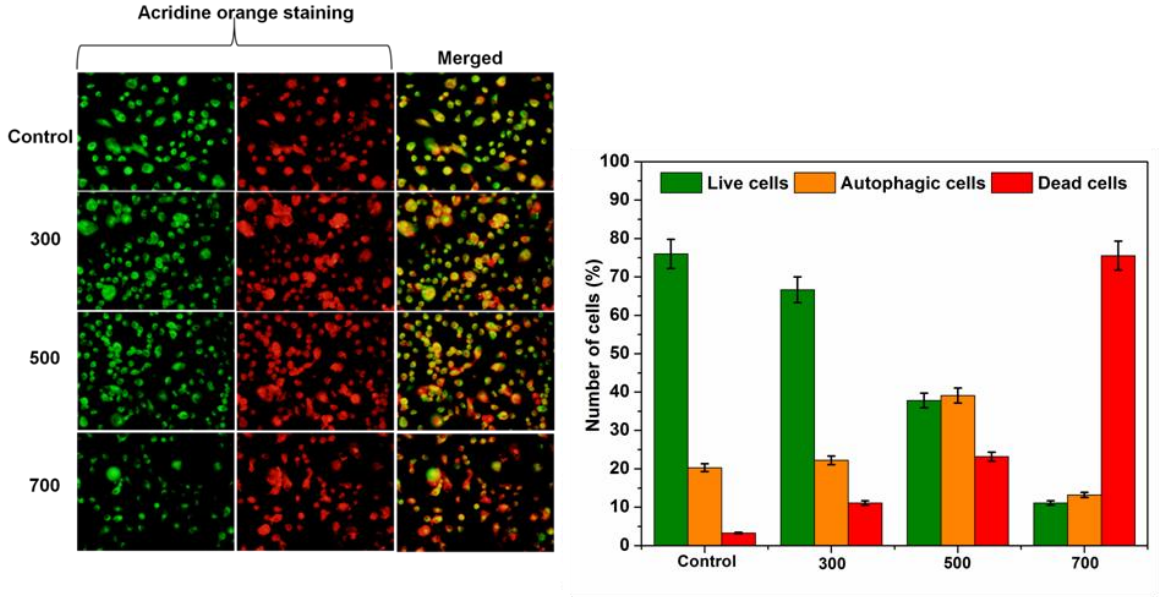

Figure 3.26. ZnONPs triggered autophagy detection by Acridine Orange assay (left panel). Histogram shows the relative percentage of autophagosomes in control and ZnONP treated samples (right panel).

3.4.4. ZnONPs treatment causes apoptotic cell death

In order to underline the cytotoxic mechanism of different ZnONPs, apoptosis inducing property of the particles against HT1080 cell was studied. During apoptosis nuclei of a cell become fragmented, and changes into highly condensed apoptotic bodies, which are quantified using DAPI staining[253-254]. In the objective, as shown in figure 3.27, the DAPI staining indicated that in control the nuclei of the cells were round, big, and had a distinct or intact nuclear membrane, with insignificant condensed nuclei population, 1 % of total nuclei only. However, upon ZnONPs treatment, the cell exhibited densely stained nuclei, indicating presence of more cells with condensed chromatin compared to control. The relative percentages of condensed chromatin population, as shown in figure 3.27e, were found 8, 19 and 29 % in the cell culture treated with the particle fabricated with 300, 500 and 700 ^{o}C calcination, respectively. Hence, the relative percentage of condensed nuclei increased gradually with increase in calcination temperature of the particle fabrication.

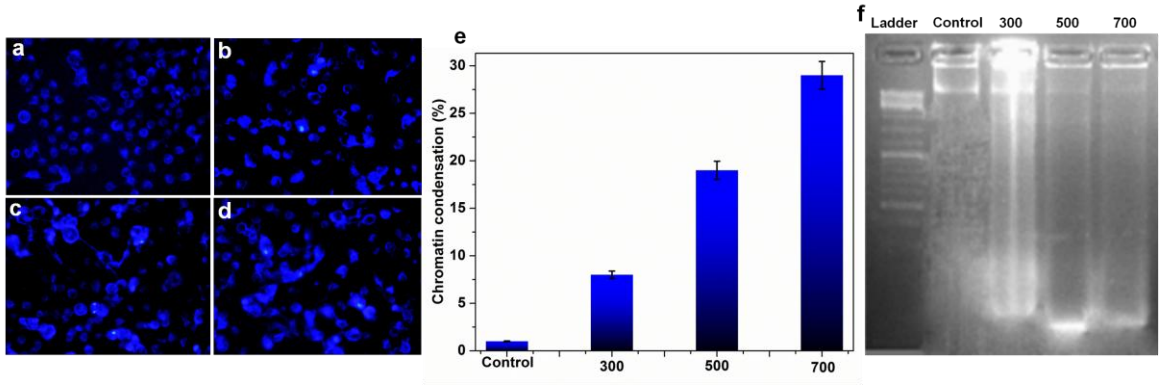

Figure 3.27. Chromatin condensation analysis in untreated (a) control and (b) 300 ^{o}C, (c) 500 ^{o}C and (d) 700 ^{o}C fabricated ZnONPs treated HT1080 cell. (e) Histogram showing the percentage of condensed chromatin, and (f) DNA fragmentation assay showing the fragmentation of DNA upon ZnONPs treatment, a hallmark feature of apoptosis.

DNA fragmentation is another technique generally used to visualise fragmented DNA which arise during apoptosis as a result of endonuclease cleavage[255]. In this technique, the DNA from the ZnONPs treated cells were extracted and separated using agarose gel electrophoresis. As shown in figure 3.27f, no DNA fragmentation was observed for untreated cell. Whereas, ZnONP treated cells exhibited fragmented DNA at the base of the lanes, along with the relatively faint bands of DNA that are present in control. Thus, both the data indicated that the irreversible ROS-mediated DNA damage in HT1080 cell treated with ZnONPs resulted in apoptotic cell death.

3.4.5. HT1080 morphology upon ZnONPs treatment

The alteration of cell shape/morphology is one of the most noticeable events to observe, upon exposure to a cytotoxic material. The change in morphological features of HT1080 cell upon ZnONP treatment is observed using FE-SEM. As shown in figure 3.28, the control cells showed intact morphology. However, HT1080 cells treated with ZnONP exhibited distinct morphological changes as compared to control. Additionally, clustering of cells was observed upon ZnONP treatment, which restricted the cell spreading capacity, unlike control cells. The reduced spreading capacity can be rationalised to disturbances in the cytoskeletal assembly or functions[247]. Various groups have also found similar results upon different NP treatment, for example Asharani, P. V. *et al* have also marked similar results in human glioblastoma cells (U251) upon starch-coated silver nanoparticle treatment.[247] Additionally, in this work blebbing of the cellular membrane (marked by arrow in Figure 3.28) upon ZnONP treatment was observed, which is a morphological indication of apoptosis. However, the ZnONP, fabricated at 700 ^{o}C calcination, showed significant membrane disruption and blebbing in HT1080 cells than other two ZnONPs.

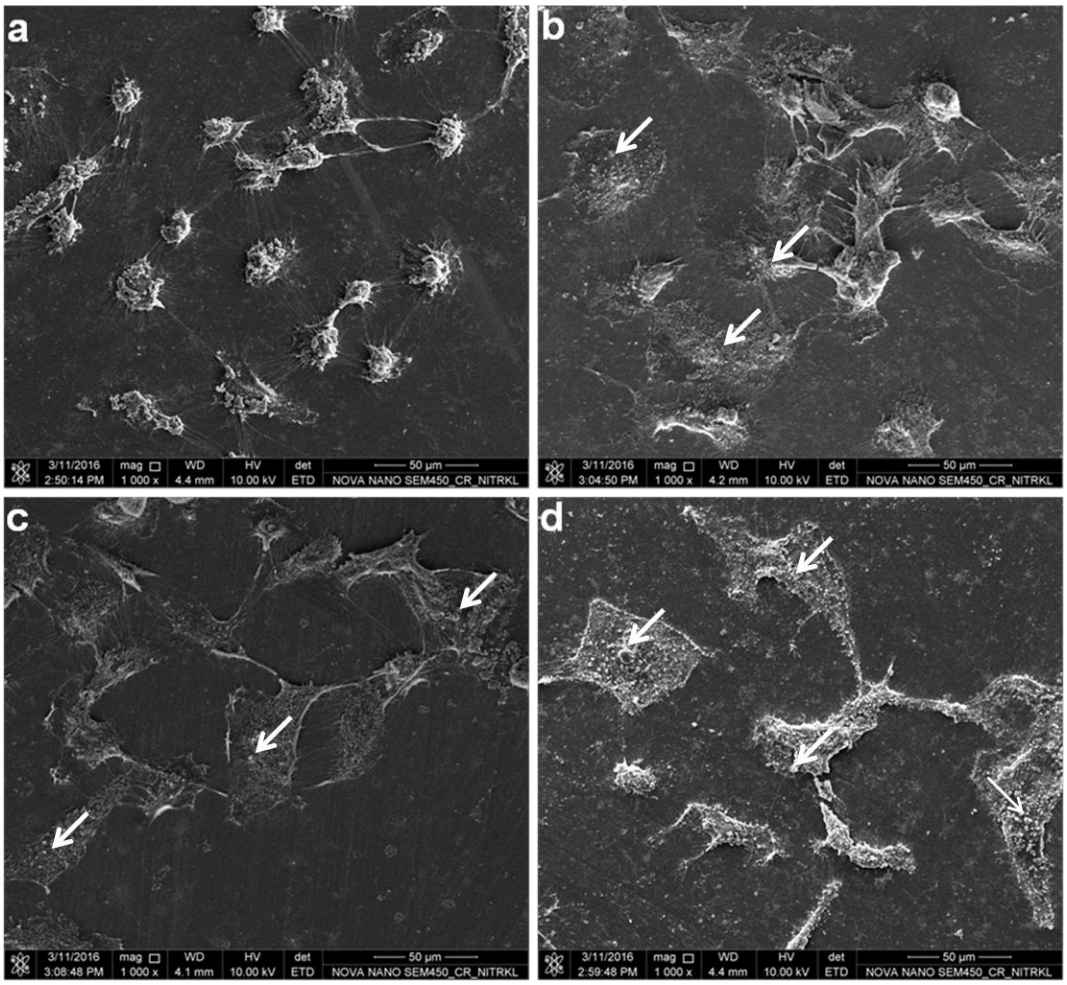

Figure 3.28. FE-SEM micrographs of (a) HT1080 cells without ZnONP treatment, and the cell treated with ZnONPs fabricated at (b) 300 ^{o}C, (c) 500 ^{o}C and (d) 700 ^{o}C calcination.

The plasma membrane which is a selectively permeable membrane acts as a boundary for cell, and maintains a suitable intracellular environment. Additionally, it allows permeabilization of small and nonpolar molecules like O_2 and CO_2, whereas polar molecules like ions and NPs of larger size are unable to diffuse across lipid bilayer. However, nanoscale molecules and supra-molecular assemblies are transported through the process of endocytosis, where the particles are enclosed in a membrane vesicle, and finally cellular uptake happens[49]. It is reported that, in case of certain NPs, the NPs are confined in membrane bound vesicles (endolysosomes), which restrict their path to reach the cytosol[49]. However, the process is not limited to all NPs. Additionally, it is also reported that many NPs possess the inherent property to penetrate the cell membrane[49]. In that case, the NPs form pores in cell membrane leading to cellular toxicity, since the pores imbalance the intracellular and extracellular ions, proteins, and other macromolecules concentration gradient, which are essential for cellular functions. Based on the surface charge of nanomaterials, cationic charged NPs have shown stronger interaction with anionic cell membrane via electrostatic interaction, and translocated easily through the cell membrane[49]. From the zeta potential study, it is found that cationic properties of the synthesized ZnONP decreases with increase in calcination temperature of the fabrication, where slightly negative potential for ZnONP fabricated at 700 ^{o}C calcinations was observed, i.e. -4.19 mV. However, the cytotoxic propensity revealed that the ZnONP fabricated at 700 ^{o}C calcination has highest cytotoxic propensity than the other two. In this context, various studies have approved the internalization of negatively charged NPs through the cell membrane, despite of unfavorable interaction between NP and membranes[49, 256]. Unlike positively charged NPs, negatively charged NPs have less efficiency for endocytosis, however, they bind non-specifically with some positive moieties on the plasma membrane with relatively less negative domain, and internalized through endocytosis[256]. During endocytosis, ROS produced because of the particle interaction with cellular moieties resulted in oxidative stress. To recover from the stress, cell adopted autophagy-mediated pathway, resulting in enhanced cell fraction in the treated samples with autophagosomes, as also observed in figure 3.26.

The cell membrane puts certain resistive forces due to stretching and elasticity of the membrane, which hinder uptake of the NPs[93]. However, different specific and non-

specific binding interactions at the nano-bio interface generate sufficient thermodynamic energy to overcome the resistive forces, and help in particle adhesion and engulfment[93]. The interfacial ROS generation also helped in destabilization of cell membrane, hence facilitating internalization of the NP. Interestingly, the narrowing of the band gap of ZnONP generated ROS more efficiently with relatively lesser amount of binding energy. Hence, the particle can easily destabilize the membrane and make internalization of NP easier. As observed in this study, the increasing calcination temperature reduced the energy band gap and produced rod shape ZnONP. Findings from different groups indicated that the rod shape NP internalized relatively efficiently than spherical shape NP[93, 257-258]. The data, altogether, indicated that the NP interaction with HT1080 cell led to interfacial and intracellular ROS generation, which resulted into irreversible DNA and membrane damage leading into cell cycle arrest in subG1-phase. The arrested cells adopt autophagy-mediated pathway to recover the damage, whereas failure of the recovery led the cell into apoptotic cell death (Figure 3.29).

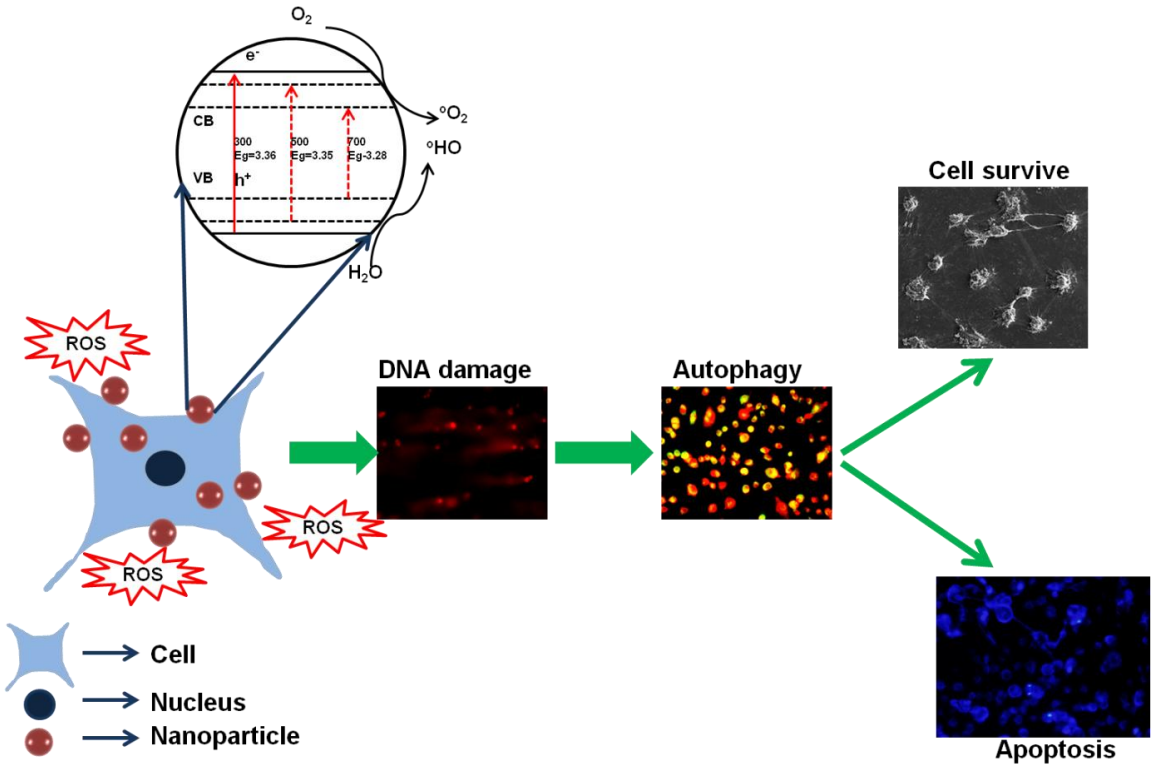

Figure 3.29. Schematic diagram illustrating the effects of ZnONP induced oxidative stress on HT1080 cell. Presence of the narrower energy band gap ZnONP enhances the ROS generation beyond a threshold ROS concentration in HT1080 cell. The increased ROS value in cell results in DNA damage, which the cell try to recover using autophagy. The cell with successful scavanging

of ROS and ROS-mediated damaged biomolecules led a normal morphology or cell cycle, whereas unsuccessful cells led into apoptotic cell death.

As a summary, the study underlines a correlation between narrowing of energy band gap and cytotoxic propensity of ZnONPs against a HT1080 cell. The findings revealed that with increasing calcination temperature, the crystallinity of ZnONP was significantly affected that in turn narrowed energy band gap of the particle. The molecular findings from our study indicated that the narrowing of energy band gap increases the oxidative stress exerted by the ZnONPs, which in turn causes chromosomal aberrations as found from the comet assay and DNA fragmentation study. Hence, the chromosomal aberrations resulted in cell cycle arrest in subG_1-phase, which the arrested cell tried to recover using autophagy-mediated pathway, as revealed by acridine orange assay. However, the cell with unsuccessful recovery led to apoptotic cell death. In the end, the objective concluded that the narrowing of ZnONP band gap increases the photocatalytic activity of the NP, which in turn increases the DNA aberrations resulting into induction of autophagy mediated recovery of the aberrations, failure of which led into cell death.

3.4.6. Antimicrobial propensity of ZnONPs

To explore the effects of surface defects on antimicrobial propensity, antimicrobial and biophysical studies against the bacteria *Bacillus subtilis* was performed. Initially, growth kinetic study of *B. subtilis* in absence and presence of different concentration of ZnONP (700 ^{o}C) was performed. From the study against HT1080 cells, it was observed that ZnONP (700 ^{o}C) has significant cytotoxic activity. Hence, initially varying concentration of ZnONP fabricated at 700 ^{o}C calcination effect on the bacterial growth kinetic was studied (Figure 3.30 a). As shown in the figure, highest inhibition of bacterial growth was observed in presence of 250 µg/mL ZnONP. Additionally, when the growth inhibition of *B. subtilis* was observed in presence of 250 µg/mL of different ZnONPs (300, 500, and 700 ^{o}C) (Figure 3.30 b), highest inhibition was observed for ZnONP (fabricated at 700 ^{o}C calcinations). Hence, from the objective, it is concluded that ZnONP (700 ^{o}C) exhibited highest antimicrobial activity. To explore the mechanism behind the antimicrobial activity, the ROS production was measured for bacterial culture treated with 250 µg/mL of different ZnONPs (Figure 3.30c). As shown in the figure, highest ROS mediated DCFH-DA oxidation was observed in case of ZnONP (700 ^{o}C), which supported our previous findings against HT1080 cell lines. Hence, the work demonstrated that, the reduction in

energy band gap because of surface defects increases the ROS mediated antimicrobial and cytotoxic activities of the particle.

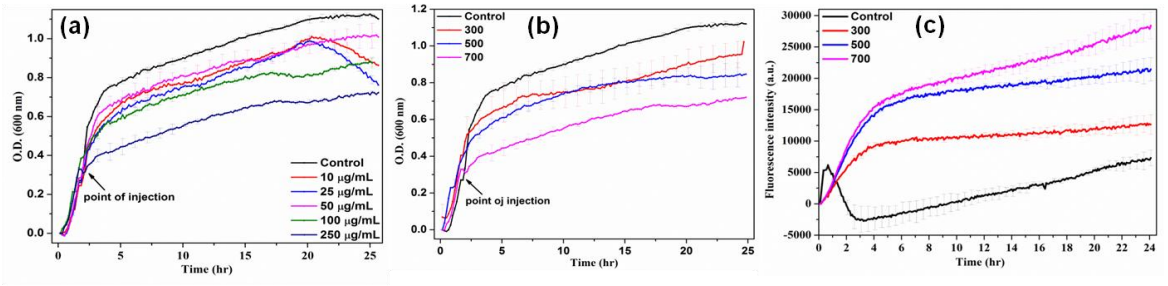

Figure 3.30. (a) Growth kinetics of *B. subtilis* in presence of different concentrations of ZnONP (700 ^{o}C), (b), Growth kinetics of *B. subtilis* at 250 µg/mL of ZnONPs (300, 500, and 700 ^{o}C), (c) ROS detection in presence of different ZnONP (300, 500, and 700 ^{o}C).

To explore the mechanistic details of ZnONP antimicrobial activity on bacterial membrane, LIVE/DEAD BacLight bacterial viability assay was performed. As shown in the figure (Figure 3.31a), the control of *B. subtilis* cells exhibited green fluorescence due to the presence of syto9 in the dye, demonstrating the presence of 100% live cells. However, in different ZnONPs treated culture, red fluorescence was observed due to staining of DNA by cell impermeable propidium iodide dye, demonstrating the presence of non-viable cells along with viable cells. However, the percentage of non-viable cells increased from ZnONP fabricated at 300 ^{o}C calcination to ZnONP fabricated at 700 ^{o}C calcination (Figure 3.31d). The study concluded that the variation in crystallinity of ZnONP significantly affects the band gap energy of ZnONPs, which determine both cytotoxic and antimicrobial propensities of the particle.

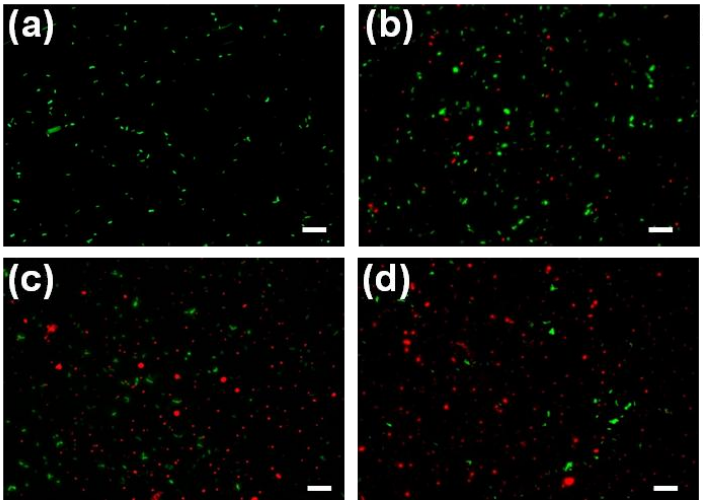

Figure 3.31. Fluorescence microscopic images of *B. subtilis* in absence and presence of ZnONP (250 µg/mL); (a) *B. subtilis*, (b) *B. subtilis* in presence of ZnONP (300 ^{o}C), (c) *B. subtilis* in

presence of ZnONP (500 ^{o}C) and (d) *B. subtilis* in presence of ZnONP (700 ^{o}C). The scale bars represent for 20 μm.

3.5. Effect of interfacial assembly of antimicrobial peptide on conformational and functional dynamics of the peptide

The emergence of resistant bacterial strains against conventional antibiotics has become a severe threat to public health worldwide. These antibiotic resistant bacterial strains cause millions of infection and thousands of death, every year. Antimicrobial peptides (AMPs) possessing the potential to inhibit the proliferation of conventional antibiotic resistant pathogens have drawn the attention of various research groups to increase their clinical use as an alternative to conventional antibiotics[259]. Generally, these AMPs are group of naturally occurring molecules playing important role as a first line of defense system to the host[229, 260]. Their broad activity and mode of action against different bacteria, virus, and fungi make them potential candidates for development of novel antibiotic strategies[229]. Members of this family share some common features like (i) AMPs are typically short (12 to 100 amino acids), hence small in size, < 10 kDa, (ii) cationic in charge, ranging from +2 to +7 at pH 7, and (iii) possess amphipathic steriogeometry[261-262]. Among these properties, the cationic property of AMP allows them to interact electrostatically with anionic fraction of bacterial membrane. However, amphipathic structure guides them for insertion into the hydrophobic layer of cell membrane, hence the insertion onsets antimicrobial activity[229, 262]. Among different AMPs, lantibiotic nisin is a small (3510 Da, containing 34 amino acids) amphiphilic peptide, produced by specific strains of *Lactococcus lactis*[263]. Because of the antimicrobial propensity and nontoxic nature against human, nisin has been adopted as a safe food additive by the food industry for controlling contamination by food spoilage microbes[264-268]. However, the efficacy of nisin in food industry is compromised due to the development of resistance in bacteria against nisin. Some bacteria like *Staphylococcus aureus*, *Streptococcus bovis*, *Lactobacillus casei etc.* have developed enzyme-based resistance due to presence of an enzyme 'nisinase', which clears the nisin from cytosol[269-270]. In addition, nisin at nanomolar concentrations shows insignificant activity against Gram negative bacteria due to presence of an additional lipopolysaccharide layer, hence called the membrane-based resistant strains[271].

The objective shows enhanced efficacy of nisin upon assembly at silver nanoparticle (AgNP) interface, which can be adopted as a broad range therapeutic formulation. Here, AgNP has been adopted as a nanoparticle interface for non-covalent

interaction with nisin, since AgNP is a Food and Drug Administration (FDA, US), Environmental Protection Agency (EPA, US), and FITI testing and research (US) approved nanoparticles[272]. To this end, the interfacial assembly of AgNP-nisin is confirmed using different biophysical techniques like zeta sizer, surface plasmon resonance property, circular dichroism spectropolarimetery, and infra-red spectroscopy. Additionally, the molecular dynamics (MD) simulation study indicated the relatively higher degree of freedom of C-terminus and hinge region residues than the N-terminus residues, for the interfacially assembled nisin. Furthermore, the biophysical investigation and antimicrobial studies, together, indicated that the membrane damage, interfacial and intracellular oxidative stress play important roles for enhanced antimicrobial propensity of the assembled nisin.

3.5.1. Interfacial assembly of nisin at AgNP interface

The AgNP-nisin conjugates at different weight/weight ratios (1:0.25, 1:0.5, 1:1) were obtained because of the interfacial assembly of cationic nisin onto the anionic AgNP interface, by establishing non-covalent interfacial interactions (predominantly electrostatic interaction). The nisin assembly at the AgNP interface was first confirmed from SPR spectra of AgNP and the conjugates, using UV-Visible spectroscope. As shown in figure 3.32a, the peak at 397 nm attributed to the surface plasmon resonance (SPR) property of AgNP. However, relatively stronger SPR property of AgNP suspension in near UV region, which is generally dedicated to the aromatic amino acids absorption i.e. 260-280 nm, masked the detection of nisin by the absorption spectroscopy. Nevertheless, the peak intensity at 397 nm reduced by 60 % with relatively broader peak, and an additional peak at 490 nm appeared possibly for the conjugates. The decrease in intensity of absorption at 397 nm rationalized to the decrease in intact/accessible AgNP surface in conjugate suspension. Whereas, red shift of the peak from 397 to 490 nm indicated the interfacial assembly of nisin at AgNP interface[167], forming NP-peptide conjugate. The precipitation in the conjugate reaction mixture increased with increase in the peptide fraction in the mixture. Hence, the reduced peak intensity at 397/490 nm rationalised to relatively less amount of either AgNP or the conjugate or both exposed to UV-Visible light. The data, altogether, indicated that the major nanoparticle population fraction was in conjugation with nisin, with characteristic peak for the conjugate at 490 nm.

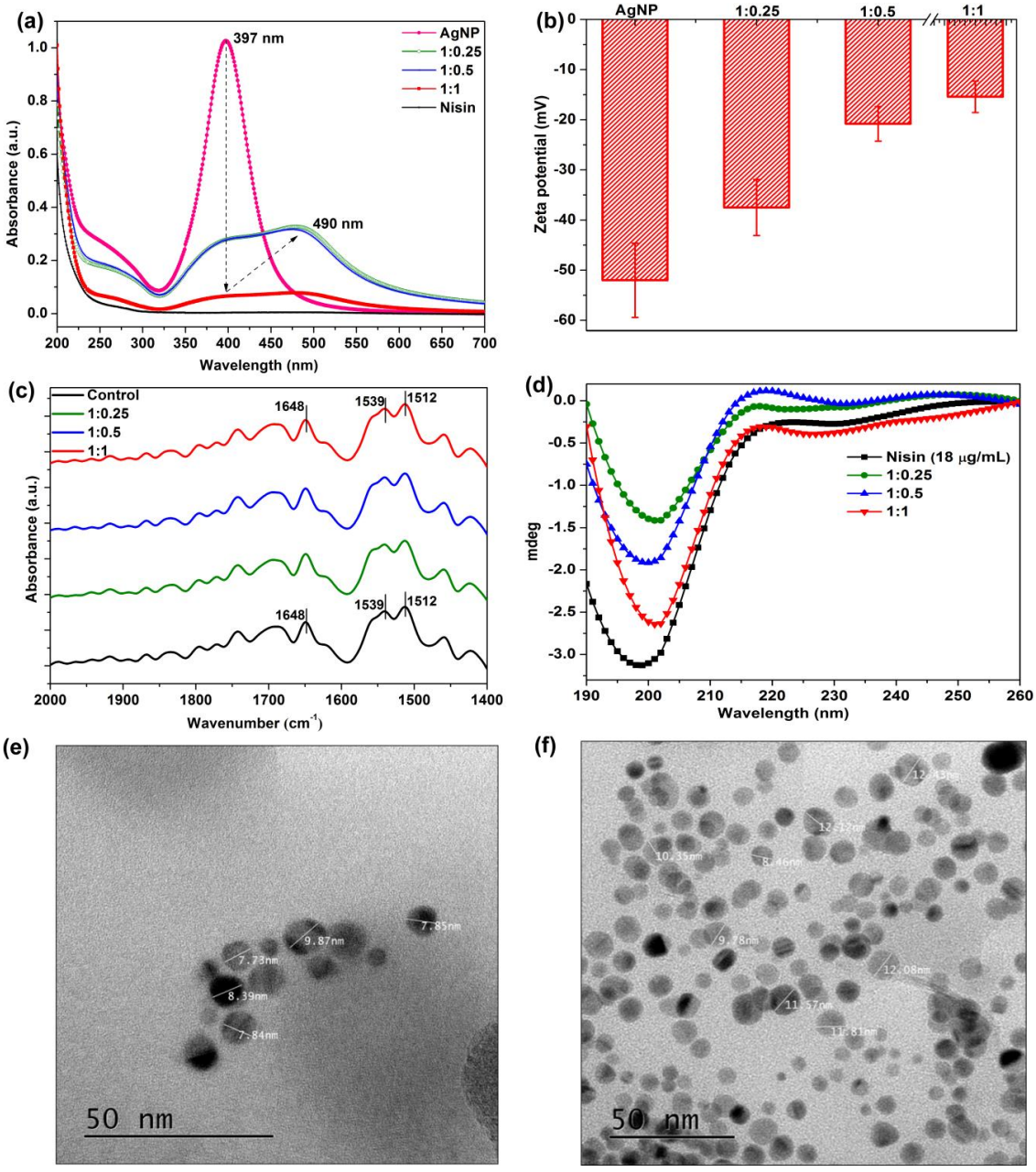

Figure 3.32. Characterization of AgNP-nisin conjugates. (a) UV-Visible spectra of AgNP, nisin, and different AgNP-nisin conjugates. (b) Zeta potential values of AgNP and different AgNP-nisin conjugates. (c) ATR-FTIR spectra of nisin and AgNP-nisin conjugates. (d) CD spectra of nisin and different AgNP-nisin conjugates, (e) TEM image of AgNP, and (f) TEM image of AgNP-nisin conjugate (1:1).

The interfacial assembly of nisin onto AgNP interface was further confirmed from the zeta potential analysis for AgNP and different AgNP-nisin ratios suspensions. As shown in figure 3.32b, the intact AgNP surface has the zeta potential of -52.0+/- 7.4 mV that neutralized upon conjugation with increasing nisin concentrations in suspension. The increasing concentrations of nisin reduced the AgNP zeta potential to neutral, from -52.0

+/- 7.4 mV to -15.4 +/- 3.14 mV for the highest AgNP-nisin ratio (1:1, w/w). Hence, the neutralization of AgNP surface potential upon addition of increasing nisin concentrations indicated the interfacial assembly of nisin onto the AgNP interface (Figure 3.32b). Similarly, Alves, C. S. *et al*229 have reported that the surface potential neutralization plays a major role in balancing the electrostatic interaction between cationic and anionic molecules. Hence, the results indicated that the non-covalent interaction, predominantly electrostatic, at the nanoparticle interface resulted in stable AgNP-nisin conjugates.

The conformational dynamics of nisin upon conjugation with AgNP was further explored using attenuated total reflection infrared (ATR-FTIR) and circular dichroism (CD) spectroscopies. Figure 3.32c showed the IR spectra of nisin and AgNP-nisin conjugates. The major peaks of nisin at 1648 cm^{-1} was due to the stretching vibrations of C=O (amide I), whereas 1512 and 1539 cm^{-1} were due to the bending vibrations of N-H (amide II), which confirmed the bond level vibrations of the peptide falling in predominantly random coil conformation. Like nisin, the amide I and amide II peaks for different ratios of AgNP-nisin conjugates were also found at same positions, confirming insignificant change in the conformation of nisin upon assembly at the AgNP interface. The hypothesis of interfacial assembly of AgNP-nisin was further strengthened by analysis of IR peaks below 800 cm^{-1}, which indicated the presence of metal-metal/metal-oxygen bonds[167]. From the observation of AgNP spectra, we found peaks at 516 and 545 cm^{-1} which were observed, representing the Ag-Ag/Ag-O bond vibrations. Interestingly, the presence of peaks at 517 and 544 cm^{-1}, in addition to amide-I and –II bonds, for AgNP-nisin (1:1) precipitate confirmed the presence of AgNP and peptide in the precipitate (Figure A12, Appendix). The retention of nisin secondary structure in conjugate was further confirmed by CD spectroscopy, where nisin and different AgNP-nisin conjugates gave negative ellipticity with prominent peaks in the range of 199-201 nm, corresponding to random coil secondary structure (Figure 3.32d). The data further supported the published work of Adhikari M. D. *et al.*, which showed nisin retains the ellipticity at 200 nm upon conjugation with gold nanoparticle[273]. However, change in peak intensity for 18 mg/mL nisin and the nisin-AgNP conjugate mixture (1:1) rationalised to settlement of the precipitate in the time frame of data collection, resulting in lower peak intensity for the conjugate mixture compared to the equal concentration of intact nisin.

The structural changes of both NP and protein upon formation of NP-protein conjugates have adverse effects in biological milieu. Hence, retention of structure of both

NP and protein is a key challenge upon the conjugation. Although, CD and IR spectroscopes revealed the retention of nisin conformation upon assembly onto the AgNP interface. It becomes essential to investigate the effect of interfacial assembly on the morphology of AgNP. Hence, the morphological features of both AgNP and AgNP-nisin conjugates were studied using transmission electron microscopy (TEM). Figure 3.32e-f is the representative TEM images of spherical shaped AgNP and AgNP-nisin conjugates (1:1), respectively. The comparative analysis of the images indicated that the interfacial assembly of nisin had insignificant effect on the morphology, and crystallinity (both possess fcc ring pattern as shown in SAED pattern, Figure A13c-d, Appendix) of the AgNP. Whereas, the assembly led to increase in average size of the AgNP 3-4 nm, only (Figure 3.32e-f). EDX data indicated the presence of additional carbon, nitrogen and sulphur atoms, supporting the presence of peptide onto AgNP interface (Figure S13e-f, Appendix).

To further explore the conjugations at atomic level, molecular dynamics (MD) simulation study was done. The study confirmed that non-covalent interactions at the AgNP interface and nisin resulted in the interfacial assembly of the peptide. The deviation between native and the simulated structure has been evaluated by measuring the root mean square deviation (RMSD) values (Figure 3.33a)[274]. The comparative RMSD values for all the peptide atoms indicated insignificant change with time (50 ns), reached a stable value of ~0.04 nm (Figure 3.33a). Moreover, the radius of gyration (Rg, ~2.18 nm) for simulated AgNP core (made up of face centred cubic, fcc, arrangement of 3871 silver elements, 10 nm diameter) showed insignificant deviation within the time frame of 50 ns (Figure 3.33b). Thus, both the results independently confirmed stability of the components, which were further used in simulation for the conjugates. Here, RMSD plot showed that the complex is stable during simulation with least fluctuations in structure of the peptide and core. A stable RMSD value of 0.02 nm has been observed for the conjugate (Figure 3.33c).

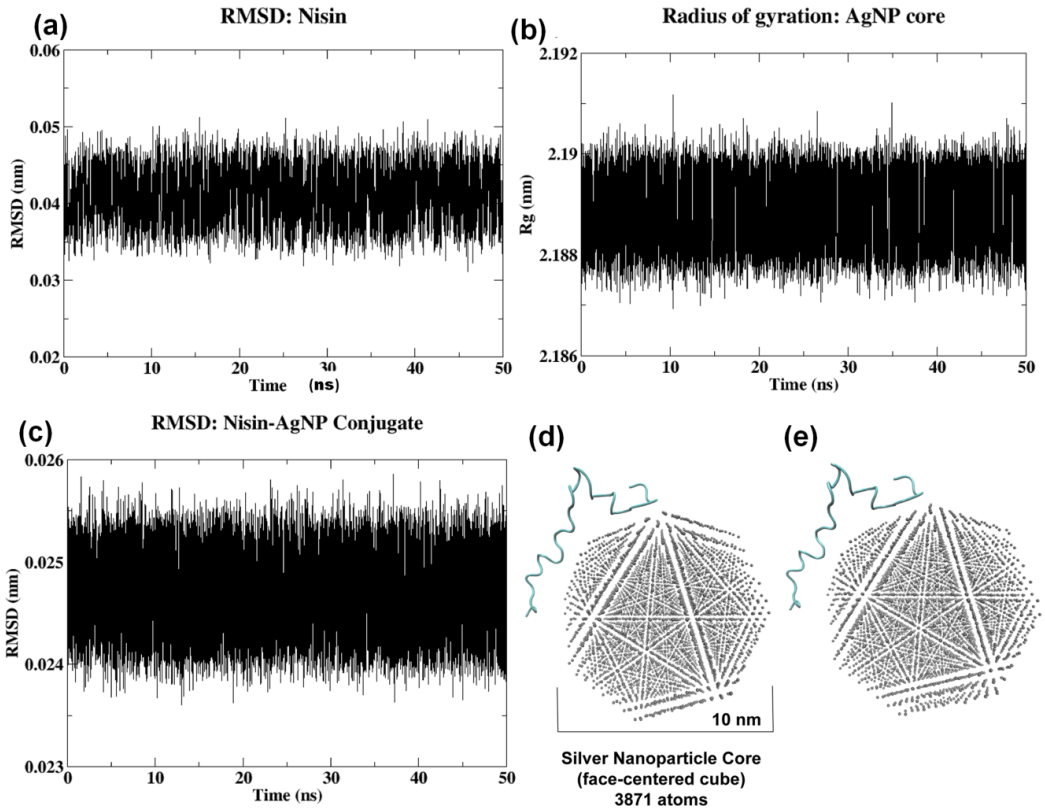

Figure 3.33. (a) RMSD of nisin peptide measured for 50 ns simulation, (b) Radius of gyration of the AgNP, (c) RMSD of nisin-AgNP conjugate measured for 50 ns simulation, and snapshots of AgNP-nisin conjugation at 0 ns (d) and 50 ns (e).

Analysis of the individual residues involved in interaction at the interface is indicated in table A2 (Appendix). The table represented the distance (in Å) of the residues that interact with the AgNP core at the initial, mid, and end stages of the simulation time frame (50 ns). It is observed that the residue numbers 1^{st}-4^{th}, 22^{nd}-26^{th}, and 31^{st}-34^{th} come relatively closer to the interface, i.e. loci of the conjugation. Although, the N-terminus residues (1^{st}-4^{th} position) are placed relatively nearer to the interface than the C-terminus residues. The observation indicated stronger interaction between the N-terminus residues and interface, than between the C-terminus and interface. However, the overall 50 ns simulation strongly suggested that the AgNP-nisin complex remains stable. The snapshots of trajectories showed that the peptide does not show any repulsive behaviour from the core, upon placing the peptide near to the core (Figure 3.33d-e and Figure S14, Appendix). Moreover, the simulation was done by taking the single peptide and NP core. For higher peptide molecules to core ratio, as predicted from neutralization study, the crowding effect will further strengthen the interaction between the residues and core. Thus, the simulation study further supported the conclusion drawn from Zeta analyser, FTIR, and CD spectra,

i.e. non-covalent interactions at the interface resulted in stable interfacial assembly of nisin onto AgNP interface without any significant change in nisin or AgNP structure.

3.5.2. The interfacial assembly enhances the antimicrobial propensity of nisin

The antimicrobial activity of 1.2 mg/mL (~2.8 nM) AgNP, 1.2 mg/mL (~340 nM) nisin, and the AgNP-nisin conjugates (1:0.25, 1:0.5, and 1:1, w/w) was evaluated by following growth kinetics of a Gram-positive bacterium, *Bacillus subtilis*, and a Gram-negative bacterium, *Escherichia coli*, in presence of the additives (Figure 3.34a-b). As shown in the figure, for studied concentrations and conditions, AgNP and nisin showed insignificant effect on either of the bacterial growth kinetics. However, in presence of AgNP-nisin conjugates (1:0.25, 1:0.5, and 1:1, w/w), where the nisin concentration varied from 0.3-1.2 mg/mL (*i.e.* 85-340 nM), and significant growth inhibitions for both the bacteria were observed. Among the studied ratios, inhibition was maximum for 1:1 ratio of AgNP-nisin conjugate. Here it is important to note that unlike other studies,[228, 275] the additives were added at mid log phase of growth kinetics, since the phase is most potent/viable phase of the bacterial growth. Hence, in log phase requirement of any antibiotic to inhibit the growth of bacteria is optimum, which indicates exact antibiotic minimum inhibitory concentration (MIC) against the bacteria[167]. Interestingly, addition of the conjugates immediately ceased the log phase of *E. coli*, whereas growth of *B. subtilis* followed original kinetics for 30 mins before showing significant inhibition (Figure 3.34a-b). Nevertheless, the growth kinetics, after a dormant phase of ~4 hrs, resumed the growth for both the bacteria. The findings indicated that the fraction of bacterial population that either become tolerant to the additives or remain unexposed to the conjugates resumed the growth. Since the bacterial culture is highly heterogeneous system with millions of cells, there is very high chance that a fraction of cell population remains unexposed to 340 nM of interfacially assembled nisin. To further support the findings, colony forming units (CFU) were quantified by taking the culture from stationary phase of treated bacterial growth. As shown in the growth kinetics, insignificant difference in viable cell numbers was observed for AgNP and nisin treated bacteria (Figure 3.34c-d). However, the AgNP-nisin conjugates had a significant effect on viable cell fraction. Compared to the untreated cells, viable cell fraction reduced to < 20 % for AgNP-nisin (1:1) conjugate treated culture; 82 and 87 % non-viable cells were found for *B. subtilis* and *E. coli*, respectively. Whereas, 85 and 170 nM interfacially assembled nisin to 2.8 nM AgNP interface reduced

the viable cell fraction by ~50 %, only (Figure 3.34c-d). Comparative analysis between antimicrobial propensity of the intact nisin (Figure A15, Apendix) and the nisin assembled at interface (Figure 3.34a) against *B. subtilis* indicated that the nisin antimicrobial propensity increased by 10 folds upon conjugation.

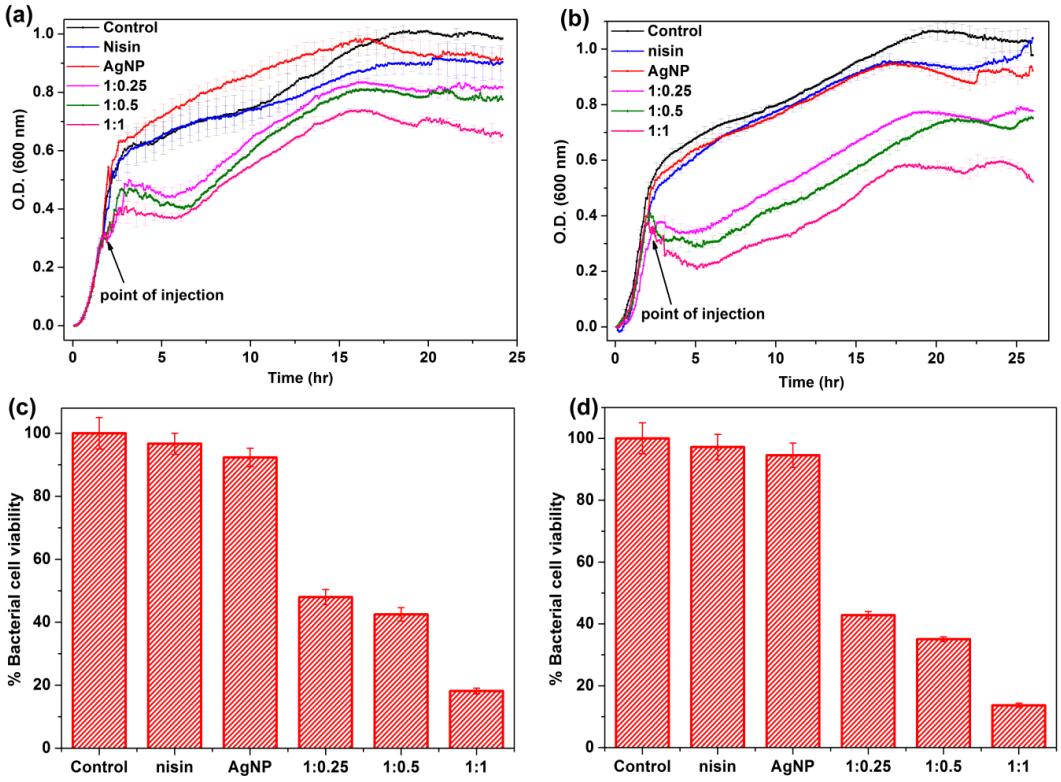

Figure 3.34. Growth kinetics of *B. subtilis* (a) and *E. coli* (b) in presence of AgNP, nisin, and different AgNP-nisin conjugates. Bacterial cell viability quantified from CFU study in the presence of AgNP, nisin, different AgNP-nisin conjugates for *B. subtilis* (c) and *E. coli* (d) respectively. Triplicate experiments were done for each reaction, and the error bar represents the standard error of mean.

Nisin is known to inhibit Gram-positive bacteria growth by interacting its N-terminal AB-lanthionine ring at nanomolar concentration with peptidoglycan precursor lipid molecule, i.e. lipid-II, which is involved in synthesis of the cell wall[276-277]. Nisin uses lipid-II as an efficient receptor to initiate the permeabilization process through plasma membrane, leaving behind pore in membrane resulting in collapse of the bacterial ion gradients[276-277]. Thus, nisin is more effective against the bacteria having higher fraction of lipid-II than the bacteria lacking the lipid-II fraction. However, presence of additional layer of lipopolysaccharide in Gram-negative bacteria makes nisin relatively ineffective[271, 278]. The growth kinetics and CFU data for the assesmbled nisin treated *E. coli* suggested that membrane-based resistance in Gram negative bacteria is eliminated upon assembly at

the NP interface. To further strengthen our findings, the growth kinetics of another Gram-negative bacterium, *Proteus vulgaris*, against different AgNP-nisin conjugates were observed (Figure A16, Appendix). Like *E. coli*, *P. vulgaris* is also insensitive to nisin, whereas the addition of AgNP-nisin conjugates delayed the growth of the bacteria by ~4 hrs. Additionally, it was also reported that upon repeated exposure of nisin to a certain Gram-positive bacteria, like *Staphylococcus aureus*, *Streptococcus bovis*, *Lactobacillus casei*, the bacteria become resistant to nisin, and the resistance is due to the expression of the nisin digesting enzyme, 'nisinase'[269-270]. To evaluate the effectiveness of AgNP-nisin conjugates against nisinase-based resistant bacteria, the growth kinetics of *S. aureus* against different AgNP-nisin conjugates were observed (Figure A17, Appendix). Interestingly, the conjugates had relatively very devastating effect on *S. aureus*, compared to *B. subtilis*. Thus, the data altogether indicated that the efficacy of nisin against membrane-based and nisinase-based resistant bacteria increases upon interfacial assembly of the peptide at AgNP interface.

3.5.3. Oxidative-stress mediated antimicrobial activity of AgNP-nisin conjugates

Photocatalytic nanoparticle interfaces, like AgNP, ZnONP, on interaction with the biomolecular surfaces enhances the generation of reactive oxygen species (ROS)[23, 167, 246]. Bacteria usually have system to neutralize certain threshold amount of ROS, however enhanced ROS production above the threshold causes oxidative stress in bacteria[23, 167]. The oxidative stress in bacterial cells results in the oxidation of biomolecules, like proteins, lipids. Thus, the ROS mediated irreversible changes at the loci of interaction is most likely to contribute in membrane dynamic change, one of the main factors that causes photocatalytic nanoparticle mediated bacterial cell death[279].

Here, the oxidative stress exerted by AgNP-nisin conjugates on bacterial cells were studied using the ROS specific dye, 2',7'-Dichlorodihydrofluorescein diacetate (DCFH-DA). Generally, ROS are highly reactive free radicals in the form of small molecules or ions like hydrogen peroxide (H_2O_2), peroxide free radicals (OH^o), or molecular oxygen ions (O_2^-)[246]. The quantum yield of dye at 523 nm increases by many folds in presence of ROS. Hence, the increasing fluorescence intensity at 523 nm with time for untreated cells indicated the production of ROS during the bacterial growth (Figure 3.35). AgNP induced the oxidative stress in both the bacteria by enhancing the production of ROS, though more

in *B. subtilis* than *E. coli* cell cultures. The observed differences in ROS production are mainly because of difference in interaction between bacteria and nanoparticle interface[167]. Whereas, nisin treatment was ineffective to enhance the ROS production in *E. coli* cells (Figure 3.35b), which supported the findings that 340 nM nisin does not have ROS mediated antimicrobial activity against the bacteria. Interestingly, the intact nisin enhanced the ROS production in *B. subtilis* culture, supporting the pervious findings that the antimicrobial peptide brings stress condition to Gram-positive bacteria (Figure 3.35a). However, 2-3 folds increase in fluorescence intensity for AgNP-nisin conjugates treated bacteria cell cultures were observed (Figure 3.35). Hence, the AgNP-nisin conjugates upon interaction with both the bacterial membrane exert the oxidative stress resulting in enhanced antimicrobial propensity.

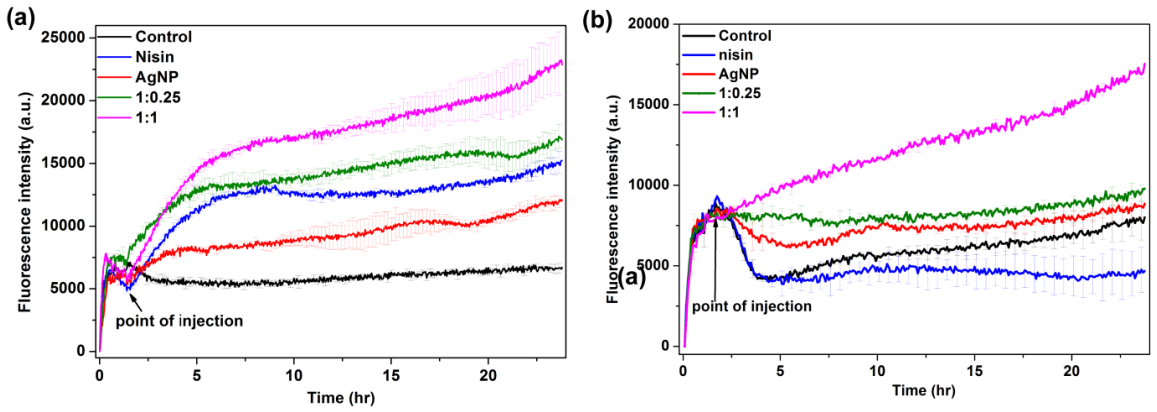

Figure 3.35: ROS detection in presence of AgNP, nisin, and AgNP-nisin conjugates (for 1:0.25 and 1:1 AgNP:nisin ratios) for *B. subtilis* (a) and *E. coli* (b), respectively. For each kinetic experiment, except control, respective additives were added at the mid-log phase (shown by arrow). The error bars represent standard error of mean calculated from three independent kinetics.

However, the interfacial and intracellular ROS generation depend primarily on the photocatalytic activity of AgNP, which arises due to localized surface plasmon resonance (SPR) property of silver nanoparticle[280-281]. Upon exposure to visible light or equivalent amount of interaction energy, AgNP absorbs the energy. As a result of energy absorption, the configuration of elemental AgNP changes into excited open shell configuration, i.e. d^9s^1 and/or d^9p^1 [280-281] The absorption results in generation of ROS in proximity to the loci of interaction[281]. However, enhanced intracellular ROS production will also have the contribution from enhanced metabolic rate of the bacteria, which is enhanced to counter the stress conditions upon insertion of AgNP-nisin conjugate onto/into the membrane.

3.5.4. Membrane destabilization by AgNP-nisin conjugates

The previous studies with photocatalytic metal nanoparticles, like ZnONP, have shown that the surface potential and accessible surface functional groups highly affect the bacterial membrane dynamics and the morphology[167]. The effect is mainly because of non-covalent interactions at the interface, resulting into enhanced level of ROS generation. The resultant ROS at the interface brings chemical or physical modifications in membrane, leading into the loss of cell viability[167]. Hence, because of the predominantly repulsive electrostatic interaction between the negative surface potential AgNP and bacterial membrane, 2.8 nM AgNP exert insignificant antimicrobial effect against both the bacteria. Whereas, upon reduction of the negative surface potential and functionalizing the interface with antimicrobial accessible functional groups (lanthionine rings/hinge region), the antimicrobial propensity enhanced by many folds.

For mechanistic details of AgNP-nisin conjugate antimicrobial effect on bacterial membrane, the LIVE/DEAD BacLight bacterial viability assay was done. The assay uses a mixture of cell permeable and impermeable nucleic acids binding dyes, Syto9 and propidium iodide (PI) dyes, respectively. Since the kit uses mixture of two dyes and PI has relatively higher affinity for nucleic acids than Syto9, PI thermodynamically intercalate strongly with nucleic acids than Syto9, in deformed cells[282]. As shown in figure 3.36, the untreated *B. subtilis* and *E. coli* cells showed all green fluorescing cells, inferring presence of 100% viable cells. However, a statistical analysis using Image J software[283] indicated 56 and 58% of non-viable cells for 1:0.25 ratio, whereas 91 and 93% non-viable cells for 1:1 ratio AgNP-nisin conjugate treated *B. subtilis* and *E. coli* cells, respectively (Figure 3.36 and Figure A18, Appendix). The statistical findings from the assay reflected the statistics observed from the CFU study. Additionally, the assay also indicated the ineffectiveness of 1.2 mg/mL nisin or AgNP against these two studied bacteria (Figure A18-A19, Appendix). Hence, the data indicated that the AgNP-nisin conjugate on interaction with the bacterial membrane are either disrupting the membrane or making pore in membrane with the lifetime long enough for PI dye to diffuse and intercalate with nucleic acids.

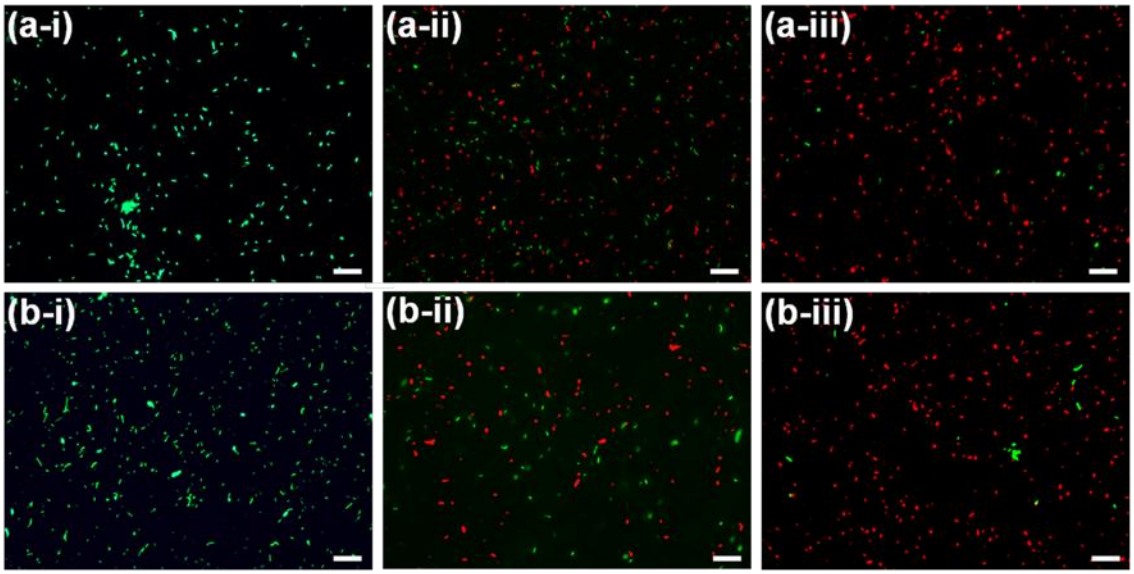

Figure 3.36: The LIVE/DEAD Baclight fluorescence microscopic images of (a-i) *B. subtilis*, (a-ii) *B. subtilis* treated with AgNP-nisin (1:0.25) conjugate, (a-iii) *B. subtilis* treated with AgNP-nisin (1:1) conjugates, and (b-i) *E. coli*, (b-ii) *E. coli* treated with AgNP-nisin (1:0.25) conjugate, (b-iii) *E. coli* treated with AgNP-nisin (1:1) conjugates, differentiating the viable cells (green) from non-viable cells (red). The scale bar represents 20 µm.

To further strengthen our findings from the BacLight assay, the AgNP-nisin conjugates treated bacterial cells were visualized using SEM. As shown in figure 3.37, the membrane of untreated *B. subtilis* and *E. coli* showed intact bacterial membrane morphology. On the other hand, the interfacially assembled nisin treated bacterial cells showed deformed cell membrane, indicating compromised membrane. The findings from the BacLight assay and SEM analysis suggested that the assembled nisin has relatively adverse effects on bacterial cell membrane.

Moreover, the permeabilization of AgNP-nisin conjugates was further confirmed by confocal microscopy (Figure 3.38). The fluorescein labelled AgNP-nisin conjugates was added to *B. subtilis* and *E. coli* cultures. Upon incubation, the cells were washed to remove residual fluorescence, and imaged using confocal microscope. In images, green fluorescence (fluorescien tagged AgNP-nisin conjugate) was co-localised with the bacterial cells, which confirmed internalization of AgNP-nisin conjugates. Since size of the conjugate found ~10 nm, the permeabilization process will cause cavity of respective size in membrane leading into membrane rupture, as observed in figure 3.37c-d. Hence, the assembled nisin primarily changes membrane dynamics upon interactions with bacterial membrane.

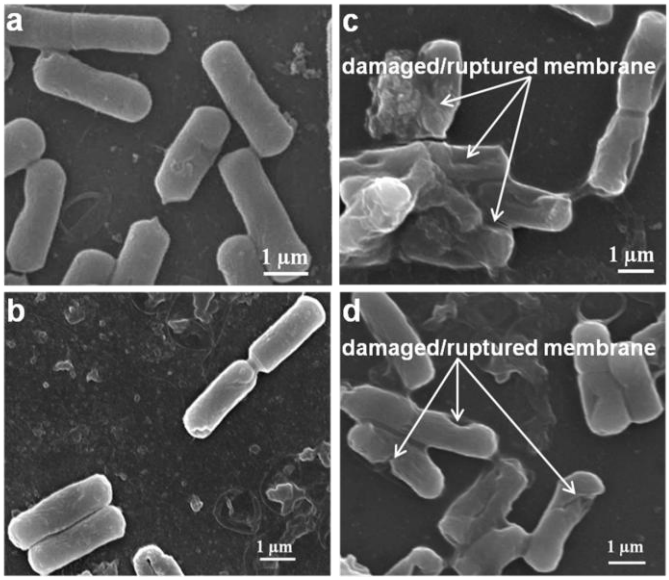

Figure 3.37: Representative SEM micrographs of (a) *B. subtilis* and (b) *E. coli* cells. The micrographs of AgNP-nisin conjugate (1:1) treated *B. subtilis* (c) and *E. coli* (d) showing the damaged/ruptured cell membrane.

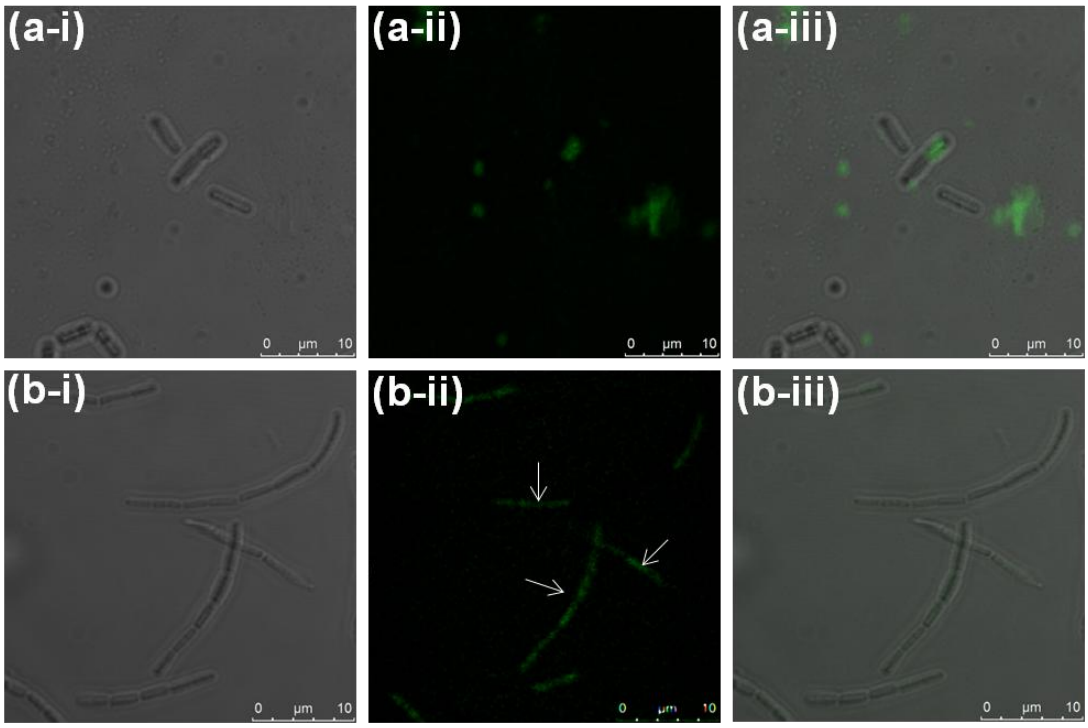

Figure .3.38: Panel a and b represent the confocal microscopy image of *B. subtilis* and *E. coli*, respectively, treated with fluorescein labelled AgNP-nisin conjugates. (a-i & b-i) phase contrast images of treated bacteria, (a-ii & b-ii) green fluorescence images of the treated bacteria, and (a-iii & b-iii) merge images of phase contrast and green fluorescence images.

The cavity or pore formed upon internalization of molecule is generally replenished by cellular lipid homeostasis[284]. To replenish the cavity, formed upon

permeabilization of the conjugate, lipid homeostasis would be taking significant time leading into ions leakage above a critical limit, resulting into the rupture of membrane. The above rationalization came from the findings that the membrane impermeable PI dye stains the cells treated with the conjugates[279, 285], whereas unable to stain cells which were either intact or treated with nisin or AgNP individually. Hence, insertion of the AgNP-nisin conjugates in cell creates cavity in membrane with lifetime more than the critical period, consequently leading into rupture of membrane and loss of cell viability. Thus, the BacLight assay, confocal microscopy and SEM data suggested that permeabilization of the assembled nisin through the Gram-positive and Gram-negative bacterial membrane leads into membrane rupture.

3.5.5. Proposed mechanism of the assembled nisin antimicrobial activity

Silver nanoparticle on interaction with bacterial membrane triggers a series of thermodynamics and physico-chemical reactions, resulting in alteration of membrane surface tension, ROS mediated chemical modification of accessible functional groups of the membrane etc[93]. Hence, interactions between the assembled nisin and bacterial membrane play an important role in determining the antimicrobial propensity of the conjugates, compared to individual entity. As an individual, since AgNP has negative surface potential, the electrostatic repulsive interaction between AgNP and anionic bacterial membrane are unfavorable to bring/initiate the changes at submicromolar concentrations. Whereas, AgNP at higher concentrations showed antimicrobial activity against bacteria due to interactions with the positive potential 'building elements' present at the bacterial membrane[30]. On the other hand, nisin causes the antimicrobial effects either through the lipid-II dependent or independent or both pathways[286]. In lipid-II dependent pathway, the first two N-terminus lanthionine rings of nisin bind at nanomolar concentrations with lipid-II fractions of bacterial membrane, and restricts the cell wall homeostasis[284]. Hence, for the bacteria with higher lipid-II content, nisin has antimicrobial effect at nanomolar concentrations. Besides the restrictions in cell wall homeostasis, the binding and subsequent insertion of nisin in membrane triggers the falling-off of the lipid molecules from the loci of interfacial interaction. Thereafter, the last two lanthionine rings along with the hinge region play an important role in pentamerization and permeabilization of the peptide into the cell[286-287]. The reduced lipid density or enhanced lipid fluidity upon significant loss of the lipid molecules from cell membrane assist the peptide oligomerization to form pore/transient pore in membrane, leading into leakage of

the vital bacterial moieties causing the cell non-viability[288]. In the lipid-II independent pathway, micromolar concentrations of cationic nisin interact non-specifically to anionic phospholipid fractions of the membrane; hence the anionic lipid fraction must be in the range of 50-60 %[286]. Unlike the lipid-II dependent pathway, the cationic C-terminus of nisin interacts with anionic phospholipid head groups of membrane. The interaction initiates the permeabilization of the peptide through membrane, leading into short-lived pores causing the antimicrobial activity[286, 289]. Although, the C-terminus residues (hinge region and last two lanthionine rings) are in interaction with AgNP core in conjugate, which are not as strong as the N-terminus residues interaction with the core (Table A2, Appendix). Hence upon coming in proximity of bacterial membrane, from cationic N- and C-terminus, C-terminus must preferably be interacting with the membrane in order to execute the antimicrobial activity, as shown by the interfacially assembled nisin.

In our study, the data altogether indicated that the conjugated nisin, if not following both the pathways, is predominantly following the lipid-II independent pathway. The lipid-II dependent pathway is not possible, since the simulation data indicated that in conjugate the N-terminus residues have relatively stronger interaction with the core than the C-terminus residues (Figure 3.33c-d and Figure A14, Appendix). Moreover, the studied bacteria lack the lipid-II fraction in its membrane, needed for the lipid-II dependent pathway[286]. Hence, the nanoparticle core in the conjugate will sterically hinder the peptide first two lanthionine rings interaction with the membrane fraction. Additionally, relatively accessible C-terminus residues of the conjugate are predominantly contributing for the non-covalent interaction with anionic membrane fraction of the bacteria, which originally initiate the peptide insertion (Stage 1, Figure 3.39). The C-terminus residues are known to interact with bacterial membrane for lipid-II independent insertion, hence, the conjugates possibly onset the antimicrobial action in lipid-II independent pathway. Additionally, as the stoichiometry of conjugation suggests, and if the homogeneous coating is considered, each NP is having ~ 100 molecules of nisin. However, the effective number of nisin interacting with the membrane will be far less than 100 molecules, considering the molecular crowding at the interface and the relative orientation of the nisin in conjugate compared to membrane interface. The effective numbers will definitely be higher than 5 molecules, since for nisin internalization 5 nisin molecules insert and pentamerise to initiate the permeabilization process (Stage 2, Figure 3.39). In case of the conjugate, considering effective numbers of the interacting nisin

molecules, a single conjugate molecule is sufficient to initiate the pentamerization and permeabilization process.

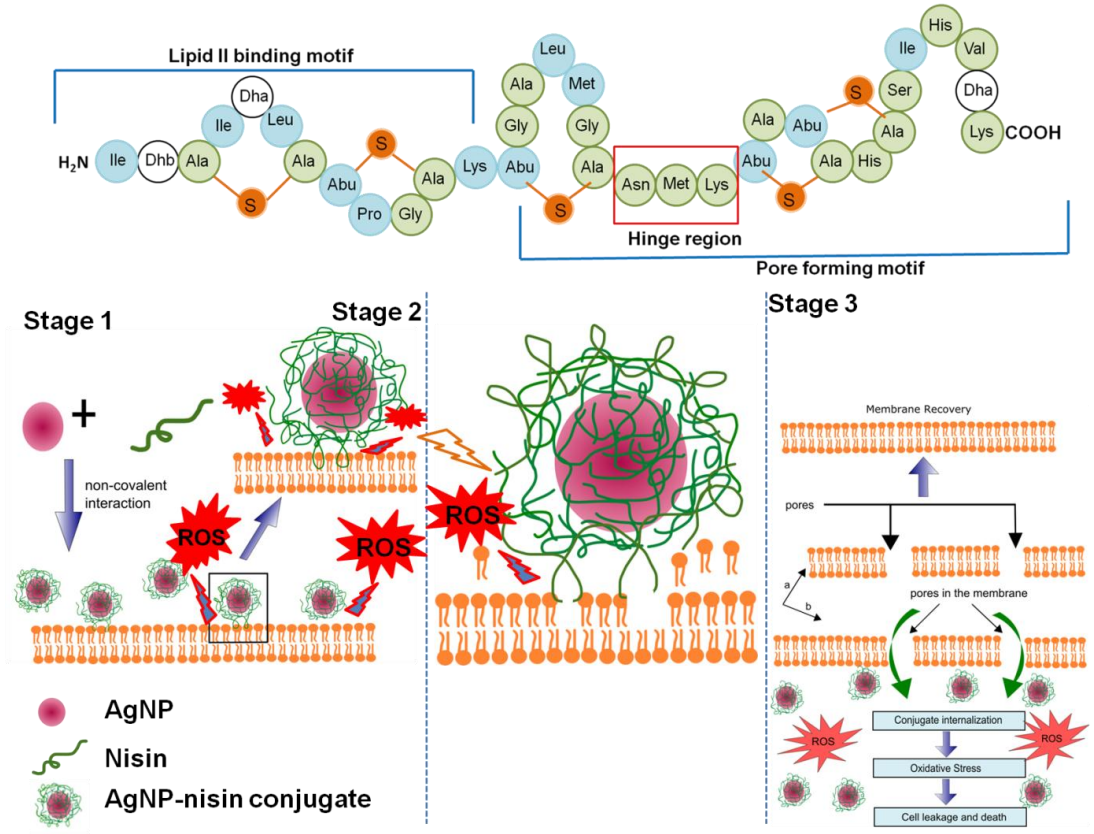

Figure 3.39: Schematic diagram showing detail mechanism of AgNP-nisin conjugates against bacteria. Stage 1: the non-covalent interaction between AgNP-nisin conjugate and bacterial membrane will bring the conjugate onto the membrane. Stage 2: the interaction results in ROS generation at the interface, and subsequently help in insertion of C-terminus lanthionine rings and hinge region into membrane. The insertion results in falling-off lipid molecules from the respective loci to maintain the surface tension. Stage 3: because of more than one peptide per conjugate is inserting at the loci of insertion, the insertion will immediately followed by internalization of the conjugate. The internalization of the conjugate results in membrane pore formation, resulting into cell death (a- in presence of sub-micromolar intact nisin, b-in presence of sub-micromolar the interfacially assembled nisin).

The physico-chemical property of AgNP assist further in permeabilization of the conjugate through change in ROS-mediated surface fluidity[167]. The non-covalent interaction arising from different functional groups present over the conjugate interface and bacterial membrane cooperatively generates sufficient amount of energy to catalyse the conjugate permeabilization process (Stage 2, Figure 3.39)[290]. Different physico-chemical property of the membrane interface, like (i) stretching and elasticity of membrane, (ii) thermal fluctuation of cell membrane, and (iii) hydrophobic exclusion of

polar surfaces by membrane, will resist the conjugate against the permeabilization. The resistive force could have split the conjugate into nanoparticle and peptide, either during or upon the permeabilization[93, 101]. However, confocal microscopy data (Figure 3.38) indicated that the conjugate interaction with membrane interface generates sufficient amount of energy to help the permeabilization without splitting the conjugate. The increase in surface tention with time at the loci of adhesion of AgNP-nisin conjugate and membrane causes the conjugate invaginate, leaving behind the pore/cavity of respective size (Stage 3, Figure 3.39). The cavity(s) results in rapid efflux of the vital cellular moieties leading to loss of cell viability[291]. However, sub-micromolar nisin interacts with bacteria, but it does not exert potential antimicrobial impact on membrane. In this case, the membrane must have instantly recovered the original texture from the distorted form caused by nisin only treatment (Stage 3, path a, Figure 3.39), hence insignificant antimicrobial activity observed. Upon internalization of conjugate, conjugate kill the bacteria by targeting and damaging various intracellular biomolecules in ROS mediated pathway, in addition to the nisin mediated cell death (Stage 3, path b, Figure 3.39)[260]. Additionally, as discussed in enzyme-based resistant bacteria like *S. aureus*, *S. bovis*, *L. casei*, nisinase clears the peptide and restores the lipid homeostasis[284]. The *S. aureus* result (Figure A17, Appendix) revealed that AgNP-nisin conjugates provide resistance against the nisinase activity, either by ROS-mediated irreversible modification of nisinase or by sterically hindering the enzyme binding to cleavage site. The data, altogether, indicated that the assembly not only enhances the efficiency of nisin, but also broadens the action of nisin against a different spectrum of microbes at sub-micromolar concentrations. Hence, the interfacial assembly of nisin at AgNP interface enhances the antimicrobial efficacy of the nisin.

Findings from the study conclude that the non-covalent interactions play important role for interfacial assembly of nisin at AgNP interface, forming stable AgNP-nisin conjugates. The interfacial assembly is confirmed by the change in nanoparticle specific SPR signature, IR signatures for metal and peptide bonds, ellipticity of peptide bonds, and surface potential neutralization. The MD simulation study further supported the interfacial assembly, and indicated the interaction pattern at the interface with time. The interaction energy and interfacial ROS generation play important role in destabilizing the membrane to favour the conjugate permeabilization process. The cavity formed in membrane on the conjugate permeabilization and the intracellular ROS generation causes the cell non-

viability. Taking altogether, the efficacy of nisin can be enhanced by interfacial assembly of nisin onto AgNP interface. Hence, the approach can be adopted as a potential antimicrobial formulation against broad spectrum of bacteria.

3.6. Effect of globular protein interfacial assembly on conformational dynamics of the protein

The three dimensional structure of protein, which is precisely regulated by a number of non-covalent interactions such as electrostatic interaction, van der Waals interaction, hydrogen bonds, hydrophilic/hydrophobic effects etc[74], controls most of the functions of protein. In addition, the conformational changes of protein are associated with various properties such as function, transportation, assembly, aggregation propensity, cytotoxicity etc[74]. Hence, study of thermodynamics and kinetics of protein folding/unfolding has received enormous attention in past decades for manifestation of various biological applications ranging from genetic information to molecular diagnostics[74, 292]. It is important to note that, the interaction network of a protein can be easily misarranged/broken by changing slightly the physico-chemical environment, which results into partially unfolded or completely unfolded protein conformation. Sometimes the proteostatis network of the cell fails to check the perturbation of the interaction network resulting in the exposure of hydrophobic core of the protein, which drives the conformation of protein into self assembly of monomers leading to formation of amyloid fibrils[78]. These amyloid fibrils are unique type of protein aggregates with cross-β structure, generally associated with various degenerative diseases like Alzheimer's disease, Huntington's disease, Parkinson's disease, amyloid polyneuropathy, diabetes type-2, Spongiform encephalopathy etc.[74, 78, 293].

Inside the biological milieu, the nanoparticles come in myriad shape and size and interact with different biomolecules. Similarly, in biological milieu, various nanoparticles bind with proteins and form a complex known as protein corona[294]. However, various specific and non specific interactions at nanoparticle protein interfaces are responsible for various biological functions of protein[74]. The preferred interaction for a successful assembly of protein and nanoparticle are covalent or electrostatic interactions for successful application of protein nanoparticle bioconjugate in biosensing, imaging etc[74, 295]. It is reported that when protein interacts with planner surfaces, significant changes to secondary structure happen, however high curvature of nanoparticles help the protein to

retain its native structure[53]. In addition, the presence of various interactions like electrostatic and hydrophobic interactions at the interface of nanoparticle and protein help in more or less conformational changes of protein, which also affect the function of proteins.

Hence, this objective intends to explore the changes in conformational dynamics of a globular protein upon interaction with photocatalytic nanopaticle such as ZnONP, at two different pH (7.4 and 9), by taking lysozyme as model globular protein. Different biophysical studies demonstrated that the assembly onto ZnONP interface led into conformational rearrangement that hinders the amyloidogenic propensity of lysozyme in studied conditions.

3.6.1. Interfacial assesmbly of lysozyme at ZnONP interface

3.6.1.1. CD spectroscopic measurement

The change in secondary structure of lysozyme at both pH upon interaction with ZnONP was explored using Far-UV-CD analysis. As reported, the CD bands at 208 and 222 nm are characteristic peaks for α-helical structure of proteins[296]. The peptide bonds present in α-helix secondary structure arrangement has $\pi \rightarrow \pi^*$ transition at 208 and 222 nm, which is represented by negative ellipticity by CD spectropolarimeter. As shown in figure 3.40, the peak intensity at 208 nm for both the pH became more negative with addition of different concentration of ZnONPs, indicating the increment of helical structure of lysozyme upon addition of ZnONP. However, the increment is independent of ZnONP concentration, no further change in regular structure was observed on increasing the ZnONP concentration. Additionally, the increment in helical content as compared to control happened at the expense of random coil region of the lysozyme, as indicated by deconvolution of the spectra using CDNN software[297] (Figure A21, Appendix). The spectra also indicated that lysozyme is having more helical content at pH 7.4 than pH 9. The structural changes of lysozyme at secondary level were further explored using ATR-FTIR spectroscope, which demonstrated insignificant changes of lysozyme upon ZnONP interaction (Figure A22, Appendix). Hence, the data indicated that the presence of ZnONP helps the lysozyme to attain relatively more regular conformation than control.

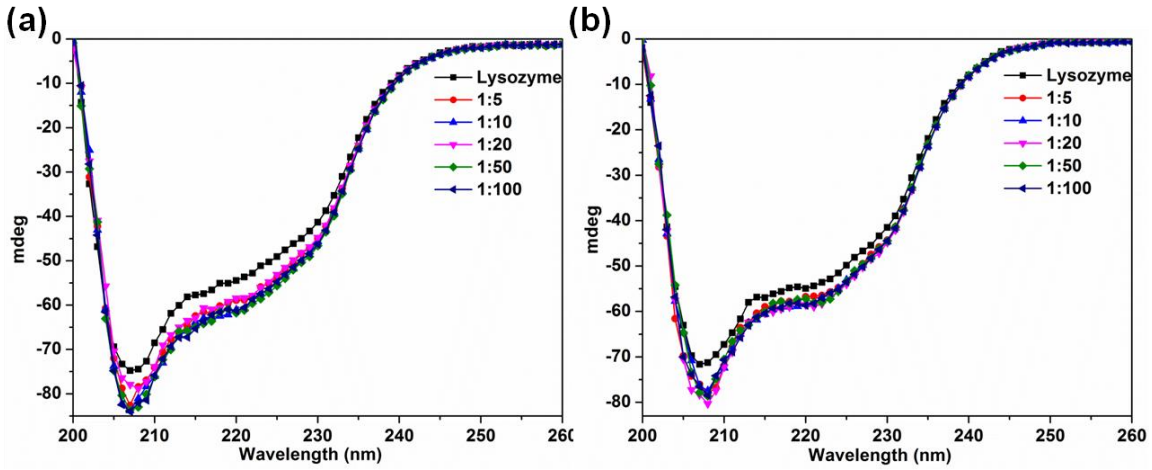

Figure 3.40. Far-UV CD spectra of 10 μM lysozyme at pH 7.4 (a) and pH 9 (b) in absence and presence of different ZnONP concentrations.

3.6.1.2. Effect of ZnONP on thermal denaturation of lysozyme

The stability of lysozyme against thermal denaturation upon interaction with ZnONP was explored by observing the thermal denaturation curve of lysozyme at two pH conditions with a temperature range of 30 to 90 ^{o}C. Figure 3.41 showed the thermal denaturation curve of lysozyme in absence and presence of ZnONP at pH 7.4 (figure 3.41a) and pH 9 (figure 3.41b). As shown in figure, the melting temperature of lysozyme was observed at 71 ^{o}C for pH 7.4, which remain unaffected with increasing fractions of ZnONP. However, at pH 9, the lysozyme melting temperature reduced to 67 ^{o}C. Interestingly, addition of varying concentrations of ZnONP to lysozyme solution at pH 9 shifted the melting temperature to 70 ^{o}C, demonstrating the stabilization of lysozyme against thermal denaturation upon interaction with ZnONP. Additionally, the comparative analysis indicated that compared to control, increasing concentrations of ZnONP reduces the change in absorbance with temperature. The decrease in absorbance with increase in ZnONP concentration is only possible when the responsible residues for absorbance at 280 nm is directly involved in interaction with the ZnONP interface, hence hindered the residues exposure to 280 nm wavelength. Hence, it can be concluded that the interaction of lysozyme with ZnONP interface has more stabilizing effect at pH 9 than pH 7.4, where the protein remain largely unperturbed with increasing concentrations of ZnONP.

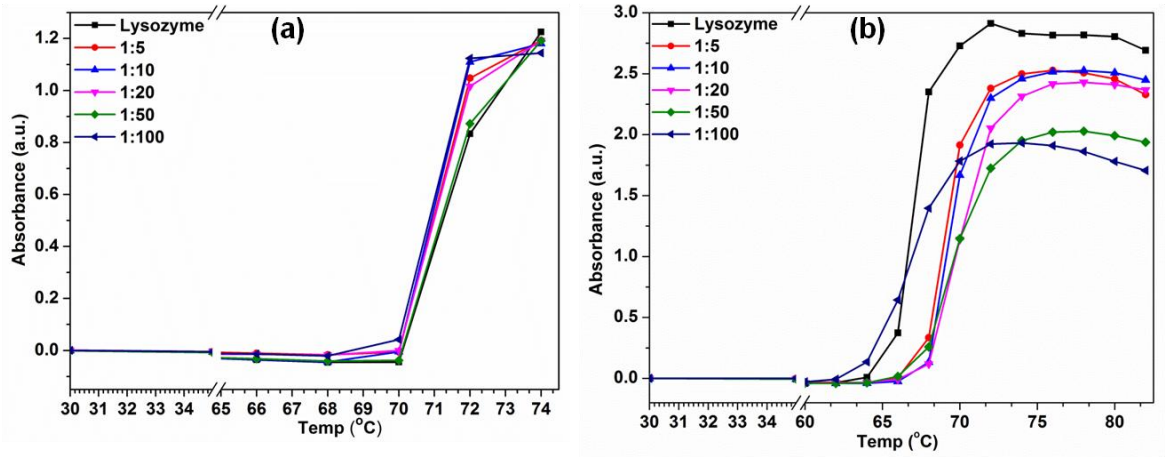

Figure 3.41. Thermal denaturation of lysozyme in absence and presence of increasing ZnONP concentrations at pH 7.4 (a) and pH 9 (b).

3.6.1.3. Intrinsic fluorescence based conformational dynamics

Fluorescence spectroscopic measurements are gerenally carried out to analyze the conformational dynamics of protein at tertiary level. In this context, tryptophan acts as an intrinsic fluoroprobe, which is widely used as a probe to monitor the conformational changes of globular proteins, and to gain information regarding local chemical environments and dynamics. The fluorescence quantum yield is largely dependent on changes of tryptophan chemical environment. Hence, any change in the environment due to folding or unfolding may lead to the change in the quantum yield. In this study, tryptophan fluorescence measurements were carried out to investigate the conformational dynamics of lysozyme on interaction with ZnONP at different studied pH conditions. Figure 3.42 showed the tryptophan emission spectrum of lysozyme at pH 7.4 and pH 9. It is reported that, the emission spectrum of tryptophan is very sensitive to polarity of solvent, which emits maximum at 350 nm upon excitation at 280 nm[298]. However, sometimes the blue shift of emission maxima is generally observed when tryptophan goes from slightly polar to non-polar environment, like hydrophobic core[298]. It is very interesting to observe that, at pH 7.4, the emission maximum of tryptophan was observed at 342 nm, inferring that the tryptophan residue is buried inside the hydrophobic environment (Figure 3.42a). However, upon interaction with ZnONP, it was observed that only 10% fluorescence intensity of lysozyme decresed with red shift of emission maximum (λmax) 346 nm, i.e. by 4 nm only, as the protein encounters high ZnONP concentration. The observation indicated that lysozyme interaction with ZnONP interface insignificantly exposes the tryptophan to polar environment at pH 7.4, which may be ZnONP interface also. Additionally, at pH 9, the emission maximum blue shifted from

350 nm to 342 nm, i.e. by 8 nm, on interaction with ZnONP interface (Figure 3.42c). Unlike pH 7.4, at pH 9 the tryptophan residues are relatively in polar environment, which in presence of ZnONP interface buried into relatively non-polar environment resulting into blue shift of the emission maxima. Interestingly, as shown in figure 3.42, besides a red shift in emission maxima for control (lysozyme only) at pH 9 compared to pH 7.4, a 32% reduction in tryptophan quantum yield for control at pH 9.0 is also observed. The comparative analysis indicated that the lysozyme is in partially unfolded state at pH 9, compared to pH 7.4. Similarly, the change in tryptophan quantum yield is more drastic at pH 9 than pH 7.4. The tryptophan fluorescence study in absence and presence of varying concentrations of ZnONP interface indicate that the interface has relatively more significant effect on unfolded protein than a folded protein.

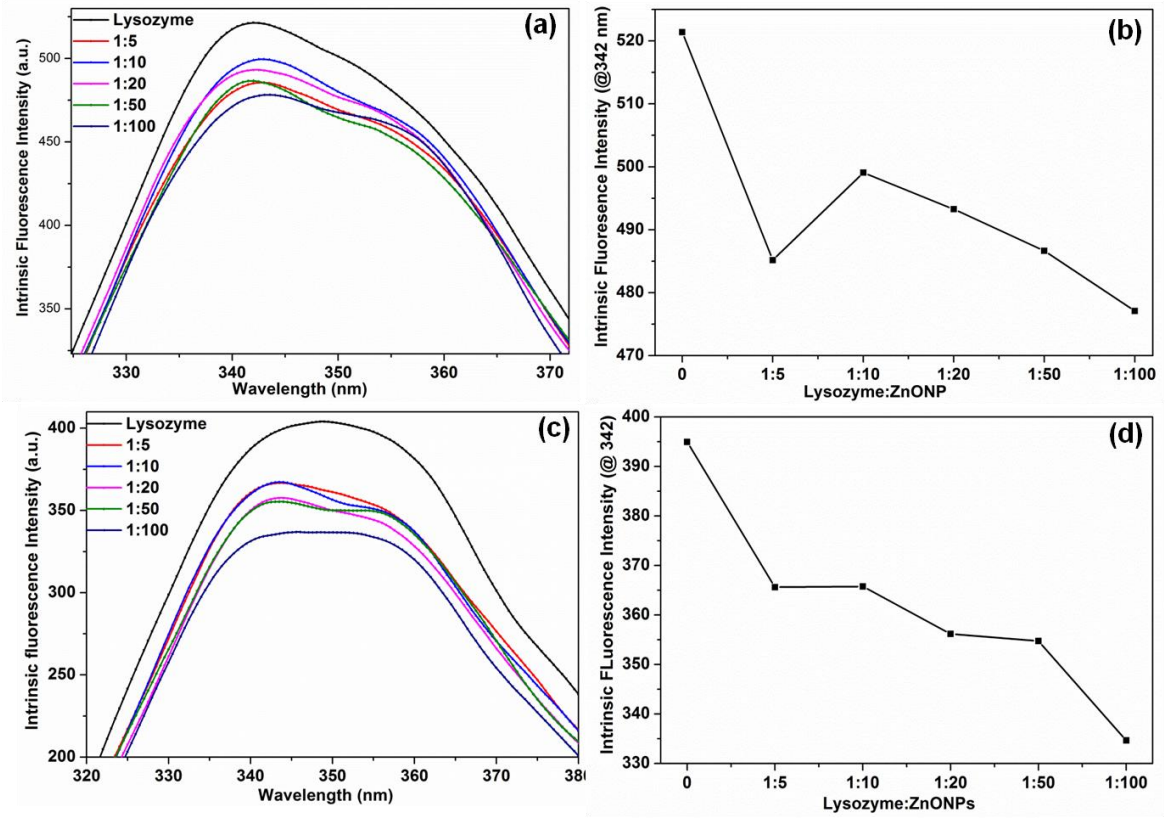

Figure 3.42. **(**a) Lysozyme fluorescence emission spectrum at pH7.4 upon excitation at 280 nm, and (b) the change in emission spectra of lysozyme at various ZnONP concentrations at pH 7.4. (c) Tryptophan fluorescence emission spectrum in lysozyme excited at pH 9, and (d) changes of emission spectra of lysozyme at various ZnONP concentrations.

3.6.1.4. ANS binding and Anisotropy Studies

8-Anilinonaphthalene-1-sulfonic acid (ANS) has affinity for hydrophobic patches present on protein surfaces. On binding to hydrophobic patches, ANS show relatively

higher quantum yield and a blue shift in the emission maxima; higher the change is, stronger will be the binding[296]. The solvent exposure of the hydrophobic surface in lysozyme at both pH, in absence and presence of ZnONP was studied by ANS-binding experiments. Figure 3.43 shows the change in ANS fluorescence emission at 520 nm upon binding lysozyme and lysozyme-ZnONP complexes at both pH. It was observed that there was very little change in the fluorescence intensity for different lysozyme-ZnONP conjugates at pH 7.4, however at pH 9.0, lysozyme showed an increase in intensity with increase concentration ZnONP. This demonstrated that lysozyme interaction with ZnONP interface at pH 9.0 enhances the ANS accessible hydrophobic patches in lysozyme.

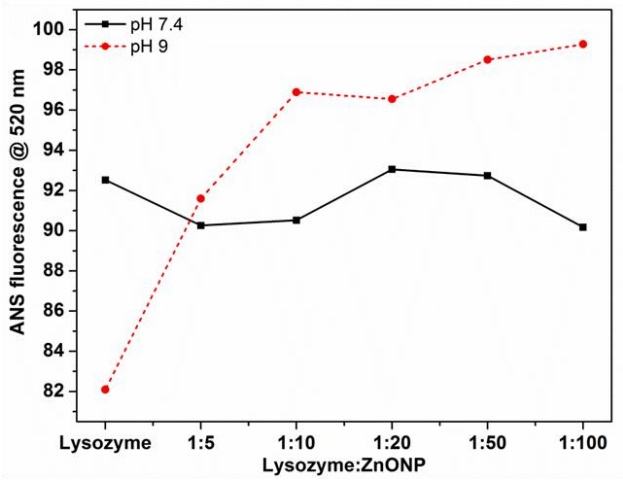

Figure 3.43. Fluorescence emission spectra of ANS binding with lysozyme and lysozyme-ZnONP conjugates at (a) pH 7.4 and (b) pH 9.0. The solution was excited at 350 nm.

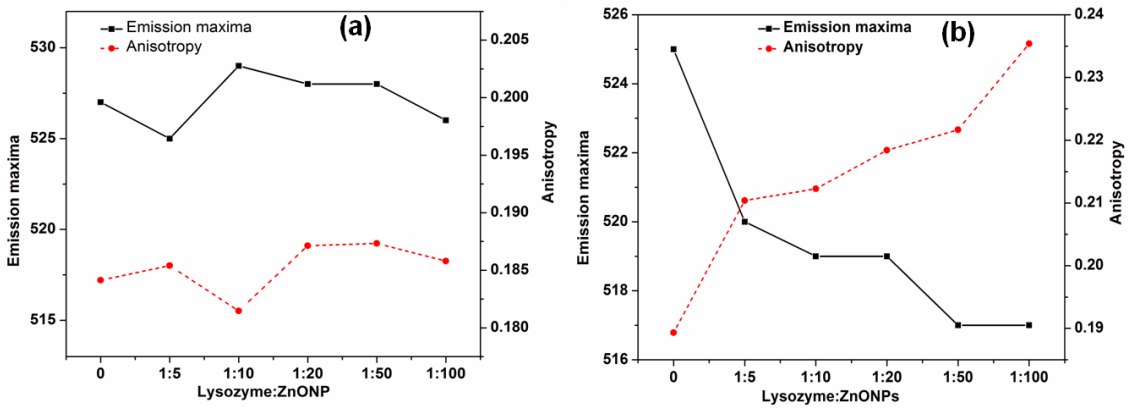

Figure 3.44. Anisotropy and emission maxima of ANS in presence of lysozyme and lysozyme-ZnONP conjugates at (a) pH 7.4 (b) 9.0. The protein was excited at 350 nm.

Anisotropy measurements reveal the average angular displacement of the fluorophore that occurs between absorption and subsequent emission of a photon, which indicates the rigidity of the fluorophore environment. ANS anisotropy at pH 7.4 and pH 9,

when bound to lysozyme and lysozyme-ZnONP conjugates, was measured (Figure 3.44). There was negligible change in the anisotropy at pH 7.4, whereas at pH 9 there was significant increase in ANS anisotropy when bound to the conjugates. Additionally, the increase in ANS anisotropy at pH 9 found to be dependent of ZnONP interface concentration in conjugates (Figure 3.44b).

Quenching of tryptophan fluorescence by acrylamide was carried out for pH 7.4 and 9 in absence and presence of ZnONPs. Acrylamide is an appropriate choice as a quenching agent because it is a hydrophobic molecule. The extent of quenching by acrylamide can be estimated by Ksv and Kq, calculated using the Stern–Volmer equation (Figure 3.45).

$$Fo / F = 1 + K_{SV}[Q] = 1 + k_q\tau_0[Q] \quad (9)$$

where Fo denotes the steady–state fluorescence intensity of lysozyme, F is the steady–state fluorescence intensity of lysozyme in the presence of varying concentrations of acrylamide, K_{SV} is the Stern–Volmer quenching constant, [Q] is the concentration of quencher, kq is the quenching rate constant, and τ_0 is the average fluorescence lifetime of molecule without quencher, which is equal to 5.78 $\times 10^{-9}$ s for bio-macromolecules.

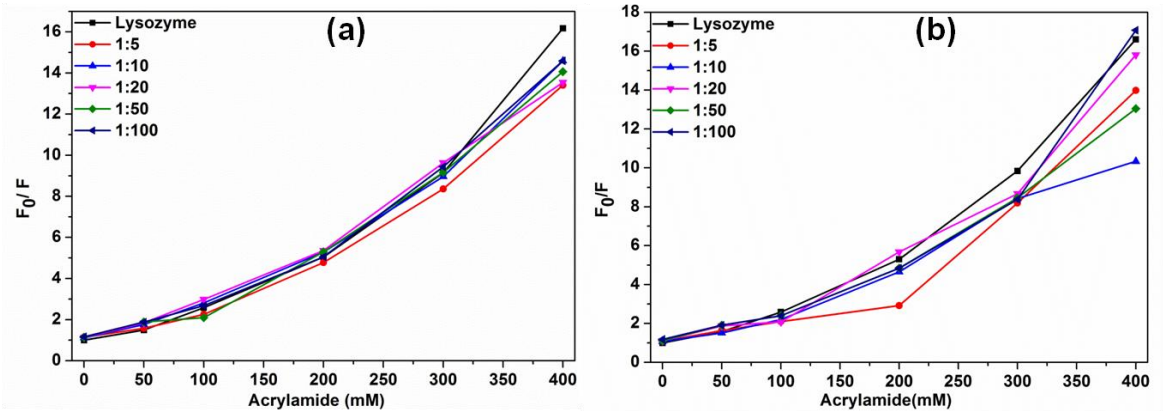

Figure 3.45. The Stern–Volmer Plot of lysozyme fluorescence quenching using increasing concentrations of acrylamide in absence and presence of ZnONPs at, (a) pH 7.4 and (b) pH 9.

As shown in figure 3.45, the Stern-Volmer plots mostly deviated from linearity towards the y-axis at very high acrylamide concentrations, > 200 mM, which indicated the involvement of both static and dynamic quenching. In the present work, we provide a semi empirical measure of the magnitude of the quenching in this system and investigated the quenching in terms of K_{SV} and kq values at low quencher concentrations (< 200 mM). The good linear fitting with R^2>.99 implied the suitability of the Stern-Volmer model below

the quencher concentration, to deduce the binding mechanism between acrylamide and lysozyme. The quenching parameters obtained by analysis of Stern–Volmer plots for both pH conditions are presented in Table.3.2.

Table 3.2: Acrylamide quenching parameters against lysozyme and lysozyme-ZnONP conjugates at pH 7.4 and pH 9.

	pH7.4		**pH9.0**	
	K_{SV} (M^{-1})	**k_q ($M^{-1}s^{-1}$)**	**K_{SV} (M^{-1})**	**k_q ($M^{-1}s^{-1}$)**
Lysozyme	15.78	2.73 x 10^9	15.83	2.73 x10^9
1:5	16.1	1.78 x 10^9	10.18	1.76 x 10^9
1:10	17	2.94 x 10^9	11.23	1.94 x 10^9
1:20	18.5	3.2 x 10^9	11.87	2.00 x 10^9
1:50	19	3.4 x 10^9	12.83	2.22 x10^9
1:100	15.15	2.62 x 10^9	12.17	2.11 x10^9

As shown in table 3.2, quenching rate constant, kq, for acrylamide quenching against lysozyme and lysozyme-ZnONP conjugates are ten folds less than the maximum scatter collision quenching rate constant generally observed for any quencher against biopolymer (2.0×10^{10} $M^{-1}s^{-1}$). Thus, the acrylamide dependent quenching is predominantly dynamic quenching below 200 mM of acrylamide concentration. However, the static terms contributed significantly to quenching only at higher concentration of acrylamide. Additionally, the relative quenching constant, K_{sv}, values of lysozyme and lysozyme-ZnONP conjugates in pH 7.4 and pH 9 indicated that the tryptophan quenching by acrylamide at lower concentration is relatively restricted at pH 7.4 than pH 9. Within the pH 7.4, the quenching constant is increasing with increase in ZnONP interface, which indicated that in pH 7.4 the interface sterially hinders the tryptophan dynamic quenching by acrylamide. Thus, the quenching data further supported the CD, tryptophan fluorescence, and ANS fluorescence data, indicating that lysozyme interaction with ZnONP interface has significantly postive impact on lysozyme conformation in pH 7.4 than pH9.

3.6.2. Antiamyloidosis propensity of ZnONP interface

Lysozyme at pH 9 in presence of 100 μM SDS is known to form amyloid fibrils. At pH 9, partially unfolded lysozyme in presence of SDS attains an amyloidogenic conformation, which with time attains a mature amyloid fibril structure[299]. In order to check the effect of ZnONP interface on lysozyme amyloidois in presence of SDS thioflavin T (ThT) binding assay was performed. As reported, ThT is an amyloid specific dye, its quantum yield at

482 nm increases many fold in presence of a fibril[300]. Interesting, at pH 7.4, no significant increase in quantum yield at 482 nm was observed with time for either lysozyme or lysozyme-ZnONP conjugate in presence of 100 μM SDS. Figure 3.46 showed the ThT fluorescence spectra of lysozyme at pH 9 in the absence and presence of different concentrations of ZnONP interface. However, the rise in the fluoroscenec intensity at pH 9 was studied at different time intervals, and the characteristic aggregation curve showed a distinct growth phase along with a saturation phase, indicating the formation of lysozyme amyloid fibrils at pH 9 in presence of SDS. The effect of ZnONP on the lysozyme amyloidosis was studied by taking different ratios of lysozyme and ZnONP interface. Interestingly, a gradual decrease in ThT quantum yield at 482 nm is observed with increasing concentration of ZnONP interface. The observation indicated that the presence of ZnONP interface hinders the conformational transition to amyloidogenic conformation on addition of 100 μM SDS, at pH 9.

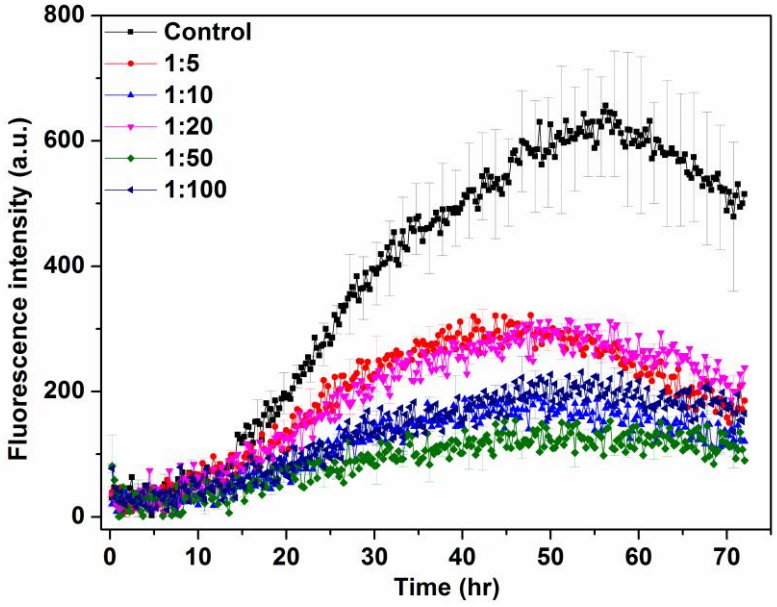

Figure 3.46. Thioflavin T binding assay showing the suppression of amyloidosis in presence of increasing ZnONP interface at pH 9.

Far-UV-CD spectroscopic analysis is one of the important techniques to analyze the conformational changes of protein at secondary level[299]. In case of amyloid fibrils, the protein known to show conformational dynamics to a predominantly β-sheet structures[299]. As shown in figure 3.47, after addition of SDS to the nanoparticle-protein conjugates at pH 7.4, no subtaintial increase in β-sheet was observed infering that at physiological pH the studied concentration of SDS unabled to induce lysozyme amyloid. However, the analysis at pH 9 provided us important findings, where lysozyme amyloid fibrils are

formed upon addition of SDS. The deconvolution of CD spectra using CDNN software showed a decrease in α-helix fraction and increase in the β-sheet fraction, further confirming the formation of amyloids as observed by ThT binding assay (Figure A , appendix). However, it was observed that with increase in ZnONP interface, β-sheet fraction decresed significantly, at pH 9.

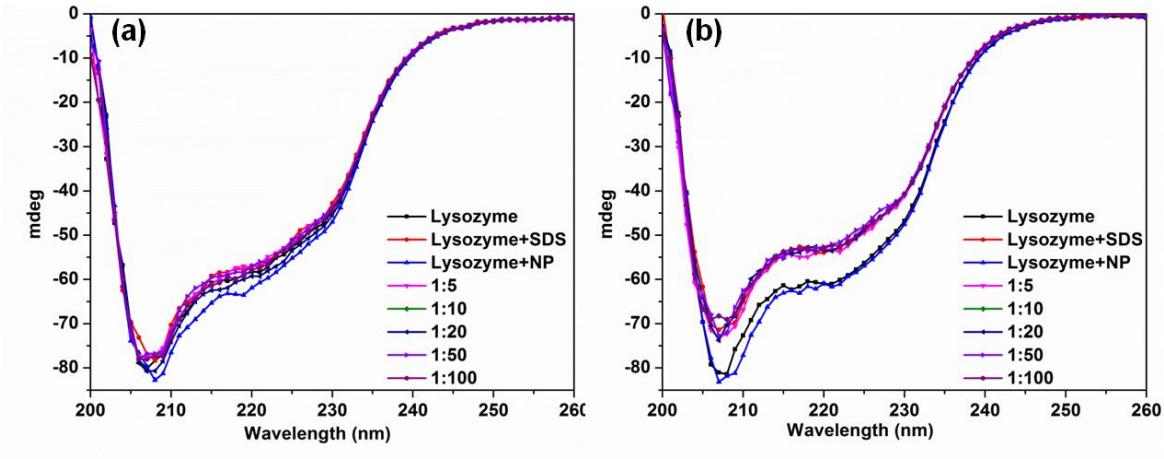

Figure 3.47. Far-UV CD spectra of 10 μM lysozyme at pH 7.4 (a) and pH 9 (b), in absence and presence of different ZnONP interface concentrations and 100 μM SDS.

The findings from CD-spectroscopic analysis were further confirmed using ATR-FTIR spectroscope. As shown in figure A24 (Appendix), insignificant variation in secondary structure of lysozyme and lysozyme interfacially assembled on ZnONP at pH 7 was observed, which was also in accordance with CD-spectroscopic analysis. Hence, the data indicated that 100 mM SDS has insignificant effect on the conformation of lysozyme at pH 7 in presence of SDS. However, as shown in figure, significant structural changes were observed at pH 9 in presence of SDS, decrease in intensity of absorbance at 1652 cm^{-1} for SDS treated lysozyme compared to control clearly demonstrated the decrease in α-helical content of the lysozyme. In addition, increase in intensity of absorbance at other peak positions like 1698 and 1683 cm^{-1} showed an increase in random coils and turns.

3.6.2.1. TEM analysis

The formation of lysozyme amyloids and the effct of ZnONP interface on the lysozyme amyloids were further explored by imaging the amyloids by TEM. As shown the figure 3.48, the TEM image of lysozyme fibrils showed that the lysozyme in presence of SDS forms amyloid fibrils. However, it was very interesting to observe that no order aggregates (fibrils) were found in presence of ZnONP interface. Hence, the findings from the objective using biophysical tools like CD spectropolarimeter, fluorescence spectroscope,

and TEM concluded that the ZnONP interface interaction with lysozyme make the lysozyme conformation relatively more compact at pH 7.4, additionally inhibits the lysozyme conformational transition into amyloid in presence of SDS at pH 9.

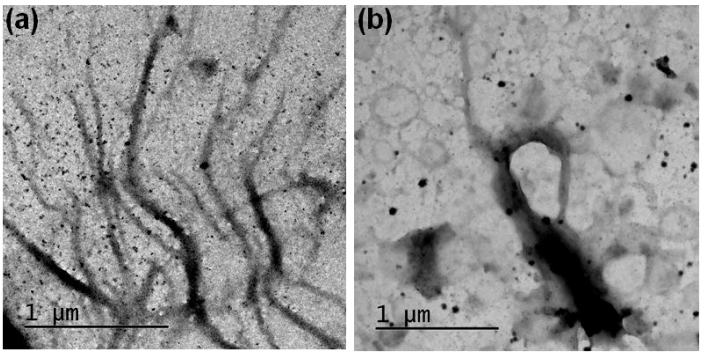

Figure 3.48. TEM image of lysozyme at pH 9 in presence of SDS showing ordered aggregates, i.e. amyloid fibrils (a), and disorder aggregates (b) in presence of ZnONP interface.

3.6.3. Summary

The objective demonstrated that lysozyme interfacial assembly onto ZnONP interface led to relatively more regular conformation in lysozyme. However, tryptophan and ANS fluorescence for interfacially assembled lysozyme indicated that at pH 7.4, insignificant conformational rearrangement observed with increasing ZnONP interface. Unlike pH 7.4, the lysozyme conformation drastically changed with increase in ZnONP interface at pH 9. Additionally, the conformational change in presence of ZnONP interface act against the amyloidogenic propensity of lysozyme in presence of SDS at pH 9.

Chapter 4

Conclusion

Based on the study carried out for the thesis, insights into the effects of photocatalytic nanoparticle interface on biomembranes and biomacromolecules were gained. The findings from the first objective demonstrated that the interfacial potential and functional groups play vital role determining the antimicrobial activity/cytocompatibility of nanoparticles. However, the findings from second objective strongly reported that the surface defects and crystallinity of the photocatalytic nanoparticle determine the rate of oxidative stress exerted by the nanoparticle leading to cytotoxic and antimicrobial activities of nanoparticle. The third objective concluded that the functional efficacy of antimicrobial peptide increased upon interaction with the phtocatalytic nanoparticles by ROS-mediated membrane depolarization and by assisting invagination of the conjugate. Whereas, fourth objective investigated the conformational dynamics and amyloidogenic propensity of lysozyme in presence of nanoparticle interface, which indicated that the interfacial interaction inhibits the SDS-mediated lysozyme amyloidogenic propensity at pH 9, without affecting the protein native conformation at pH 7.4.

Scope for Further Research

The following studies are, hereby, proposed for further extension of the work:

1. The role of interfacial potential of other nanoparticle upon mammalian cells vs cancerous cells can be explored, which might have diverse applications from diagnostic to therapeutic applications.
2. Like functionalization of ioron oxide nanoparticles, other attempts can be taken to functionalize nanoparticles with different biocompatible agents to make cytotoxic nanoparticle a cytocompatible for biological applications.
3. The conformational and functional dynamics of other amyloidogenic peptides, like Aβ peptide can be explored upon interfacially assesmbly at different photocatalytic nanoparticles. The positive outcomes might be used as diagnostic and therapeutic purposes.

Appendices

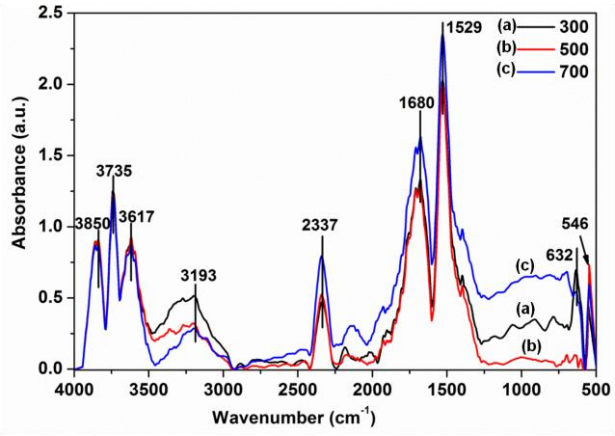

Figure A1. ATR-FTIR absorption spectra of ZnONPs synthesized at 300, 500, and 700 ^{o}C calcinations.

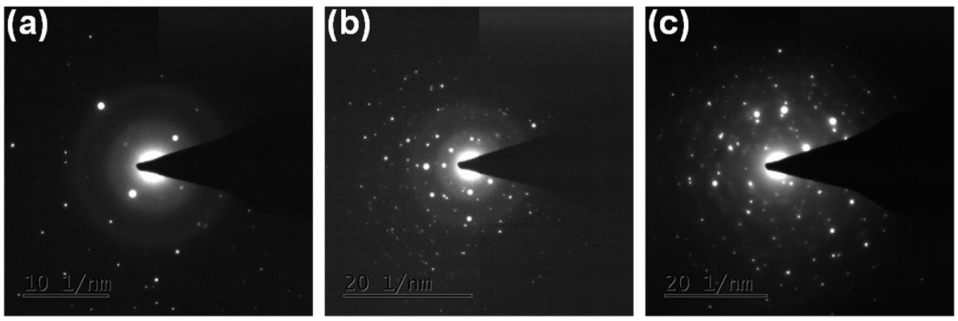

Figure A2. SAED patterns of ZnONPs synthesized at (a) 300, (b) 500, and (c) 700 ^{o}C calcinations respectively.

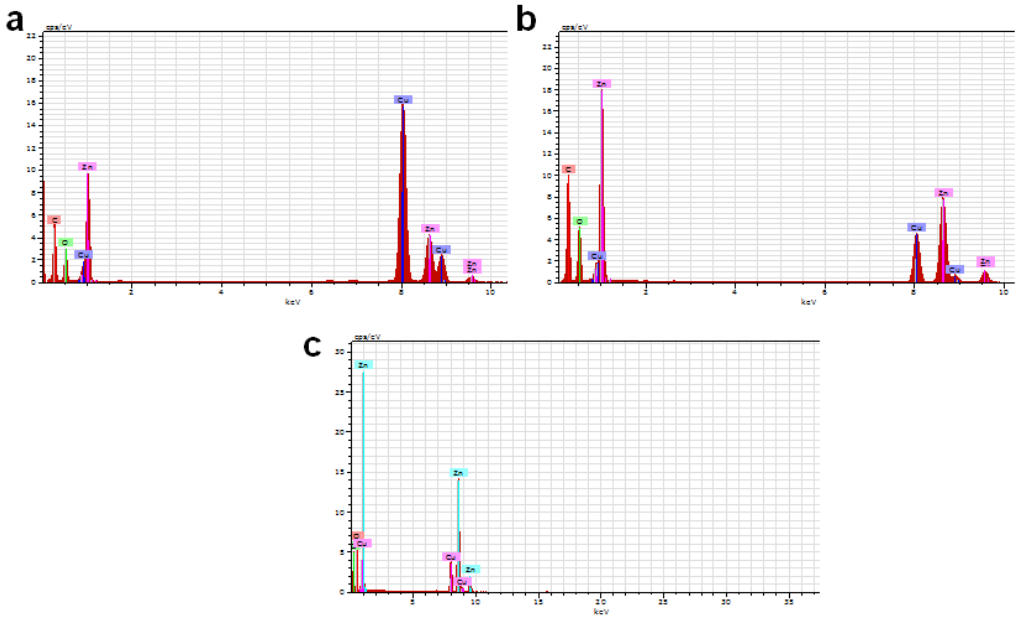

Figure A3: EDX images of ZnO nanoparticles synthesized at 300. 500, and 700 ^{o}C calcinations.

Table A1. Mass and atom percentage of Zn and oxygen in synthesized ZnONPs.

Elements	Mass %			Atom %		
	300	500	700	300	500	700
Zn	77.92	78.78	82.7	46.33	47.6	53.91
O	22.08	21.22	17.3	53.67	52.4	46.09
Total	100	100	100	100	100	100

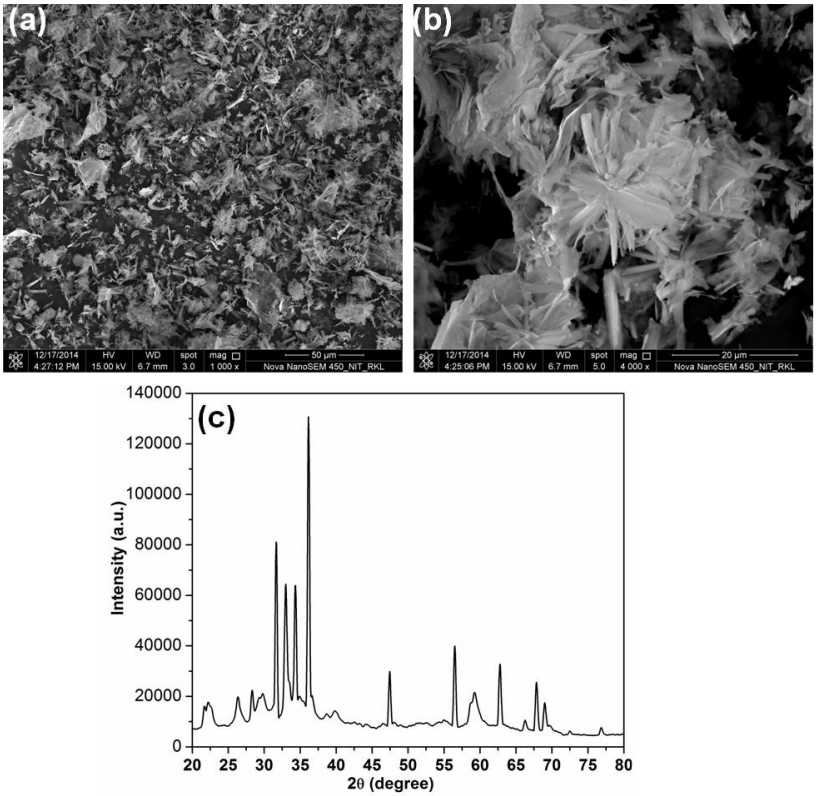

Figure A4. FE-SEM micrographs of hydrozincite demonstrating unspecific structure (a) low magnification, (b) high magnification, (c) XRD spectra of hydrozincite. The intermediate formed was analyzed by X-pert high score software and found to be hydrozincite having reference code-72-1100.

For the synthesis of ZnO nanoparticles, zinc acetate dihydrate as metal and urea as reducing agent were taken, and the possible mechanism for synthesis of ZnONP from zinc acetate dihydrate and urea is illustrated as follows

$(NH_2)CO+H_2O \longrightarrow 2NH_3+ CO_2$ Eq (1)

$CO_2+H_2O \longrightarrow 2H^+ + CO_3^{2-}$ Eq (2)

$NH_3 + H_2O \longrightarrow NH_4^+ + OH^-$ Eq (3)

$5Zn^{2+} + 2CO_3^{2-} + 6OH^- \longrightarrow Zn_5(CO_3)_2(OH)_6$ Eq (4)

$Zn_5(CO_3)_2(OH)_6 \longrightarrow 5ZnO + 2CO_2\uparrow + 3H_2O$ Eq (5)

At experimental temperature (115 ^oC in our experiment), urea decomposes to NH_3 and CO_2 (Eq. (1)), which combine again to produce carbonate (CO_3^{2-}), ammonium ion (NH_4^+) and hydroxide (OH^-) ions (Eq. (2) and Eq. (3)). Under basic conditions, the intermediate complex hydrozincite, $Zn_5(CO_3)_2(OH)_6$ (Eq. (4)), is formed by the

combination of free CO_3^{2-} ion and Zn^{2+} ion. Upon calcinating at 300, 500 and 700 ^oC, the complete conversion of hydrozincite leads to formation of ZnONP (Eq. (5)). Here it is important to note that the intermediate hydrozincite formed does not possess any specific shape or crystal structure (Figure A4).

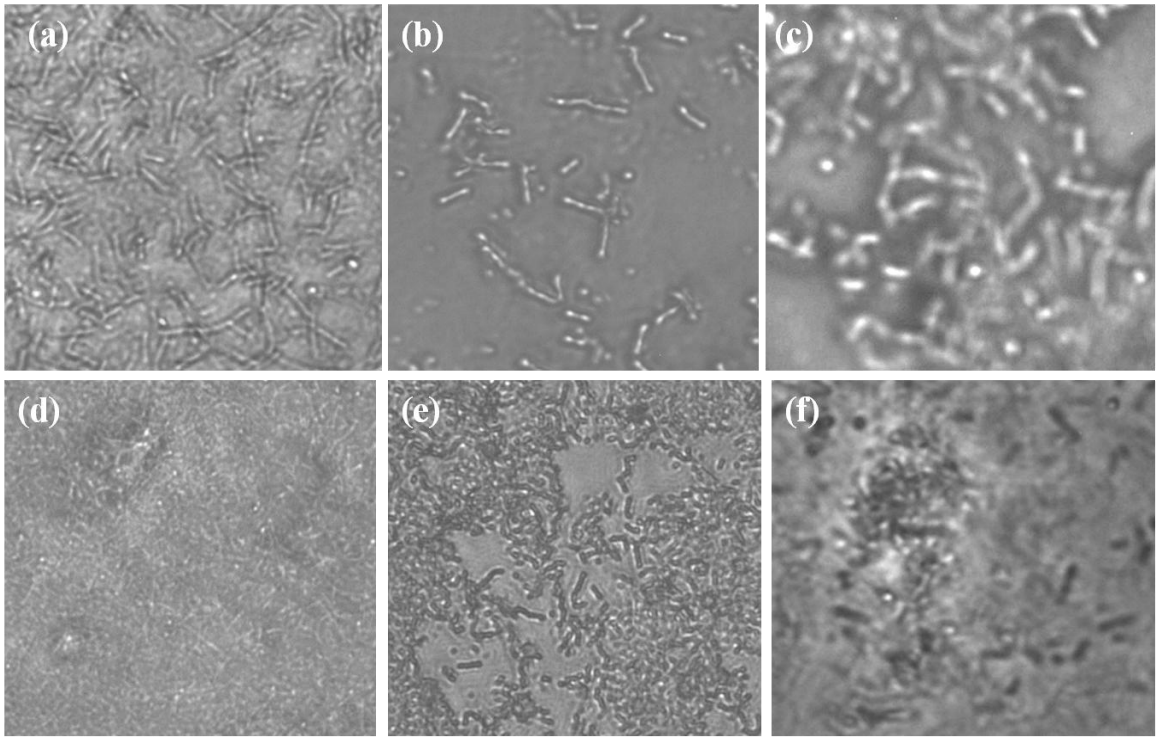

Figure A5. Morphological changes of Gram positive bacteria (*B. subtilis*, *B. thuringiensis* and *S. aureus*) at 100 µg/mL concentration of p-ZnONP by phase contrast microscopy. Untreated cells of *B. subtilis* (a), *B. thuringiensis* (b), and *S. aureus* (c) show intact surface morphology, whereas p-ZnONP treated cells show aggregation of cells (*B. subtilis* (d), *B. thuringiensis* (e), and *S. aureus* (f)), confirming bacterial cell membrane lysis.

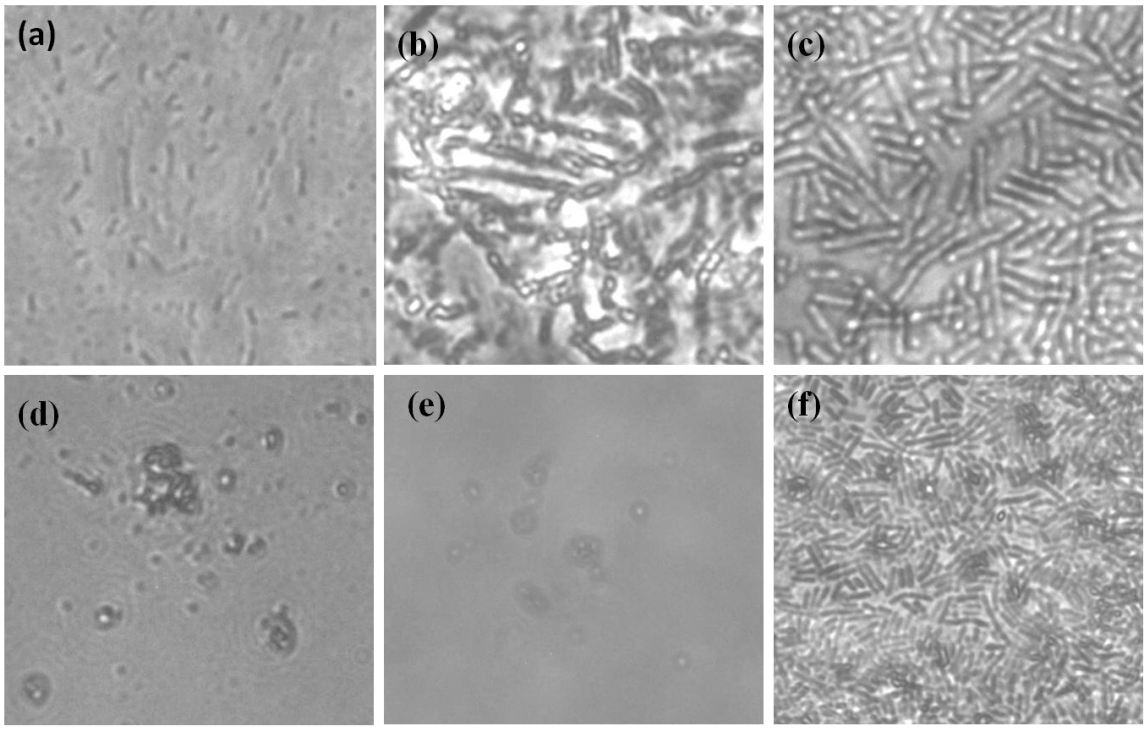

Figure A6. Morphological changes of Gram negative bacteria (*E. coli*, *S. flexneri* and *P. vulgaris*) at 50 µg/mL concentration of p-ZnONP by phase contrast microscopy. Untreated cells of *E. coli* (a), *S. flexneri* (b), and *P. vulgaris* (c) show intact surface morphology, whereas p-ZnONP treated cells show aggregation of cells (*E. coli* (d), *S. flexneri* (e), and *P. vulgaris* (f)) confirming bacterial cell membrane lysis.

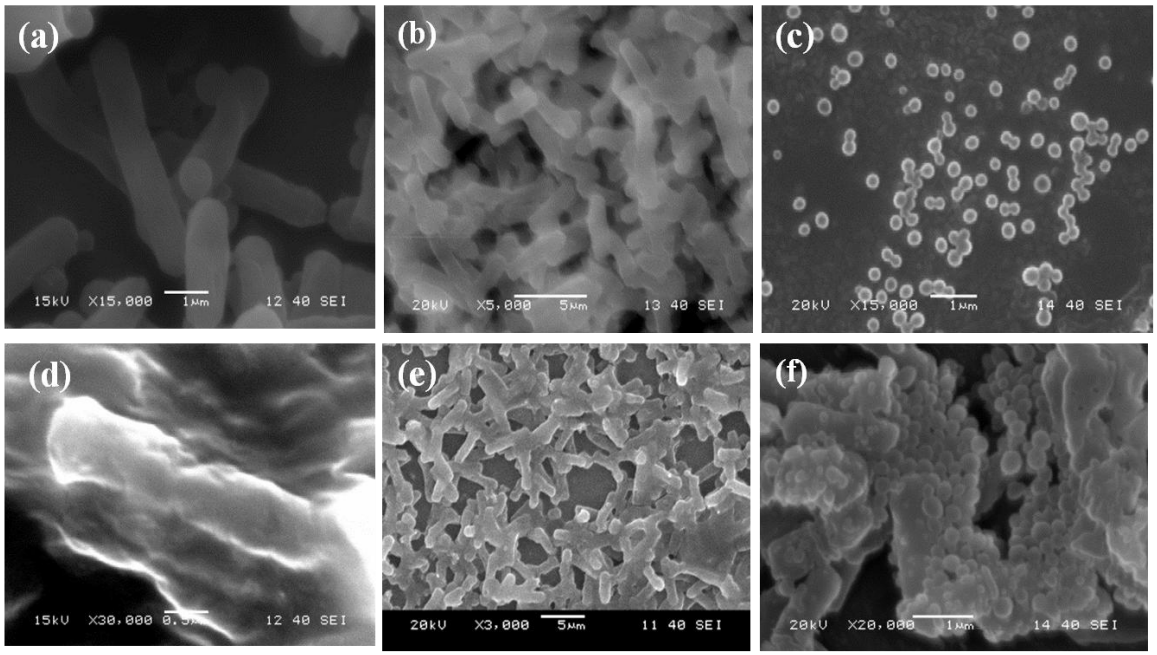

Figure A7. Morphological changes of Gram-positive bacteria (*B. subtilis*, *B. thuringiensis* and *S. aureus*) at 100 µg/mL concentration of p-ZnONP by SEM. Untreated cells of *B. subtilis* (a), *B. thuringiensis* (b), and *S. aureus* (c) show intact surface morphology, whereas p-ZnONP treated cells show aggregation as well as membrane rupture of cells (*B. subtilis* (d), *B. thuringiensis* (e), and *S. aureus* (f)) confirming bacterial cell membrane lysis.

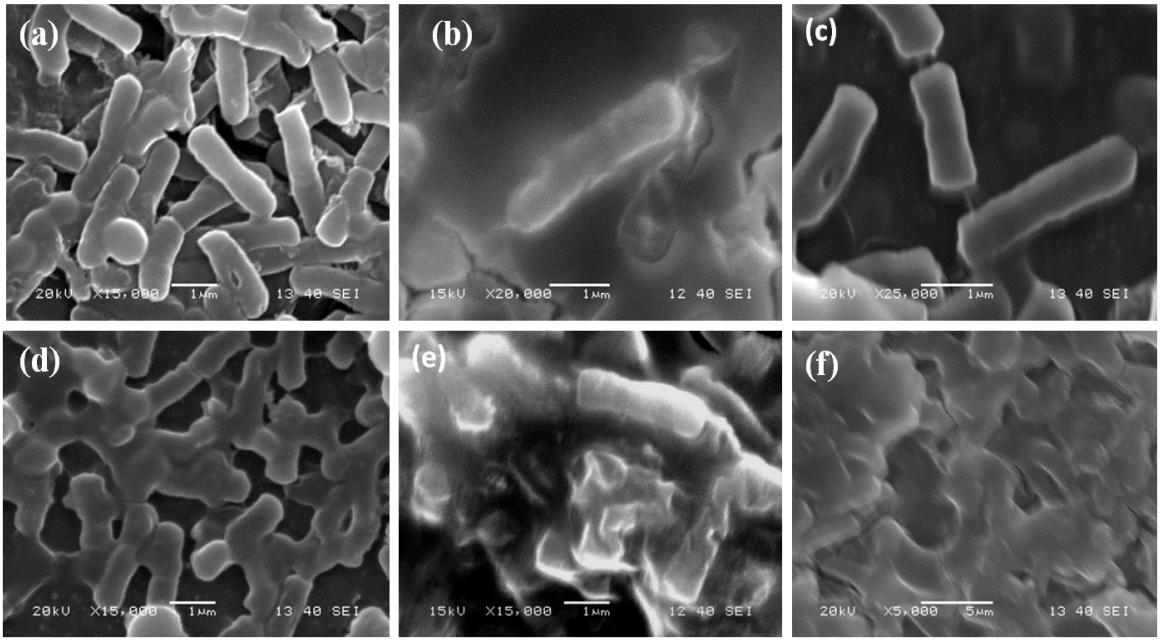

Figure A8. Morphological changes of Gram negative bacteria (*E. coli*, *S. flexneri* and *P. vulgaris*) at 50 µg/mL concentration of p- ZnONP by SEM. Untreated cells of *E. coli* (a), *S. flexneri* (b), and *P. vulgaris* (c) show intact surface morphology, whereas p-ZnONP treated cells show aggregation as well as membrane rupture of cells (*E. coli* (d), *S. flexneri* (e), and *P. vulgaris* (f)) confirming bacterial cell membrane lysis.

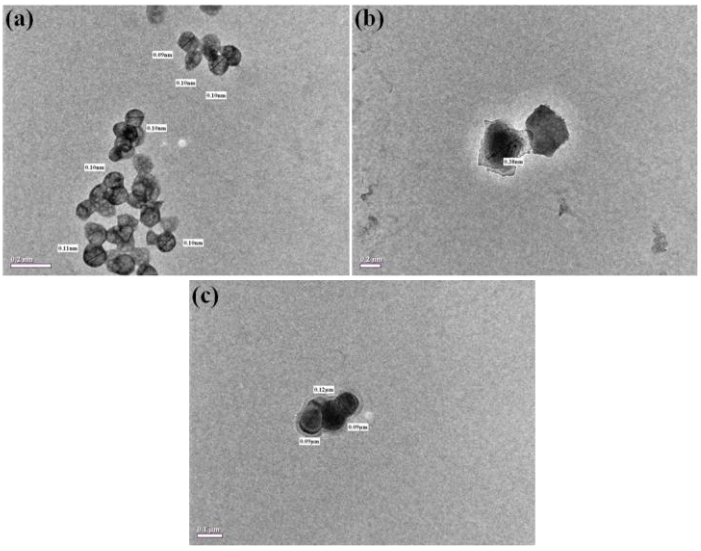

Figure A9. TEM micrograph of n-IONP and p-IONP showing the ultra-fine iron oxide nanoparticles having size of 0.1 nm (a) and 0.3 nm (b) respectively , and nanoparticles of size ~ 90 nm IONP (c).

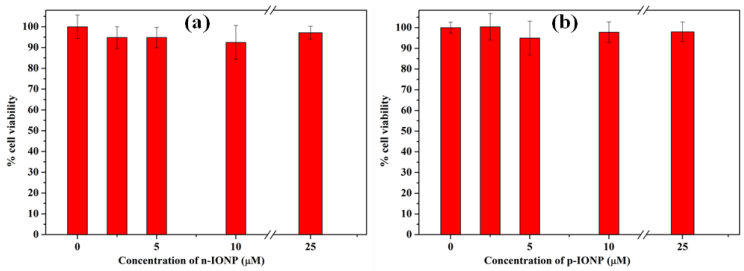

Figure A10. Cytotoxicity of both n-IONP and p-IONP against Human Embryonic Kidney 293 (HEK 293) cell line using Alamar Blue dye reduction assay. Both the nanoparticles show cytocompatible nature against the studied cell line.

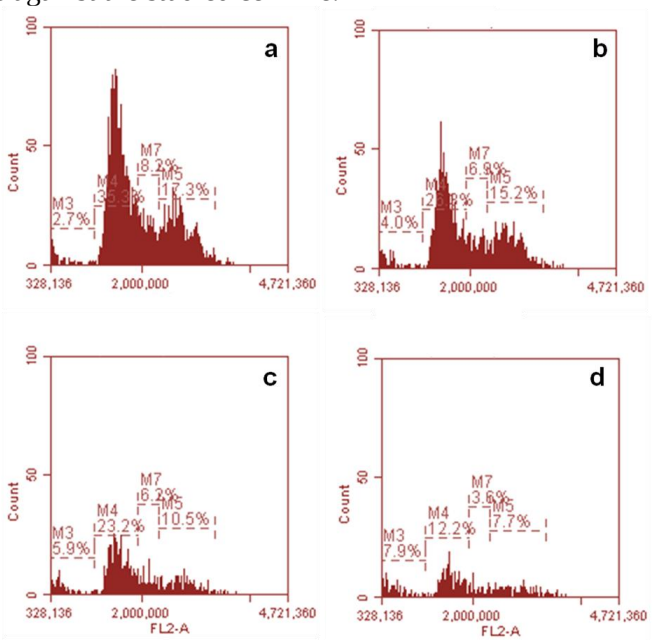

Figure A11. Histograms showing cell cycle analysis of HT1080 cells. (a) Control representing normal distribution of different phases like subG1, G1, S and G2/M, and upon treatment with

ZnONP synthesis at (b) ZnONP 300 ^{o}C, (c) 500 ^{o}C, and (d) 700 ^{o}C calcinations. The data revealed a gradual increase population in G1 phase confirming the induction of apoptosis.

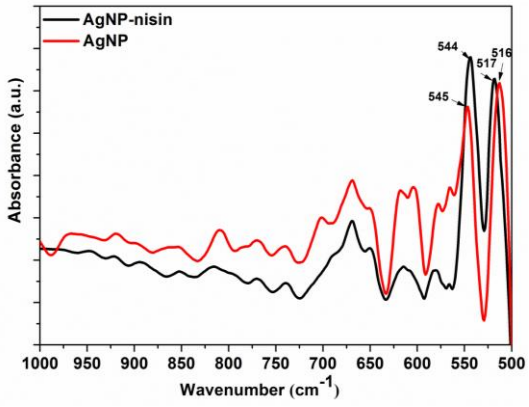

Figure A12. ATR-FTIR spectra of AgNP, and AgNP-nisin conjugate (1:1). The presence of prominent peaks at 545, 516 cm^{-1} for AgNP and at 544, and 517 cm^{-1} for conjugate confirm the presence of Ag-Ag/Ag-O bonds in both the samples.

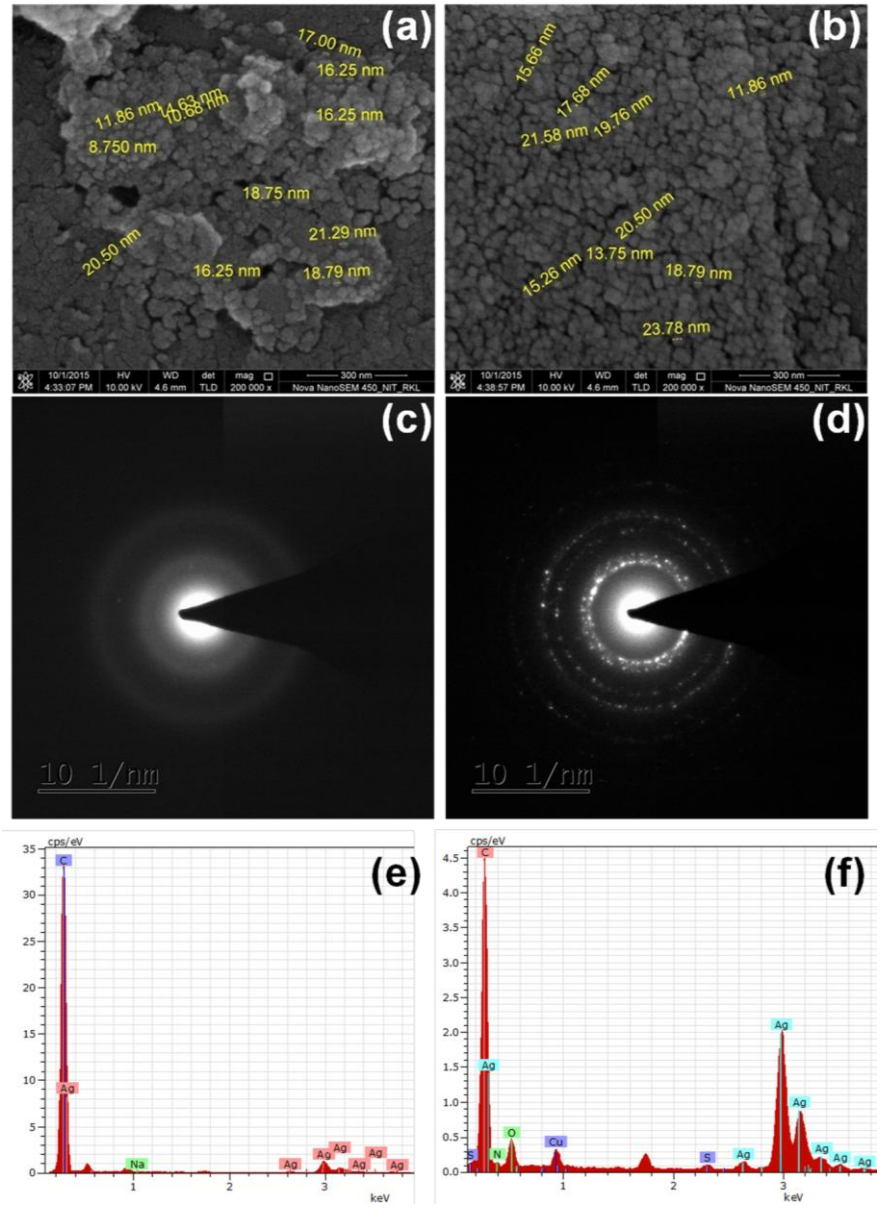

Figure A13. FE-SEM representative image of AgNP (a) and AgNP-nisin conjugate (1:1) (b). The statistical calculation of size for 50 NPs in images indicated an average diameter of 17.87 +/- 0.8 nm and 19.12+/-0.81 nm for intact AgNP and AgNP-nisin conjugate, respectively. Crystalline nature is confirmed by SAED patterns of AgNP (c) and AgNP-nisin conjugate (1:1) (d). Whereas, EDX spectra of AgNP (e) and AgNP-nisin conjugate (1:1) (f) respectively, proved the presence of the peptide in AgNP-nisin conjugate.

Table A2. Distance of interacting residues of nisin from AgNP core in the conjugate.

Residue Number	Initial	Mid	End
1	7.7	7.3	7.5
2	7.0	7.0	7.0
3	3.4	3.1	3.0
4	3.0	3.2	2.9
22	7.9	8.2	7.7
23	7.9	8.0	8.0
24	5.2	6.3	5.4
25	5.9	4.7	4.7
26	9.7	9.0	9.0
31	7.4	7.3	7.0
32	9.7	9.4	9.2
33	11.3	10.8	10.5
34	13.3	12.8	12.8

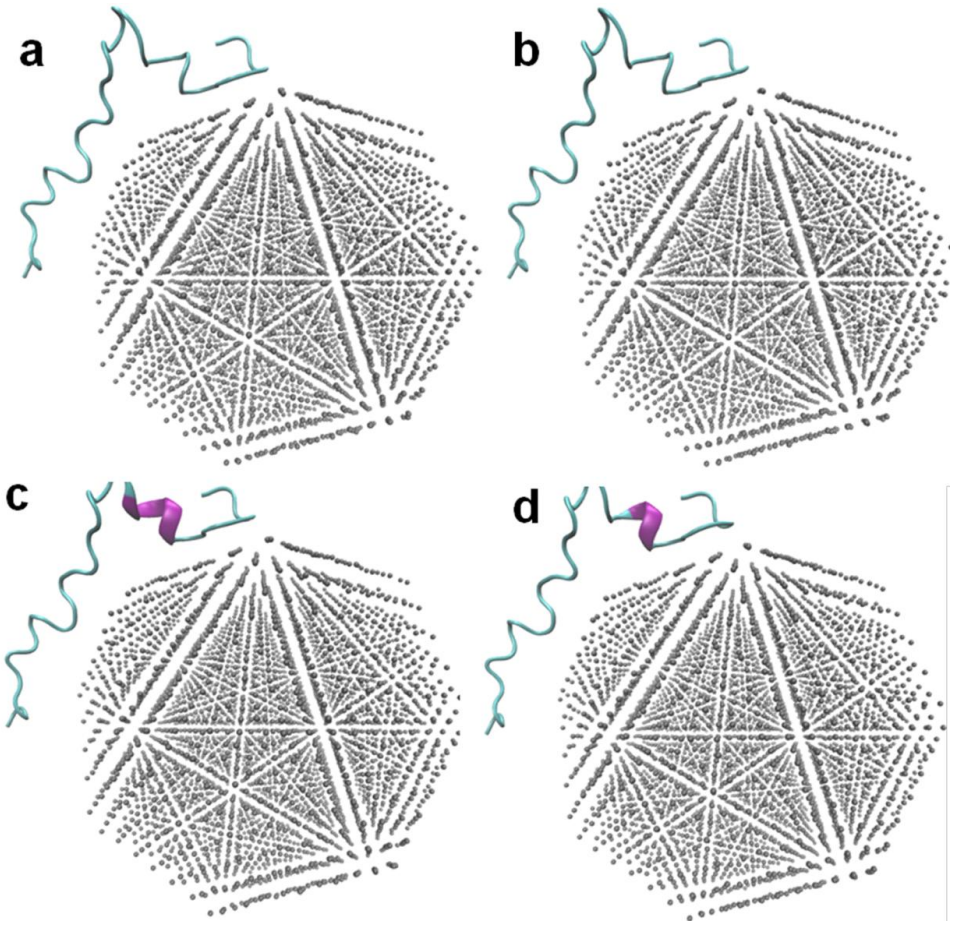

Figure A14. Snapshots of AgNP-nisin conjugation at different time interval, (a) 10 ns, (b) 20 ns, (c) 30 ns, and (d) 40 ns in a 50 ns production run.

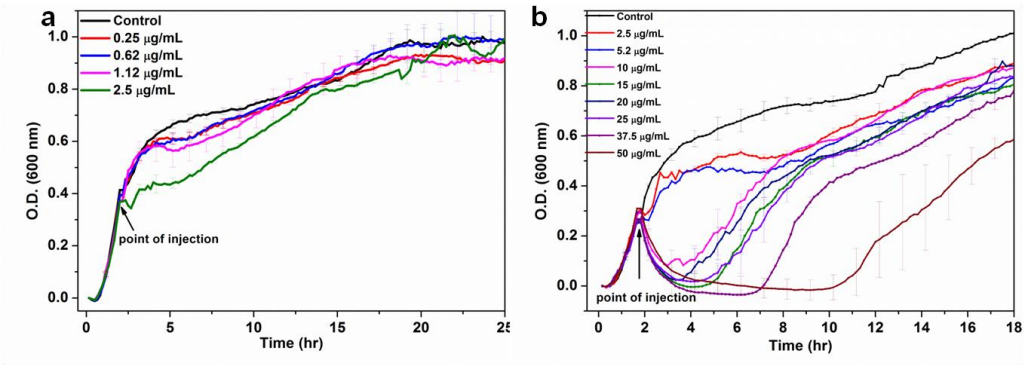

Figure A15. Growth kinetics of *B. subtilis* in presence of different concentration of nisin.

To clearly spel out the enhanced antimicrobial activity of AgNP-nisin conjugates than nisin or AgNP, the growth kinetics of *B. subtilis* in presence of different concentrations of intact nisin was observed. As shown in figure A15, we observed that upto 5.2 µg/mL of nisin concentration, the growth inhibition of *B. subtilis* was insignificant. However, a brief comparison with growth kinetics of *B. subtilis* in presence of AgNP-nisin conjugates indicated that very concentration (85 nm) of nisin conjugated with AgNP showed significant antimicrobial activity against *B. subtilis* cells. Hence, AgNP-nisin conjugates are found to be stronger antimicrobial agent than intact nisin peptide against *B. subtilis*.

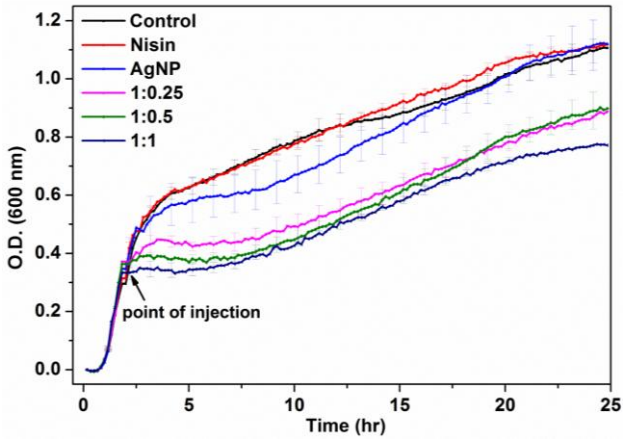

Figure A16. Growth kinetics of *Proteus vulgaris* in presence of AgNP-nisin conjugates.

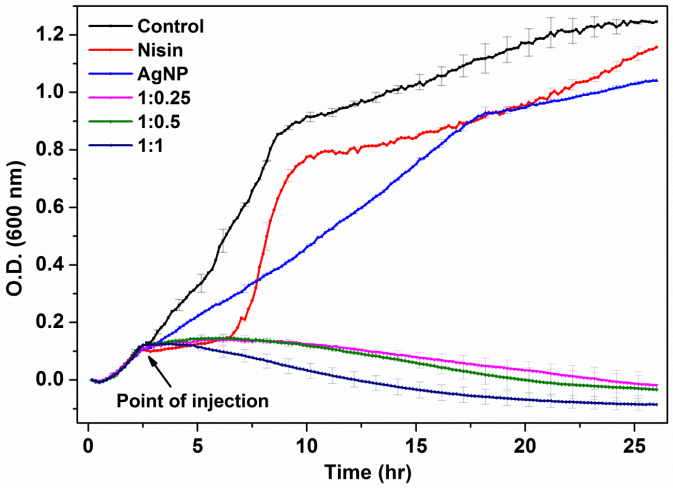

Figure A17. Growth kinetics of *Staphylococcus aureus* in presence of AgNP-nisin conjugates.

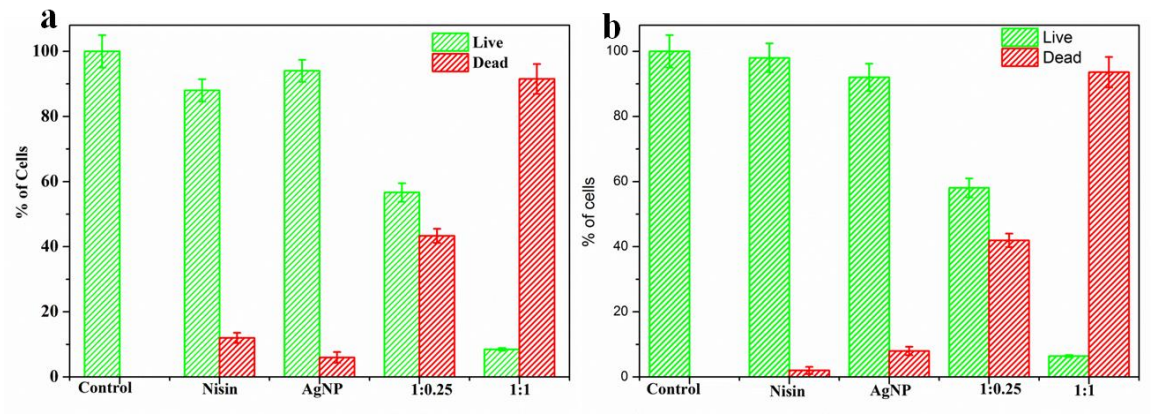

Figure A18. Percentage of live and dead cells of *B. subtilis* (a), and *E. coli* (b) upon treatment with nisin, AgNP, and AgNP-nisin conjugates, determined statistically from fluorescence microscopy images, using Image J software.

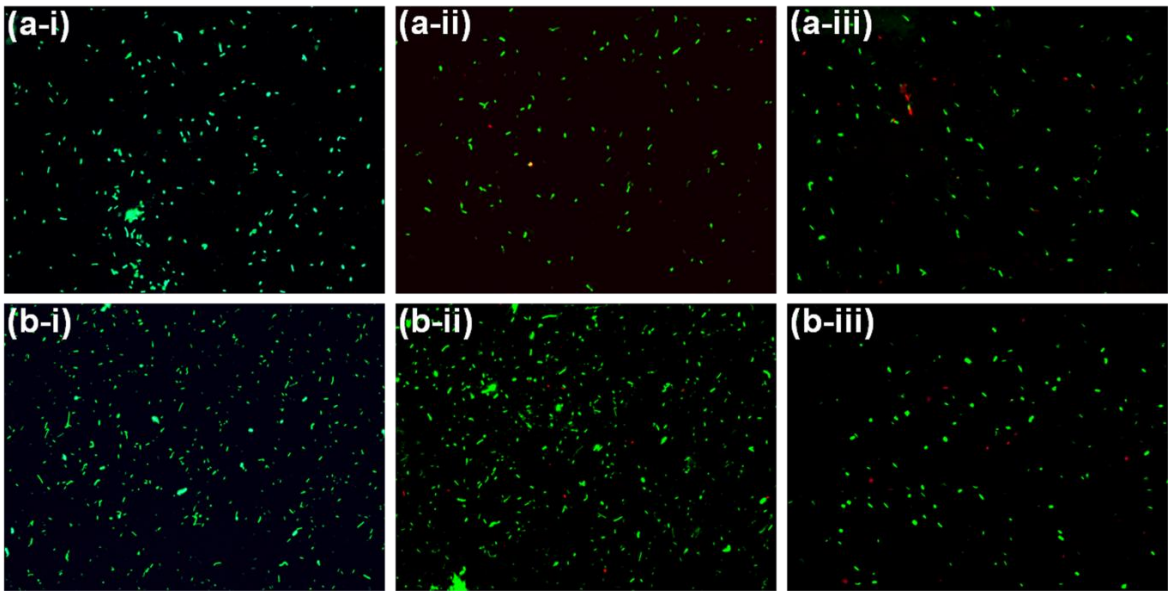

Figure A19. Panel a-fluorescence image of (a-i) *B. subtilis*, (a-ii) *B. subtilis* with nisin, and (a-iii) *B. subtilis* with AgNP. Panel b- fluorescence image of (b-i) *E. coli*, (b-ii) *E. coli* with nisin, and (b-iii) *E. coli* with AgNP.

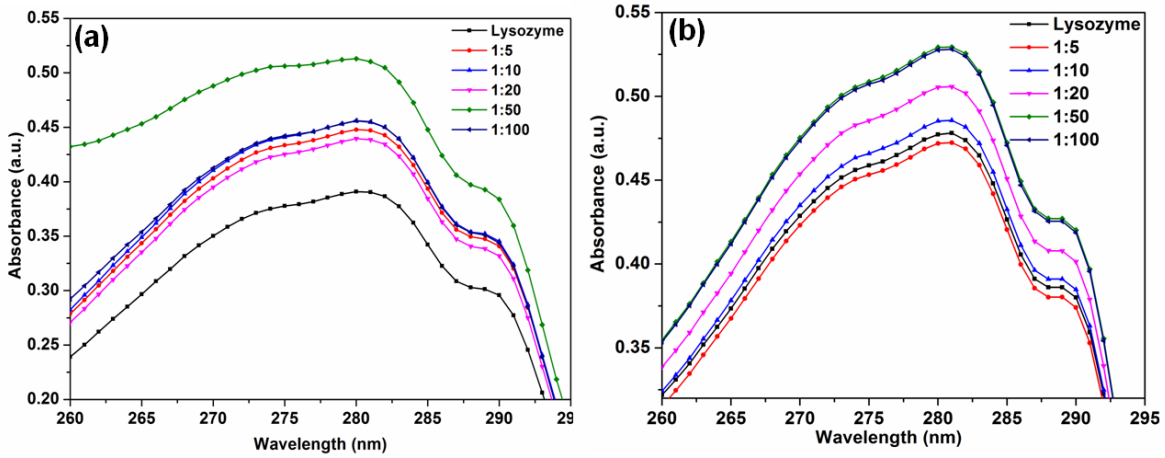

Figure A20. UV-Visible absorption spectra of lysozyme in absence and presence of increasing fractions of ZnONPs in conjugate at (a) pH 7.4, and (b) pH 9.

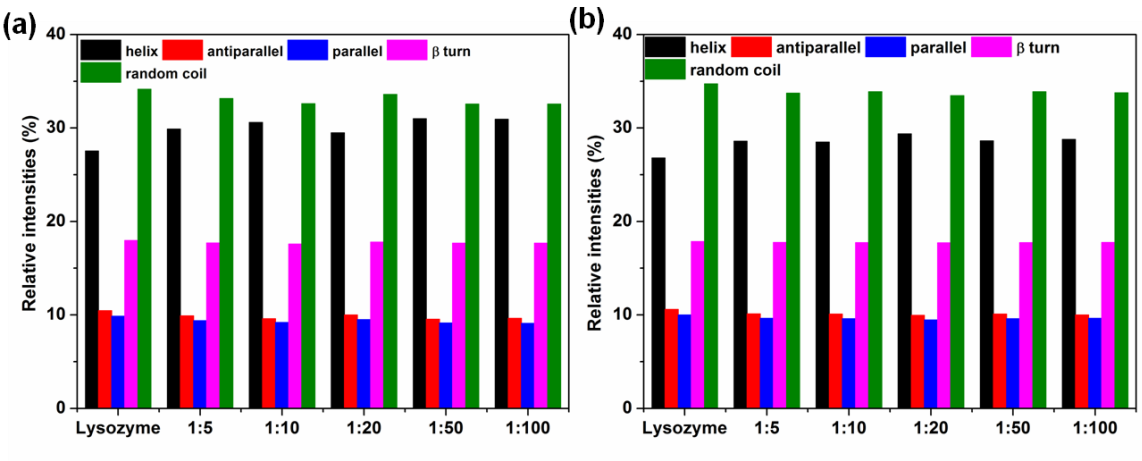

Figure A21.The secondary structure composition of lysozyme at pH 7.4 (a) and pH 9 (b) upon ZnONP interaction determined from CD spectra using CDNN deconvulation software.

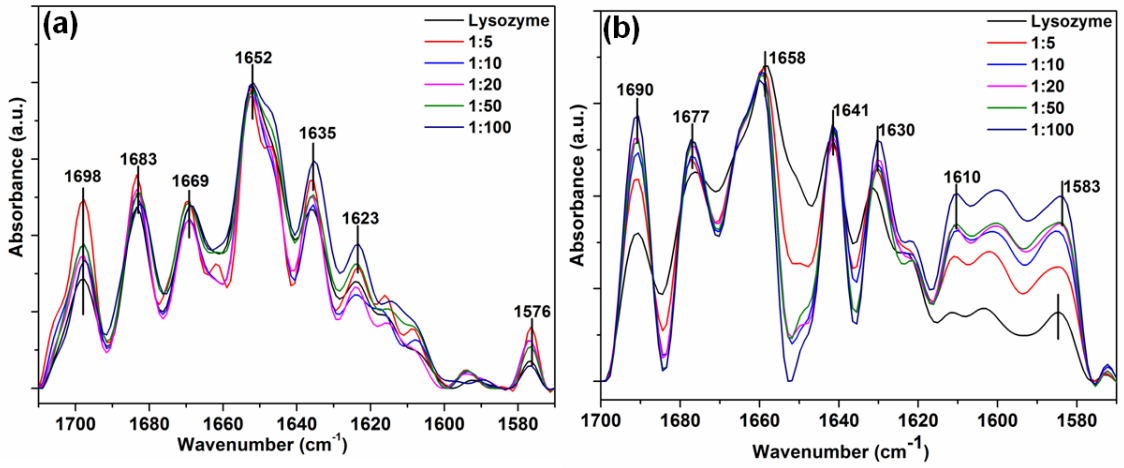

Figure A22. ATR-FTIR spectra of lysozyme in absence and presence of different fractions of ZnONP at (a) pH 7.4, and (b) pH 9.

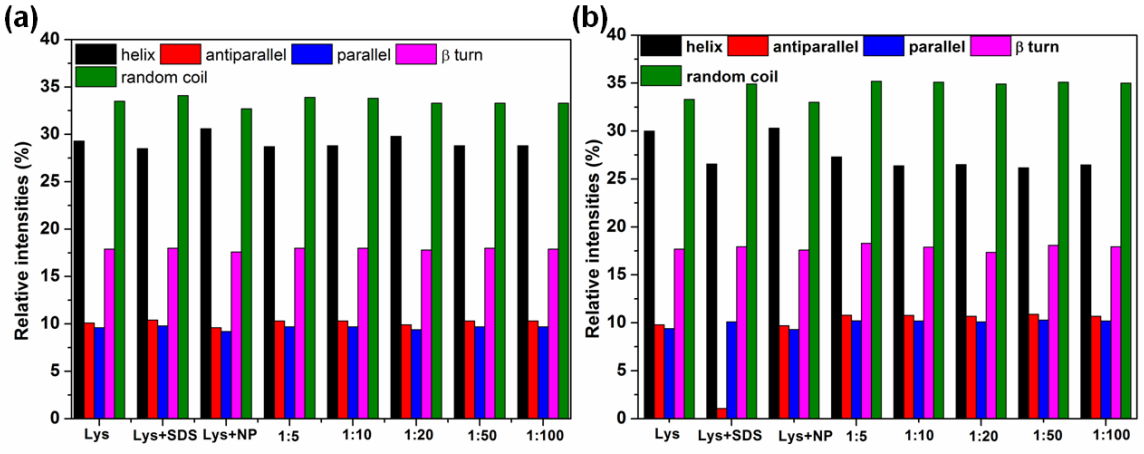

Figure A 23.The secondary structure composition of lysozyme at (a) pH 7.4 and, (b) pH 9 upon ZnONP interaction in presence of SDS, determined from CD spectra using CDNN deconvolution software.

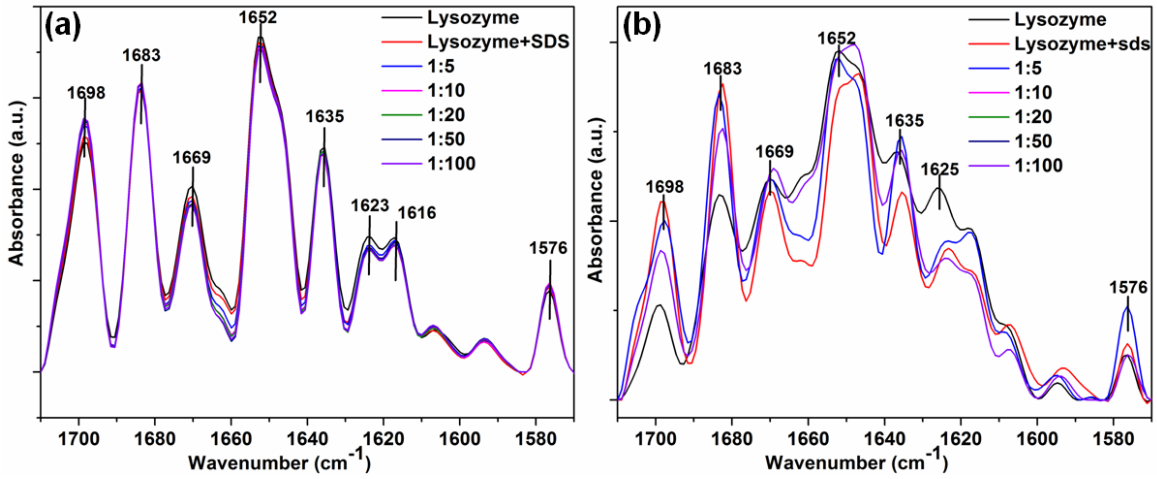

Figure A24. ATR-FTIR spectra of lysozyme in absence and presence SDS upon conjugation to ZnONP at (a) pH 7.4 and (b) pH 9.

References

1. Toumey, C., Plenty of Room, Plenty of History. *Nature nanotechnology* **2009,** *4* (12), 783-784.
2. Feynman, R. P., There's Plenty of Room at the Bottom. *Miniaturization"(HD Gilbert, ed.) Reinhold, New York* **1961**.
3. Bhattacharyya, D.; Singh, S.; Satnalika, N.; Khandelwal, A.; Jeon, S.-H., Nanotechnology, Big Things from a Tiny World: A Review. *Nanotechnology* **2009,** *2* (3).
4. Kim, H. R.; Kim, M. J.; Lee, S. Y.; Oh, S. M.; Chung, K. H., Genotoxic Effects of Silver Nanoparticles Stimulated by Oxidative Stress in Human Normal Bronchial Epithelial (Beas-2b) Cells. *Mutation Research/Genetic Toxicology and Environmental Mutagenesis* **2011,** *726* (2), 129-35.
5. Thakkar, K. N.; Mhatre, S. S.; Parikh, R. Y., Biological Synthesis of Metallic Nanoparticles. *Nanomedicine: Nanotechnology, Biology and Medicine* **2010,** *6* (2), 257-262.
6. Fang, M.; Chen, J. H.; Xu, X. L.; Yang, P. H.; Hildebrand, H. F., Antibacterial Activities of Inorganic Agents on Six Bacteria Associated with Oral Infections by Two Susceptibility Tests. *International journal of antimicrobial agents* **2006,** *27* (6), 513-517.
7. Sreeprasad, T. S.; Pradeep, T., Noble Metal Nanoparticles. In *Springer Handbook of Nanomaterials*, Springer: **2013**, pp 303-388.
8. Rai, M.; Duran, N., *Metal Nanoparticles in Microbiology*. Springer Science & Business Media: **2011**.
9. Ko, S.; Gunasekaran, S., Preparation of Sub-100-Nm B-Lactoglobulin (Blg) Nanoparticles. *Journal of microencapsulation* **2006,** *23* (8), 887-898.
10. Lohcharoenkal, W.; Wang, L.; Chen, Y. C.; Rojanasakul, Y., Protein Nanoparticles as Drug Delivery Carriers for Cancer Therapy. *BioMed research international* **2014,** *2014*.
11. Langer, K.; Balthasar, S.; Vogel, V.; Dinauer, N.; Von Briesen, H.; Schubert, D., Optimization of the Preparation Process for Human Serum Albumin (Hsa) Nanoparticles. *International journal of pharmaceutics* **2003,** *257* (1), 169-180.
12. Yang, L.; Cui, F.; Cun, D.; Tao, A.; Shi, K.; Lin, W., Preparation, Characterization and Biodistribution of the Lactone Form of 10-Hydroxycamptothecin (Hcpt)-Loaded Bovine Serum Albumin (Bsa) Nanoparticles. *International journal of pharmaceutics* **2007,** *340* (1), 163-172.
13. Yang, N.; Aoki, K., Voltammetry of the Silver Alkylcarboxylate Nanoparticles in Suspension. *Electrochimica acta* **2005,** *50* (25), 4868-4872.
14. Duan, H.; Wang, D.; Li, Y., Green Chemistry for Nanoparticle Synthesis. *Chemical Society Reviews* **2015,** *44* (16), 5778-5792.
15. Banerjee, P.; Satapathy, M.; Mukhopahayay, A.; Das, P., Leaf Extract Mediated Green Synthesis of Silver Nanoparticles from Widely Available Indian Plants: Synthesis, Characterization, Antimicrobial Property and Toxicity Analysis. *Bioresources and Bioprocessing* **2014,** *1* (1), 1-10.
16. Zhang, X.; Qin, J.; Xue, Y.; Yu, P.; Zhang, B.; Wang, L.; Liu, R., Effect of Aspect Ratio and Surface Defects on the Photocatalytic Activity of Zno Nanorods. *Scientific reports* **2014,** *4*.
17. Shoeb, M.; Singh, B. R.; Khan, J. A.; Khan, W.; Singh, B. N.; Singh, H. B.; Naqvi, A. H., Ros-Dependent Anticandidal Activity of Zinc Oxide Nanoparticles Synthesized by Using Egg Albumen as a Biotemplate. *Advances in Natural Sciences: Nanoscience and Nanotechnology* **2013,** *4* (3), 035015.
18. Srivastava, V.; Gusain, D.; Sharma, Y. C., Synthesis, Characterization and Application of Zinc Oxide Nanoparticles (N-Zno). *Ceramics International* **2013,** *39* (8), 9803-9808.
19. Zhang, H.-J.; Xiong, H.-M., Biological Applications of Zno Nanoparticles. *Current Molecular Imaging* **2013,** *2* (2), 177-192.
20. Wang, E. C.; Wang, A. Z., Nanoparticles and Their Applications in Cell and Molecular Biology. *Integrative Biology* **2014,** *6* (1), 9-26.
21. Daniel, M.-C.; Astruc, D., Gold Nanoparticles: Assembly, Supramolecular Chemistry, Quantum-Size-Related Properties, and Applications toward Biology, Catalysis, and Nanotechnology. *Chemical reviews* **2004,** *104* (1), 293-346.

22. Weissleder, R., Molecular Imaging in Cancer. *Science* **2006,** *312* (5777), 1168-1171.
23. Arakha, M.; Pal, S.; Samantarrai, D.; Panigrahi, T. K.; Mallick, B. C.; Pramanik, K.; Mallick, B.; Jha, S., Antimicrobial Activity of Iron Oxide Nanoparticle Upon Modulation of Nanoparticle-Bacteria Interface. *Scientific reports* **2015,** *5*.
24. Zhao, M.; Beauregard, D. A.; Loizou, L.; Davletov, B.; Brindle, K. M., Non-Invasive Detection of Apoptosis Using Magnetic Resonance Imaging and a Targeted Contrast Agent. *Nature medicine* **2001,** *7* (11), 1241-1244.
25. Mahdavi, M.; Ahmad, M. B.; Haron, M. J.; Namvar, F.; Nadi, B.; Rahman, M. Z. A.; Amin, J., Synthesis, Surface Modification and Characterisation of Biocompatible Magnetic Iron Oxide Nanoparticles for Biomedical Applications. *Molecules* **2013,** *18* (7), 7533-7548.
26. Gu, H.; Xu, K.; Xu, C.; Xu, B., Biofunctional Magnetic Nanoparticles for Protein Separation and Pathogen Detection. *Chemical Communications* **2006,** (9), 941-949.
27. Mody, V. V.; Siwale, R.; Singh, A.; Mody, H. R., Introduction to Metallic Nanoparticles. *Journal of Pharmacy and Bioallied Sciences* **2010,** *2* (4), 282.
28. Qin, Y., Silver-Containing Alginate Fibres and Dressings. *International wound journal* **2005,** *2* (2), 172-176.
29. Atiyeh, B. S.; Costagliola, M.; Hayek, S. N.; Dibo, S. A., Effect of Silver on Burn Wound Infection Control and Healing: Review of the Literature. *burns* **2007,** *33* (2), 139-148.
30. Sondi, I.; Salopek-Sondi, B., Silver Nanoparticles as Antimicrobial Agent: A Case Study on *E. Coli* as a Model for Gram-Negative Bacteria. *Journal of colloid and interface science* **2004,** *275* (1), 177-182.
31. Jain, N.; Bhargava, A.; Majumdar, S.; Tarafdar, J.; Panwar, J., Extracellular Biosynthesis and Characterization of Silver Nanoparticles Using *Aspergillus Flavus* Njp08: A Mechanism Perspective. *Nanoscale* **2011,** *3* (2), 635-641.
32. Bangham, A., Liposomes: The Babraham Connection. *Chemistry and physics of lipids* **1993,** *64* (1), 275-285.
33. Torchilin, V. P., Recent Advances with Liposomes as Pharmaceutical Carriers. *Nature reviews Drug discovery* **2005,** *4* (2), 145-160.
34. Felgner, P. L.; Ringold, G., Cationic Liposome-Mediated Transfection. *Nature* **1989,** *337* (6205), 387.
35. Felgner, P. L.; Gadek, T. R.; Holm, M.; Roman, R.; Chan, H. W.; Wenz, M.; Northrop, J. P.; Ringold, G. M.; Danielsen, M., Lipofection: A Highly Efficient, Lipid-Mediated DNA-Transfection Procedure. *Proceedings of the National Academy of Sciences* **1987,** *84* (21), 7413-7417.
36. Elzoghby, A. O.; Samy, W. M.; Elgindy, N. A., Albumin-Based Nanoparticles as Potential Controlled Release Drug Delivery Systems. *Journal of controlled release* **2012,** *157* (2), 168-182.
37. Miele, E.; Spinelli, G. P.; Miele, E.; Tomao, F.; Tomao, S., Albumin-Bound Formulation of Paclitaxel (Abraxane Abi-007) in the Treatment of Breast Cancer. *International Journal of Nanomedicine* **2009,** *4* (1), 99-105.
38. Hawkins, M. J.; Soon-Shiong, P.; Desai, N., Protein Nanoparticles as Drug Carriers in Clinical Medicine. *Advanced drug delivery reviews* **2008,** *60* (8), 876-885.
39. Gradishar, W. J.; Tjulandin, S.; Davidson, N.; Shaw, H.; Desai, N.; Bhar, P.; Hawkins, M.; O'Shaughnessy, J., Phase Iii Trial of Nanoparticle Albumin-Bound Paclitaxel Compared with Polyethylated Castor Oil–Based Paclitaxel in Women with Breast Cancer. *Journal of clinical oncology* **2005,** *23* (31), 7794-7803.
40. Gref, R.; Minamitake, Y.; Peracchia, M. T.; Trubetskoy, V.; Torchilin, V.; Langer, R., Biodegradable Long-Circulating Polymeric Nanospheres. *Science* **1994,** *263* (5153), 1600-1603.
41. Torchilin, V. P., Micellar Nanocarriers: Pharmaceutical Perspectives. *Pharmaceutical research* **2007,** *24* (1), 1-16.
42. Wang, A. Z.; Gu, F.; Zhang, L.; Chan, J. M.; Radovic-Moreno, A.; Shaikh, M. R.; Farokhzad, O. C., Biofunctionalized Targeted Nanoparticles for Therapeutic Applications. *Expert opinion on biological therapy* **2008,** *8* (8), 1063-1070.
43. Chen, L.; Remondetto, G. E.; Subirade, M., Food Protein-Based Materials as Nutraceutical Delivery Systems. *Trends in Food Science & Technology* **2006,** *17* (5), 272-283.

44. Collier, C.; Vossmeyer, T.; Heath, J., Nanocrystal Superlattices. *Annual Review of Physical Chemistry* **1998,** *49* (1), 371-404.
45. Jovin, T. M., Quantum Dots Finally Come of Age. *Nature biotechnology* **2003,** *21* (1), 32-33.
46. Chang, Y. P.; Pinaud, F.; Antelman, J.; Weiss, S., Tracking Bio-Molecules in Live Cells Using Quantum Dots. *Journal of biophotonics* **2008,** *1* (4), 287-298.
47. Chan, W. C.; Maxwell, D. J.; Gao, X.; Bailey, R. E.; Han, M.; Nie, S., Luminescent Quantum Dots for Multiplexed Biological Detection and Imaging. *Current opinion in biotechnology* **2002,** *13* (1), 40-46.
48. Jamieson, T.; Bakhshi, R.; Petrova, D.; Pocock, R.; Imani, M.; Seifalian, A. M., Biological Applications of Quantum Dots. *Biomaterials* **2007,** *28* (31), 4717-4732.
49. Verma, A.; Stellacci, F., Effect of Surface Properties on Nanoparticle–Cell Interactions. *Small* **2010,** *6* (1), 12-21.
50. Jiang, W.; Kim, B. Y.; Rutka, J. T.; Chan, W. C., Nanoparticle-Mediated Cellular Response Is Size-Dependent. *Nature nanotechnology* **2008,** *3* (3), 145-150.
51. Vertegel, A. A.; Siegel, R. W.; Dordick, J. S., Silica Nanoparticle Size Influences the Structure and Enzymatic Activity of Adsorbed Lysozyme. *Langmuir* **2004,** *20* (16), 6800-6807.
52. Shang, W.; Nuffer, J. H.; Dordick, J. S.; Siegel, R. W., Unfolding of Ribonuclease a on Silica Nanoparticle Surfaces. *Nano letters* **2007,** *7* (7), 1991-1995.
53. Fei, L.; Perrett, S., Effect of Nanoparticles on Protein Folding and Fibrillogenesis. *International journal of molecular sciences* **2009,** *10* (2), 646-655.
54. Wu, X.; Narsimhan, G., Effect of Surface Concentration on Secondary and Tertiary Conformational Changes of Lysozyme Adsorbed on Silica Nanoparticles. *Biochimica et Biophysica Acta (BBA)-Proteins & Proteomics* **2008,** *1784* (11), 1694-1701.
55. Khan, J. A.; Pillai, B.; Das, T. K.; Singh, Y.; Maiti, S., Molecular Effects of Uptake of Gold Nanoparticles in Hela Cells. *Chembiochem* **2007,** *8* (11), 1237-1240.
56. Xie, J.; Xu, C.; Kohler, N.; Hou, Y.; Sun, S., Controlled Pegylation of Monodisperse Fe_3o_4 Nanoparticles for Reduced Non-Specific Uptake by Macrophage Cells. *Advanced Materials* **2007,** *19* (20), 3163-3166.
57. Harush-Frenkel, O.; Debotton, N.; Benita, S.; Altschuler, Y., Targeting of Nanoparticles to the Clathrin-Mediated Endocytic Pathway. *Biochemical and biophysical research communications* **2007,** *353* (1), 26-32.
58. Chen, K. L.; Bothun, G. D., Nanoparticles Meet Cell Membranes: Probing Nonspecific Interactions Using Model Membranes. *Environmental science & technology* **2013,** *48* (2), 873-880.
59. Hajipour, M. J.; Fromm, K. M.; Ashkarran, A. A.; de Aberasturi, D. J.; de Larramendi, I. R.; Rojo, T.; Serpooshan, V.; Parak, W. J.; Mahmoudi, M., Antibacterial Properties of Nanoparticles. *Trends in biotechnology* **2012,** *30* (10), 499-511.
60. Scott, J. R.; Barnett, T. C., Surface Proteins of Gram-Positive Bacteria and How They Get There. *Annual Review of Microbiology* **2006,** *60*, 397-423.
61. Nicolson, G. L., The Fluid—Mosaic Model of Membrane Structure: Still Relevant to Understanding the Structure, Function and Dynamics of Biological Membranes after More Than 40years. *Biochimica et Biophysica Acta (BBA)-Biomembranes* **2014,** *1838* (6), 1451-1466.
62. Li, L.; Shi, X.; Guo, X.; Li, H.; Xu, C., Ionic Protein–Lipid Interaction at the Plasma Membrane: What Can the Charge Do? *Trends in biochemical sciences* **2014,** *39* (3), 130-140.
63. Lombard, J., Once Upon a Time the Cell Membranes: 175 Years of Cell Boundary Research. *Biology direct* **2014,** *9* (1), 1-35.
64. Hu, Y.; Litwin, T.; Nagaraja, A. R.; Kwong, B.; Katz, J.; Watson, N.; Irvine, D. J., Cytosolic Delivery of Membrane-Impermeable Molecules in Dendritic Cells Using Ph-Responsive Core-Shell Nanoparticles. *Nano Letters* **2007,** *7* (10), 3056-3064.
65. Sandhu, K. K.; McIntosh, C. M.; Simard, J. M.; Smith, S. W.; Rotello, V. M., Gold Nanoparticle-Mediated Transfection of Mammalian Cells. *Bioconjugate chemistry* **2002,** *13* (1), 3-6.
66. Wolff, J. A.; Malone, R. W.; Williams, P.; Chong, W.; Acsadi, G.; Jani, A.; Felgner, P. L., Direct Gene Transfer into Mouse Muscle in Vivo. *Science* **1990,** *247* (4949), 1465-1468.

67. Liu, G.; Li, D.; Pasumarthy, M. K.; Kowalczyk, T. H.; Gedeon, C. R.; Hyatt, S. L.; Payne, J. M.; Miller, T. J.; Brunovskis, P.; Fink, T. L., Nanoparticles of Compacted DNA Transfect Postmitotic Cells. *Journal of Biological Chemistry* **2003,** *278* (35), 32578-32586.
68. Rojas-Chapana, J. A.; Correa-Duarte, M. A.; Ren, Z.; Kempa, K.; Giersig, M., Enhanced Introduction of Gold Nanoparticles into Vital Acidothiobacillus Ferrooxidans by Carbon Nanotube-Based Microwave Electroporation. *Nano Letters* **2004,** *4* (5), 985-988.
69. Tkachenko, A. G.; Xie, H.; Coleman, D.; Glomm, W.; Ryan, J.; Anderson, M. F.; Franzen, S.; Feldheim, D. L., Multifunctional Gold Nanoparticle-Peptide Complexes for Nuclear Targeting. *Journal of the American Chemical Society* **2003,** *125* (16), 4700-4701.
70. Pauling, L.; Corey, R. B., A Proposed Structure for the Nucleic Acids. *Proceedings of the National Academy of Sciences* **1953,** *39* (2), 84-97.
71. Csáki, A.; Maubach, G.; Born, D.; Reichert, J.; Fritzsche, W., DNA-Based Molecular Nanotechnology. *Single Molecules* **2002,** *3* (5-6), 275-280.
72. Prado-Gotor, R.; Grueso, E., A Kinetic Study of the Interaction of DNA with Gold Nanoparticles: Mechanistic Aspects of the Interaction. *Physical Chemistry Chemical Physics* **2011,** *13* (4), 1479-1489.
73. Pershina, A. G.; Sazonov, A.; Filimonov, V. D., Magnetic Nanoparticles–DNA Interactions: Design and Applications of Nanobiohybrid Systems. *Russian Chemical Reviews* **2014,** *83* (4), 299.
74. Shao, Q.; Wu, P.; Gu, P.; Xu, X.; Zhang, H.; Cai, C., Electrochemical and Spectroscopic Studies on the Conformational Structure of Hemoglobin Assembled on Gold Nanoparticles. *The Journal of Physical Chemistry B* **2011,** *115* (26), 8627-8637.
75. Luheshi, L. M.; Dobson, C. M., Bridging the Gap: From Protein Misfolding to Protein Misfolding Diseases. *FEBS letters* **2009,** *583* (16), 2581-2586.
76. Jahn, T. R.; Radford, S. E., The Yin and Yang of Protein Folding. *Febs Journal* **2005,** *272* (23), 5962-5970.
77. Horwich, A., Protein Aggregation in Disease: A Role for Folding Intermediates Forming Specific Multimeric Interactions. *The Journal of clinical investigation* **2002,** *110* (9), 1221-1232.
78. Bellotti, V.; Chiti, F., Amyloidogenesis in Its Biological Environment: Challenging a Fundamental Issue in Protein Misfolding Diseases. *Current opinion in structural biology* **2008,** *18* (6), 771-779.
79. Jha, S.; Sellin, D.; Seidel, R.; Winter, R., Amyloidogenic Propensities and Conformational Properties of Proiapp and Iapp in the Presence of Lipid Bilayer Membranes. *Journal of Molecular Biology* **2009,** *389* (5), 907-20.
80. Xue, W. F.; Hellewell, A. L.; Gosal, W. S.; Homans, S. W.; Hewitt, E. W.; Radford, S. E., Fibril Fragmentation Enhances Amyloid Cytotoxicity. *Journal of Biological Chemistry* **2009,** *284* (49), 34272-82.
81. Antosova, A.; Gazova, Z.; Fedunova, D.; Valusova, E.; Bystrenova, E.; Valle, F.; Daxnerova, Z.; Biscarini, F.; Antalik, M., Anti-Amyloidogenic Activity of Glutathione-Covered Gold Nanoparticles. *Materials Science and Engineering: C* **2012,** *32* (8), 2529-2535.
82. Gilman, S.; Koller, M.; Black, R. S.; Jenkins, L.; Griffith, S. G.; Fox, N. C.; Eisner, L.; Kirby, L.; Rovira, M. B.; Forette, F.; Orgogozo, J. M., Clinical Effects of Abeta Immunization (An1792) in Patients with Ad in an Interrupted Trial. *Neurology* **2005,** *64* (9), 1553-62.
83. Rinne, J. O.; Brooks, D. J.; Rossor, M. N.; Fox, N. C.; Bullock, R.; Klunk, W. E.; Mathis, C. A.; Blennow, K.; Barakos, J.; Okello, A. A.; Rodriguez Martinez de Liano, S.; Liu, E.; Koller, M.; Gregg, K. M.; Schenk, D.; Black, R.; Grundman, M., 11c-Pib Pet Assessment of Change in Fibrillar Amyloid-Beta Load in Patients with Alzheimer's Disease Treated with Bapineuzumab: A Phase 2, Double-Blind, Placebo-Controlled, Ascending-Dose Study. *Lancet Neurol* **2010,** *9* (4), 363-72.
84. Salloway, S.; Sperling, R.; Gilman, S.; Fox, N. C.; Blennow, K.; Raskind, M.; Sabbagh, M.; Honig, L. S.; Doody, R.; van Dyck, C. H.; Mulnard, R.; Barakos, J.; Gregg, K. M.; Liu, E.; Lieberburg, I.; Schenk, D.; Black, R.; Grundman, M., A Phase 2 Multiple Ascending Dose Trial of Bapineuzumab in Mild to Moderate Alzheimer Disease. *Neurology* **2009,** *73* (24), 2061-70.
85. Schnabel, J., Vaccines: Chasing the Dream. *Nature* **2011,** *475* (7355), S18-S19.

86. Velkova, A.; Tatarek-Nossol, M.; Andreetto, E.; Kapurniotu, A., Exploiting Cross-Amyloid Interactions to Inhibit Protein Aggregation but Not Function: Nanomolar Affinity Inhibition of Insulin Aggregation by an Iapp Mimic. *Angewandte Chemie International Edition* **2008,** *47* (37), 7114-8.
87. Gazova, Z.; Bellova, A.; Daxnerova, Z.; Imrich, J.; Kristian, P.; Tomascikova, J.; Bagelova, J.; Fedunova, D.; Antalik, M., Acridine Derivatives Inhibit Lysozyme Aggregation. *European Biophysics Journal* **2008,** *37* (7), 1261-1270.
88. Huggins, K. N.; Bisaglia, M.; Bubacco, L.; Tatarek-Nossol, M.; Kapurniotu, A.; Andersen, N. H., Designed Hairpin Peptides Interfere with Amyloidogenesis Pathways: Fibril Formation and Cytotoxicity Inhibition, Interception of the Preamyloid State. *Biochemistry* **2011,** *50* (38), 8202-12.
89. Bellova, A.; Bystrenova, E.; Koneracka, M.; Kopcansky, P.; Valle, F.; Tomasovicova, N.; Timko, M.; Bagelova, J.; Biscarini, F.; Gazova, Z., Effect of Fe_3o_4 Magnetic Nanoparticles on Lysozyme Amyloid Aggregation. *Nanotechnology* **2010,** *21* (6), 065103.
90. Fu, Z.; Luo, Y.; Derreumaux, P.; Wei, G., Induced Beta-Barrel Formation of the Alzheimer's Abeta25-35 Oligomers on Carbon Nanotube Surfaces: Implication for Amyloid Fibril Inhibition. *Biophysical journal* **2009,** *97* (6), 1795-1803.
91. Rocha, S.; Thunemann, A. F.; Pereira Mdo, C.; Coelho, M.; Mohwald, H.; Brezesinski, G., Influence of Fluorinated and Hydrogenated Nanoparticles on the Structure and Fibrillogenesis of Amyloid Beta-Peptide. *Biophysical Chemistry* **2008,** *137* (1), 35-42.
92. Moyano, D. F.; Rotello, V. M., Nano Meets Biology: Structure and Function at the Nanoparticle Interface. *Langmuir* **2011,** *27* (17), 10376-10385.
93. Nel, A. E.; Madler, L.; Velegol, D.; Xia, T.; Hoek, E. M.; Somasundaran, P.; Klaessig, F.; Castranova, V.; Thompson, M., Understanding Biophysicochemical Interactions at the Nano-Bio Interface. *Nature Materials* **2009,** *8* (7), 543-57.
94. Sigmund, W.; Pyrgiotakis, G.; Daga, A., 11 Theory and Applications of Colloidal Processing. *Chemical Processing of Ceramics* **2005**, 269.
95. Inbaraj, B. S.; Tsai, T.-Y.; Chen, B.-H., Synthesis, Characterization and Antibacterial Activity of Superparamagnetic Nanoparticles Modified with Glycol Chitosan. *Science and Technology of Advanced Materials* **2016**.
96. Dwivedi, S.; Wahab, R.; Khan, F.; Mishra, Y. K.; Musarrat, J.; Al-Khedhairy, A. A., Reactive Oxygen Species Mediated Bacterial Biofilm Inhibition Via Zinc Oxide Nanoparticles and Their Statistical Determination. *PloS one* **2014,** *9* (11), e111289.
97. Jiang, W.; Yang, K.; Vachet, R. W.; Xing, B., Interaction between Oxide Nanoparticles and Biomolecules of the Bacterial Cell Envelope as Examined by Infrared Spectroscopy. *Langmuir* **2010,** *26* (23), 18071-18077.
98. Adams, L. K.; Lyon, D. Y.; Alvarez, P. J., Comparative Eco-Toxicity of Nanoscale Tio 2, Sio 2, and Zno Water Suspensions. *Water research* **2006,** *40* (19), 3527-3532.
99. Brayner, R.; Ferrari-Iliou, R.; Brivois, N.; Djediat, S.; Benedetti, M. F.; Fiévet, F., Toxicological Impact Studies Based on Escherichia Coli Bacteria in Ultrafine Zno Nanoparticles Colloidal Medium. *Nano Letters* **2006,** *6* (4), 866-870.
100. Zhang, S.; Gao, H.; Bao, G., Physical Principles of Nanoparticle Cellular Endocytosis. *ACS nano* **2015,** *9* (9), 8655-8671.
101. Decuzzi, P.; Ferrari, M., The Role of Specific and Non-Specific Interactions in Receptor-Mediated Endocytosis of Nanoparticles. *Biomaterials* **2007,** *28* (18), 2915-2922.
102. Pramanik, S.; Chatterjee, S.; Saha, A.; Devi, P. S.; Suresh Kumar, G., Unraveling the Interaction of Silver Nanoparticles with Mammalian and Bacterial DNA. *The Journal of Physical Chemistry B* **2016**.
103. An, H.; Jin, B., Prospects of Nanoparticle–DNA Binding and Its Implications in Medical Biotechnology. *Biotechnology advances* **2012,** *30* (6), 1721-1732.
104. Monopoli, M. P.; Aberg, C.; Salvati, A.; Dawson, K. A., Biomolecular Coronas Provide the Biological Identity of Nanosized Materials. *Nature nanotechnology* **2012,** *7* (12), 779-786.
105. Chithrani, B. D.; Ghazani, A. A.; Chan, W. C., Determining the Size and Shape Dependence of Gold Nanoparticle Uptake into Mammalian Cells. *Nano Letters* **2006,** *6* (4), 662-8.

106. De Jong, W. H.; Hagens, W. I.; Krystek, P.; Burger, M. C.; Sips, A. J.; Geertsma, R. E., Particle Size-Dependent Organ Distribution of Gold Nanoparticles after Intravenous Administration. *Biomaterials* **2008,** *29* (12), 1912-9.
107. Dobrovolskaia, M. A.; Aggarwal, P.; Hall, J. B.; McNeil, S. E., Preclinical Studies to Understand Nanoparticle Interaction with the Immune System and Its Potential Effects on Nanoparticle Biodistribution. *Molecular Pharmaceutics* **2008,** *5* (4), 487-95.
108. McNeil, S. E., Nanotechnology for the Biologist. *Journal of Leukocyte Biology* **2005,** *78* (3), 585-94.
109. Tomalia, D. A.; Reyna, L. A.; Svenson, S., Dendrimers as Multi-Purpose Nanodevices for Oncology Drug Delivery and Diagnostic Imaging. *Biochemical Society Transactions* **2007,** *35* (Pt 1), 61-7.
110. Tyrrell, D. A.; Richardson, V. J.; Ryman, B. E., The Effect of Serum Protein Fractions on Liposome-Cell Interactions in Cultured Cells and the Perfused Rat Liver. *Biochimica et Biophysica Acta (BBA)-General Subjects* **1977,** *497* (2), 469-480.
111. Kiwada, H.; Miyajima, T.; Kato, Y., Studies on the Uptake Mechanism of Liposomes by Perfused Rat Liver. Ii. An Indispensable Factor for Liver Uptake in Serum. *Chemical & pharmaceutical bulletin* **1987,** *35* (3), 1189.
112. Dutta, D.; Sundaram, S. K.; Teeguarden, J. G.; Riley, B. J.; Fifield, L. S.; Jacobs, J. M.; Addleman, S. R.; Kaysen, G. A.; Moudgil, B. M.; Weber, T. J., Adsorbed Proteins Influence the Biological Activity and Molecular Targeting of Nanomaterials. *Toxicological Sciences* **2007,** *100* (1), 303-315.
113. Lynch, I., Are There Generic Mechanisms Governing Interactions between Nanoparticles and Cells? Epitope Mapping the Outer Layer of the Protein-Material Interface. *Physica A: Statistical Mechanics and its Applications* **2007,** *373*, 511-520.
114. Aggarwal, P.; Hall, J. B.; McLeland, C. B.; Dobrovolskaia, M. A.; McNeil, S. E., Nanoparticle Interaction with Plasma Proteins as It Relates to Particle Biodistribution, Biocompatibility and Therapeutic Efficacy. *Advanced drug delivery reviews* **2009,** *61* (6), 428-437.
115. Dobrovolskaia, M. A.; Patri, A. K.; Zheng, J.; Clogston, J. D.; Ayub, N.; Aggarwal, P.; Neun, B. W.; Hall, J. B.; McNeil, S. E., Interaction of Colloidal Gold Nanoparticles with Human Blood: Effects on Particle Size and Analysis of Plasma Protein Binding Profiles. *Nanomedicine* **2009,** *5* (2), 106-17.
116. Goppert, T. M.; Muller, R. H., Protein Adsorption Patterns on Poloxamer- and Poloxamine-Stabilized Solid Lipid Nanoparticles (Sln). *European Journal of Pharmaceutics and Biopharmaceutics* **2005,** *60* (3), 361-72.
117. Kim, H. R.; Andrieux, K.; Delomenie, C.; Chacun, H.; Appel, M.; Desmaele, D.; Taran, F.; Georgin, D.; Couvreur, P.; Taverna, M., Analysis of Plasma Protein Adsorption onto Pegylated Nanoparticles by Complementary Methods: 2-De, Ce and Protein Lab-on-Chip System. *Electrophoresis* **2007,** *28* (13), 2252-61.
118. Goppert, T. M.; Muller, R. H., Polysorbate-Stabilized Solid Lipid Nanoparticles as Colloidal Carriers for Intravenous Targeting of Drugs to the Brain: Comparison of Plasma Protein Adsorption Patterns. *Journal of drug targeting* **2005,** *13* (3), 179-187.
119. Lynch, I.; Dawson, K. A., Protein-Nanoparticle Interactions. *Nano Today* **2008,** *3* (1), 40-47.
120. Oberdorster, G.; Ferin, J.; Gelein, R.; Soderholm, S. C.; Finkelstein, J., Role of the Alveolar Macrophage in Lung Injury: Studies with Ultrafine Particles. *Environ Health Perspect* **1992,** *97*, 193-9.
121. Donaldson, K.; Li, X. Y.; MacNee, W., Ultrafine (Nanometre) Particle Mediated Lung Injury. *Journal of Aerosol Science* **1998,** *29* (5), 553-560.
122. Brown, D. M.; Wilson, M. R.; MacNee, W.; Stone, V.; Donaldson, K., Size-Dependent Proinflammatory Effects of Ultrafine Polystyrene Particles: A Role for Surface Area and Oxidative Stress in the Enhanced Activity of Ultrafines. *Toxicology and applied pharmacology* **2001,** *175* (3), 191-199.

123. Adiseshaiah, P. P.; Hall, J. B.; McNeil, S. E., Nanomaterial Standards for Efficacy and Toxicity Assessment. *Wiley Interdisciplinary Reviews: Nanomedicine and Nanobiotechnology* **2009,** *2* (1), 99-112.
124. Lynch, I.; Cedervall, T.; Lundqvist, M.; Cabaleiro-Lago, C.; Linse, S.; Dawson, K. A., The Nanoparticle-Protein Complex as a Biological Entity; a Complex Fluids and Surface Science Challenge for the 21st Century. *Advances in colloid and interface science* **2007,** *134*, 167-174.
125. Calzolai, L.; Franchini, F.; Gilliland, D.; Rossi, F., Protein-- Nanoparticle Interaction: Identification of the Ubiquitin--Gold Nanoparticle Interaction Site. *Nano letters* **2010,** *10* (8), 3101-3105.
126. Lynch, I.; Dawson, K. A.; Linse, S., Detecting Cryptic Epitopes Created by Nanoparticles. *Science Signalling* **2006,** *2006* (327), pe14.
127. Shang, L.; Wang, Y.; Jiang, J.; Dong, S., Ph-Dependent Protein Conformational Changes in Albumin: Gold Nanoparticle Bioconjugates: A Spectroscopic Study. *Langmuir* **2007,** *23* (5), 2714-2721.
128. Dizaj, S. M.; Lotfipour, F.; Barzegar-Jalali, M.; Zarrintan, M. H.; Adibkia, K., Antimicrobial Activity of the Metals and Metal Oxide Nanoparticles. *Materials Science and Engineering: C* **2014,** *44*, 278-284.
129. Seil, J. T.; Webster, T. J., Antimicrobial Applications of Nanotechnology: Methods and Literature. *International journal of nanomedicine* **2012,** *7*, 2767.
130. Rasmussen, J. W.; Martinez, E.; Louka, P.; Wingett, D. G., Zinc Oxide Nanoparticles for Selective Destruction of Tumor Cells and Potential for Drug Delivery Applications. *Expert opinion on drug delivery* **2010,** *7* (9), 1063-1077.
131. Nel, A.; Xia, T.; Mädler, L.; Li, N., Toxic Potential of Materials at the Nanolevel. *Science* **2006,** *311* (5761), 622-627.
132. Zhang, Y.; Chen, W.; Wang, S.; Liu, Y.; Pope, C., Phototoxicity of Zinc Oxide Nanoparticle Conjugatesin Human Ovarian Cancer Nih: Ovcar-3 Cells. *Journal of Biomedical Nanotechnology* **2008,** *4* (4), 432-438.
133. Punnoose, A.; Kongara, M. R.; Wingett, D., Preferential Killing of Cancer Cells and Activated Human T Cells Using Zno Nanoparticles. U.S. Patent: **2012**; Vol. 8,187, p 638.
134. Vinardell, M. P.; Mitjans, M., Antitumor Activities of Metal Oxide Nanoparticles. *Nanomaterials* **2015,** *5* (2), 1004-1021.
135. Shawkey, A. M.; Rabeh, M. A.; Abdulall, A. K.; Abdellatif, O., Green Nanotechnology: Anticancer Activity of Silver Nanoparticles Using Citrullus Colocynthis Aqueous Extracts. *Advances in Life Science and Technology* **2013,** *13* (2013), 60-70.
136. Shen, W.; Xiong, H.; Xu, Y.; Cai, S.; Lu, H.; Yang, P., Zno− Poly (Methyl Methacrylate) Nanobeads for Enriching and Desalting Low-Abundant Proteins Followed by Directly Maldi-Tof Ms Analysis. *Analytical chemistry* **2008,** *80* (17), 6758-6763.
137. Dorfman, A.; Parajuli, O.; Kumar, N.; Hahm, J.-i., Novel Telomeric Repeat Elongation Assay Performed on Zinc Oxide Nanorod Array Supports. *Journal of nanoscience and nanotechnology* **2008,** *8* (1), 410-415.
138. Walter, S., Structure and Function of the Groe Chaperone. *Cellular and Molecular Life Sciences CMLS* **2002,** *59* (10), 1589-1597.
139. Young, J. C.; Agashe, V. R.; Siegers, K.; Hartl, F. U., Pathways of Chaperone-Mediated Protein Folding in the Cytosol. *Nature reviews Molecular cell biology* **2004,** *5* (10), 781-791.
140. Tandon, S.; Horowitz, P., Detergent-Assisted Refolding of Guanidinium Chloride-Denatured Rhodanese. The Effect of Lauryl Maltoside. *Journal of Biological Chemistry* **1986,** *261* (33), 15615-15618.
141. Karuppiah, N.; Sharma, A., Cyclodextrins as Protein Folding Aids. *Biochemical and biophysical research communications* **1995,** *211* (1), 60-66.
142. Rozema, D.; Gellman, S. H., Artificial Chaperones: Protein Refolding Via Sequential Use of Detergent and Cyclodextrin. *Journal of the American Chemical Society* **1995,** *117* (8), 2373-2374.
143. Cleland, J. L.; Hedgepeth, C.; Wang, D., Polyethylene Glycol Enhanced Refolding of Bovine Carbonic Anhydrase B. Reaction Stoichiometry and Refolding Model. *Journal of Biological Chemistry* **1992,** *267* (19), 13327-13334.

144. Cleland, J. L.; Wang, D. I. In *Cosolvent Effects on Refolding and Aggregation*, ACS Symposium Series, AMER CHEMICAL SOC 1155 16TH ST, NW, WASHINGTON, DC 20036: **1993**; pp 151-166.
145. Nomura, Y.; Ikeda, M.; Yamaguchi, N.; Aoyama, Y.; Akiyoshi, K., Protein Refolding Assisted by Self-Assembled Nanogels as Novel Artificial Molecular Chaperone. *FEBS letters* **2003,** *553* (3), 271-276.
146. Colvin, V. L.; Kulinowski, K. M., Nanoparticles as Catalysts for Protein Fibrillation. *Proceedings of the National Academy of Sciences* **2007,** *104* (21), 8679-8680.
147. Sear, R. P., Nucleation: Theory and Applications to Protein Solutions and Colloidal Suspensions. *Journal of Physics: Condensed Matter* **2007,** *19* (3), 033101.
148. Auer, S.; Trovato, A.; Vendruscolo, M., A Condensation-Ordering Mechanism in Nanoparticle-Catalyzed Peptide Aggregation. *PLoS Comput Biol* **2009,** *5* (8), e1000458.
149. Zaman, M.; Ahmad, E.; Qadeer, A.; Rabbani, G.; Khan, R. H., Nanoparticles in Relation to Peptide and Protein Aggregation. *International journal of nanomedicine* **2014,** *9*, 899.
150. Wu, W. H.; Sun, X.; Yu, Y. P.; Hu, J.; Zhao, L.; Liu, Q.; Zhao, Y. F.; Li, Y. M., Tio_2 Nanoparticles Promote Beta-Amyloid Fibrillation in Vitro. *Biochem Biophys Res Commun* **2008,** *373* (2), 315-8.
151. Linse, S.; Cabaleiro-Lago, C.; Xue, W.-F.; Lynch, I.; Lindman, S.; Thulin, E.; Radford, S. E.; Dawson, K. A., Nucleation of Protein Fibrillation by Nanoparticles. *Proceedings of the National Academy of Sciences* **2007,** *104* (21), 8691-8696.
152. De, M.; Rotello, V. M., Synthetic "Chaperones": Nanoparticle-Mediated Refolding of Thermally Denatured Proteins. *Chemical communications (Cambridge, England)* **2008,** *14* (30), 3504.
153. Rozema, D.; Gellman, S. H., Artificial Chaperone-Assisted Refolding of Denatured-Reduced Lysozyme: Modulation of the Competition between Renaturation and Aggregation. *Biochemistry* **1996,** *35* (49), 15760-15771.
154. Sivakama Sundari, C.; Raman, B.; Balasubramanian, D., Artificial Chaperoning of Insulin, Human Carbonic Anhydrase and Hen Egg Lysozyme Using Linear Dextrin Chains--a Sweet Route to the Native State of Globular Proteins. *FEBS letters* **1999,** *443* (2), 215-219.
155. You, C. C.; Miranda, O. R.; Gider, B.; Ghosh, P. S.; Kim, I. B.; Erdogan, B.; Krovi, S. A.; Bunz, U. H. F.; Rotello, V. M., Detection and Identification of Proteins Using Nanoparticle-Fluorescent Polymer 'Chemical Nose' Sensors. *Nature nanotechnology* **2007,** *2* (5), 318-323.
156. Shemetov, A. A.; Nabiev, I.; Sukhanova, A., Molecular Interaction of Proteins and Peptides with Nanoparticles. *Acs Nano* **2012,** *6* (6), 4585-4602.
157. Pihlasalo, S.; Kirjavainen, J.; Hänninen, P.; Härmä, H., High Sensitivity Luminescence Nanoparticle Assay for the Detection of Protein Aggregation. *Analytical chemistry* **2011,** *83* (4), 1163-1166.
158. Karran, E.; Mercken, M.; De Strooper, B., The Amyloid Cascade Hypothesis for Alzheimer's Disease: An Appraisal for the Development of Therapeutics. *Nature reviews Drug discovery* **2011,** *10* (9), 698-712.
159. Pillay, S.; Pillay, V.; Choonara, Y. E.; Naidoo, D.; Khan, R. A.; du Toit, L. C.; Ndesendo, V. M. K.; Modi, G.; Danckwerts, M. P.; Iyuke, S. E., Design, Biometric Simulation and Optimization of a Nano-Enabled Scaffold Device for Enhanced Delivery of Dopamine to the Brain. *International journal of pharmaceutics* **2009,** *382* (1), 277-290.
160. Trapani, A.; De Giglio, E.; Cafagna, D.; Denora, N.; Agrimi, G.; Cassano, T.; Gaetani, S.; Cuomo, V.; Trapani, G., Characterization and Evaluation of Chitosan Nanoparticles for Dopamine Brain Delivery. *International journal of pharmaceutics* **2011,** *419* (1), 296-307.
161. Md, S.; Khan, R. A.; Mustafa, G.; Chuttani, K.; Baboota, S.; Sahni, J. K.; Ali, J., Bromocriptine Loaded Chitosan Nanoparticles Intended for Direct Nose to Brain Delivery: Pharmacodynamic, Pharmacokinetic and Scintigraphy Study in Mice Model. *European Journal of Pharmaceutical Sciences* **2013,** *48* (3), 393-405.
162. Yang, X.; Zheng, R.; Cai, Y.; Liao, M.; Yuan, W.; Liu, Z., Controlled-Release Levodopa Methyl Ester/Benserazide-Loaded Nanoparticles Ameliorate Levodopa-Induced Dyskinesia in Rats. *International journal of nanomedicine* **2012,** *7*, 2077.

163. Azeem, A.; Talegaonkar, S.; Negi, L. M.; Ahmad, F. J.; Khar, R. K.; Iqbal, Z., Oil Based Nanocarrier System for Transdermal Delivery of Ropinirole: A Mechanistic, Pharmacokinetic and Biochemical Investigation. *International journal of pharmaceutics* **2012,** *422* (1), 436-444.
164. Ikeda, K.; Okada, T.; Sawada, S.-i.; Akiyoshi, K.; Matsuzaki, K., Inhibition of the Formation of Amyloid B-Protein Fibrils Using Biocompatible Nanogels as Artificial Chaperones. *FEBS letters* **2006,** *580* (28), 6587-6595.
165. Baek, M.; Kim, M. K.; Cho, H. J.; Lee, J. A.; Yu, J.; Chung, H. E.; Choi, S. J. In *Factors Influencing the Cytotoxicity of Zinc Oxide Nanoparticles: Particle Size and Surface Charge*, Journal of Physics: Conference Series, IOP Publishing: p 012044.
166. Mohammadi-Samani, S.; Miri, R.; Salmanpour, M.; Khalighian, N.; Sotoudeh, S.; Erfani, N., Preparation and Assessment of Chitosan-Coated Superparamagnetic Fe_3o_4 Nanoparticles for Controlled Delivery of Methotrexate. *Research in pharmaceutical sciences* **2013,** *8* (1), 25.
167. Arakha, M.; Saleem, M.; Mallick, B. C.; Jha, S., The Effects of Interfacial Potential on Antimicrobial Propensity of Zno Nanoparticle. *Scientific reports* **2015,** *5*.
168. Durairaj, R.; Amirulhusni, A. N.; Palanisamy, N. K.; Mohd-Zain, Z.; Ping, L. J., Antibacterial Effect of Silver Nanoparticles on Multi Drug Resistant Pseudomonas Aeruginosa. *International Science Index* **2012,** *6* (7), 07-22.
169. De, J.; Ramaiah, N.; Vardanyan, L., Detoxification of Toxic Heavy Metals by Marine Bacteria Highly Resistant to Mercury. *Marine Biotechnology* **2008,** *10* (4), 471-477.
170. Possel, H.; Noack, H.; Augustin, W.; Keilhoff, G.; Wolf, G., 2, 7-Dihydrodichlorofluorescein Diacetate as a Fluorescent Marker for Peroxynitrite Formation. *FEBS letters* **1997,** *416* (2), 175-178.
171. Kang, M.; So, E.; Simons, A.; Spitz, D.; Ouchi, T., DNA Damage Induces Reactive Oxygen Species Generation through the H2ax-Nox1/Rac1 Pathway. *Cell death & disease* **2012,** *3* (1), e249.
172. Olive, P. L.; Banáth, J. P., The Comet Assay: A Method to Measure DNA Damage in Individual Cells. *NATURE PROTOCOLS-ELECTRONIC EDITION*- **2006,** *1* (1), 23.
173. Lu, Z.; Zhang, C.; Zhai, Z., Nucleoplasmin Regulates Chromatin Condensation During Apoptosis. *Proc. Natl. Acad. Sci.* **2005,** *102* (8), 2778-2783.
174. Suman, S.; Pandey, A.; Chandna, S., An Improved Non-Enzymatic "DNA Ladder Assay" for More Sensitive and Early Detection of Apoptosis. *Cytotechnology* **2012,** *64* (1), 9-14.
175. Wang, J.; Deng, X.; Zhang, F.; Chen, D.; Ding, W., Zno Nanoparticle-Induced Oxidative Stress Triggers Apoptosis by Activating Jnk Signaling Pathway in Cultured Primary Astrocytes. *Nanoscale research letters* **2014,** *9* (1), 1-12.
176. Bainor, A.; Chang, L.; McQuade, T. J.; Webb, B.; Gestwicki, J. E., Bicinchoninic Acid (Bca) Assay in Low Volume. *Analytical Biochemistry* **2011,** *410* (2), 310-312.
177. Van Der Spoel, D.; Lindahl, E.; Hess, B.; Groenhof, G.; Mark, A. E.; Berendsen, H. J., Gromacs: Fast, Flexible, and Free. *Journal of Computational Chemistry* **2005,** *26* (16), 1701-1718.
178. Hsu, S.-T. D.; Breukink, E.; Tischenko, E.; Lutters, M. A.; de Kruijff, B.; Kaptein, R.; Bonvin, A. M.; van Nuland, N. A., The Nisin–Lipid Ii Complex Reveals a Pyrophosphate Cage That Provides a Blueprint for Novel Antibiotics. *Nature Structural & Molecular Biology* **2004,** *11* (10), 963-967.
179. Malde, A. K.; Zuo, L.; Breeze, M.; Stroet, M.; Poger, D.; Nair, P. C.; Oostenbrink, C.; Mark, A. E., An Automated Force Field Topology Builder (Atb) and Repository: Version 1.0. *Journal of Chemical Theory and Computation* **2011,** *7* (12), 4026-4037.
180. Kyrychenko, A.; Korsun, O. M.; Gubin, I. I.; Kovalenko, S. M.; Kalugin, O. N., Atomistic Simulations of Coating of Silver Nanoparticles with Poly (Vinylpyrrolidone) Oligomers: Effect of Oligomer Chain Length. *The Journal of Physical Chemistry C* **2015,** *119* (14), 7888-7899.
181. Berendsen, H. J.; Postma, J. P. M.; van Gunsteren, W. F.; DiNola, A.; Haak, J., Molecular Dynamics with Coupling to an External Bath. *Journal of Chemical Physics* **1984,** *81* (8), 3684-3690.
182. Hess, B.; Bekker, H.; Berendsen, H. J.; Fraaije, J. G., Lincs: A Linear Constraint Solver for Molecular Simulations. *Journal of Computational Chemistry* **1997,** *18* (12), 1463-1472.
183. Darden, T.; York, D.; Pedersen, L., Particle Mesh Ewald: An N· Log (N) Method for Ewald Sums in Large Systems. *J. Chem. Phys* **1993,** *98* (12), 10089-10092.

184. Humphrey, W.; Dalke, A.; Schulten, K., Vmd: Visual Molecular Dynamics. *Journal of Molecular Graphics* **1996,** *14* (1), 33-38.
185. Jha, S.; Patil, S. M.; Gibson, J.; Nelson, C. E.; Alder, N. N.; Alexandrescu, A. T., Mechanism of Amylin Fibrillization Enhancement by Heparin. *Journal of Biological Chemistry* **2011,** *286* (26), 22894-22904.
186. Jha, S.; Snell, J. M.; Sheftic, S. R.; Patil, S. M.; Daniels, S. B.; Kolling, F. W.; Alexandrescu, A. T., Ph Dependence of Amylin Fibrillization. *Biochemistry* **2014,** *53* (2), 300-310.
187. Ghorbani, H. R.; Mehr, F. P.; Pazoki, H.; Rahmani, B. M., Synthesis of Zno Nanoparticles by Precipitation Method. *Oriental Journal of Chemistry* **2015,** *31* (2), 1219-1221.
188. Zak, A. K.; Majid, W. A.; Darroudi, M.; Yousefi, R., Synthesis and Characterization of Zno Nanoparticles Prepared in Gelatin Media. *Materials Letters* **2011,** *65* (1), 70-73.
189. Kumar, S. S.; Venkateswarlu, P.; Rao, V. R.; Rao, G. N., Synthesis, Characterization and Optical Properties of Zinc Oxide Nanoparticles. *International Nano Letters* **2013,** *3* (1), 1-6.
190. Xiong, H. M.; Shchukin, D. G.; Möhwald, H.; Xu, Y.; Xia, Y. Y., Sonochemical Synthesis of Highly Luminescent Zinc Oxide Nanoparticles Doped with Magnesium (Ii). *Angewandte Chemie International Edition* **2009,** *48* (15), 2727-2731.
191. Che, M.; Védrine, J. C., *Characterization of Solid Materials and Heterogeneous Catalysts: From Structure to Surface Reactivity*. John Wiley & Sons: **2012**.
192. Baruah, S.; Dutta, J., Ph-Dependent Growth of Zinc Oxide Nanorods. *Journal of Crystal Growth* **2009,** *311* (8), 2549-2554.
193. Khan, M. M.; Ansari, S. A.; Pradhan, D.; Ansari, M. O.; Lee, J.; Cho, M. H., Band Gap Engineered Tio $_2$ Nanoparticles for Visible Light Induced Photoelectrochemical and Photocatalytic Studies. *Journal of Materials Chemistry A* **2014,** *2* (3), 637-644.
194. Wang, J.; Wang, Z.; Huang, B.; Ma, Y.; Liu, Y.; Qin, X.; Zhang, X.; Dai, Y., Oxygen Vacancy Induced Band-Gap Narrowing and Enhanced Visible Light Photocatalytic Activity of Zno. *ACS applied materials & interfaces* **2012,** *4* (8), 4024-4030.
195. Sifontes, A. B.; Rosales, M.; Méndez, F. J.; Oviedo, O.; Zoltan, T., Effect of Calcination Temperature on Structural Properties and Photocatalytic Activity of Ceria Nanoparticles Synthesized Employing Chitosan as Template. *Journal of Nanomaterials* **2013,** *2013*, 1.
196. Hjiri, M.; Mir, L. E.; Leonardi, S. G., Synthesis, Characterization and Sensing Properties of Azo and Izo Nanomaterials. *Chemosensors* **2014,** *2* (2), 121-130.
197. Tankhiwale, R.; Bajpai, S., Preparation, Characterization and Antibacterial Applications of Zno-Nanoparticles Coated Polyethylene Films for Food Packaging. *Colloids and Surfaces B: Biointerfaces* **2012,** *90*, 16-20.
198. Vigneshwaran, N.; Kumar, S.; Kathe, A.; Varadarajan, P.; Prasad, V., Functional Finishing of Cotton Fabrics Using Zinc Oxide–Soluble Starch Nanocomposites. *Nanotechnology* **2006,** *17* (20), 5087.
199. Bang, S.; Lee, S.; Park, T.; Ko, Y.; Shin, S.; Yim, S.-Y.; Seo, H.; Jeon, H., Dual Optical Functionality of Local Surface Plasmon Resonance for Ruo 2 Nanoparticle–Zno Nanorod Hybrids Grown by Atomic Layer Deposition. *Journal of Materials Chemistry* **2012,** *22* (28), 14141-14148.
200. Marotti, R.; Giorgi, P.; Machado, G.; Dalchiele, E., Crystallite Size Dependence of Band Gap Energy for Electrodeposited Zno Grown at Different Temperatures. *Solar Energy Materials and Solar Cells* **2006,** *90* (15), 2356-2361.
201. Gupta, A. K.; Curtis, A. S., Lactoferrin and Ceruloplasmin Derivatized Superparamagnetic Iron Oxide Nanoparticles for Targeting Cell Surface Receptors. *Biomaterials* **2004,** *25* (15), 3029-3040.
202. Mahmoudi, M.; Hofmann, H.; Rothen-Rutishauser, B.; Petri-Fink, A., Assessing the in Vitro and in Vivo Toxicity of Superparamagnetic Iron Oxide Nanoparticles. *Chemical reviews* **2011,** *112* (4), 2323-2338.
203. Bucak, S.; Sezer, A. D.; Yavuztürk, B., *Magnetic Nanoparticles: Synthesis, Surface Modifications and Application in Drug Delivery*. Citeseer: **2012**.
204. Shan, Z.; Yang, W.-S.; Zhang, X.; Huang, Q.-M.; Ye, H., Preparation and Characterization of Carboxyl-Group Functionalized Superparamagnetic Nanoparticles and T He Potential for Bio-Applications. *Journal of the Brazilian Chemical Society* **2007,** *18* (7), 1329-1335.

205. Song, K.; Lee, Y.; Jo, M. R.; Nam, K. M.; Kang, Y.-M., Comprehensive Design of Carbon-Encapsulated Fe3o4 Nanocrystals and Their Lithium Storage Properties. *Nanotechnology* **2012,** *23* (50), 505401.
206. Zhang, M.; Zhang, X.; He, X.; Chen, L.; Zhang, Y., A Self-Assembled Polydopamine Film on the Surface of Magnetic Nanoparticles for Specific Capture of Protein. *Nanoscale* **2012,** *4* (10), 3141-3147.
207. Arokiyaraj, S.; Saravanan, M.; Prakash, N. U.; Arasu, M. V.; Vijayakumar, B.; Vincent, S., Enhanced Antibacterial Activity of Iron Oxide Magnetic Nanoparticles Treated with Argemone Mexicana L. Leaf Extract: An in Vitro Study. *Materials Research Bulletin* **2013,** *48* (9), 3323-3327.
208. Hong, S.; Chang, Y.; Rhee, I., Chitosan-Coated Ferrite (Fe_3o_4) Nanoparticles as a T2 Contrast Agent for Magnetic Resonance Imaging. *Journal of the Korean Physical Society* **2010,** *56*, 868-873.
209. ur Rahman, O.; Mohapatra, S. C.; Ahmad, S., Fe_3o_4 Inverse Spinal Super Paramagnetic Nanoparticles. *Materials Chemistry and Physics* **2012,** *132* (1), 196-202.
210. Unsoy, G.; Yalcin, S.; Khodadust, R.; Gunduz, G.; Gunduz, U., Synthesis Optimization and Characterization of Chitosan-Coated Iron Oxide Nanoparticles Produced for Biomedical Applications. *Journal of Nanoparticle Research* **2012,** *14* (11), 1-13.
211. Yu, S.; Chow, G. M., Carboxyl Group (–Co 2 H) Functionalized Ferrimagnetic Iron Oxide Nanoparticles for Potential Bio-Applications. *Journal of Materials Chemistry* **2004,** *14* (18), 2781-2786.
212. Johnson, D. B., Chemical and Microbiological Characteristics of Mineral Spoils and Drainage Waters at Abandoned Coal and Metal Mines. *Water, Air and Soil Pollution: Focus* **2003,** *3* (1), 47-66.
213. Castro-Silva, M. A.; Lima, A. O. d. S.; Gerchenski, A. V.; Jaques, D. B.; Rodrigues, A. L.; Souza, P. L. d.; Rörig, L. R., Heavy Metal Resistance of Microorganisms Isolated from Coal Mining Environments of Santa Catarina. *Brazilian Journal of Microbiology* **2003,** *34*, 45-47.
214. Fayaz, A. M.; Balaji, K.; Girilal, M.; Yadav, R.; Kalaichelvan, P. T.; Venketesan, R., Biogenic Synthesis of Silver Nanoparticles and Their Synergistic Effect with Antibiotics: A Study against Gram-Positive and Gram-Negative Bacteria. *Nanomedicine: Nanotechnology, Biology and Medicine* **2010,** *6* (1), 103-109.
215. Chowdhury, S.; Basu, A.; Kundu, S., Green Synthesis of Protein Capped Silver Nanoparticles from Phytopathogenic Fungus Macrophomina Phaseolina (Tassi) Goid with Antimicrobial Properties against Multidrug-Resistant Bacteria. *Nanoscale research letters* **2014,** *9* (1), 1-11.
216. Ramanathan, R.; Field, M. R.; O'Mullane, A. P.; Smooker, P. M.; Bhargava, S. K.; Bansal, V., Aqueous Phase Synthesis of Copper Nanoparticles: A Link between Heavy Metal Resistance and Nanoparticle Synthesis Ability in Bacterial Systems. *Nanoscale* **2013,** *5* (6), 2300-2306.
217. Bar, H.; Bhui, D. K.; Sahoo, G. P.; Sarkar, P.; De, S. P.; Misra, A., Green Synthesis of Silver Nanoparticles Using Latex of Jatropha Curcas. *Colloids and surfaces A: Physicochemical and engineering aspects* **2009,** *339* (1), 134-139.
218. Vijayaraghavan, K.; Nalini, S. K.; Prakash, N. U.; Madhankumar, D., One Step Green Synthesis of Silver Nano/Microparticles Using Extracts of *Trachyspermum Ammi* and *Papaver Somniferum*. *Colloids and Surfaces B: Biointerfaces* **2012,** *94*, 114-117.
219. Mohan, S.; Oluwafemi, O. S.; George, S. C.; Jayachandran, V.; Lewu, F. B.; Songca, S. P.; Kalarikkal, N.; Thomas, S., Completely Green Synthesis of Dextrose Reduced Silver Nanoparticles, Its Antimicrobial and Sensing Properties. *Carbohydrate polymers* **2014,** *106*, 469-474.
220. Sadowski, Z., Biosynthesis and Application of Silver and Gold Nanoparticles. **2010**.
221. Huang, Z.; Zheng, X.; Yan, D.; Yin, G.; Liao, X.; Kang, Y.; Yao, Y.; Huang, D.; Hao, B., Toxicological Effect of Zno Nanoparticles Based on Bacteria. *Langmuir* **2008,** *24* (8), 4140-4144.
222. Jones, N.; Ray, B.; Ranjit, K. T.; Manna, A. C., Antibacterial Activity of Zno Nanoparticle Suspensions on a Broad Spectrum of Microorganisms. *FEMS microbiology letters* **2008,** *279* (1), 71-76.

223. Leung, Y.; Chan, C.; Ng, A.; Chan, H.; Chiang, M.; Djurišić, A.; Ng, Y.; Jim, W.; Guo, M.; Leung, F., Antibacterial Activity of Zno Nanoparticles with a Modified Surface under Ambient Illumination. *Nanotechnology* **2012,** *23* (47), 475703.
224. Liu, S.; Huang, G.; Yu, J.; Ng, T. W.; Yip, H. Y.; Wong, P. K., Porous Fluorinated Sno2 Hollow Nanospheres: Transformative Self-Assembly and Photocatalytic Inactivation of Bacteria. *ACS applied materials & interfaces* **2014,** *6* (4), 2407-2414.
225. Su, H.-L.; Chou, C.-C.; Hung, D.-J.; Lin, S.-H.; Pao, I.-C.; Lin, J.-H.; Huang, F.-L.; Dong, R.-X.; Lin, J.-J., The Disruption of Bacterial Membrane Integrity through Ros Generation Induced by Nanohybrids of Silver and Clay. *Biomaterials* **2009,** *30* (30), 5979-5987.
226. Tavares, A. F. N.; Teixeira, M.; Romão, C. C.; Seixas, J. D.; Nobre, L. S.; Saraiva, L. M., Reactive Oxygen Species Mediate Bactericidal Killing Elicited by Carbon Monoxide-Releasing Molecules. *Journal of Biological Chemistry* **2011,** *286* (30), 26708-26717.
227. Xie, Y.; He, Y.; Irwin, P. L.; Jin, T.; Shi, X., Antibacterial Activity and Mechanism of Action of Zinc Oxide Nanoparticles against *Campylobacter Jejuni*. *Applied and environmental microbiology* **2011,** *77* (7), 2325-2331.
228. Dutta, R.; Nenavathu, B. P.; Gangishetty, M. K.; Reddy, A., Studies on Antibacterial Activity of Zno Nanoparticles by Ros Induced Lipid Peroxidation. *Colloids and Surfaces B: Biointerfaces* **2012,** *94*, 143-150.
229. Alves, C. S.; Melo, M. N.; Franquelim, H. G.; Ferre, R.; Planas, M.; Feliu, L.; Bardají, E.; Kowalczyk, W.; Andreu, D.; Santos, N. C., Escherichia Coli Cell Surface Perturbation and Disruption Induced by Antimicrobial Peptides Bp100 and Pepr. *Journal of Biological Chemistry* **2010,** *285* (36), 27536-27544.
230. Espitia, P. J. P.; Soares, N. d. F. F.; dos Reis Coimbra, J. S.; de Andrade, N. J.; Cruz, R. S.; Medeiros, E. A. A., Zinc Oxide Nanoparticles: Synthesis, Antimicrobial Activity and Food Packaging Applications. *Food and Bioprocess Technology* **2012,** *5* (5), 1447-1464.
231. Becheri, A.; Dürr, M.; Nostro, P. L.; Baglioni, P., Synthesis and Characterization of Zinc Oxide Nanoparticles: Application to Textiles as Uv-Absorbers. *Journal of Nanoparticle Research* **2008,** *10* (4), 679-689.
232. Seven, O.; Dindar, B.; Aydemir, S.; Metin, D.; Ozinel, M.; Icli, S., Solar Photocatalytic Disinfection of a Group of Bacteria and Fungi Aqueous Suspensions with Tio 2, Zno and Sahara Desert Dust. *Journal of Photochemistry and Photobiology A: Chemistry* **2004,** *165* (1), 103-107.
233. Padmavathy, N.; Vijayaraghavan, R., Enhanced Bioactivity of Zno Nanoparticles—an Antimicrobial Study. *Science and Technology of Advanced Materials* **2016**.
234. Kairyte, K.; Kadys, A.; Luksiene, Z., Antibacterial and Antifungal Activity of Photoactivated Zno Nanoparticles in Suspension. *Journal of Photochemistry and Photobiology B: Biology* **2013,** *128*, 78-84.
235. Tran, N.; Mir, A.; Mallik, D.; Sinha, A.; Nayar, S.; Webster, T. J., Bactericidal Effect of Iron Oxide Nanoparticles on Staphylococcus Aureus. *International Journal of Nanomedicine* **2010,** *5*, 277-283.
236. Chatterjee, S.; Bandyopadhyay, A.; Sarkar, K., Effect of Iron Oxide and Gold Nanoparticles on Bacterial Growth Leading Towards Biological Application. *Journal of Nanobiotechnology* **2011,** *9* (34), 1.
237. Iconaru, S. L.; Prodan, A. M.; Le Coustumer, P.; Predoi, D., Synthesis and Antibacterial and Antibiofilm Activity of Iron Oxide Glycerol Nanoparticles Obtained by Coprecipitation Method. *Journal of Chemistry* **2012,** *2013*.
238. Borcherding, J.; Baltrusaitis, J.; Chen, H.; Stebounova, L.; Wu, C.-M.; Rubasinghege, G.; Mudunkotuwa, I. A.; Caraballo, J. C.; Zabner, J.; Grassian, V. H., Iron Oxide Nanoparticles Induce Pseudomonas Aeruginosa Growth, Induce Biofilm Formation, and Inhibit Antimicrobial Peptide Function. *Environmental Science: Nano* **2014,** *1* (2), 123-132.
239. Zheng, L.-Y.; Zhu, J.-F., Study on Antimicrobial Activity of Chitosan with Different Molecular Weights. *Carbohydrate polymers* **2003,** *54* (4), 527-530.
240. González-Flecha, B.; Demple, B., Metabolic Sources of Hydrogen Peroxide in Aerobically Growing Escherichia Coli. *Journal of Biological Chemistry* **1995,** *270* (23), 13681-13687.
241. Kumar, S. R.; Imlay, J. A., How Escherichia Coli Tolerates Profuse Hydrogen Peroxide Formation by a Catabolic Pathway. *Journal of bacteriology* **2013,** *195* (20), 4569-4579.

242. Auffan, M.; Rose, J.; Wiesner, M. R.; Bottero, J.-Y., Chemical Stability of Metallic Nanoparticles: A Parameter Controlling Their Potential Cellular Toxicity in Vitro. *Environmental Pollution* **2009,** *157* (4), 1127-1133.
243. Tian, L.; Lin, B.; Wu, L.; Li, K.; Liu, H.; Yan, J.; Liu, X.; Xi, Z., Neurotoxicity Induced by Zinc Oxide Nanoparticles: Age-Related Differences and Interaction. *Scientific reports* **2015,** *5*.
244. Hu, X.; Cook, S.; Wang, P.; Hwang, H.-m., In Vitro Evaluation of Cytotoxicity of Engineered Metal Oxide Nanoparticles. *Science of the Total Environment* **2009,** *407* (8), 3070-3072.
245. Hanley, C.; Layne, J.; Punnoose, A.; Reddy, K.; Coombs, I.; Coombs, A.; Feris, K.; Wingett, D., Preferential Killing of Cancer Cells and Activated Human T Cells Using Zno Nanoparticles. *Nanotechnology* **2008,** *19* (29), 295103.
246. Applerot, G.; Lellouche, J.; Lipovsky, A.; Nitzan, Y.; Lubart, R.; Gedanken, A.; Banin, E., Understanding the Antibacterial Mechanism of Cuo Nanoparticles: Revealing the Route of Induced Oxidative Stress. *Small* **2012,** *8* (21), 3326-3337.
247. AshaRani, P.; Low Kah Mun, G.; Hande, M. P.; Valiyaveettil, S., Cytotoxicity and Genotoxicity of Silver Nanoparticles in Human Cells. *ACS nano* **2008,** *3* (2), 279-290.
248. Al-Nasiry, S.; Geusens, N.; Hanssens, M.; Luyten, C.; Pijnenborg, R., The Use of Alamar Blue Assay for Quantitative Analysis of Viability, Migration and Invasion of Choriocarcinoma Cells. *Human reproduction* **2007,** *22* (5), 1304-1309.
249. Yin, Y.; Lin, Q.; Sun, H.; Chen, D.; Wu, Q.; Chen, X.; Li, S., Cytotoxic Effects of Zno Hierarchical Architectures on Rsc96 Schwann Cells. *Nanoscale Res. Lett.* **2012,** *7* (1), 1-8.
250. Wong, V. K.; Li, T.; Law, B. Y.; Ma, E. D.; Yip, N.; Michelangeli, F.; Law, C. K.; Zhang, M.; Lam, K. Y.; Chan, P., Saikosaponin-D, a Novel Serca Inhibitor, Induces Autophagic Cell Death in Apoptosis-Defective Cells. *Cell death & disease* **2013,** *4* (7), e720.
251. Kanzawa, T.; Kondo, Y.; Ito, H.; Kondo, S.; Germano, I., Induction of Autophagic Cell Death in Malignant Glioma Cells by Arsenic Trioxide. *Cancer research* **2003,** *63* (9), 2103-2108.
252. Kundu, S.; Kim, T. H.; Yoon, J. H.; Shin, H.-S.; Lee, J.; Jung, J. H.; Kim, H. S., Viriditoxin Regulates Apoptosis and Autophagy Via Mitotic Catastrophe and Microtubule Formation in Human Prostate Cancer Cells. *International journal of oncology* **2014,** *45* (6), 2331-2340.
253. Deb, M.; Sengupta, D.; Rath, S. K.; Kar, S.; Parbin, S.; Shilpi, A.; Pradhan, N.; Bhutia, S. K.; Roy, S.; Patra, S. K., Clusterin Gene Is Predominantly Regulated by Histone Modifications in Human Colon Cancer and Ectopic Expression of the Nuclear Isoform Induces Cell Death. *Biochimica et Biophysica Acta (BBA)-Molecular Basis of Disease* **2015,** *1852* (8), 1630-1645.
254. Toné, S.; Sugimoto, K.; Tanda, K.; Suda, T.; Uehira, K.; Kanouchi, H.; Samejima, K.; Minatogawa, Y.; Earnshaw, W. C., Three Distinct Stages of Apoptotic Nuclear Condensation Revealed by Time-Lapse Imaging, Biochemical and Electron Microscopy Analysis of Cell-Free Apoptosis. *Experimental cell research* **2007,** *313* (16), 3635-3644.
255. Gurunathan, S.; Han, J. W.; Eppakayala, V.; Jeyaraj, M.; Kim, J.-H., Cytotoxicity of Biologically Synthesized Silver Nanoparticles in Mda-Mb-231 Human Breast Cancer Cells. *BioMed research international* **2013,** *2013*.
256. Villanueva, A.; Canete, M.; Roca, A. G.; Calero, M.; Veintemillas-Verdaguer, S.; Serna, C. J.; del Puerto Morales, M.; Miranda, R., The Influence of Surface Functionalization on the Enhanced Internalization of Magnetic Nanoparticles in Cancer Cells. *Nanotechnology* **2009,** *20* (11), 115103.
257. Gratton, S. E.; Ropp, P. A.; Pohlhaus, P. D.; Luft, J. C.; Madden, V. J.; Napier, M. E.; DeSimone, J. M., The Effect of Particle Design on Cellular Internalization Pathways. *Proceedings of the National Academy of Sciences* **2008,** *105* (33), 11613-11618.
258. Karaman, D. S.; Desai, D.; Senthilkumar, R.; Johansson, E. M.; Råtts, N.; Odén, M.; Eriksson, J. E.; Sahlgren, C.; Toivola, D. M.; Rosenholm, J. M., Shape Engineering Vs Organic Modification of Inorganic Nanoparticles as a Tool for Enhancing Cellular Internalization. *Nanoscale research letters* **2012,** *7* (1), 1-14.
259. López-Meza, J. E.; Ochoa-Zarzosa, A.; Barboza-Corona, J. E.; Bideshi, D. K., Antimicrobial Peptides: Current and Potential Applications in Biomedical Therapies. *BioMed Research International* **2015,** *2015*.

260. Zasloff, M., Antimicrobial Peptides of Multicellular Organisms. *Nature* **2002,** *415* (6870), 389-395.
261. Jenssen, H.; Hamill, P.; Hancock, R. E., Peptide Antimicrobial Agents. *Clinical Microbiology Reviews* **2006,** *19* (3), 491-511.
262. Yount, N. Y.; Yeaman, M. R., Multidimensional Signatures in Antimicrobial Peptides. *Proceedings of the National Academy of Sciences* **2004,** *101* (19), 7363-7368.
263. Hasper, H. E.; de Kruijff, B.; Breukink, E., Assembly and Stability of Nisin-Lipid Ii Pores. *Biochemistry* **2004,** *43* (36), 11567-11575.
264. Hyde, A. J.; Parisot, J.; McNichol, A.; Bonev, B. B., Nisin-Induced Changes in Bacillus Morphology Suggest a Paradigm of Antibiotic Action. *Proceedings of the National Academy of Sciences* **2006,** *103* (52), 19896-19901.
265. Breukink, E.; Wiedemann, I.; Van Kraaij, C.; Kuipers, O.; Sahl, H.-G.; De Kruijff, B., Use of the Cell Wall Precursor Lipid Ii by a Pore-Forming Peptide Antibiotic. *Science* **1999,** *286* (5448), 2361-2364.
266. Mantovani, H. C.; Russell, J. B., Nisin Resistance of *Streptococcus Bovis*. *Applied and environmental microbiology* **2001,** *67* (2), 808-813.
267. Tai, Y.-C.; McGuire, J.; Neff, J. A., Nisin Antimicrobial Activity and Structural Characteristics at Hydrophobic Surfaces Coated with the Peo–Ppo–Peo Triblock Surfactant Pluronic® F108. *Journal of colloid and interface science* **2008,** *322* (1), 104-111.
268. Sun, Z.; Zhong, J.; Liang, X.; Liu, J.; Chen, X.; Huan, L., Novel Mechanism for Nisin Resistance Via Proteolytic Degradation of Nisin by the Nisin Resistance Protein Nsr. *Antimicrobial agents and chemotherapy* **2009,** *53* (5), 1964-1973.
269. Jarvis, B., Resistance to Nisin and Production of Nisin-Inactivating Enzymes by Several *Bacillus Species*. *Microbiology* **1967,** *47* (1), 33-48.
270. Zhou, H.; Fang, J.; Tian, Y.; Lu, X. Y., Mechanisms of Nisin Resistance in Gram-Positive Bacteria. *Annals of Microbiology* **2014,** *64* (2), 413-420.
271. Karam, L.; Jama, C.; Dhulster, P.; Chihib, N.-E., Study of Surface Interactions between Peptides, Materials and Bacteria for Setting up Antimicrobial Surfaces and Active Food Packaging. *Journal of Materials and Environmental Science* **2013,** *4* (5), 798-821.
272. Korbekandi, H.; Iravani, S., *Silver Nanoparticles*. INTECH: **2012**.
273. Adhikari, M. D.; Das, G.; Ramesh, A., Retention of Nisin Activity at Elevated Ph in an Organic Acid Complex and Gold Nanoparticle Composite. *Chemical Communications* **2012,** *48* (71), 8928-8930.
274. Zuo, G.; Huang, Q.; Wei, G.; Zhou, R.; Fang, H., Plugging into Proteins: Poisoning Protein Function by a Hydrophobic Nanoparticle. *ACS Nano* **2010,** *4* (12), 7508-7514.
275. Maiti, S.; Krishnan, D.; Barman, G.; Ghosh, S. K.; Laha, J. K., Antimicrobial Activities of Silver Nanoparticles Synthesized from Lycopersicon Esculentum Extract. *Journal of Analytical Science and Technology* **2014,** *5* (1), 1-7.
276. Slootweg, J. C.; van der Wal, S.; Quarles van Ufford, H.; Breukink, E.; Liskamp, R. M.; Rijkers, D. T., Synthesis, Antimicrobial Activity, and Membrane Permeabilizing Properties of C-Terminally Modified Nisin Conjugates Accessed by Cuaac. *Bioconjugate Chem.* **2013,** *24* (12), 2058-2066.
277. de Kruijff, B.; van Dam, V.; Breukink, E., Lipid Ii: A Central Component in Bacterial Cell Wall Synthesis and a Target for Antibiotics. *Prostaglandins Leukot. Essent. Fatty Acids* **2008,** *79* (3), 117-121.
278. Bhatia, S.; Bharti, A., Evaluating the Antimicrobial Activity of Nisin, Lysozyme and Ethylenediaminetetraacetate Incorporated in Starch Based Active Food Packaging Film. *Journal of Food Science and Technology* **2014,** *52* (6), 3504-3512.
279. Perreault, F.; de Faria, A. F.; Nejati, S.; Elimelech, M., Antimicrobial Properties of Graphene Oxide Nanosheets: Why Size Matters. *ACS nano* **2015,** *9* (7), 7226-7236.
280. Wu, Z.-C.; Zhang, Y.; Tao, T.-X.; Zhang, L.; Fong, H., Silver Nanoparticles on Amidoxime Fibers for Photo-Catalytic Degradation of Organic Dyes in Waste Water. *Applied Surface Science* **2010,** *257* (3), 1092-1097.

281. Saeed, K.; Khan, I.; Shah, T.; Park, S.-Y., Synthesis, Characterization and Photocatalytic Activity of Silver Nanoparticles/Amidoxime-Modified Polyacrylonitrile Nanofibers. *Fibers and Polymers* **2015,** *16* (9), 1870-1875.
282. Stiefel, P.; Schmidt-Emrich, S.; Maniura-Weber, K.; Ren, Q., Critical Aspects of Using Bacterial Cell Viability Assays with the Fluorophores Syto9 and Propidium Iodide. *BMC Microbiol* **2015,** *15* (1), 36.
283. Schneider, C. A.; Rasband, W. S.; Eliceiri, K. W., Nih Image to Imagej: 25 Years of Image Analysis. *Nat. Methods* **2012,** *9* (7), 671-675.
284. Zhang, Y.-M.; Rock, C. O., Membrane Lipid Homeostasis in Bacteria. *Nature Rev. Microbiol.* **2008,** *6* (3), 222-233.
285. Tyagi, P.; Singh, M.; Kumari, H.; Kumari, A.; Mukhopadhyay, K., Bactericidal Activity of Curcumin I Is Associated with Damaging of Bacterial Membrane. *PloS one* **2015,** *10* (3).
286. AlKhatib, Z.; Lagedroste, M.; Fey, I.; Kleinschrodt, D.; Abts, A.; Smits, S. H., Lantibiotic Immunity: Inhibition of Nisin Mediated Pore Formation by Nisi. *PloS one* **2014**.
287. Healy, B.; Field, D.; O'Connor, P. M.; Hill, C.; Cotter, P. D.; Ross, R. P., Intensive Mutagenesis of the Nisin Hinge Leads to the Rational Design of Enhanced Derivatives. *PloS one* **2013**.
288. Hyde, A. J.; Parisot, J.; McNichol, A.; Bonev, B. B., Nisin-Induced Changes in Bacillus Morphology Suggest a Paradigm of Antibiotic Action. *Proc. Natl. Acad. Sci.* **2006,** *103* (52), 19896-19901.
289. Wiedemann, I.; Breukink, E.; van Kraaij, C.; Kuipers, O. P.; Bierbaum, G.; de Kruijff, B.; Sahl, H.-G., Specific Binding of Nisin to the Peptidoglycan Precursor Lipid Ii Combines Pore Formation and Inhibition of Cell Wall Biosynthesis for Potent Antibiotic Activity. *J. Biol. Chem.* **2001,** *276* (3), 1772-1779.
290. Rezansoff, A.; Hunter, H.; Jing, W.; Park, I.; Kim, S.; Vogel, H., Interactions of the Antimicrobial Peptide Ac-Frwwhr-Nh2 with Model Membrane Systems and Bacterial Cells. *J Pept Res* **2005,** *65* (5), 491-501.
291. Karam, L.; Jama, C.; Dhulster, P.; Chihib, N.-E., Study of Surface Interactions between Peptides, Materials and Bacteria for Setting up Antimicrobial Surfaces and Active Food Packaging. *J Mater Environ Sci* **2013,** *4* (5), 798-821.
292. Sawaya, M. R.; Sambashivan, S.; Nelson, R.; Ivanova, M. I.; Sievers, S. A.; Apostol, M. I.; Thompson, M. J.; Balbirnie, M.; Wiltzius, J. J.; McFarlane, H. T., Atomic Structures of Amyloid Cross-&Bgr; Spines Reveal Varied Steric Zippers. *Nature* **2007,** *447* (7143), 453-457.
293. Zou, Y.; Hao, W.; Li, H.; Gao, Y.; Sun, Y.; Ma, G., New Insight into Amyloid Fibril Formation of Hen Egg White Lysozyme Using a Two-Step Temperature-Dependent Ftir Approach. *The Journal of Physical Chemistry B* **2014,** *118* (33), 9834-9843.
294. Sanfins, E.; Dairou, J.; Rodrigues-Lima, F.; Dupret, J.-M. In *Nanoparticle-Protein Interactions: From Crucial Plasma Proteins to Key Enzymes*, Journal of Physics: Conference Series, IOP Publishing: **2011**; p 012039.
295. Rana, S.; Yeh, Y.-C.; Rotello, V. M., Engineering the Nanoparticle–Protein Interface: Applications and Possibilities. *Current opinion in chemical biology* **2010,** *14* (6), 828-834.
296. Chakraborti, S.; Chatterjee, T.; Joshi, P.; Poddar, A.; Bhattacharyya, B.; Singh, S. P.; Gupta, V.; Chakrabarti, P., Structure and Activity of Lysozyme on Binding to Zno Nanoparticles. *Langmuir* **2009,** *26* (5), 3506-3513.
297. Böhm, G.; Muhr, R.; Jaenicke, R., Quantitative Analysis of Protein Far Uv Circular Dichroism Spectra by Neural Networks. *Protein engineering* **1992,** *5* (3), 191-195.
298. Möller, M.; Denicola, A., Protein Tryptophan Accessibility Studied by Fluorescence Quenching. *Biochemistry and Molecular Biology Education* **2002,** *30* (3), 175-178.
299. Chaturvedi, S. K.; Khan, J. M.; Siddiqi, M. K.; Alam, P.; Khan, R. H., Comparative Insight into Surfactants Mediated Amyloidogenesis of Lysozyme. *International journal of biological macromolecules* **2016,** *83*, 315-325.
300. Khan, J. M.; Chaturvedi, S. K.; Rahman, S. K.; Ishtikhar, M.; Qadeer, A.; Ahmad, E.; Khan, R. H., Protonation Favors Aggregation of Lysozyme with Sds. *Soft Matter* **2014,** *10* (15), 2591-2599.

Dissemination

Internationally indexed journals

1. **Arakha, M**., Borah, S. M., Saleem, M., Jha, A. N., Jha, S. Interfacial assembly at silver nanoparticle enhances the antibacterial efficacy of nisin, ***Free Radical Biology & Medicine***, 101, 434-445 (2016).
2. **Arakha, M.,** Saleem, M., Mallick, B.C., & Jha, S. The effects of interfacial potential on antimicrobial propensity of ZnO nanoparticle, ***Scientific Reports***, 5, 9578 (2015)**.**
3. **Arakha, M**., Pal, S., Samantarrai, D., Panigrahi, T.K., Mallick, B.C., Pramanik, K., Mallick, B., & Jha, S. Antimicrobial activity of iron oxide nanoparticle upon modulation of nanoparticle-bacteria interface, ***Scientific Reports***, 5, 14813 (2015)**.**
4. **Arakha, M**., Roy, J., Nayak, P. S., Mallick, B., & Jha, S., Zinc oxide nanoparticle energy band gap reduction triggers the oxidative stress resulting into autophagy-mediated apoptotic cell death (***under revision***).
5. Nayak, P.S.[†] , **Arakha, M.**[†] , Kumar , A., Asthana, S. , Mallick , B.C., & Jha, S., An approach towards continuous production of silver nanoparticle using *Bacillus thuringiensis*, ***RSC Advances,*** 6, 8232 (2016).
6. Prince, A., Sandhu, P., Dash, E., Sharma, S., **Arakha, M.,** Jha, S., Akhter, Y., Saleem, M., Lipid-II independent antimicrobial mechanism of nisin depends on its crowding and degree of oligomerization, ***Scientific Reports,*** 6:37908 (2016).
7. Panda, S., Yadav, K., Nayak, P.S., **Arakha, M.**[*]**,** & Jha, S. Screening of metal resistant coal mine bacteria for biofabrication of elemental silver nanoparticles, ***Bulletin of Material Science,*** 39.2, 397-404 (2016)**.**
8. Satish, L., Rana. S., **Arakha, M.,** Rout, L., Ekka, B., Jha, S., Dash, P., Sahoo, H. K., Impact of imidazolium based ionic liquids on the structure and stability of lysozyme, ***Spectroscopy Letters,*** 49.6, 383-390 (2016).

***Corresponding Author**

[†] Equal first Author

Patent

Indian Patent: Suman Jha, **Manoranjan Arakha**, Parth Sarthi Nayak, "**Method for continuous production of silver nanoparticle using *Bacillus thuringiensis***" (CBR No. 2977), Ref. N. 201631007436

Conferences

1 **Arakha, M.** & Jha, S. (2015), The effects of interfacial potential on antimicrobial propensity of ZnO nanoparticle, International conference on small science (ICSS), Phuket, Thailand.

2 **Arakha, M.** & Jha, S. (2015), Antimicrobial activity of iron oxide nanoparticle upon modulation of nanoparticle-bacteria interface, Bringing the Nanoworld Together 2015, An oxford instrument Seminar (BTNT-2015), Indian Institute of Technology, Madras, Chennai, India.

3 **Arakha, M.,** Saleem, M., Mallick, B.C., & Jha, S. (2015) The effects of interfacial potential on antimicrobial propensity of ZnO nanoparticle, National Symposium on Biophysics and Golden Jubilee Meeting of Indian Biophysical Society, Jamia Millia Islamia, New Delhi, India.

4 **Arakha, M.** & Jha, S. (2014) The effects of chitosan coating on antimicrobial propensity of Fe_3O_4 nanoparticle, 4^{th} International Science Congress (ISC-2014), Pacific University, Udaipur, Rajasthan, India.

5 **Arakha, M.** & Jha, S. (2013), Synthesis, characterization and concentration dependent inhibitory effect of ZnO nanoparticles on bacterial colony formation, International conference on nanotechnology (ICNT 2013), Haldia Institute of Technology, Kolkata, India.